ABSTRACT

Title of Dissertation: ENABLING THE DISCOVERY AND CHARACTERIZATION OF NEW WORLDS VIA SPACE-BASED DIRECT IMAGING

Ellis Bogat
Doctor of Philosophy, 2026

Dissertation Directed by: Professor Benedikt Diemer
Department of Astronomy
Dr. Joshua Schlieder
NASA's Goddard Space Flight Center

The demographics and atmospheric properties of giant exoplanets reveal key insights into the formation and evolution of planetary systems. The occurrence rate of giant planets is known to correlate with both orbital semimajor axis and host star mass, however the exterior regions (beyond 10 au) around the lowest-mass stars (M dwarfs) have remained chronically under-investigated. In addition, giant planets form at high temperatures and cool gradually, which results in significant atmospheric changes over million-year timescales. Observations of giant planets at a range of planet ages are thus needed to constrain models of their atmospheric evolution. This thesis approaches such observational challenges with the direct imaging technique, which simultaneously provides sensitivity to wide-orbit giant planets and allows the direct characterization of atmospheric properties.

First, I completed the data reduction and analysis of a JWST NIRCam survey of nine

nearby, young M dwarf stars to search for planetary-mass companions (JWST GTO 1184, PI Schlieder). This study achieved unprecedented mass sensitivity for wide-orbit giant planets, and placed the first occurrence rate constraints on sub-Jupiter-mass exoplanets beyond 10 au around M dwarfs to be < 0.10 and < 0.16 objects per star with 1- and 3-σ confidence respectively. Additionally, we identified a marginally significant exoplanet candidate near the target 2M J0944.

Second, I led a follow-up observation campaign to attempt the confirmation of the planet candidate near 2M J0944 (JWST GO 3840, PI Bogat). We executed a similar observing strategy as in GTO 1184 with an increased exposure time, however this resulted in a non-detection and thus the dismissal of that source as a possible exoplanet. We did however redetect two extended sources which we show via astrometric and photometric analysis to be background galaxies, highlighting the unparalleled flux sensitivity of JWST NIRCam.

Finally, I explored the feasibility of observing mature (age > 1 Gyr) giant planets in reflected, visible light with the soon-to-launch Roman Coronagraph. I performed modeling of confirmed planets discovered by the radial velocity technique, quantified the probability of successful detection with the Roman Coronagraph during the first 18 months of its primary mission, and identified the planet upsilon Andromedae d as the best target for the first reflected light observation of an exoplanet.

This collection of work has leveraged emerging technology and observation strategies in space-based direct imaging to enable new demographics constraints and to open novel discovery space for benchmark giant exoplanets.

ENABLING THE DISCOVERY AND CHARACTERIZATION OF NEW WORLDS VIA SPACE-BASED DIRECT IMAGING

by

Ellis Bogat

Dissertation submitted to the Faculty of the Graduate School of the
University of Maryland, College Park in partial fulfillment
of the requirements for the degree of
Doctor of Philosophy
2026

Advisory Committee:
Professor Benedikt Diemer, Chair/Advisor
Dr. Joshua Schlieder, Co-Advisor
Professor Megan Weiner Mansfield
Professor Ronald Walsworth
Dr. Julien Girard

Preface

The work presented in Chapter 2 has been published in the Astronomical Journal (AJ) as "Probing the Outskirts of M Dwarf Planetary Systems with a Cycle 1 JWST NIRCam Coronagraphy Survey" as a first-author paper [1] and is presented here with minimal modification. I led the data reduction, image analysis, and interpretation of the results; my collaborator Kellen Lawson contributed atmospheric models; my collaborators Yiting Li and Michael Meyer contributed population synthesis modeling for demographics analyses; and my advisor Joshua Schlieder provided the initial data, general guidance, and feedback on the manuscript.

The work in Chapter 3 is a complete paper manuscript that has been circulated to coauthors and will be submitted shortly to AJ as a first author paper. The work conducted in this chapter was enabled by the JWST General Observer (GO) program 3840 which I led as PI, with co-PI Joshua Schlieder.

Chapter 4 contains analysis and results which were driven by mission requirements for the Roman Space Telescope Coronagraph Instrument. This work was formally delivered to the Roman Coronagraph Community Participation Program for integration into observation plans on January 15, 2026. I co-developed the open-source software used for orbit propagation and detection probability calculations with my collaborator Clarissa Do O (now hosted on GitHub[1]), and received guidance on the mission priorities and analysis strategy from Vanessa Bailey and Marie Ygouf. This work will be expanded into a paper manuscript for publication in AJ.

[1] https://github.com/clarissardoo/roman-planets-table

Dedication

To all those who have looked to the stars for answers.

Acknowledgments

This thesis would not have come together without the unwavering support of my advisor, Josh Schlieder. Thank you for always encouraging me, for instilling independence and confidence in my work, and for reassuring me that as astronomers we are all stumbling around in the dark together.

Thank you also to my committee members Benedikt Diemer, Megan Weiner Mansfield, Ronald Walsworth, and Julien Girard for your time, support, and guidance over these past years.

I would also like to thank my former advisor Tad Komacek, whose rampant enthusiasm and encyclopedic knowledge of the ArXiv will always be inspiring to me. Oxford is lucky to have you.

To my collaborators and friends in the STScI Extrasolar Planetary Systems Imaging Group, thank you for adopting me as one of your own. And to those in the Roman Coronagraph CPP, you have all provided invaluable mentorship to me, and made me feel truly welcome in the direct imaging community.

To my fellow grad students at UMD, and especially to my dear officemates Katya and Serena, it has been a privilege to step into the world of academia with you all. I will treasure the memories of ACE coffee hours, BANG! seminars, craft nights, and gym sessions. We made it through radiative class, and we can make it through anything.

I must of course also thank my family: especially Mom, Dad, and Dave for giving me the

best possible foundation to make the most out of life; Antonio for always challenging the way I think; Nana for being an ever-present hug in good times and bad, and Grandpa for indulging my endless questions about electricity which clearly spiraled out of control.

To my dear friends in DC (and Maryland and Virginia), thank you for making me feel like a regular, sane person while undertaking the monumental task of an astronomy PhD. Thank you for being nerds and hippies and fighters and thinkers and wanderers. Thank you for being people I have looked up to and leaned on. Thank you all.

And finally to the littlest, but not least, member of my world: Thank you Egg for being the cat every moody academic dreams of.

Table of Contents

List of Tables

List of Figures

List of Abbreviations

2MASS	Two Micron All-Sky Survey
ADI	Angular Differential Imaging
AJ	The Astronomical Journal
AO	Adaptive Optics
AU	Astronomical Unit
B25	Bogat et al. 2025 [1]
BD	Brown Dwarf
DI	Direct Imaging
FOV	Field of View
GO	General Observer
GP	Giant Planet
GPI	Gemini Planet Imager
GTO	Guaranteed Time Observation
HGCA	Hipparcos-Gaia Catalog of Accelerations
HIP	Hipparcos
HLC	Hybrid Lyot Coronagraph
IPAC	Infrared Processing and Analysis Center
IR	Infrared
IWA	Inner Working Angle
JADES	JWST Advanced Deep Extragalactic Survey
JWST	James Webb Space Telescope
KL	Karhunen-Loève
KLIP	Karhunen-Loève Image Processing
L2	Second Sun-Earth Lagrange Point
LOCI	Locally Optimized Combination of Image
MAST	Barbara A. Mikulski Archive for Space Telescopes
MCMC	Markov Chain Monte Carlo
MCRDI	Model-Constrained Reference Differential Imaging
MIRI	Mid-Infrared Instrument
NASA	National Aeronautics and Space Administration
ND	Neutral Density
NIRCam	Near Infrared Camera
OWA	Outer Working Angle
PCA	Principal Component Analysis

PSF	Point Spread Function
RDI	Reference Differential Imaging
RMS	Root-Mean-Squared
Roman	Nancy Grace Roman Space Telescope
RV	Radial Velocity
SED	Spectral Energy Distribution
SNR	Signal-to-Noise Ratio
SNRE	SNR per Resolution Element
SPHERE	???
TVAC	Thermal and Vacuum
VLT	Very Large Telescope
WCS	World Coordinate System
WFE	Wavefront Error
WFI	Wide Field Instrument

Chapter 1: Introduction

1.1 Motivation and Outline

Great discoveries in astronomy have the tendency to render philosophical quandaries suddenly scientific. The first detection of planets outside our own Solar System was one such discovery. In 1992, A. Wolszczan and D. Frail detected two planets orbiting the neutron star PSR1257+12 [2], and shortly thereafter Michel Mayor and Didier Queloz discovered a planet orbiting the Sun-like star 51 Pegasi [3]. These results launched the field of extra-solar planet (a.k.a. exoplanet) astronomy, which has enabled the quantitative investigation of questions like: How did our Solar System form? How unique is our world? And are we alone in the Universe?

While many theories of planetary system formation had been posited throughout the 20th century [4–6], these were only founded on observations of a single outcome of the planet formation process – our Solar System. The assumption that the inner region of a planetary system should contain small terrestrial planets (like Mercury, Venus, Earth, and Mars) and the outer region should host giant planets (like Jupiter, Saturn, Uranus, and Neptune) was immediately challenged by Mayor and Queloz's discovery of the planet 51 Pegasi b, a Jupiter-mass planet which completed a full orbit of its host star every 4.2 days. Suddenly it was apparent that not every planetary system was like ours, and that our theory of planetary formation must be able to account for a wide diversity of possible planet types and planetary system architectures.

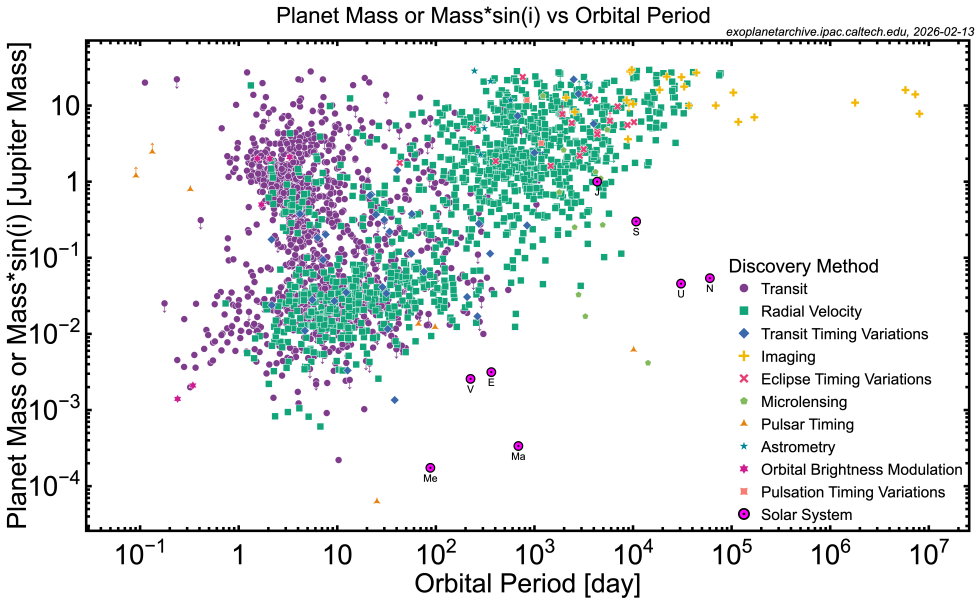

Figure 1.1: Every confirmed exoplanet on the NASA Exoplanet Archive as of February 13th 2026 [7], with the x axis showing the orbital period in days and the y axis showing planet mass (or mass times the sine of the orbital inclination in the case of planets discovered by radial velocity measurements). The marker shape and color show the method by which each planet was discovered, and the separate regions of parameter space probed by each method are clearly visible. The Solar System planets are shown by the magenta dotted circles.

Advances in observational techniques have exponentially increased the rate of exoplanet detections in the last few decades, and at the time of writing over 6,000 confirmed exoplanets have been cataloged by NASA IPAC Exoplanet Archive, as shown in Figure 1.1 [7]. With access to so many unique instances of planetary formation, we can now complete population level demographics studies and identify relationships between parameters such as planet mass, host star mass, orbital period (the time required for a planet to complete one orbit), and host star metallicity (the ratio of iron to hydrogen in the star compared to that of the Sun), which provide insight into the planet formation process.

While many exoplaneteers are particularly interested in the formation and evolution of potentially habitable, Earth-like worlds, it is critical to understand the environment in which these worlds form. In our own Solar System, Jupiter is theorized to have had significant impacts

on the formation of the inner planets, sculpting the early structure of the disk from which the planets formed, and influencing the delivery of water to Earth from the icy outer reaches of the Solar System [8, 9]. The Grand Tack model [10–12] and the Early Instability model [13] both invoke the migration of Jupiter and Saturn to explain the current day architecture of the inner Solar System. By extension, the observation of Jupiter-analog exoplanets provides context for the inner-region planets we have already discovered and expands the population that we can sample for hints about habitability and planet evolution throughout the galaxy.

Our current understanding of giant planets (GPs) has not deviated significantly from the structural theories of Hubbard, which propose a solid core, large gas envelope, and molecular atmosphere [14]. It is broadly understood that planets form from the disk of gas and dust which surrounds a forming star, however, two competing theories exist to explain how giant planets in particular can grow to their gargantuan masses before the gas portion of the disk is dissipated by the star's radiation [15]. In the core accretion (CA) model [16, 17], dust in the disk gradually coalesces into pebbles and eventually into self-gravitating planetary cores called "planetesimals". These planetesimals can then exhibit runaway growth by gravitationally attracting nearby solid material in the disk, and once they have reached several times the Earth's mass, their gravity is strong enough to attract a massive gas envelope. Due to the low density of material in outer regions of the disk, simulations of CA struggle to form giant planets beyond a few au (the Earth-Sun distance, a.k.a. "Astronomical Unit") [18–21]. By contrast, the gravitational instability (GI) model [22, 23] suggests that giant planets could form by the fracturing of the disk into dense clumps which then undergo gravitational collapse. This model preferentially forms planets more massive than Jupiter at separations beyond 30 au from the star, as the conditions required for collapse are most readily achieved in the outer regions of the most massive disks [24]. Each of

these formation mechanisms predicts different initial temperatures at the time of planet formation, with CA resulting in much cooler temperatures than GI [25]. Over time, a planet will cool to reach an equilibrium with the incident radiation from its host star, but within the first 100 Myr, measurements of the planet's luminosity can constrain its temperature and assist in distinguishing the formation mechanism [26].

While it is nearly impossible to determine any mature (age $\gtrsim$ 1 Gyr) planet's formation mechanism definitively, studies of GP populations at the demographic level have provided significant insight into the question. In general, $\sim 20\%$ of Sun-like stars host giant planets (defined as planets with mass > 0.1 M_{Jup}) [27]. GP discoveries from transit surveys (where the periodic passing of a planet in front of its host star produces a detectable dimming effect) and radial velocity surveys (RV, where the gravitational force of a planet on its host star causes the starlight to be cyclically Doppler shifted) show that giant planets are comparatively rare interior to 1 au (~ 0.05 GPs per star), and become more common between 2-6 au (0.1-0.2 GPs per star) [27, 28]. These surveys have also revealed a trend in GP occurrence which scales with both host star mass and metallicity. Microlensing studies (where a star-planet system magnifies the light of a background star) similarly support the peak of GP occurrence in the 1-10 au region [29, 30]. Finally, the outer reaches of planetary systems can be explored via the direct imaging (DI) method, where the starlight and planet light are resolved and detected separately. DI surveys have historically only been sensitive to planets more massive than ~ 5 M_{Jup}, and shown their occurrence to be $\lesssim 0.05$ GPs per star beyond 10 au [31, 32]. Due to this limitation, the occurrence of GPs less massive than Jupiter (a.k.a. sub-Jupiters) beyond 10 au has remained largely unconstrained.

The peak of GP occurrence near 1-10 au may be explained physically by the presence of the water "ice line" at ~ 3 au for Sun-like stars, where the disk temperature falls low enough

for water to condense into solid materials and contribute to planetesimal formation in the CA scenario [33,34]. The increase in GP occurrence with host star mass and with host star metallicity also suggest formation by CA, as these characteristics are understood to correspond to the budget of solid material in the circumstellar disk from which to build planet cores [27, 35, 36]. The GPs which have been detected by direct imaging, however, are largely assumed to have formed by GI due to their high masses and wide separations [18–21, 24]. The lack of detection sensitivity to wide-orbit sub-Jupiters thus invites the question: do these planets exist? And if so, do they represent the low-mass tail of planet formation by gravitational instability or the wide-orbit tail of formation by core accretion?

The planetary systems surrounding M dwarf stars (defined as having a mass less than or equal to 0.6 times the solar mass, $M_\odot$) draw particular interest from the exoplanet community. M dwarfs account for $\sim 70\%$ of the stars in the Galaxy [37], and thus host the majority of planetary systems in the universe. They also provide favorable conditions for planet detection compared to Sun-like stars as, for a given planet, RV and microlensing signals are amplified by a lower host star mass, transit signals are amplified by a lower stellar radius, and direct imaging is made easier by a lower stellar luminosity (as detailed in § 1.2.1). Transit and RV surveys of the inner regions of M dwarf planetary systems show that M dwarf disks tend to generate more planets with lower masses, while Sun-like planetary systems contain fewer but more massive planets [38,39,39–44]. However, these results are generally limited to the inner 10 au of the planetary systems.

Extrapolations of the empirical RV planet occurrence rates performed by Fernandes et al. (2019) [28] have predicted the occurrence of giant planets (mass $> 0.1 M_{Jup}$) between 1 and 100 au to be $\sim 30\%$, which is increased significantly compared to the occurrence of super-Jupiters (mass $> 1 M_{Jup}$) being 6% for the same separation region. This is supported by the Fulton et

al. (2021) prediction of GP occurrence between $0.3-30$ au to be 34%. While these estimates are expected to be dependent on host star mass, they do imply together that sub-Jupiters $(0.1-1\mathrm{M_{Jup}})$ should be more common than super-Jupiters, and that observations sensitive to wide-orbit sub-Jupiters should result in a higher detection yield than those only sensitive to super-Jupiters. Furthermore, microlensing surveys suggest that wide-orbit sub-Jupiters around M dwarfs may in fact be common, with a possible peak in the mass distribution between 0.03 and 0.13 $\mathrm{M_{Jup}}$ beyond the snow line [30].

The results outlined above demonstrate a clear need for the exploration of wide-orbit giant planets at a range of system ages and host star masses, and with sensitivity to planets below the mass of Jupiter. Such observations can be achieved with the direct imaging method, which provides access to GPs beyond 10 au. The remainder of this chapter will provide an introduction to the theory and practice of direct imaging (§ 1.2), as well as a summary of the work completed in this thesis (§ 1.3).

1.2 Directly Imaging Exoplanets

The overwhelming majority of planet discoveries has been through the indirect techniques of transit photometry and radial velocity (RV), most sensitive to the innermost regions of planetary systems, as shown in Figure 1.1 [7]. More widely separated exoplanets have both a lower probability of transit and a reduced gravitational impact on the host star, vastly decreasing observational completeness in these kinds of surveys [45, 46]. The sensitivity of the absolute stellar astrometry technique actually improves with planet-star separation, however confirmation of candidate signals requires extremely long temporal baselines (on the order of decades) to span

the full orbital period [47]. Microlensing is also sensitive to wide-orbit giant planets, however these events are intrinsically rare and the large distances to typical microlensing systems render follow-up characterization extremely challenging [48]. Direct imaging, that is resolving the flux from the planet separately from the starlight, may then be the best avenue to detect, confirm, and characterize new exoplanets in the exterior regions of their planetary systems.

DI methods have already been proven effective on the ground with instruments like the Gemini Planet Imager (GPI), and in space with the Hubble Space Telescope and the James Webb Space Telescope (JWST) NIRCam and MIRI instruments [49–51]. Furthermore, confirmation of a candidate planet does not require the full orbital period to be observed. As DI targets are very nearby, they typically exhibit significant proper motion; thus, within a few months a companion candidate which is in fact an unbound or background object will appear be "left behind" in the sky while a bound object can be observed to be traveling with the host star [52]. The final distinguishing characteristic of the direct imaging technique is its sensitivity to young systems. Due to their intrinsic thermal emission from gravitational contraction, younger planets are actually easier to detect directly compared to their older, cooler counterparts [53]. By contrast, young planets are more difficult to detect via transits and RV due to the increased variability of young host stars [54, 55]. The unique access to newly formed planets via direct imaging provides insights into early planetary system architecture, planet migration and formation pathways, and the thermal evolution of giant exoplanets.

1.2.1 DI Theory

The two main characteristics which make direct imaging (DI) so challenging are the angular planet-star separation (how far apart the planet and star are on the sky) and the planet-star flux contrast (how much fainter the planet is compared to the star). To determine the rough requirements for directly imaging an exoplanet, let us consider the following example case: a young (100 Myr) Jupiter-analog exoplanet orbiting 10 au from a solar-type star, observed at infrared (IR) wavelengths.

The angular resolution required to detect a star and exoplanet separately is found simply by geometry:

$$\theta_{\text{sep}} = \frac{r}{d} \times 206265\text{"} \tag{1.1}$$

where r is the physical distance between the star and planet projected onto the plane of the sky, d is the distance to the system, and θ_{sep} is measured in arcseconds. Therefore to resolve the young Jupiter analog, we need an angular resolution of approximately 1.0". Then we can use Lord Rayleigh's criterion for angular resolution:

$$\theta_{\text{limit}} = \frac{\lambda}{D} \times 1.22\text{"} \tag{1.2}$$

to determine that a primary mirror only 1 meter in diameter is required to resolve the young Jupiter analog at a wavelength of 4 microns in the diffraction-limited case.

We can then calculate a young planet's luminosity by using the Stefan-Boltzmann law:

$$L_{\text{p}} = 4\pi R_{\text{p}}^2 \sigma T_{\text{eff}}^4 \tag{1.3}$$

where σ is the Stefan-Boltzmann constant and T_{tot} is the effective temperature such that

$$T_{\text{eff}}^4 = T_{\text{int}}^4 + T_{\text{eq}}^4 \tag{1.4}$$

Here, T_{int} is the temperature due to the interior heat of the planet, and T_{eq} is the equilibrium temperature induced by the irradiance from the host star [56]. Given the fact that the temperatures in the above equation are raised to the fourth power, we can see that even a small difference between T_{int} and T_{eff} will cause one heat source to completely dominate the other.

For a planet whose temperature (and thus luminosity) is dominated by stellar heating, L_{p} can be estimated by assuming that the planet reflects some fraction of the starlight incident upon it (described numerically by the bond albedo) and then absorbs and re-radiates the rest isotropically as a blackbody. This gives us a planet luminosity at a particular wavelength of

$$L_{\text{p}}(\lambda) = \frac{R_{\text{p}}^2}{4r_{\text{p}}^2} L_*(\lambda) \times (1 - A_{\text{B}}(\lambda)) \tag{1.5}$$

where R_{p} is the planet radius, r_{p} is the physical distance from the planet to the star, and $L_*(\lambda)$ and $A_{\text{B}}(\lambda)$ are the stellar luminosity and planetary bond albedo respectively at the given wavelength. Substituting the luminosity using Equation 1.3, we can rearrange to find the equilibrium temperature:

$$T_{\text{eq}} = \left(\frac{L_*(1 - A_{\text{B}})}{16\sigma\pi r^2} \right)^{1/4}. \tag{1.6}$$

Assuming an IR bond albedo for Jupiter of 0.343 [57] the estimated equilibrium temperature of our Jupiter analog at 10 au is 79 K.

For a planet whose temperature is dominated by its internal heat, predictions of T_{int} are

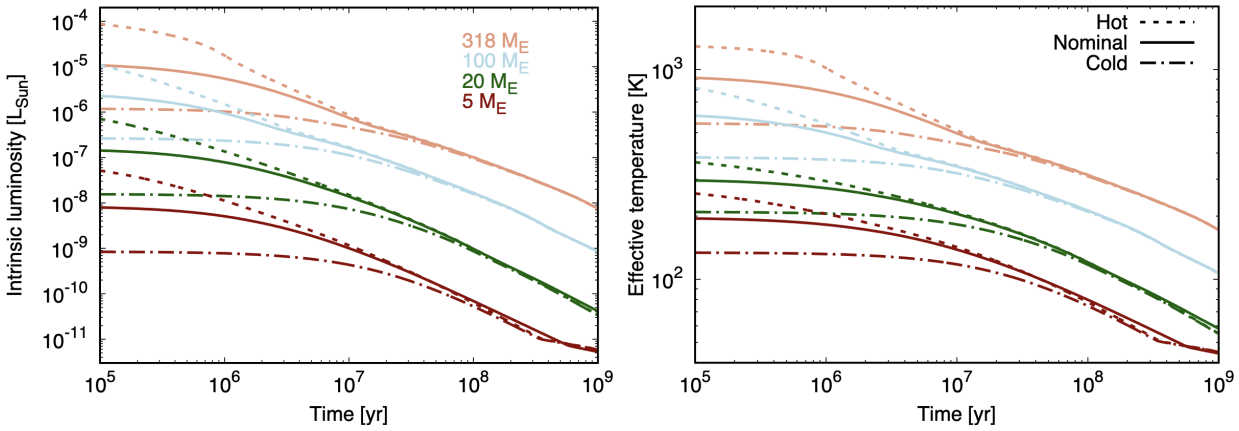

Figure 1.2: Cooling curves from Linder et al. 2019 [58] Fig. 9 showing a dependence on post-formation temperature. The intrinsic luminosity of sub-Jupiter exoplanets with different masses and arbitrary initial temperatures is shown as a function of time elapsed since formation. As different formation theories (gravitational instability vs. core accretion) predict different initial temperatures, the independent measurement of a planet's mass, age, and luminosity can potentially reveal its formation mechanism [26].

highly model dependent. In general, planets have a high temperature at formation, from the conversion of gravitational potential energy into heat, and then they cool over time, as shown by the Linder et al. models in Figure 1.2 [58]. However, the exact temperature and cooling rate depends on planet mass, age, formation mechanism, interior structure, and atmospheric composition, among other factors. TMORBIhese parameters are extremely challenging to constrain a priori, but measurements of exoplanet luminosities via direct imaging, coupled with measurements of the mass and radius from other methods, can potentially allow us to distinguish between the competing formation mechanism theories of direct gravitational collapse (a.k.a. "hot start") and core accretion (a.k.a. "cold start"), which can cause the planet luminosities at the end of accretion and the beginning of cooling to differ by as much as a factor of 100 [26, 59]. For the case of a Jupiter-mass planet with an age of 100 Myr, the Linder et al. cooling curves predict that $T_{\rm int} \simeq 400K$, which dominates significantly over the equilibrium temperature of 79 K found above.

The flux contrast is then found by a simple ratio: the planet flux from internal heat divided by the host star's flux. Using a simple blackbody model for a G2V star ($T \simeq 5800$ K), and the nominal cooling model in Figure 1.2 for a young Jupiter ($T_{\rm int} \simeq 400$ K), we find that its flux contrast at 4 microns is on the order of 10^{-6} at an age of 100 Myr [58]. We note here that the same planet orbiting an M dwarf star with $T \simeq 3000$ K would result in a much shallower flux contrast requirement of $\sim 10^{-4}$, due to the steep temperature dependence on the total stellar luminosity.

Predicting flux contrasts for observations in visible wavelengths is more complicated as the flux is dominated by starlight reflected by the planet, rather than by the planet's thermal emission. In this case, the planet's brightness depends not only on the albedo, but also on the portion of the planet's illuminated face which is visible from the perspective of the observer which changes over the course of its orbit. We can quantify how much of the illuminated face of the planet is visible using the observer-star-planet angle, a.k.a. phase angle:

$$\alpha = \cos^{-1}\left(\frac{z_{\rm p}}{r}\right), \tag{1.7}$$

where r is the physical distance between the planet and star projected onto the plane of the sky, and we have used the approximation that the observer-star distance is much greater than the planet-star distance. By this definition, a phase angle of 0° corresponds to the planet appearing directly behind the star and thus being fully illuminated, and a phase angle of 180° corresponds to the planet appearing directly between the star and the observer such that only the dark side is visible. The flux ratio is then given by

$$\frac{F_{\rm p}}{F_*} = \left(\frac{R_{\rm p}}{r_{\rm p}}\right)^2 A_{\rm g}(\lambda)\Phi(\alpha(t),\lambda). \tag{1.8}$$

Here, A_g is the geometric albedo as a function of wavelength λ, which describes the observed brightness of a celestial body at a phase of 0° compared to an idealized sphere which scatters all incident light such that the reflected intensity depends only on the observer angle rather than the angle of incidence (a.k.a a Lambertian surface). The term Φ in the above equation is then the scattering law (a.k.a "phase curve") which describes variation of planet flux as a function of phase, normalized such that $\Phi(0^\circ) = 1$ and $\Phi(180^\circ) = 0$. While the exact form of a phase curve depends on the microphysical scattering properties of the planet's atmosphere, a common approximation is a Lambertian phase curve [60], which assumes the planet's atmosphere acts as a Lambertian surface and is given by

$$\Phi(\alpha) = \frac{\sin\alpha + (\pi - \alpha)\cos\alpha}{\pi}. \tag{1.9}$$

Assuming the geometric albedo of Jupiter in visible light to be 0.538, we can estimate the flux ratio of a Jupiter-radius planet 10 au from a Sun-like star to be $\sim 1.2 \times 10^{-9}$ at full phase, increasing the difficulty of the detection by about three orders of magnitude compared to IR observations of thermal emission. However, at full phase, the planet would be directly behind the star and thus unobservable, making even this extreme contrast only a lower limit. As the equation for the flux ratio in reflected light does not depend directly on the host star luminosity as in the IR case, observing an intrinsically dimmer host star does not reduce the contrast in this case. However, the contrast in reflected light does depend on the physical distance between the planet and star, thus a true Jupiter analog (with semimajor axis 5.2 au) would have a flux contrast at full phase of $\sim 4.5 \times 10^{-9}$. In short, direct observations of giant exoplanets in visible, reflected light will be extremely challenging to execute as compared to young exoplanets in thermal IR

emission.

1.2.2 DI In Practice

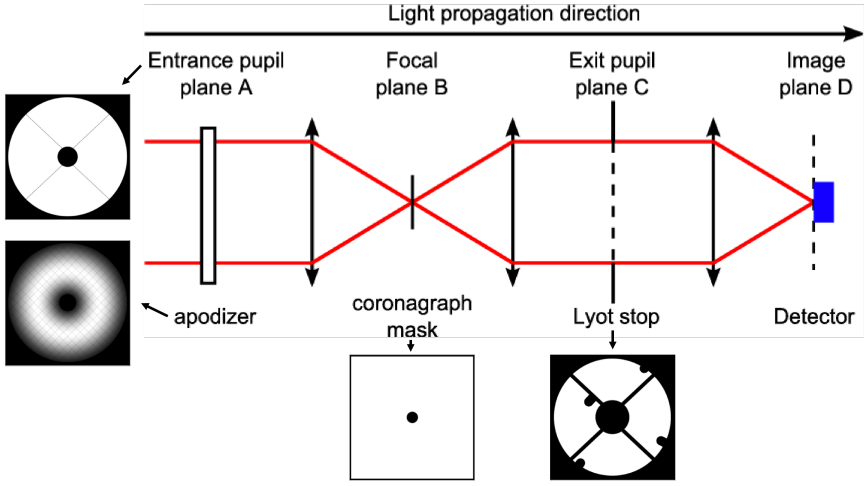

Figure 1.3: Schematic of the apodized-pupil Lyot Coronagraph hosted on the Gemini Planet Imager, adapted from Fig. 1 of [61] and Figs 2 and 3 of [62]. The red lines indicate the optical path as light propagates from left to right. At plane A, an entrance pupil restricts the incoming light to a particular field of view (FOV), and an apodizer suppresses light diffraction around the hard edges of the entrance pupil. At plane B, the light is focused and a coronagraph mask blocks light at the very center of the FOV. At plane C, the light is defocused and the Lyot stop suppresses light diffracted by the coronagraph mask. At plane D, the light is focused onto the detector, and approximately 99% of the starlight has been suppressed.

To image objects with such high flux contrast and low angular separation, a significant portion of the light originating from the host star must be blocked or otherwise diverted away from the detector. This can be achieved in large part with a Lyot coronagraph, originally developed to study the corona of the Sun [63]. The optical path of the instrument (shown by the schematic in Figure 1.3) is comprised first of the entrance pupil, i.e. the opening through which light enters the instrument, which shows the "shadow" of the secondary mirror and support struts. Then an occulting mask in the focal plane suppresses light originating from the center of the field of view (FOV), and a specialized "Lyot stop" in the pupil plane suppresses excess starlight that

has diffracted around the occulting mask. The classical Lyot coronagraph design is capable of suppressing all but 1.5% of the starlight, at the cost of also suppressing any planet signal that happens to be too near the center of the FOV. This central region is described by the "inner working angle" (IWA), and is defined as the angle from the center of the coronagraph mask within which 50% or less of the incident light is transmitted. Conversely, the "outer working angle" (OWA) describes the widest angle accessible in the FOV. Since the introduction of the Lyot coronagraph, many modifications have been made to improve the starlight suppression capability. In the case of the Gemini Planet Imager, an apodized-pupil Lyot Coronagraph is used, in which an apodizing mask (whose transmission varies smoothly over the surface) in the entrance pupil plane helps to suppress the diffraction of light around the pupil edges, shown in plane A of Figure 1.3 [62]. Efforts to stabilize the incoming wavefront of the light have also been employed to increase contrast sensitivity. For example, the W. M. Keck Observatory Adaptive Optics (AO) system employs wavefront sensors and deformable mirrors to counteract the wavefront distortions induced by the Earth's atmosphere [64].

Even with the vast majority of incident starlight removed by optical elements, astrophysical sources near the star (a.k.a. off-axis sources) may still be much fainter than the residual starlight that reaches the detector. To address this, a variety of post-processing techniques are employed to separate the flux from off-axis sources from the stellar flux. The simplest is angular differential imaging (ADI, illustrated in Figure 1.4), which makes use of the fact that the orientation of the stellar point-spread function (PSF) is fixed with the orientation of the telescope while astrophysical sources are fixed in the sky. Thus if a system is imaged at two or more different roll angles, the stellar PSF can be measured and removed from the image. However, PSF subtraction via ADI can also result in "self-subtraction," where some of the signal from off-axis sources is also

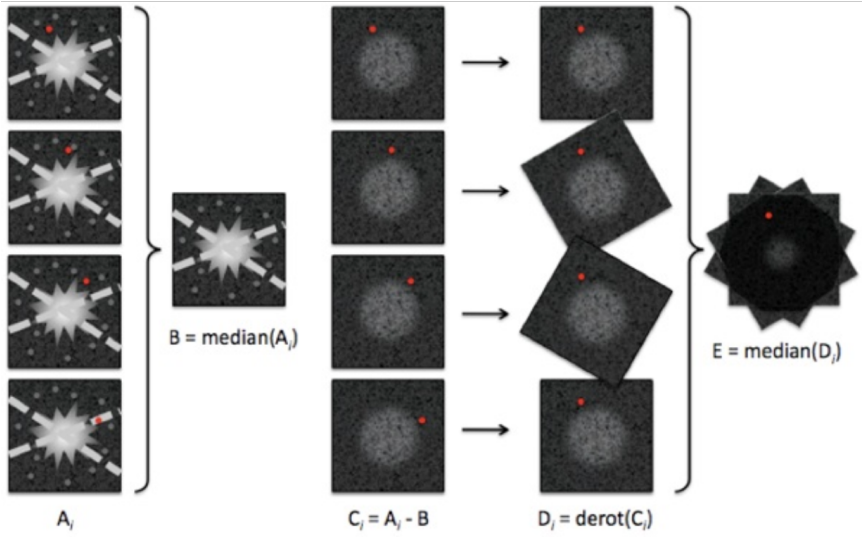

Figure 1.4: Schematic of the Angular Differential Imaging (ADI) method for stellar PSF subtraction in direct imaging, adapted from C. Thalman. First, we image the target system at n roll angles (A_i), where n is at least two. Without de-rotating the images, we find the median of the images A_i to measure the stellar PSF (B) and suppress any off-axis signals by a factor of $1/n$. Then, we subtract the stellar PSF from each image (C_i), derotate them all (D_i), and take the median of those images to isolate the planet signal (E) [65].

removed, especially at small separations from the target star and when the roll angle difference is small.

The second technique relevant to this work is reference differential imaging (RDI, illustrated in Figure 1.5), which uses a reference star to measure the stellar PSF and then subtract it from the science observation [66–68]. Because the stellar PSF is wavelength dependent, it is critical to use a reference star with a spectral type as similar as possible to the science star. It is also possible for artifacts to be introduced to the observation if the reference star has any off-axis sources in its FOV, which may not be possible to verify before observing. To mitigate the effects of spectral differences and potential contaminating off-axis sources, as well the suppression degrading effects of imperfect alignment of the coronagraph mask over the target star, it is possible to observe multiple reference stars and construct a model stellar PSF to subtract from the science observation. This can be achieved with the Karhunen-Loève Image Projection

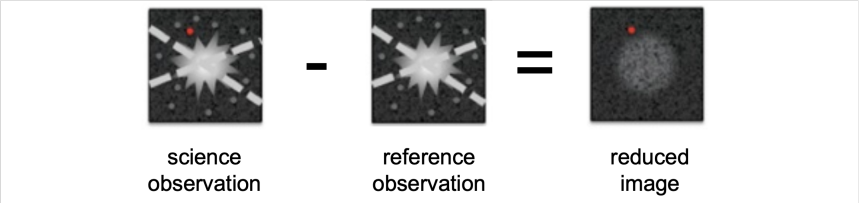

Figure 1.5: Schematic of Reference Differential Imaging (RDI) for PSF subtraction adapted from C. Thalmann. Here, the target system is imaged only once, and a reference system with a star of similar spectral type and no nearby bright object is imaged to measure the PSF. Then the reference PSF is scaled and subtracted from the image to reveal the companion signal. In practice, multiple reference observations may be collected, and an optimal PSF model can be constructed using principal component analysis with Karhunen-Loève eigenimages [66–68].

(KLIP, [67]) algorithm, which uses a Karhunen-Loève transform of the reference observations to build an orthogonal basis of eigenimages that are then fit to the science observation. This can still result in off-axis artifacts and over- or under-subtraction in localized regions of the science FOV, but it does reduce the error in the recovered astrometry and photometry of faint signals as compared to the competing Locally Optimized Combination of Images (LOCI) algorithm for PSF subtraction [69].

The sensitivity of high-contrast a observation is typically described by the "5σ contrast curve." This metric represents the faintest signal that can be detected with a confidence of 5σ as a function of separation from the target star, in units of flux contrast. Many, many contrast curves will be shown throughout this thesis work. Due to the complex data reduction processes described above, contrast curves are typically computed by the injection-recovery technique. This involves "injecting" synthetic planet signals into the data before PSF subtraction, then performing PSF subtraction, and finally assessing the final signal-to-noise ratio (SNR) of the injected planets to determine the lowest planet flux which can be recovered with 5σ confidence. Contrast curves typically reveal a steep slope near the IWA due to residual starlight speckles as well as flux attenuation by the coronagraph, which is referred to as the speckle-limited regime. The curves

tend to flatten out towards the edge of the FOV as background noise becomes the dominant factor, in what is called the background-limited regime. An example contrast curve can be seen in the discussion of early JWST results in the below section.

1.2.2.1 JWST NIRCam Coronagraphy

The James Webb Space Telescope (JWST) is a space-based observatory located at the second Sun-Earth Lagrange point (L2), and is designed for deep studies of the infrared universe. With a 6.5 meter diameter primary mirror, active wavefront sensing, and coronagraph capability with a sub-arcsecond inner working angle, it is a significant advance in absolute flux sensitivity as well as contrast sensitivity for the purpose of directly imaging young, self-luminous exoplanets [70].

The JWST Near InfraRed Camera (NIRCam) instrument is a dedicated imager designed to operate from 2-5 microns, and is equipped with a wide variety of wavelength filters and coronagraphic masks. The widest bandpasses are the most useful for the discovery of faint objects, as they maximize the number of detected photons during a given exposure.

NIRCam's detectors operate using a nondestructive "up-the-ramp" photon counting technique, illustrated in Figure 1.6. The detector records the saturation level of each pixel over a series of "frames" in a "group" spaced evenly in time without clearing the pixels until the end of an"integration," which is composed of a specified number of groups. This allows the observer to fine tune the overall readout method to optimize total data volume and dynamic flux range, as well as to reject individual groups in the event of cosmic ray (CR) hits or other anomalies. Finally, a given "exposure" is composed of a series of integrations, so that photon flux can be

measured over long exposures without over-saturating the pixels. JWST users have the choice of several pre-defined readout patterns which specify the number of frames per group, as well as the number of groups per integration and the number of integrations per exposure. Each of these parameters affect total exposure time, noise level, and risk of pixel over-saturation for a given target [71].

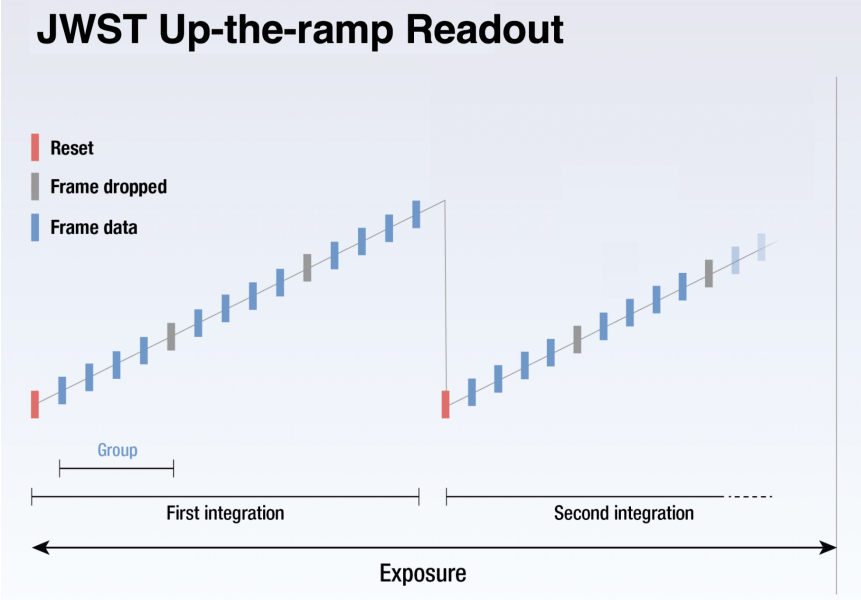

Figure 1.6: A schematic of the JWST "up-the-ramp" detector readout method. Each reading of the detector is one "frame," and the user-selected readout pattern ("RAPID," "MEDIUM8," "DEEP2," etc.) determines the number of frames in a group, the number of frames within each group that are averaged before downlinking, and the number of frames dropped at the end of each group. The user can then also select the number of groups in an integration before the detector is reset to prevent pixel saturation, and the number of integrations in an exposure to reach the desired total exposure time [71].

NIRCam's coronagraphic modes include three round masks and two bar-shaped masks, each with nominal operating wavelength ranges and inner working angles, and which can be paired with a range of wavelength filters. In general, the coronagraph masks suited for longer operating wavelengths have wider inner working angles, so there is a trade-off between the mass sensitivity to young exoplanets in the final images and angular resolution of each coronagraph.

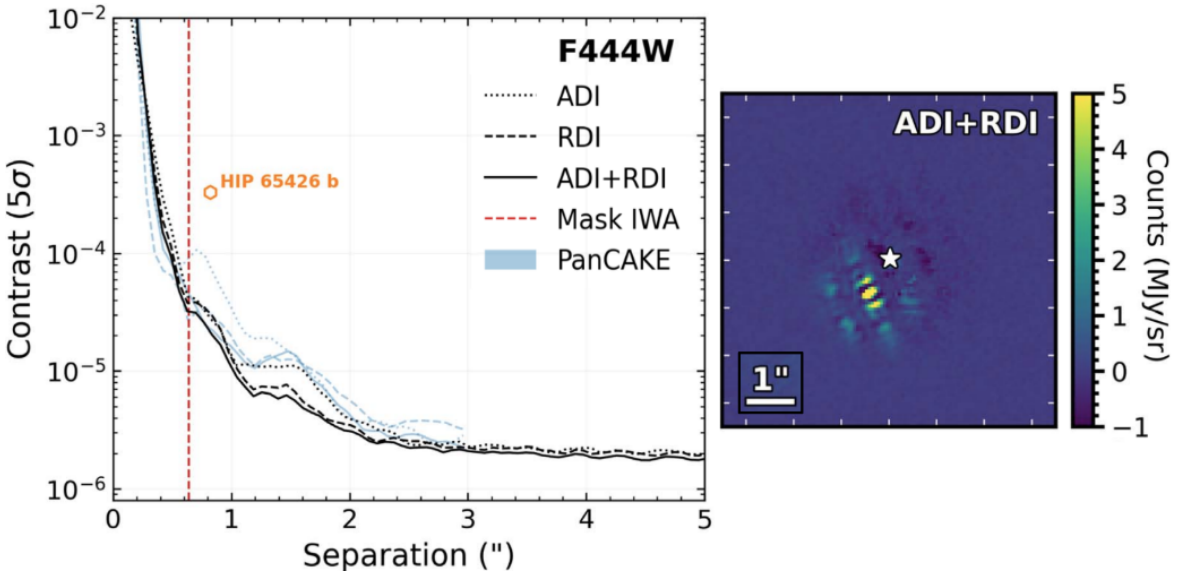

Figure 1.7: Results for the NIRCam coronagraphic observations of HIP 65426b in the F444W filter performed by the JWST Early Release Science team [50]. The 5σ contrast curves are displayed in the left panel, where the black lines show the sensitivity using ADI (dotted lines), RDI (dashed lines), and ADI+RDI (solid lines). Predicted contrast sensitivity from PanCAKE simulations [72] are shown in light blue, and the effective inner working angle (IWA) is shown as a dashed red line. The right panel shows PSF-subtracted data using ADI+RDI, demonstrating a clear detection of HIP 65426 b.

NIRCam coronagraphy has been exercised both in the commissioning and Early Release Science phases of JWST's operation. During commissioning NIRCam successfully observed HD 114174 B, a white dwarf companion to the G5IV-V star HD 114174 A with a flux contrast of 10^{-4} and angular separation of $0.5''$. This observation surpassed the required flux contrast sensitivity within $1''$ and additionally achieved a background limited flux sensitivity of 5×10^{-7} at separations greater than $2''$ [73]. The NIRCam Early Release Science team then completed the first successful direct observation of an exoplanet with JWST: the 14 Myr old super-Jupiter HIP 65426 b with a flux contrast of 4×10^{-6} and separation of $1''$ from its A2V class host star, shown in Figure 1.7. These observations confirmed that JWST NIRCam's coronagraphic modes exceed the predicted performance capability by up to a factor of 10 in flux contrast sensitivity [50] and that JWST would become the premier observatory for the study of young giant exoplanets.

1.2.2.2 The Roman Coronagraph Instrument

NASA's next flagship mission is the Nancy Grace Roman Space Telescope (Roman), with a 2.4 meter primary mirror and an expected launch to L2 in late 2026. While the Wide Field Instrument (WFI) is Roman's only full science instrument, its Coronagraph Instrument will act as a technology demonstration and will carry major upgrades in space-based high-contrast imaging capability. In order to meet its requirement to achieve a flux contrast sensitivity of 10^{-7} within planet-star separations of $0.5''$, the Roman Coronagraph will employ several new technologies and operating strategies [74]. Most notably, it will demonstrate active wavefront sensing with deformable mirrors in space for the first time. The use of deformable mirrors on the ground has become standard practice in "adaptive optics" (AO), where perturbations to the wavefront of incoming light due to turbulence in the Earth's atmosphere are counteracted by fast acting sensors and optical elements [75]. While operation in space means there is no atmosphere to perturb the wavefront and thus blur the PSF, the same technologies can be used to divert additional starlight not suppressed by the coronagraph away from the detectors. This process is referred to as "digging the dark hole," and is the key to achieving the 100- to 1000-fold improvement in contrast sensitivity expected by the Roman Coronagraph, as compared to current state-of-the-art high-contrast imaging facilities (see Figure 1.8).

As a technology demonstration instrument, the Roman Coronagraph has only one fully supported observing mode: a Hybrid Lyot Coronagraph (HLC) operating in Band 1 (575 nm) with an IWA and OWA of 3 λ/D ($\sim 150''$) and 9 λ/D ($\sim 450''$) respectively. The central wavelength of Band 1 corresponds to visible yellow light, meaning that this instrument will be operating in a fundamentally different wavelength regime compared to the IR bands used by JWST NIRCam.

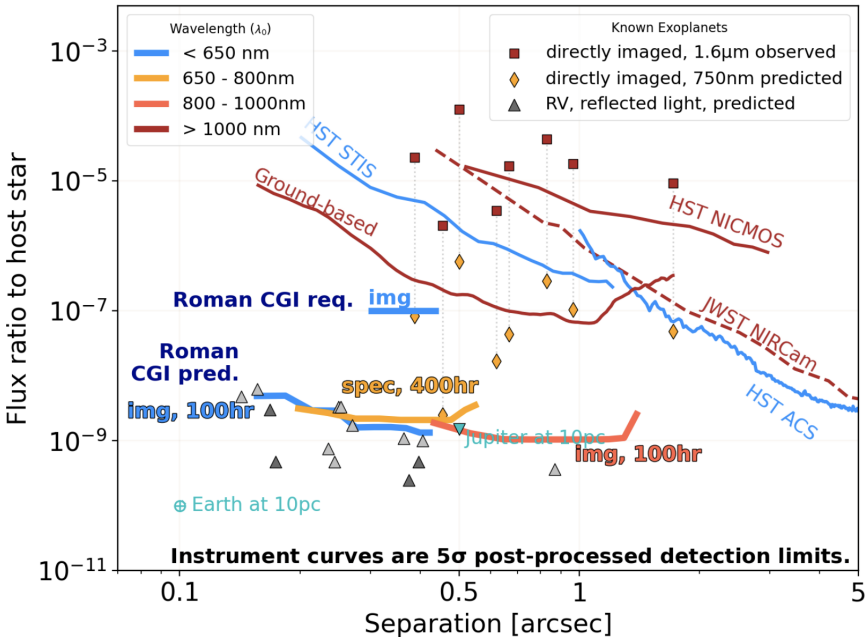

Figure 1.8: Expected contrast sensitivity of the Roman Coronagraph, shown in the bold lines for Band 1 in blue, Band 3 in yellow, and Band 4 in orange, assuming optimistic instrument performance. For comparison, the sensitivity extant high-contrast imaging instruments are shown in the blue lines for wavelengths less than 650 nm and in the red lines for wavelengths greater than 1 micron. Exoplanets and brown dwarfs which have been imaged previously are shown with their measured IR contrast in the red squares and predicted contrast at 750 nm in the yellow diamonds. The predicted reflected light flux contrast at quadrature of planets which were considered to be the best targets for reflected light imaging as of 2023 are shown by the gray triangles, and the flux contrast of a Jupiter and Earth analog at quadrature 10 pc away are shown in teal. Figure adapted from Bailey et al. (2023) [76].

As current optimistic performance estimates for the Roman Coronagraph in Band 1 predict a contrast sensitivity on the order of a few $\times 10^{-9}$, giant planets orbiting within $\sim$ 5 au of their host stars could be detected in visible reflected light for the first time (see § 1.2.1). If the Band 1 observations are timely and successful, we may also be able to exercise several "best-effort" observing modes, including spectroscopic capabilities in Band 3 (from 669-791 nm, visible red) and wide FOV (6-20 λ/D) observations in Band 4 (825 nm, deep red/NIR).

Each Roman Coronagraph observing mode would provide critical tools for the characterization of both self-luminous objects at visible wavelengths and mature planets in visible,

reflected light. In particular, observations of reflected light planets at multiple orbital phases would allow the characterization of the phase curve and potentially distinguish between Lambertian, isotropic, and other scattering functions [77]. These detections would also improve our knowledge of the planets' orbits, enabling planet mass measurements which are independent of atmospheric models [78, 79]. Spectroscopic observations, which are expected to be sensitive to methane absorption, would provide insight into the atmospheric composition of giant planets, providing constraints on cloud properties and formation mechanisms [80].

In addition to the science gained from the photometric and spectroscopic characterization of giant exoplanets, the Roman Coronagraph will be a major step towards the future Habitable Worlds Observatory (HWO) [81]. The driving goal of the HWO is to image an Earth-like planet orbiting a Sun-like star, which will require a flux contrast sensitivity on the order of 10^{-10} to 10^{-11} within $0.3''$. It is expected to target nearby systems, some of which host planets confirmed by indirect detection methods (namely RV and astrometry), and will need to be able to propagate uncertainties in the planet's orbital configuration and atmospheric composition to predict the location and brightness of a given planet over time and plant its observations [82]. With sensitivity to exoplanets in reflected light for the first time, the Roman Coronagraph will provide the opportunity to test the complex observation scheduling processes which will be critical to the success of the HWO mission.

1.3 This Work

The theme of work undertaken in this thesis is to advance our understanding of the demographics of giant planets and to enable novel discovery space via direct imaging with emerging

space-based coronagraphic techniques. In the following chapters I will address two open questions within this topic: What are the demographics of wide-orbit sub-Jupiters around low mass stars? And how can we plan direct observations of mature giant planets in reflected light based on indirect measurements?

I approached the first question by leading the data reduction and analysis of a JWST NIRCam survey of nine nearby, young M dwarf stars to search for planetary-mass companions, as detailed in Chapter 2 and published in *The Astronomical Journal* [1]. In this survey, we placed the first occurrence rate constraints on sub-Jupiter-mass exoplanets beyond 10 au around M dwarfs and identified a marginally significant exoplanet candidate near one of the targets. I then led a follow-up observation campaign to re-observe the candidate with the same JWST observing mode, which resulted in the dismissal of that source as a possible exoplanet. These observations are detailed in Chapter 3 and soon to be submitted to *The Astronomical Journal*.

To address the second question, I performed modeling of confirmed planets discovered by the radial velocity technique and quantified the probability of successful detection with the Roman Coronagraph during the first 18 months of its primary mission. This work, described in Chapter 4, has been formally delivered to the Roman Coronagraph observation planning team leads to support the prioritization of targets for the first reflected light observation of an exoplanet.

In Chapter 5 of this thesis, I conclude with a summary of the completed work, a description of additional collaboration and software development that I have contributed to the direct imaging community, and a statement of my intended future research.

Chapter 2: Probing the Outskirts of M Dwarf Planetary Systems with a Cycle 1 JWST NIRCam Coronagraphy Survey

2.1 Introduction

The population distribution of exoplanet masses, radii, and semi-major axes provides critical insight into the phenomena that govern planet formation and evolution, including those of our own planet and its neighbors. However, the overwhelming majority of planet discoveries have been through the techniques of transit photometry and radial velocity, most sensitive to the inner ($\lesssim$ 1 AU) regions of planetary systems [7, 45, 46]. Gravitational microlensing observations in dense star fields toward the Milky Way bulge provide access to exoplanets at intermediate to wide separations (0.5 - 10 AU) [83], but the nature of the measurement does not allow direct detection and deep characterization of individual planets.

Using the technique of direct imaging with coronagraphy, light originating from the planet can be separated from the starlight, and the sensitivity to exoplanets actually improves with increased planet-star separation. This is achieved by suppressing the starlight with a series of physical masks in the instrument's optical path, in combination with specific observational approaches and image post-processing techniques. Such detections provide access to direct information about the planet's thermal and atmospheric properties. As new and more capable observatories with di-

rect imaging instruments come online, we gain access to widely separated exoplanets in new parts of parameter space (temperature, mass, age, etc.), providing context for the inner planets we have already discovered in large numbers, and enabling further insights into planet formation, evolution, and habitability throughout the galaxy.

In addition, the observation of young systems ($\lesssim$1 Gyr) allows us to link our knowledge of mature planets and disks with their formation and early history [26, 32, 84]. Theoretical models generally predict that planets form either by core accretion [17] or by direct gravitational collapse [22], and then cool over time until they reach thermal equilibrium with the radiation from the host star and with heat generated by gravitational contraction [85]. A planet's early temperature evolution ($\lesssim$100 Myr) is highly dependent on its formation mechanism [86], so direct measurements of the temperature (via direct imaging), mass (via combining with RV or stellar astrometry), and age (via host star or planet properties) are critical for constraining current models [87].

M dwarfs (< 0.6 $M_\odot$, $T_{eff} \lesssim 4000$ K) are the most common outcome of star formation, by number comprising $\sim 70\%$ of the Milky Way's stellar content [37,88]. Statistics from *Kepler* led to the surprising revelation that M dwarfs host Earth to Neptune-sized planets in great numbers at small physical separations ($\lesssim$0.5 AU) [89, 90]. Results from RV surveys support these planet demographics at small separations [44, 91], but they also reveal longer-term periodic signals or trends in a few stars, consistent with $\sim$1 M_{Jup} planets at 1–5 AU and a steeper planet mass-function than higher-mass stars [92, 93].

Gravitational microlensing surveys have revealed a significant population of Neptune to Jupiter mass planets on $\sim$0.5-10 AU orbits [94, 95], with the majority of the host stars in the M

dwarf mass regime[1]. The estimated occurrence rates of these planets are also consistent with a steep mass-function where Jovian planets are relatively rare and ice giants are more common [30, 96–99]. Recent results suggest a double gaussian distribution in the planet-star mass ratio of microlensing planets, with peaks located at 7.4 and 770 $q_{\rm Earth}$, where $q_{\rm Earth}$ is the Earth-Sun mass ratio, and the latter mass ratio peak would correspond to roughly a Saturn mass for a host star mass of 0.5 $M_\odot$ [100]. The inferred population of M dwarf ice-giants is supported by disk theory, which predicts a pile-up of both icy solids and gas in the vicinity of the sublimation radii of volatile species (H_2O, CO, N_2 etc.) thereby providing a favorable environment for planet formation via core-accretion processes [101]. Further evidence has been provided by high-resolution imaging of the transitional disk of the low-mass star TW Hya that reveals a gap, a dust/gas ring, and CO tracer species at the predicted ice-line separations [102]. In low-mass M dwarf disks, analytical approximations place the primordial CO ice-line at a few 10's of AU [103] and the ice-lines of other volatile species further out.

Due to high sky backgrounds, ground-based thermal imaging observations of young M dwarfs are only sensitive to planets with masses $\gtrsim 1$ $M_{\rm Jup}$ at separations $\gtrsim 10$ AU and reveal their occurrence to be $2.3^{+2.9}_{-0.7}\%$ (for masses 2-14 $M_{\rm Jup}$ and separations 8-400 AU [104]). Long term astrometric observations with VLTI/GRAVITY have shown sensitivity to Neptune-mass planets within 5 AU of M stars [105], and in the near future, long-baseline high precision astrometric orbits from *Gaia* are expected to identify thousands of giant exoplanets orbiting M dwarfs [106]. Recent results from *Gaia* DR3 are already yielding promising planetary mass candidates, and providing astrometric measurements of some known M dwarf giants [107–109]. However, the

[1] $173/235$, or 74% of microlensing planet hosts have masses ≤ 0.6 $M_\odot$ (NASA Exoplanet Archive, queried February 22, 2025)

population of sub-Jupiter mass companions orbiting M dwarfs at wide separation ($\gtrsim$10 AU) remains unconstrained and we lack a complete picture of M dwarf planet demographics. On the other hand, the relatively high predicted occurrence rates result in a population of low-mass planets that are both scientifically valuable and potentially detectable using more sensitive direct imaging capabilities.

In addition to their scientifically interesting planet populations, M dwarf stars are ideal candidates for direct imaging surveys for two intrinsic reasons. First, they are the most abundant and long-lived stars in the universe and therefore provide the largest population of nearby target stars for imaging. Second, their low intrinsic brightness results in more favorable star to planet contrasts for the direct imaging of companions with a given mass [53, 110, 111]. The amount of residual starlight not suppressed by the coronagraph is proportional to the apparent brightness of the star, therefore fainter host stars allow fainter (and thus lower mass) planets to be observed. However, as M dwarfs are often too faint to effectively drive ground-based adaptive optics systems, the outskirts of these systems are among the least observed from the ground, resulting in significant uncertainty in exoplanet population statistics and planetary formation models [29,32].

Having identified the ideal target stars for an exoplanet direct-imaging survey, we now consider the ideal instrument. The Near InfraRed Camera (NIRCam) [70] on the JWST [112] was predicted to demonstrate a major improvement in exoplanet direct imaging sensitivity [53, 111, 113], especially in the 3-5 μm wavelength range where the intrinsic thermal emission of young planets is significant [58, 114]. NIRCam's coronographic mode was exercised both in the commissioning and Early Release Science (ERS) phases of JWST operation to understand the key capabilities. During commissioning, NIRCam successfully observed HD 114174 B, a white dwarf companion to the G5IV-V star HD 114174 A with a flux contrast of 10^{-4} and angular

separation of 0.5". This observation surpassed the required 5σ flux contrast sensitivity of 10^{-4} at 1.0", and additionally achieved a background limited flux sensitivity of 5×10^{-7} at separations greater than 2" [73]. The Direct Exoplanet Imaging ERS team [115] completed the first successful direct observation of an exoplanet with JWST: the 14 Myr old super-Jupiter HIP 65426 b with a flux contrast of 4×10^{-6} and separation of 1" from its A2V class host star. These observations confirmed that JWST NIRCam's coronagraphic modes exceed the predicted performance capability by up to a factor of 10 in flux contrast sensitivity [50]. NIRCam coronagraphy has since been used to continue characterization of known planetary mass companions [116], aid in the discovery of new planets [108], and identify interesting candidates that were previously out of reach [117,118]. The demonstrated capabilities of this instrument mode now enable routine direct observations of sub-Jupiter-mass giant planets orbiting young M dwarf stars at wide separations ($\gtrsim 10$ AU) for the first time.

In this work, we perform the first direct imaging survey with JWST NIRCam coronography to observe a population of stars with no previous observational detection of wide orbit companions, and we provide the first context on the demographics of sub-Jupiters on wide-orbits around M dwarfs. We describe our coronagraphic imaging observations of 9 nearby, young M dwarfs under the Cycle 1 Guaranteed Time Observation (GTO) program 1184 [2]. In Section 2.2 we motivate the target selection and observation strategy for the survey. In Section 2.3, we describe the data reduction techniques used to measure our sensitivity to planetary mass companions and identify point source candidates. In Section 2.4, we summarize the overall performance of JWST NIRCam in the GTO 1184 observations, catalog newly detected sources, and describe several in-

[2]PI J. Schlieder, allocated as part of the NIRCam Exoplanets GTO sub-program. `https://www.stsci.edu/jwst/science-execution/program-information?id=1184`

teresting candidates identified in the data. In Section 2.5, we compare the survey results to yield estimates, discuss their implications for exoplanet demographics, describe lessons learned, and comment on future work. Finally, we summarize the key findings of this study in Section 2.6.

2.2 Survey Design

2.2.1 Target Selection

When developing the GTO 1184 survey, we aimed to achieve the deepest companion mass sensitivity limits of any exoplanet direct imaging program and to access new mass-separation parameter space to further understand the wide-orbit M dwarf planet population. Our focus on M dwarfs, with their intrinsically low luminosities, allows deep sensitivity even in the contrast limited regime of NIRCam. We further selected for the youngest and closest of these stars to maximize sensitivity to warm, self-luminous planets and to access the smallest planet-star separations. This combination of intrinsically low luminosity, youth, and proximity made the M dwarfs in nearby young moving groups and associations [119] some of the most optimal targets. In 2014 and 2015, we searched through several dozen literature sources reaching back more than a decade to identify all late-K and M dwarf stars confirmed or proposed as members of young moving groups and associations and compile a candidate list [120–124]. We then supplemented this with a literature search for additional very nearby, young field stars not associated with a known group or association [125, 126]. This led to a list of more than 400 candidate targets, which were then vetted for known multiple systems and close background sources in projection using further literature crosschecks and archival imaging data in order to limit known contaminating sources for high contrast imaging [127–130].

Short Name	Standard Name	Spec. Type	Distance (pc)	Age (Myr)	W1 (mag)	W2 (mag)
OBS GROUP 1						
AU Mic	HD 197481	M1	9.9 ± 0.10	$24 \pm 3,^{a}$	4.50	4.00
HIP 17695	G 80-21	M3	16.1 ± 0.80	$149^{+51}_{-19},^{a}$	6.81	6.68
TYC 5899	LP 776-25	M3	16.3 ± 0.40	$149^{+51}_{-19},^{a}$	6.77	6.60
G 7-34	G 7-34	M4	13.6 ± 0.20	$149^{+51}_{-19},^{a}$	8.01	7.82
OBS GROUP 2						
Fomalhaut C	* alf PsA C	M4	7.6 ± 0.07	$440 \pm 40,^{c}$	6.99	6.80
AP Col	V* AP Col	M4.5	8.4 ± 0.07	$50^{+5}_{-10},^{b}$	6.64	6.40
2M J0944	G 161-71	M5	13.3 ± 0.15	$50^{+5}_{-10},^{b}$	7.41	7.20
OBS GROUP 3						
LP 944-20	LP 944-20	M9	6.4 ± 0.04	$329 \pm 80,^{d}$	9.13	8.81
2M J0443	2MASSI J0443376+000205	M9	21.1 ± 0.45	$24 \pm 3,^{a}$	10.83	10.48

Table 2.1: All stars targeted for observation in JWST GTO program 1184 (PI J. Schlieder). Each target star is listed with its spectral type, distance in parsecs, estimated age in Myr, and observation group number. The observation group numbers show which stars were imaged in back-to-back observations during GTO 1184 to minimize wavefront error (WFE) drift. Superscripts in the age column denote the stellar aging methods used: moving group membership (a: [132] and b: [133]), association with Fomalhaut A (c: [125]), or lithium depletion (d: [134])

These selection criteria led to a shortlist of more than 50 young M dwarf targets within 25 pc. We further scrubbed this list to only the closest stars and made sub-selections to include targets with a broad range of M spectral types and luminosities. This final part of the selection and prioritization process was subjective by design to include a variety of targets and provide a final data set that enables exploration of NIRCam coronagraphy capabilities in this early survey. We also continued to monitor the literature for new targets or updated information on our prioritized list over the years. This included crosschecks with Gaia data [131] and the consideration of newly identified young moving group members and candidates based on those data [119]. The final target list was solidified in 2020 and consisted of nine of the closest, youngest M dwarfs, as detailed in Table 2.1.

Here we provide a few notes on the targets. Two, AU Microscopii (AU Mic) and Fomalhaut C, are already known to have extended debris disks [135, 136]. Lawson et al. 2023 [137] provides a focused analyses of the AU Mic disk which is detected at 3 - 5 μm wavelengths for the first time in GTO 1184. Lawson et al. 2024 [138] describes our first-of-its-kind direct-imaging detection of the very faint Fomalhaut C disk, adding a new entry in the short list of M dwarfs with debris disks resolved in reflected light. Each of these papers also reports on the deep sensitivity to wide-orbit planets achieved in those systems, and the independent analyses performed later in this manuscript support those results. AU Mic also has two confirmed transiting planets with semimajor axes 0.065 and 0.11 AU [139, 140], corresponding to angular separations of 6.6 milli-arcseconds (mas) and 10 mas which are far interior to the NIRCam coronagraph inner working angle (IWA, defined as the separation within which more than 50% of the incident light is suppressed) and thus undetectable in these observations. TYC 5899 was the latest addition to the target list. It replaced the star GJ 393 which was revealed to potentially be $>$1 Gyr old with the inclusion of new observations and analyses [141]. TYC 5899 has a known star within a few arcseconds (see Fig. 2.5), but we included it as a target due to its youth, spectral type, and proximity. Target 2M J0443's model predicted mass is substellar given its luminosity and young age [142, 143]. We include it in the survey to explore NIRCam's contrast performance with a faint target and to search for wide-orbit planets around a substellar target.

2.2.2 Observation Strategy

We observe each target with NIRCam for approximately 1 hour in the F444W filter centered on 4.44 μm (3.881 - 4.982 μm). This is the longest wavelength, wide-bandpass filter available

for use with the NIRCam coronagraphic modes, which maximizes the detection of planet flux for a given exposure time (models predict young giant exoplanets to be bright in the 4-5 μm wavelength range) [58]. We use the readout pattern SHALLOW2 for the observations of AU Mic with 35 integrations in the F444W filter. We use the MEDIUM8 pattern for every other target with 17 integrations per exposure and 10 groups per integration as defined in the NIRCam Detector Readout Patterns page of the JWST User Documentation[3]. We also observe each target for approximately 30 minutes in the F356W filter centered on 3.56 μm (3.135 - 3.981 μm), using the same readout settings except reducing the number of integrations per exposure to 17 for AU Mic, and 8 for the other targets. This enables color-based rejection of background contaminants such as stars and the most common galaxies, as we expect young giant exoplanets to be significantly red in the 3-5 μm wavelength range [58, 114]. The total observation time in both filters is split evenly across two roll angles separated by $\sim$10°, which is typically the maximum allowed by the observatory due to solar avoidance restrictions. The two roll angles enable stellar point-spread function (PSF) subtraction via angular differential imaging (ADI, [144]). ADI leverages the fact that the stellar PSF is fixed to the orientation of the observatory while the position of the planet remains fixed on the sky to disentangle the star and planet flux. All of the aforementioned observations use the subarray SUB320 with a field of view of 20 x 20 arcseconds, enabling the observation of companions at separations up to $\sim$200 AU in GTO 1184, depending on the distance to the individual target star. Finally, each observation uses the coronagraphic mask MASK335R, which is the narrowest round mask available for use with the F444W filter. It provides an inner working angle (IWA) of 0.6" [145], which corresponds to a typical projected separation of $\sim$12

[3] https://jwst-docs.stsci.edu/jwst-near-infrared-camera/nircam-instrumentation/nircam-detector-overview/nircam-detector-readout-patterns

AU in this survey.

Our choice to perform the survey using coronagraphy rather than non-coronagraphic direct imaging was based on detailed predictions for each target using the dedicated software package `WebbPSF` for JWST PSF modeling [146]. We simulated the expected contrast and planet mass sensitivities for each of the 9 targets with MASK335R coronagraph using the F444W filter, and compared with the direct imaging mode using the F480M filter. We explored a range of possible pre-launch wave-front error (WFE) drift values between the science target and reference, adopting ΔWFE $\in$ [0, 2, 5, 10] nm. These simulations revealed that for all targets except the faintest two, 2M J0944 and LP 944-20, the direct imaging mode was significantly more sensitive to WFE drift. This was particularly true at angular separations $\lesssim$2". Thus, if worse case pre-launch WFE drift predictions were reflected in flight performance, coronagraphy would yield equal or better contrast and mass sensitivity performance at small separations for most targets. For this reason, and to preserve the same observing mode for all targets in the interest of a self referenced survey (see below), we chose to perform the survey entirely in NIRCam's coronagraphic mode.

Even with the vast majority of the target starlight suppressed by NIRCam's coronagraphic optical elements, astrophysical sources near the star (a.k.a. off-axis sources) may still be much fainter than the residual starlight that reaches the detector. To address this, an additional star is typically observed to measure a reference stellar PSF, which can then be scaled to and subtracted from the target star observation to reveal faint, close-in sources. This approach is known as reference differential imaging (RDI, [66]), and is expected to be more efficient than ADI at removing residual starlight while preserving flux from off-axis sources at small ($\lesssim$ 2") angular separations due to the limited range of roll angles available with JWST.

In contrast to previous coronagraphic observations with JWST, we do not allocate observ-

ing time to dedicated reference stars. We instead use the entire set of science observations as a library of potential reference PSFs to maximize the number of science targets that can be observed within the survey time allocated to GTO 1184. This strategy is made more feasible given that all of the target stars are of similar spectral type, minimizing the variation due to wavelength-dependent PSF structure. We observe the targets in three unbroken sequences grouped by early-, mid-, and late-type M dwarfs to further reduce wavefront error drift between adjacent observations (See Table 2.1). Grouping the targets by spectral type does occasionally result in slews between each target of $\sim 50^{\circ}$ or more, however pre-launch thermal and optical modeling (supported later by measurements during commissioning) indicated that the observatory would be stable enough to handle these without introducing significant additional wavefront error [147].

The GTO 1184 observations were executed successfully[4] between September 6th and November 27th, 2022 (UTC) with the exception of the second roll angle observation of TYC 5899, which failed due to a target acquisition error. Then, the two rolls of TYC 5899 were re-observed in 2023 on different dates due to a sequential observation link error in the observing plan. The two rolls were observed on February 11th and 22nd (UTC), respectively. All three observations of TYC 5899 were used in the analysis, however the high proper motion of the star (243 mas yr^{-1} [131]) and the 4-month delay between the first and last observations result in the apparent blurring of off-axis background sources, so only the final two observations are shown in the survey images and used for off-axis PSF fitting.

[4]The data are publicly available at MAST: doi: 10.17909/1zm1-4x90]10.17909/1zm1-4x90

2.3 Analysis Methods

The following subsections detail our approach to data reduction, post-processing, and the search for and characterization of point source candidates.

2.3.1 Data Reduction

The raw JWST data, comprised of non-destructive detector array reads averaged over each group of frames within each integration and exposure (shown in panel a of Figure 2.1), becomes accessible on the Mikulski Archive for Space Telescopes (MAST) within about 48 hours of the observations being executed. However, significant calibration and post-processing is required before the data can be used for science analysis and interpretation. The Space Telescope Science Institute (STScI) has thus developed the JWST Science Calibration Pipeline (a.k.a. `jwst`) to perform the reduction of all JWST data, composed of three stages described below [148].

Stage 1 applies detector-level calibrations to the raw data, including checking for pixel saturation and persistence, as well as performing dark field subtraction, detector gain corrections, and ramp slope fitting. The ramp slope refers to the rate of flux signal build up in each detector pixel during the integration, and it should be linear if the astrophysical source is not variable over the integration timescale. Therefore, if anomalies such as cosmic ray (CR) hits cause significant deviations from the linear ramp slope between two adjacent groups (called "ramp jumps"), this can be detected and the slope can be fit along each jump-free segment. The threshold for flagging ramp jumps, in number of sigmas above the noise, is one of many calibration parameters which can be specified by the user. The output of this stage is a 3D array of the uncalibrated photon rate in each pixel during each integration, with an example shown in panel b of Figure 2.1 after

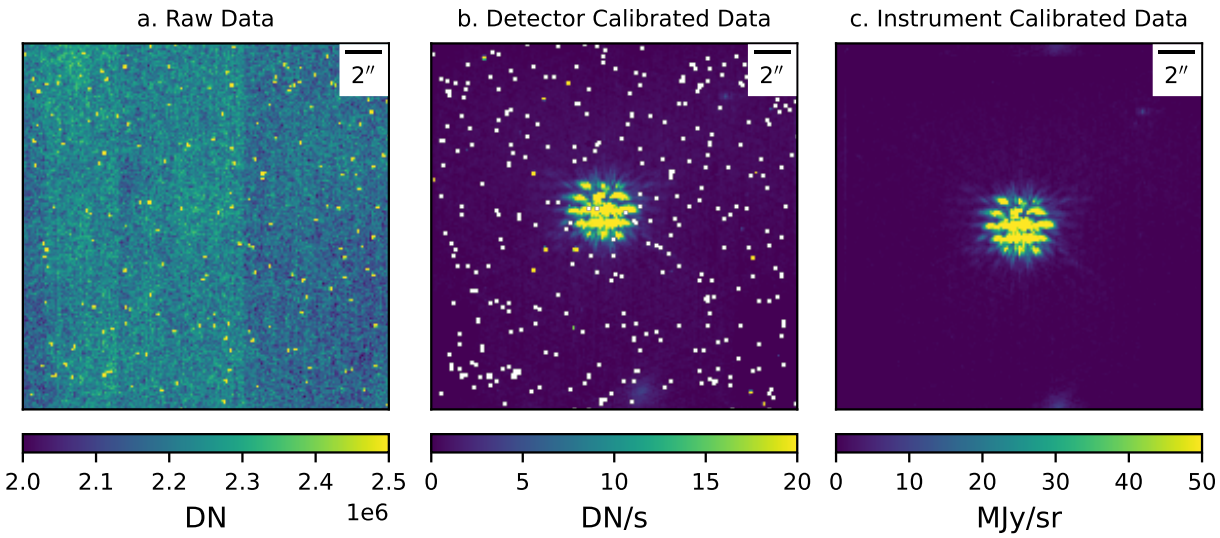

Figure 2.1: Results of data reduction steps for GTO 1184 target G 7-34 (roll 1 in the F444W filter), using the JWST Calibration Pipeline wrapped by `spaceKLIP` [148,149]. We also include additional custom processing steps for flagging cosmic ray persistence. Panel a shows the raw data as downloaded from the MAST archive. Panel b shows the output of the first stage of the pipeline, which flags and corrects for detector-level errors. Panel c shows the output of the second stage, which corrects instrument-specific errors, smooths over unreliable pixels, and converts the image to physical fluxes. Significant residual starlight is still present in the center of the frame, which needs to be removed with PSF subtraction techniques.

averaging over the integrations.

Stage 2 provides physical and instrument-specific corrections to individual integrations to generate a fully calibrated exposure. For the purpose of this study we are concerned only with the NIRCam image calibration steps, which include applying World Coordinate System (WCS) information to transform between pixels and physical coordinates, flat field corrections from instrument and detector response, and flux calibration to convert between counts per second and MJy per steradian. The output of this stage is a 3D array of the calibrated flux (in MJy/str) in each pixel during each integration. The calibrated image for each exposure can then be attained by simply averaging over the integrations, as shown in panel c of Figure 2.1.

Finally, stage 3 performs additional processing for observational techniques that require

the combination of multiple exposures, such as stellar PSF subtraction with ADI and/or RDI. The stage 3 module for coronagraphy applies CR and outlier flags to all science target and PSF reference observations, aligns the PSF references with each target image, and performs the desired PSF subtraction method via Karhunen-Loève Image Processing (KLIP, [67]).

2.3.1.1 Pre-Processing

The "pre-processing" steps encompass everything leading up to PSF subtraction, including the steps shown in Figure 2.1. In addition these include the alignment of images for each science target exposure as well as the preparation of reference PSF images.

Given that the JWST pipeline was developed to cover the broadest possible set of applications, we chose instead to use the publicly available python package `spaceKLIP`[5] which tunes the JWST pipeline specifically for high-contrast coronagraphic imaging of exoplanets [149]. `spaceKLIP` essentially wraps the first two JWST pipeline stages in a set of user-friendly python functions and provides custom steps to account for phenomena such as erroneous ramp jump detections, low quality dark current subtraction, flux variations between integrations, and hot or otherwise unreliable pixels. We also use the `spaceKLIP` steps for background subtraction, masking and replacing bad pixels, correcting the coronagraph location, and aligning the frames. In general, we adopt the default settings for the step parameters, however we did reduce the jump detection threshold from 4σ to 3σ, and reduced the sigma clipping threshold in the `spaceKLIP` bad pixel cleaning step from 5 to 3, which improved the flagging of cosmic ray hits.

The most significant hurdle we encountered during this phase was the unflagged persistence of several CR hits. The `spaceKLIP` ramp-fitting step successfully flags pixels in the first

[5]The specific version used in this study is linked in the Acknowledgments

integration affected by a given CR, however for a large enough hit, core pixels can remain warm across multiple integrations in an exposure, such that it can mimic a faint off-axis PSF in the final post-processed image. CR persistence can be unambiguously differentiated from an astrophysical source by inspecting the individual integrations in the affected exposure. As the CR masking by the `jwst` pipeline is imperfect, residuals will be clearly visible in the affected frames, and can be masked manually before PSF subtraction. In our first reductions of the survey data, these artifacts led to several spurious "detections" of a faint source in F444W with no detection in F356W, mimicking the expected signal of a sub-Jupiter mass planet. To ensure that this effect did not cause further issues, we thoroughly examined every group of each observation for CR persistence by subtracting the per-pixel median of the integrations in an exposure from the mean of those integrations and identified places where an outlier existed only in one or a few integrations out of the set. CR persistence stands out using this method and we flagged each instance by eye and masked those pixels only in the affected integrations before higher level processing.

2.3.1.2 PSF Library Preparation

As this survey does not contain dedicated reference stars, we perform an additional processing step for each science image so that it can also serve as a reference PSF free of contaminating off-axis sources. We first mask each off-axis source revealed in a first-pass ADI reduction of the science targets as described above, using a signal-to-noise ratio per resolution element (SNRE) threshold of 5, then replace each masked pixel in each science frame with the median value of the non-masked pixels in that location across all other frames in the library. This effectively removes contaminating sources from the reference PSF library while preserving the stellar PSF structure

and avoids biasing the subtraction with a uniform fill value. The resulting images are treated as the reference PSF library for the survey. We exclude from the reference library TYC 5899, which had an extremely bright source at about 3" separation, as well as Fomalhaut C and AU Microscopii which host circumstellar disks, making the stellar PSF difficult to sample. The remaining 6 stars are referred to throughout this paper as the "full reference library".

2.3.1.3 KLIP Processing

PSF subtraction is performed via the Karhunen-Loève Image Processing (KLIP, [67]), which uses a Karhunen-Loève transform of the reference observations to build an orthogonal basis of eigenimages (a.k.a. KLIP modes) that are then fit to the science observation. The `spaceKLIP` implementation of this method is based on the python package `pyKLIP` [150] and can perform PSF subtraction via ADI and RDI with more flexibility than the `jwst` pipeline, as well as a combination of the techniques (ADI+RDI). The science image can also be separated into a number of annuli (concentric circular regions) and position-angle (PA) subsections, so that the PSF subtraction can be performed independently in multiple subsections of the image. This is particularly helpful to avoid bias due to a bright, off-axis source in the science image affecting the PSF subtraction quality in the rest of the image. In our reductions, we use four evenly spaced annuli and no position angle divisions, which provided the best balance of isolating bright off-axis sources while keeping each individual region large enough to avoid error inflation from small sample statistics near the IWA. One can also tune the number of KL modes (i.e. principal components) used for the final PSF model. We opt to use 6 KL modes to reduce the probability of astrophysical signals being subtracted by the KLIP algorithm, following the prescription used

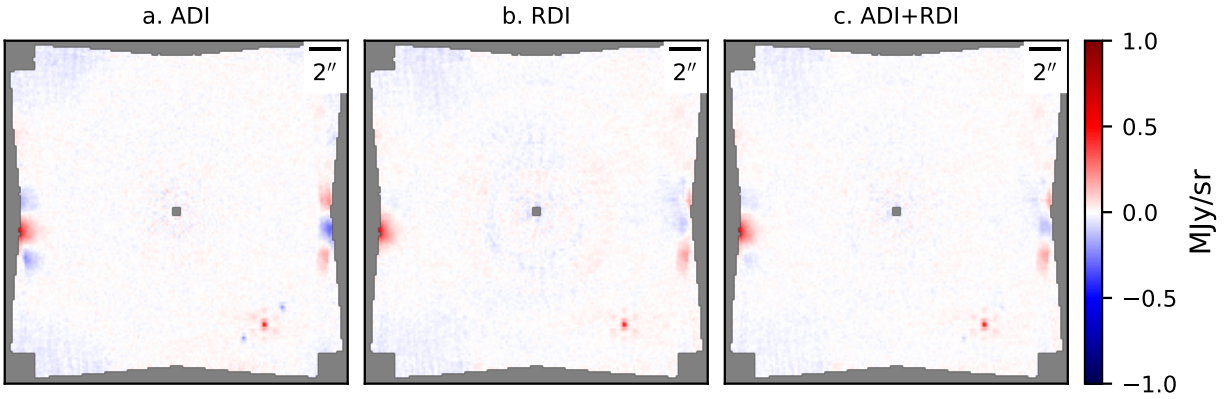

Figure 2.2: Results of PSF subtraction via ADI, RDI, and ADI+RDI using `spaceKLIP`, for G 7-34 in the F444W filter. The positive signal is shown in red, and the negative signal (due to subtraction artifacts) is shown in blue. Panel a shows the ADI result, where each off-axis source has clear negative residuals due to the 10° roll angle difference. Panel b shows the RDI result using only HIP 17695 (the target star with the cleanest FOV) as a reference, and panel c shows the ADI + RDI result, which is performed just like the RDI method but including the second roll of the science target as an element in the reference PSF library [149].

in Carter et al. 2022 [50].

ADI is performed by reducing each roll angle of a given science target using the alternate roll angle of that same science target as the reference observation. After each roll angle is PSF-subtracted via the KLIP algorithm as described above, the resulting images are de-rotated and averaged. The presence of the same off-axis sources in the science and reference observations for this method creates a characteristic negative-positive-negative signal in the final image (as in Panel a of Figure 2.2), where the negative artifacts are separated from the positive signal by the same angle that separates the two observational rolls. However at small separations from the host star, this can result in "self-subtraction," where the negative and positive lobes are separated by a distance less than the width of the PSF, thus reducing the throughput of the KLIP algorithm in that region.

RDI is performed by processing each roll angle of a given science target using the PSF library (excluding the science target) as "references", before de-rotating and averaging the two PSF-subtracted images. We do not rescale the PSF references to a common flux before running KLIP, as the amplitude of each PSF eigenimage is scaled automatically by the algorithm when fitting the science PSF. This method, shown in Figure 2.2 Panel b, avoids the self-subtraction effect, however the PSF subtraction quality is more sensitive to spectral type and WFE differences between the science and reference targets as well as to off-axis sources present in the reference observations.

Finally, ADI+RDI is performed by applying RDI as above to each roll observation separately, while including the alternate rolls of the science target in the PSF reference library for subtraction. We then de-rotate and sum the two PSF-subtracted images. This enables the use of the science star as a reference while somewhat suppressing the effect of self-subtraction in pure ADI, as shown in Panel c of Figure 2.2.

2.3.2 Image Analysis

Because of the artifacts produced during PSF subtraction, especially in the case of ADI, photometric analysis cannot be performed through traditional aperture photometry. Instead we use the `spaceKLIP` routines developed to measure contrast sensitivity and off-axis source photometry via PSF forward modeling and injection-recovery.

We characterize the sensitivity of our observations based on the 5-σ flux contrast sensitivity, (a.k.a. the "5σ contrast") which the is the flux contrast of an off-axis source relative to the star that could be detected with a signal-to-noise ratio of 5, equivalent to a false alarm probability of

2.9×10^{-7}. This is determined by sampling the radial noise profile at twice the angular resolution of the observing system and quantifying the 5σ flux threshold using Student t-statistics. The combined throughput of the PSF subtraction algorithm is then accounted for by injecting an off-axis PSF model with a pre-determined flux (generated by `WebbPSF` [146]) into the pre-PSF-subtracted images on a grid of planet-star separations between 0.1" and 5" and position angles separated by $60°$. We then perform the PSF subtraction, recover the resulting source photometry by fitting a 2D gaussian via least squares optimization, and divide by the input flux to measure the dimensionless throughput as a function of separation. This is implemented in a routine provided by `pyKLIP` and wrapped by `spaceKLIP`, which includes the effects of small-sample statistics at narrow separations following Mawet et al. 2014 [151]. The throughput of the NIRCam coronagraphic optical system is then accounted for by applying the transmission map for the M335R mask configuration provided by `WebbPSF`.

We used the G 7-34 system as an example to study the effect of different PSF subtraction methods and reference PSF libraries on the final contrast sensitivity. Figure 2.3 shows the results of PSF subtraction of using ADI with no reference stars, and using RDI or ADI+RDI combined with either HIP 17695 as a reference, or with all of the good quality science observations as references. In this example, the inclusion of additional reference stars improves contrast sensitivity in the background-limited regime beyond ~ 3 arcseconds. However within the speckle-limited regime of $\lesssim 3$ arcsec, we do not see the same improvement. We understand this to be caused by G 7-34 and HIP 17695 being very closely matched both in wavefront error (due to the back-to-back observations) and in star-coronagraph alignment (by coincidence). The mean difference in star-coronagraph alignment between the G 7-34 observations and the HIP 17695 observations is 0.088 pixels, compared to 0.155 pixels between G 7-34 and the rest of the library. Thus, as we

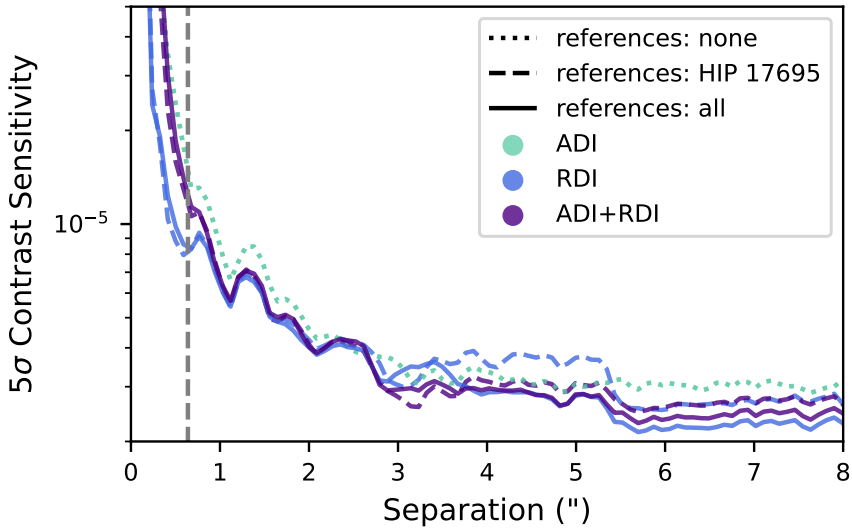

Figure 2.3: 5σ contrast sensitivity curves for different PSF subtraction techniques and reference PSF choices applied to the G 7-34 observation in F444W, as a function of angular separation from the target star. The teal, blue, and purple lines show the results for ADI, RDI, and ADI+RDI respectively. Reductions using the full library of PSF references are shown with a solid line, those using only HIP 17695 as a reference are shown with a dashed line, and those using no references (ADI only) are shown with a dotted line. The 0.6" coronagraph inner working angle (IWA) is shown as a vertical gray dashed line. We can see that RDI and ADI+RDI outperform ADI alone at nearly all separations, regardless of the number of references used.

add more reference observations, which have more significant differences in wavefront error and coronagraph alignment compared to HIP 17695, we do not see significant improvements in the PSF subtraction quality within 3 arcsec.

We note that RDI with the full reference library results in the deepest contrast sensitivity both within the IWA, denoted by the vertical dashed line in Fig. 2.3, and in the background-limited regime beyond 5 arcsec, therefore we use this method for our primary analysis. We do however cross check with the alternate methods to ensure that a given off-axis source is astrophysical and not an artifact of one of the subtraction algorithms.

The `spaceKLIP` routine for measuring the photometry of an off-axis source, similar to the contrast curve measurement, generates an off-axis PSF model at the approximate planet-star separation of the companion, then applies a forward model of the stellar PSF subtraction method

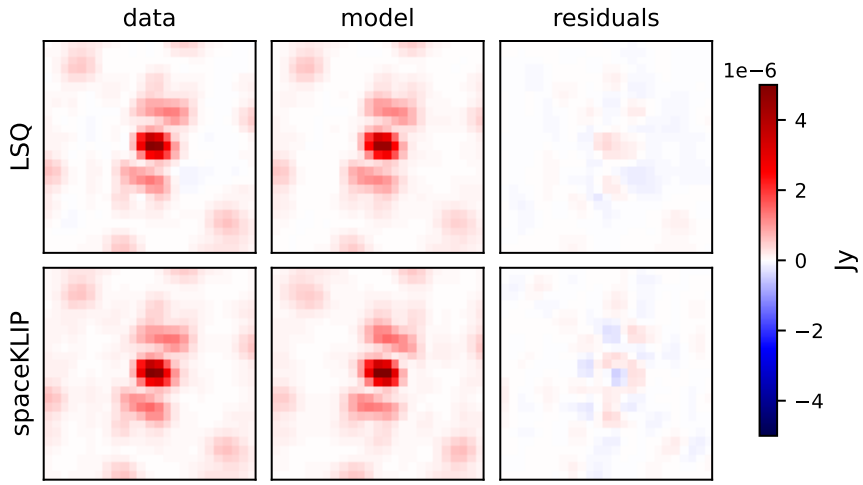

Figure 2.4: Examples of the two different approaches used for forward-model PSF fitting, showing source P1 near TYC 5899 as an example. The left column shows the image data, the center column shows the best-fit PSF model, and the right column shows the residuals. The result from the least-squares PSF fitting routine are shown in the top row, while the default spaceKLIP fitting routine is shown in the bottom row and produces a similar result.

used in the data reduction, and finally fits the resulting off-axis PSF model to the data using a Markov Chain Monte Carlo (MCMC) approach. This allows us to measure the luminosity of the off-axis source relative to the target star while accounting for any self-subtraction or local under/over-subtraction due to the KLIP algorithm. An example of this method applied to a well-detected, off-axis source in the vicinity of TYC 5899 is shown in the bottom row of Figure 2.4.

In some cases with lower SNR or significantly non-zero background, the `spaceKLIP` photometry measurement produces a result that is visually erroneous in diagnostic images, so we have developed a semi-independent routine to measure the photometry of these objects. We produce a normalized PSF model using `WebbPSF`, which we fit to the data using a least-squares (LSQ) minimization. We then use the separation-dependent measurement of the KLIP algorithm and coronagraph mask throughput measured by `spaceKLIP` during the contrast curve calculation to convert from the PSF model amplitude to the source flux. We determine the measurement uncertainty via the bootstrap method, wherein the model fit residuals are shuffled in the image

plane, the shuffled residuals are added back to the data, and the model fit is repeated 1000 times to produce a posterior distribution of best-fit parameter values. This produces a similar result (typically agreeing within 1-2 σ) to the `spaceKLIP`-derived photometry and astrometry for robustly detected sources, as shown visually in the top row of Figure 2.4. More marginal sources (i.e. SNR < 10) show greater discrepancies between the spaceKLIP and LSQ fit, and in these cases we report higher astrometric uncertainties to account for this.

2.4 Results

We reduced all observations for each target using the RDI technique described in Section 2.3.1.3 with the full PSF reference library. We then calculated the signal-to-noise ratio per resolution element (SNRE) in each pixel by convolving the final image with a 2D full-width-half-max top-hat model (of width 0.114" for F356W and 0.140" for F444W) and dividing by the finite-element-corrected noise profile. The resulting SNRE maps for each target in F444W and F356W are shown in Figures 2.5 and 2.6 respectively, with candidate point sources magnified in the image insets and the extended sources labeled but not magnified. The survey images in physical units (MJy/steradian) are available for reference in Section 2.7.1. As noted previously, we do not include the first of the three TYC 5899 observations in these maps as the 4-month delay between the first and second observations, combined with the high proper motion of the target star, causes a non-trivial blurring of background objects.

We recover the bright, edge-on, circumstellar disk of AU Mic, whose analysis is detailed in Lawson et al. 2023 [137]. The circumstellar disk of Fomalhaut C is not obvious in these reductions, however this is because our analysis is optimized to recover point-like sources, rather

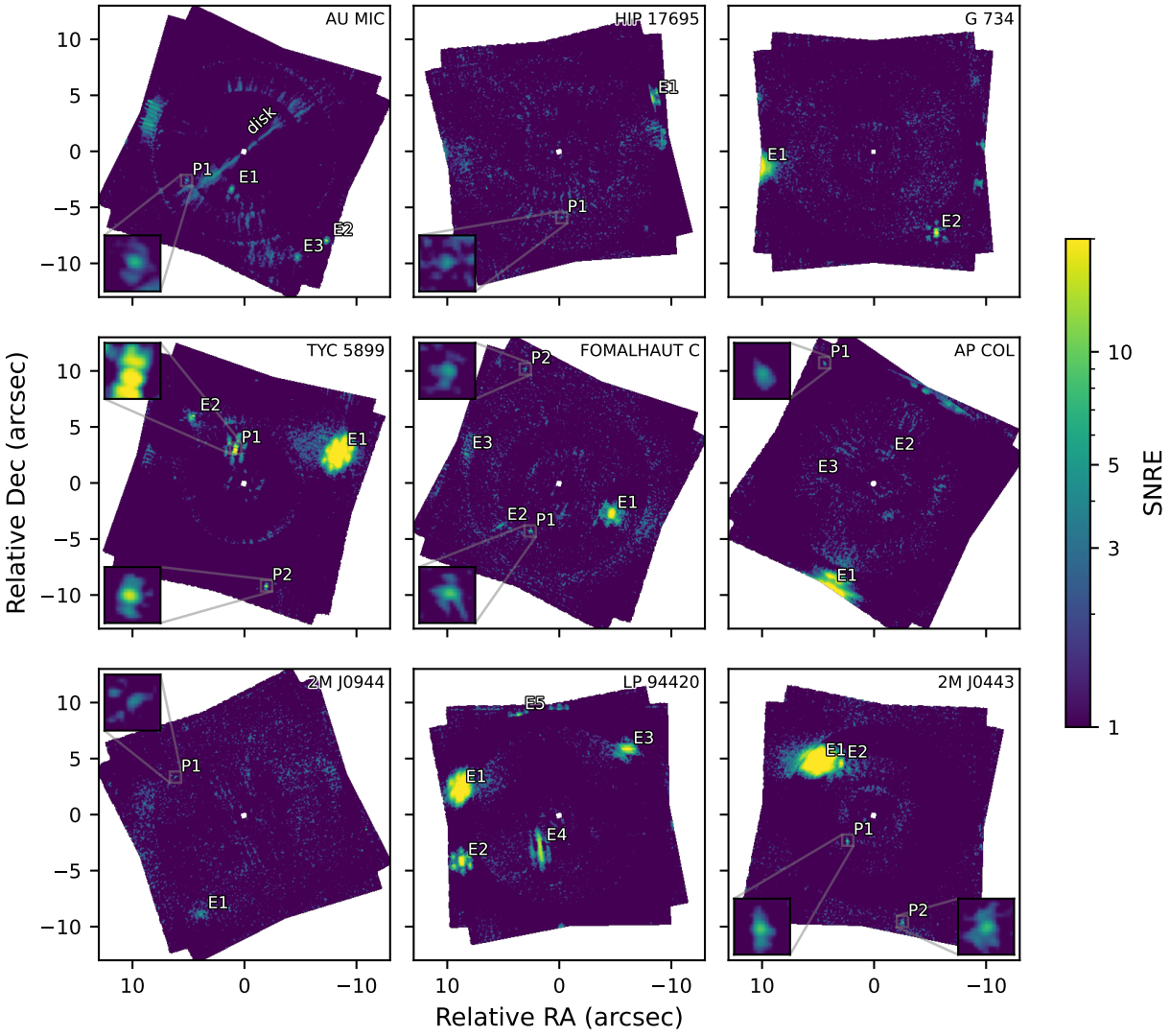

Figure 2.5: Signal-to-noise ratio per resolution element (SNRE) maps of all targets in GTO 1184, in the F444W filter. All observations were reduced with RDI using the full library of reference PSFs. Point-like and extended sources are labeled in the images (with names beginning with "P" and "E" respectively), and the point-like sources are magnified in the image insets. Extended background sources are abundant in the survey, and the edge-on disk of AU Mic is clearly detected.

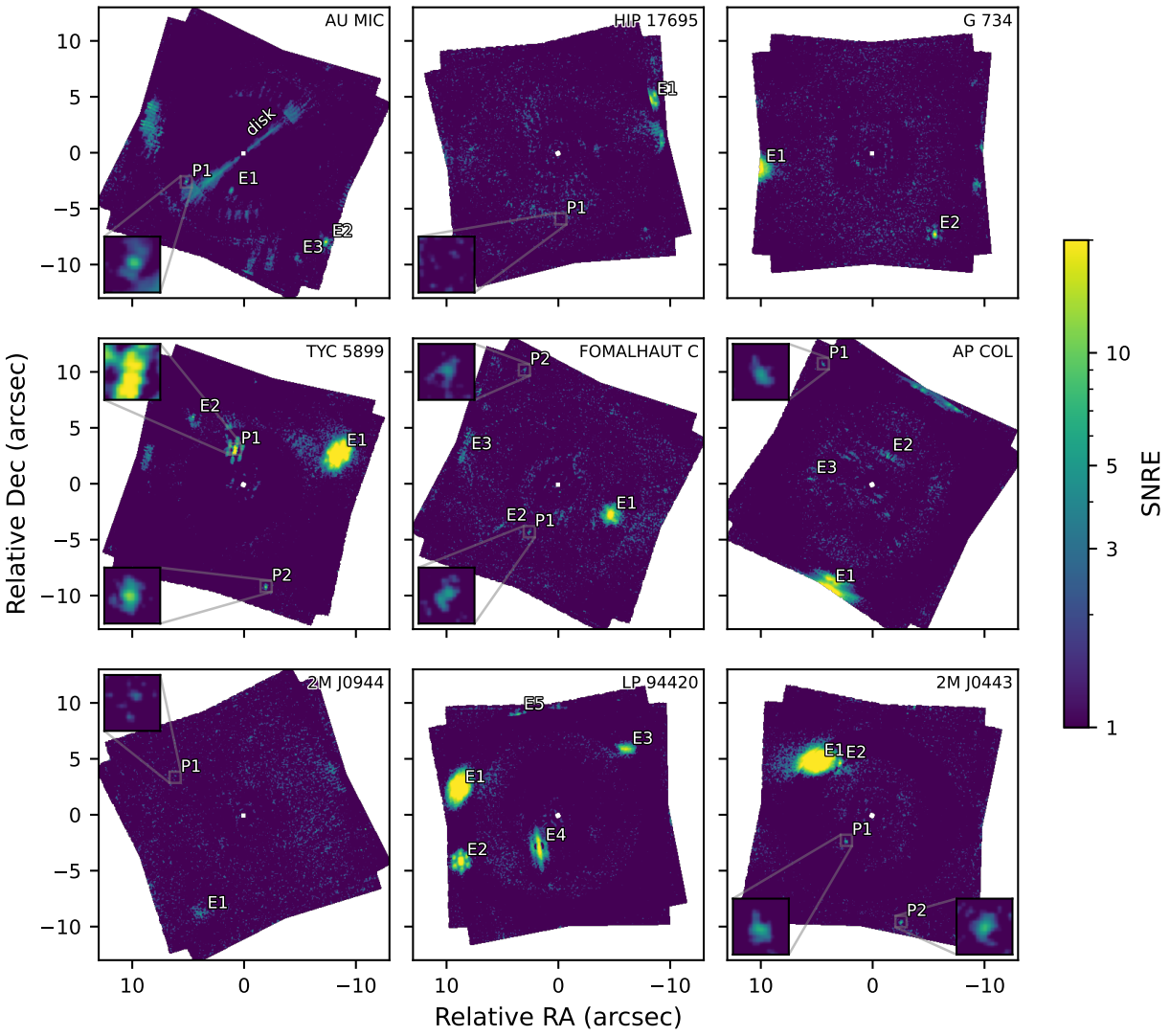

Figure 2.6: Signal-to-noise ratio per resolution element (SNRE) maps of all targets in GTO 1184, in the F356W filter. All observations were reduced with RDI using the full library of reference PSFs. Point-like and extended sources are labeled in the images (with names beginning with "P" and "E" respectively), and the point-like sources are magnified in the image insets. In cases where the candidate source is not detected in the F356W filter, we still label it and provide an inset image to demonstrate its non-detection. Extended background sources are abundant in the survey, and the edge-on disk of AU Mic is clearly detected.

than diffuse emission. The disk is however detected and analyzed using Model-Constrained RDI in Lawson et al. 2024 [138]. As we aim in this paper to detect and analyze potential substellar companions, we use the best-fit disk models from the papers described above to subtract the disk emission from AU Microscopii and Fomalhaut C before characterizing the contrast sensitivity and photometry of these observations.

2.4.1 Survey Sensitivity

Figure 2.7 shows the median survey sensitivity in units of flux contrast (upper panel) and apparent magnitude (lower panel) in both filters (F444W in red and F356W in blue). We achieve a median 5σ sensitivity of 1.5×10^{-5} (and median magnitude sensitivity of 19.3 mag) at a separation of 1" and 2.7×10^{-6} (21.2 mag) in the background-limited regime (i.e. at separations $\gtrsim$ 3") with the F444W filter, as measured via the methods described in Section 2.3.2. In the F356W filter, the median sensitivity is 1.3×10^{-5} (19.7 mag) at 1" and 1.7×10^{-6} (21.8 mag) at 5". For reference, we provide the flux contrast and apparent magnitude sensitivity curves for each target individually in Section 2.7.2.

We then convert the flux contrasts to planet mass sensitivities using published evolution models for stellar- and planetary-mass objects. For masses below 2 M_{Jup} we use `BEX-petitCODE` models [58], for masses below 0.075 $M_\odot$ ($\sim$ 80 M_{Jup}) we use `ATMO-CEQ` models [152], and for all stellar masses we use `Ames-COND` models [153]. As an example, we show the 5σ mass sensitivity curves in units of companion mass for target G 7-34 in Figure 2.8, demonstrating sensitivity to sub-Saturn mass companions in the F444W filter. Despite slightly deeper flux contrasts, F356W has significantly shallower mass sensitivity. This is due both to the intrinsic redness of

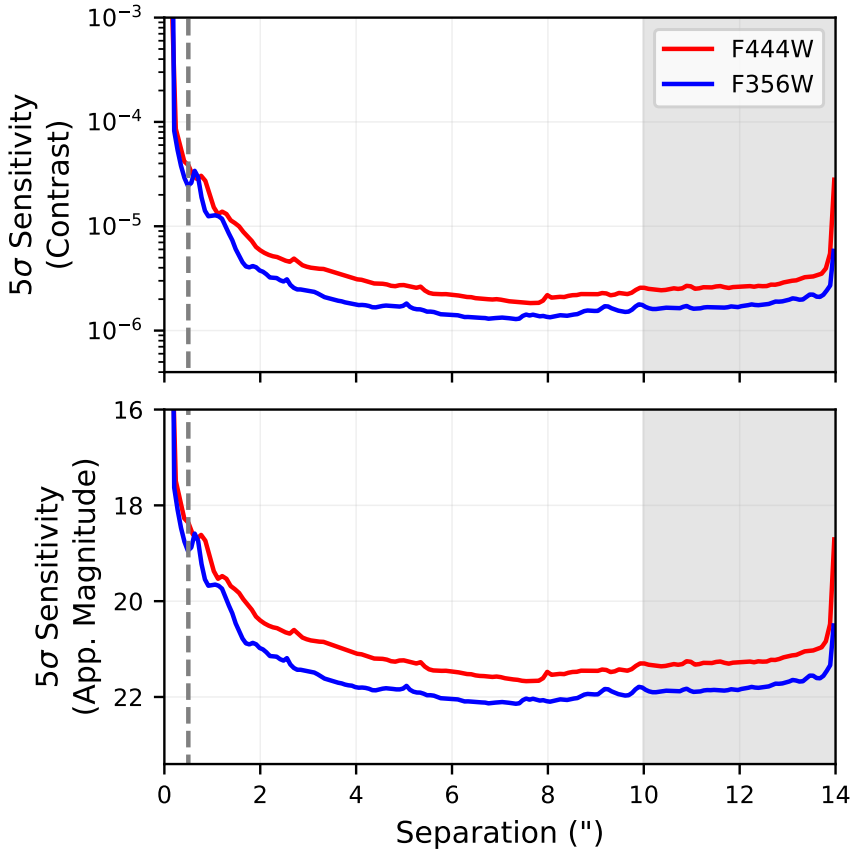

Figure 2.7: The median 5σ sensitivity curves for the entire survey in the F444W filter (red lines) and F356W filter (blue lines). The sensitivity is given in units of planet-star flux contrast in the upper panel, and apparent magnitude in the lower panel. The coronagraph inner working angle (IWA) is shown in the gray dashed line. The separations where only partial coverage exists due to square framed observations at multiple roll angles is shown by the gray shaded region. We demonstrate deep limits in absolute flux at close angular separations.

young planetary mass objects and the shorter exposure time in F356W compared to F444W. Due to this difference in sensitivity, we expect significantly sub-Jupiter-mass companions to appear as "F356W dropouts", e.g. being detectable in the F444W observations, but not in F356W.

In this analysis, we also assume an underlying distribution of orbital eccentricities (positive half-normal with a mean of 0 and sigma of 0.3), and uniformly random orientations in space (corresponding to uniform $\cos i$, longitude of ascending node [0-2π], and longitude of periapse in [0-2π]) to account for projection effects. We can then measure the detection probability as a

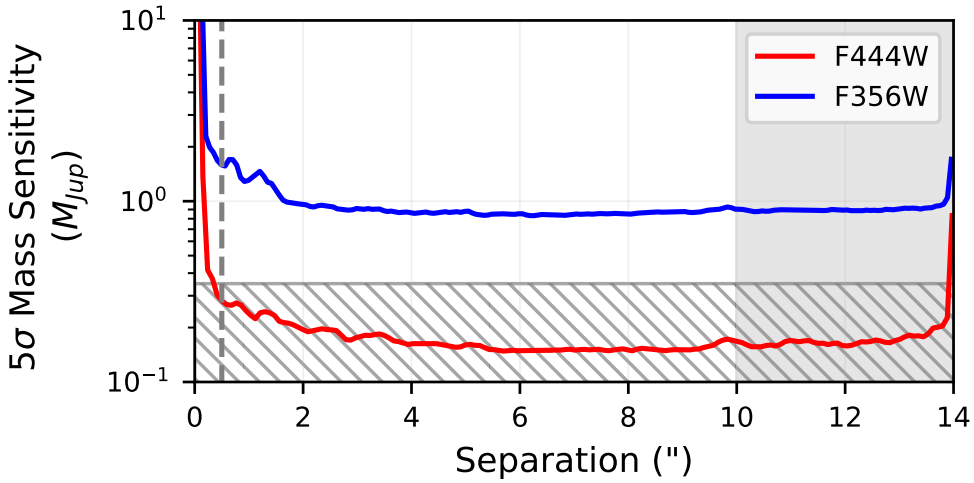

Figure 2.8: The 5σ mass sensitivity curves for the G 7-34 observations, as a function of angular separation from the target star, demonstrate extremely deep mass sensitivity with the F444W filter (in red) as compared to the F356W filter (in blue). Due to this difference in sensitivity, we expect significantly sub-Jupiter-mass companions to appear as an "F356W dropout", e.g. being detectable at F444W, but not at F356W. The masses are derived from the `BEX-petitCODE` cooling curve models, and the hatched region shows where we have extrapolated the model grid to temperatures below the lower limit of 150 K.

function of mass and semimajor axis by injecting a population of planets with the above distribution and calculating the percentage of planets that would be detectable with 5σ confidence based on the apparent magnitude sensitivity curve for each target star. Figure 2.9 shows the detection probability in the F444W filter (the more mass-sensitive of the two) in mass and semi-major axis space for each target, with the hatched region denoting where our observations are sensitive to planet temperatures below the 150 K lower limit of the `BEX-petitCODE` model grid. In this region we have extrapolated the cooling curves in log space to be able to visualize the probable detection space, though we note that inaccuracies are likely beyond the edge of the model grid. This being said, the extrapolations are not needed to show that we clearly demonstrate sensitivity to Saturn-mass (0.3 M_{Jup}) objects in the vicinity of 8 of our 9 targets, and very likely in the case of Fomalhaut C as well. In addition, we are sensitive (>50% detection probability) to Saturn-mass exoplanets at Saturn-like separations (9.5 AU) for at least 6 targets. These are the deepest mass

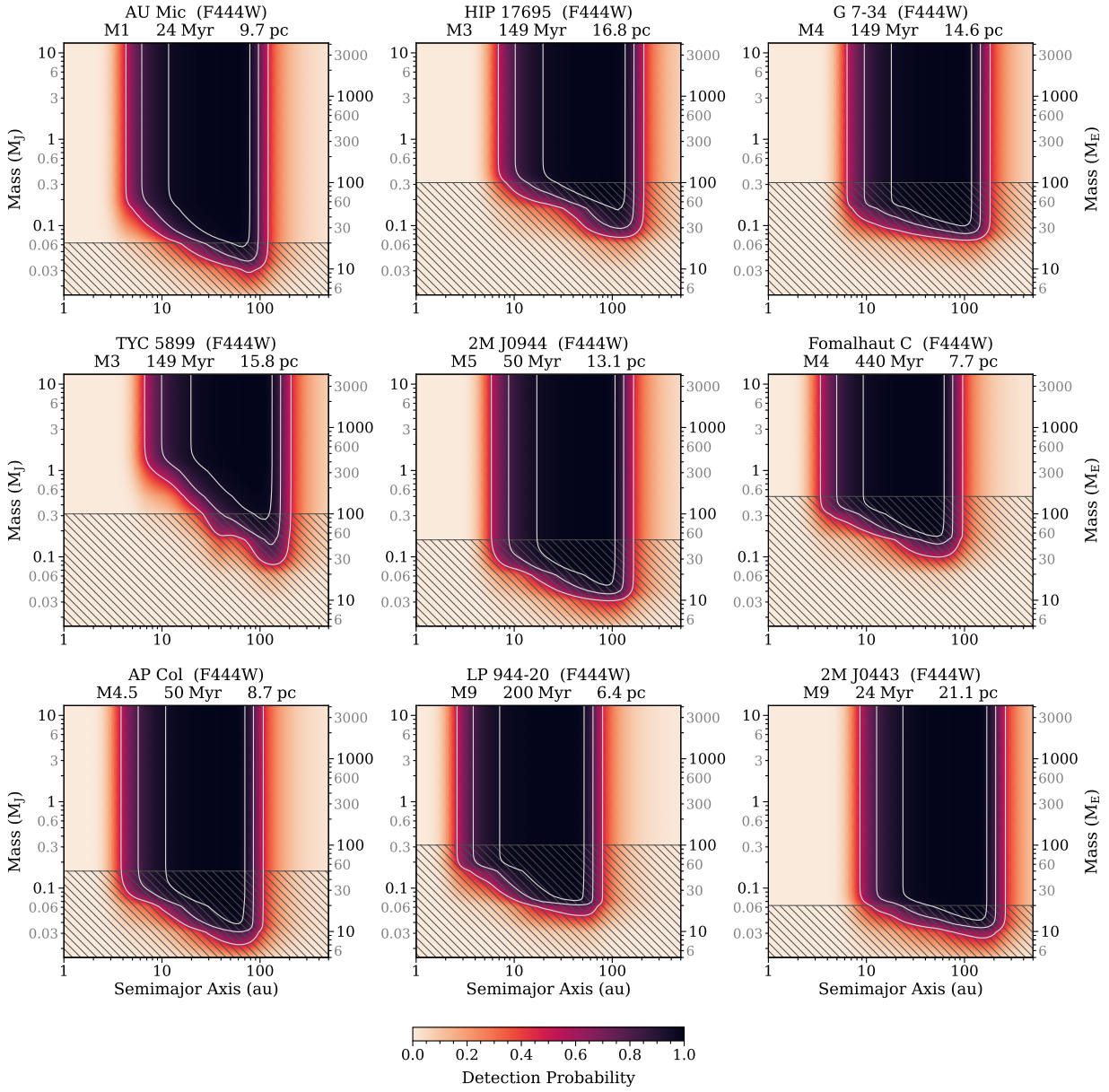

Figure 2.9: Detection probability maps in mass and semimajor axis space for each survey target, demonstrating sensitivity to Saturn-mass exoplanets around all targets, and specifically to Saturn-mass exoplanets with a Saturn-like semimajor axes (9.5 AU) around at least 6 of the 9 targets. We show the mass sensitivity achieved in the F444W filter, as the `Ames-Cond`, `ATMO-CEQ`, and `BEX-petitCODE` cooling curves predict sub-stellar objects to be the brightest in this filter as compared to F356W. The solid white lines show detection probability contours of 50%, 80%, and 95%, and the hatched region shows where our observations are sensitive to masses below the lower limit of the available model grids for a given target's age, and thus we have extrapolated the cooling curves to lower masses (lower temperatures) for visualization purposes. The mass sensitivity of the GTO 1184 survey surpasses the low-mass limit of available planet evolution and atmosphere grids for every target, regardless of age or intrinsic brightness.

sensitivity limits for any direct exoplanet imaging survey to date, demonstrating the power of JWST coronagraphy to explore the outskirts of young M dwarf systems.

2.4.2 Source Catalog

We use a two-tiered search for off-axis point sources to catalog both robust and marginal detections. For robust detections we use an SNRE threshold of 5.0 in either F444W or F356W, and for marginal dropout detections we require an SNRE greater than 4.0 in F444W and less than 3.0 in F356W. This is due to the predicted relative brightness of sub-Jupiter-mass objects in F444W as compared to F356W. We categorize objects as point-like, as opposed to extended, by visual inspection of the PSF fit residuals. As the PSF fit assumes a point-like flux distribution, extended sources will result in a positive "halo" or other distributions of residual flux around the PSF core.

Across all targets in the survey, we identify 10 point-like sources. Eight of these are robustly detected in both filters, and we display the measured SNRE, relative astrometry, F444W and F356W magnitudes, and F444W-F356W color, for each source in Table 2.2. We also note which PSF fitting method was used for each source, however we report the results of both methods (described in Section 2.3.2) in an extended table in Section 2.7.3.

The remaining 2 sources are marginally detected in F444W (SNRE > 4), but not in F356W (SNRE < 3, a.k.a "F356W dropouts"). For these sources, we report the SNRE in each filter, relative astrometry, projected separation in AU, F444W magnitude, F356W magnitude limit, and the 3- and 1-σ lower limit on the F444W-F356W color (as determined from the contrast sensitivity curve for that target at the same angular separation) in Table 2.3. The data, best-fit

Target	Src.	RA ["]	Dec ["]	F444W SNRE	F444W Flux [mag]	F444W SNR
AU Mic	P1	$5.057^{+0.014}_{-0.014}$	$-2.510^{+0.011}_{-0.011}$	7.21	$18.947^{+0.144}_{-0.127}$	7.68
TYC 5899	P1	$0.745^{+0.007}_{-0.007}$	$3.031^{+0.007}_{-0.007}$	68.69	$14.634^{+0.004}_{-0.004}$	75.11
TYC 5899	P2	$-1.979^{+0.008}_{-0.008}$	$-9.107^{+0.007}_{-0.007}$	12.97	$19.540^{+0.032}_{-0.032}$	33.86
Fomalhaut C	P1	$2.521^{+0.058}_{-0.058}$	$-4.219^{+0.112}_{-0.112}$	9.03	$20.980^{+0.174}_{-0.150}$	6.83
Fomalhaut C	P2	$2.992^{+0.042}_{-0.042}$	$10.216^{+0.014}_{-0.014}$	5.76	$21.153^{+0.108}_{-0.098}$	5.76
AP Col	P1	$4.385^{+0.037}_{-0.037}$	$10.692^{+0.013}_{-0.013}$	5.81	$21.042^{+0.125}_{-0.112}$	4.04
2M J0443	P1	$2.311^{+0.011}_{-0.010}$	$-2.259^{+0.011}_{-0.010}$	5.94	$20.678^{+0.085}_{-0.068}$	11.29
2M J0443	P2	$-2.537^{+0.056}_{-0.056}$	$-9.475^{+0.009}_{-0.009}$	8.44	$20.865^{+0.095}_{-0.088}$	5.96

(cont'd) Target	Src.	F356W SNRE	F356W Flux [mag]	F356W SNR	F356W-F444W Color [mag]	Method
AU Mic	P1	9.26	$19.203^{+0.118}_{-0.106}$	7.89	$0.257^{+0.186}_{-0.166}$	sklip
TYC 5899	P1	68.46	$14.804^{+0.006}_{-0.006}$	68.02	$0.170^{+0.007}_{-0.007}$	sklip
TYC 5899	P2	11.38	$20.003^{+0.041}_{-0.041}$	25.63	$0.463^{+0.052}_{-0.052}$	lsq
Fomalhaut C	P1	5.41	$21.688^{+0.111}_{-0.101}$	5.84	$0.708^{+0.207}_{-0.181}$	sklip
Fomalhaut C	P2	4.59	$21.997^{+0.157}_{-0.138}$	4.10	$0.844^{+0.191}_{-0.169}$	sklip
AP Col	P1	5.39	$21.828^{+0.215}_{-0.180}$	3.72	$0.786^{+0.249}_{-0.212}$	sklip
2M J0443	P1	5.84	$21.334^{+0.142}_{-0.086}$	9.44	$0.657^{+0.165}_{-0.109}$	lsq
2M J0443	P2	7.99	$21.444^{+0.083}_{-0.077}$	7.09	$0.579^{+0.126}_{-0.117}$	sklip

Table 2.2: We detected 8 point-like sources with $\geq 5\sigma$ significance in both F444W and F356W. We report each source (as labeled in Figures 2.5 and 2.6) with its position relative to the target star; as well as the peak SNRE, apparent magnitude from PSF fitting, and PSF fit SNR in each filter; the two-filter color, and the method used for PSF fitting as described in Section 2.3.2. As we expect sub-stellar companions to have a F356W-F444W color greater than ~ 2, none of these sources have been flagged as planetary mass companion candidates (See Figure 2.11).

Target	Source	RA ["]	Dec ["]	Proj. Sep. [AU]	F444W SNRE	F444W Flux [mag]	F444W SNR
HIP 17695	P1	$-0.281^{+0.007}_{-0.007}$	$-5.837^{+0.009}_{-0.007}$	94.1	4.84	$22.481^{+0.282}_{-0.195}$	1.64
2M J0944	P1	$6.098^{+0.018}_{-0.018}$	$3.423^{+0.022}_{-0.022}$	93.0	4.02	$21.842^{+0.093}_{-0.085}$	3.91

(cont'd) Target	Source	F356W SNRE	F356W 3σ Flux Limit [mag]	F356-F444W 3σ (1σ) Color [mag]	Method
HIP 17695	P1	-0.389	> 22.865	>0.38 (>1.58)	lsq
2M J0944	P1	2.976	> 22.863	>1.02 (>2.21)	sklip

Table 2.3: We detected 2 point-like dropout sources with marginal (SNRE $>4\sigma$) flux in F444W and insignificant (SNRE $<3\sigma$) flux in F356W. We report each source (as labeled in Figures 2.5 and 2.6) with its position relative to the target star, as well as the projected separation in AU. We also show the peak SNRE in F444W, the apparent magnitude and SNR from PSF fitting in F444W, the SNRE and 3σ magnitude limit from the contrast curve at the associated location in F356W, and the corresponding 3σ two-filter color limit (the 1σ limit is shown in parentheses). The last column shows the method used for PSF fitting as described in Section 2.3.2. The low PSF fit SNR of HIP 17695 P1 in F444W makes it less compelling as an exoplanet candidate.
Note: In regions where the background or noise fluctuation is slightly negative and there is no significant astrophysical flux, the SNRE can be slightly negative.

PSF model, and residuals for each dropout source in F444W are shown in Figure 2.10. In this figure we also show the F356W data at the same position, however as the SNRE of each signal in F356W falls below the threshold of 3, we do not perform a PSF model fit for the data in that filter. While the reader may observe a positive blob in the F356W data for 2M J0944 P1, we note that this blob is offset from the position of 2M J0944 P1 in F444W by several pixels, and is of similar amplitude to the background noise fluctuations that appear in F444W.

As our primary goal is to detect candidate substellar companions, which we expect to be point sources, we do not characterize the extended sources in detail. However we did detect 22 extended sources with SNRE > 5 in either F444W or F356W, and we catalog their approximate position and peak SNRE in Section 2.7.4. Due to an artifact of the `spaceKLIP` image alignment

step, some of the extended sources near the edge of the field of view are wrapped to the other side of the image. We have noted in the table which sources this affects.

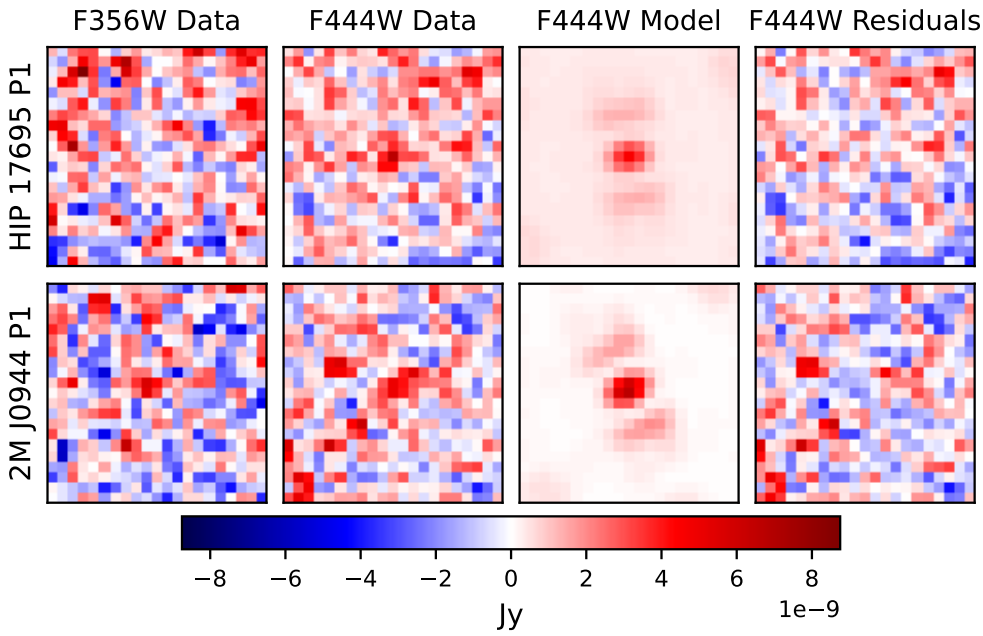

Figure 2.10: Data and PSF fit results for the marginally detected "F356W dropout" sources. The first column on the left shows the F356W data, the second column shows the F444W data, the third column shows the best-fit PSF in F444W (using the least-squares fit for HIP 17605 P1 and the spaceKLIP fit for 2M J0944 P1), and the right column shows the residuals in F444W. The PSF fit SNR of HIP 17695 P1 in F444W is 1.64, leading it to be less compelling as an exoplanet candidate. 2M J0944 P1 is detected with an SNR of 3.91, and remains as a marginal detection. As the SNRE of each signal in F356W falls below the threshold of 3, we do not perform a PSF model fit for the data in that filter. We note that the positive blob visible in the F356W data for 2M J0944 P1 is offset by several pixels from the location of the source in F444W, and that it has an amplitude similar to the F444W residuals.

2.4.2.1 Background Source Rejection

To determine if a given off-axis source is likely to be a companion associated with the target star, we compare the off-axis source photometry to an "isochrone curve" based on the evolution model grids described in Section 2.3.2. This curve predicts the apparent magnitude in a given filter and the two-filter color for objects across a range of masses, assuming the same

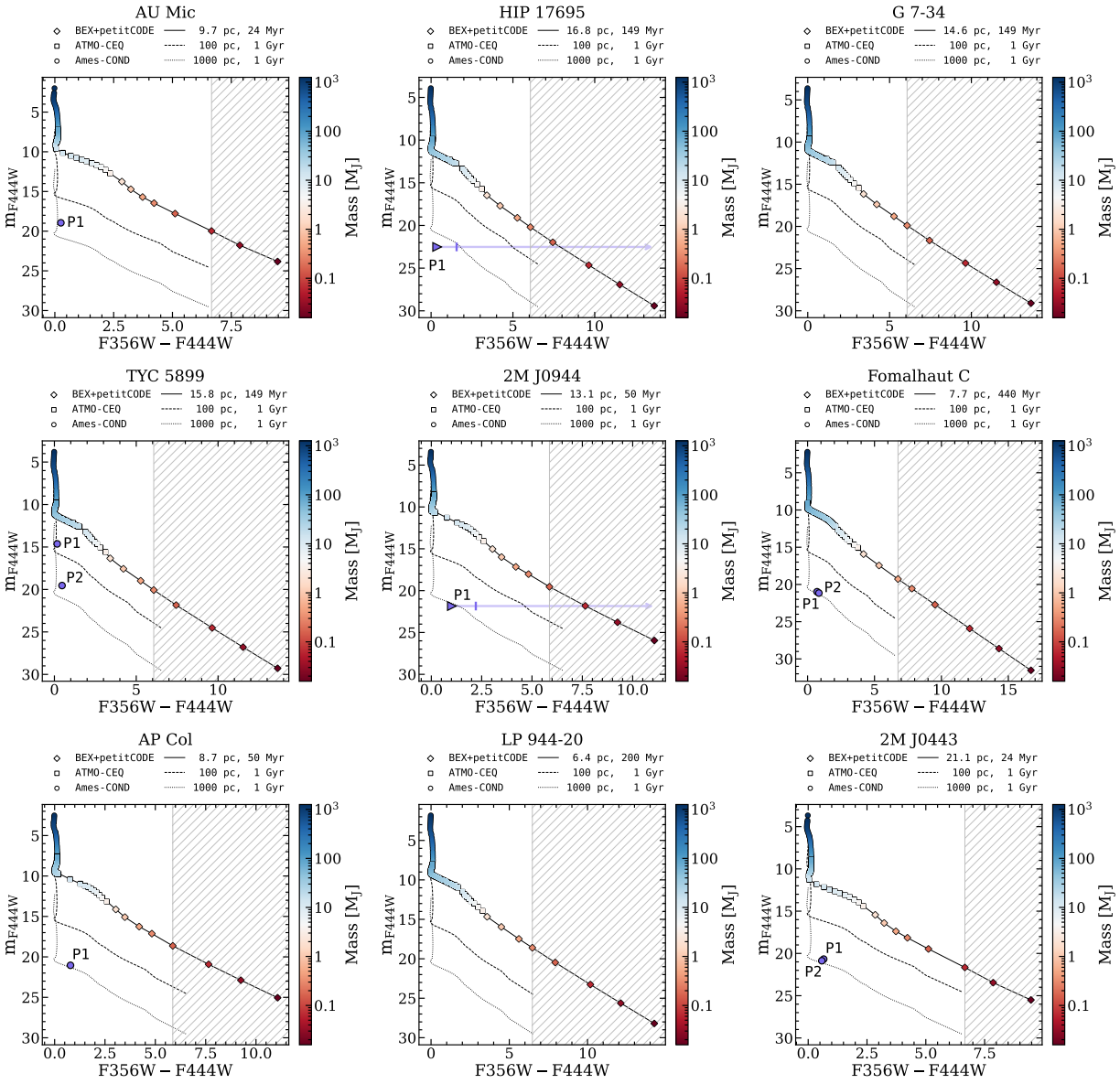

Figure 2.11: We compare the F444W photometry and F356W-F444W color of each detected point source (labeled purple icons) to the predicted photometry of stellar and substellar objects modeled at the age and distance of each target star (a.k.a. "isochrone curve", shown in the solid line) in order to rule out background contaminants. The point sources detected in both filters (purple circles) are far removed from the isochrone and thus unlikely to be associated with the target system, however the two F356W dropout sources (purple triangle at the 3-σ color limit, and vertical bar at the 1-σ color limit) are consistent both with substellar field objects and in the limit of their colors, with a sub-Saturn-mass companion. The color of the marker on the isochrone curve corresponds to the object mass, and the predicted photometry is based on the `Ames-COND` (circle markers, for M $>$ 0.075 $M_\odot$), `ATMO-CEQ` (square markers, for 0.075 $M_\odot >$ M $>$ 2 M_{Jup}), and `BEX-petitCODE` (for M $\leq$ 2 M_{Jup}) with the extrapolation to very low masses denoted by the hatched background. For comparison, we show isochrone curves for field age (1 Gyr) populations at 100 pc and 1000 pc in the dashed and dotted lines respectively.

age and distance as the host star. Off-axis sources whose magnitude and two-filter color do not coincide with the target star's isochrone curve are most likely background objects and can be ruled out as potential companions. We show the detected point source position in relation to the system isochrones for each target star in the survey in Figure 2.11, along with 1 Gyr isochrones to represent possible field objects at distances of 100 and 1000 pc. Each point source which we detect in both filters (marked in the figure with a purple circle) is offset to significantly fainter magnitudes than the isochrone for its would-be host star given its colors, thus they can all be ruled out as more distant background sources. As mentioned previously, we obtained 3 total observations of TYC 5899 over a temporal baseline of 4 months. Given the high proper motion of this target, we were able to visually confirm that TYC 5899 P1 and P2, shown in Figure 2.11 to be likely background objects, exhibited an apparent motion of approximately 0.5 pixels relative to TYC 5899 over the 4 months, confirming their status as background contaminants.

Each F356W dropout source detected via SNRE is marked in the figure with a purple triangle at the position of the F444W photometry measurement and the 3σ lower limit on F356W-F444W color, as well as a vertical bar at the position of the 1σ lower limit, with an arrow extending to the right showing the range of colors possible. Comparing these results with the isochrones shown in Figure 2.11, we can see that the F444W magnitudes of the sources are fainter than the lowest planet masses available in the [58] models for their respective target stars, but in the limit of their F356W-F444W colors they may be consistent with the color-magnitude space expected of a sub-Jupiter mass companion. If confirmed, these objects would be the lowest mass exoplanets ever imaged directly.

For both dropout sources, stellar background contaminants are ruled out by the positive F356W-F444W color limits. However, Figure 2.11 shows that the available photometric con-

Target	Source	Expected Warm BDs 3σ (1σ)	Expected Cool BDs 3σ (1σ)	Expected Galaxies 3σ (1σ)
HIP 17695	P1	0.021 (0.0)	0.003 (0.002)	3.7 (0.012)
2M J0944	P1	0.001 (0.0)	0.001 (4.3×10^{-4})	0.021 (0.004)

Table 2.4: Here we show the expected number of contaminating background objects in a given observation that would mimic a dropout point source candidate, based on the 3σ F356W-F444W color limits (with results from the 1σ color limits in parentheses). The estimated warm ($T_{eff} >$ 900 K) brown dwarf contamination is calculated from the TRILEGAL model of the galactic disk distribution of field substellar objects, the cool ($T_{eff} <$ 900 K) brown dwarf contamination is based on an analysis of the 20 pc census in [154], and the galaxy contamination is calculated from the observed population of galaxies in the JADES GOODS-S deep field.

straints are also consistent with older isolated brown dwarfs (BDs) or planetary mass objects in the distance range of 100s of parsecs, and in some cases out to 1000 pc. Given the galactic latitude and longitude of each target star, we can quantify the probability of contamination by the Galactic disk population of isolated brown dwarfs (down to effective temperatures of $\sim$900 K) using the TRILEGAL model distribution [155], following the prescription used in [156]. We calculate the expected number of isolated brown dwarfs mimicking each dropout signal by counting the number of brown dwarfs in a cone extending in the direction of a given target star and which has a solid angle equal to that of an individual GTO 1184 observation ($\sim$400 square arcsec). We then filter for only the BDs with a predicted F444W magnitude less than the F444W magnitude upper limit of the dropout source as well as a predicted F356W magnitude greater than the flux limit of that dropout source. We present the expected number of contaminating background L dwarfs for each source, showing both the 1σ and 3σ F356W flux limit case in Table 2.4. As our 1σ flux limits in F356W correspond to colors redder than those of the coolest brown dwarfs included in the TRILEGAL model (approximately spectral type T7), we effectively rule out brown dwarfs warmer than 900 K (a.k.a. "warm BDs") and report 0 expected contaminating objects for that

case. However in the 3σ flux limit case, we expect 0.021 contaminating warm BDs mimicking HIP 17695 P1 and a mere 0.001 contaminating warm BDs mimicking 2M J0944 P1.

However, the GTO 1184 observations are sensitive to background objects significantly cooler than TRILEGAL's lower temperature limit of $\sim$900 K. In particular, brown dwarfs with $T_{eff} < 900$ K (a.k.a "cool BDs") are expected to have F356W-F444W colors greater than 1 magnitude and could still appear in our data as dropout signals. As these objects are not all included in the TRILEGAL model, we quantify the likelihood of their appearance by analyzing the volume-limited census of stellar and substellar objects within 20 parsecs compiled in [154]. We collect all the objects provided in the published database with effective temperatures below 900 K, ignoring those which are companions of more massive stars. We then bin by effective temperature, grouping objects between 900-750 K (67 objects), 750-500 K (99 objects), and 500-250 K (48 objects). For each of these categories, we calculate the mean number density per pc^3 within the observed volume, as well as the range of distances at which the objects would be detectable with a F444W magnitude less than a given dropout source but undetectable at F356W (i.e. having an apparent magnitude greater than the 3- or 1-σ sensitivity limit in F356W at the separation of the dropout source). To do this, we use the provided WISE Band 1 and 2 magnitudes as a proxy for JWST F356W and F444W magnitudes respectively, given their similarity in wavelength coverage [157]. We then scale the number density of each category of BDs to the volume of space in which they would be observable as an object mimicking the dropout source according to our 3- and 1-σ F356W detection limits. While this assumes the number density of cool BDs is uniform out to potentially 1.5 kpc (the furthest distance at which we could detect early T-dwarfs as dropout sources according to the 1σ F356W limits), we expect the results displayed in Table 2.4 to be a conservative overestimate of the expected contaminating objects given that HIP 17695 and

2M J0944 are separated by $> 100^{\circ}$ from the galactic center and by $> 30^{\circ}$ from the plane of the galactic disk, where we would in reality expect the brown dwarf population density to decrease with distance. Even in this conservative case, we predict with 3σ confidence only 0.01 cool BDs to mimic HIP 17695, and only 0.001 cool BDs to mimic 2M J0944, given their intrinsic rarity and the narrow field of view of the NIRCam coronagraphic subarray.

In addition, some galaxies may occupy the same magnitude and color space as a young, low-mass planet (as revealed by WISE and Spitzer observations), which is particularly problematic if they are also small and/or distant enough to appear point-like. Early-type galaxies have 3-5 μm colors comparable to stars [158]. However, low red-shift Quasars, obscured Active Galactic Nuclei (AGN), and Luminous Infrared Galaxies are redder, with quasars and AGN typically displaying colors ranging from $\sim$0.8 – 1.5 mags [159]. To determine the probability of contamination by such galaxies quantitatively, we interpret the early results of the JWST Advanced Deep Extragalactic Survey (JADES) [160–162]. JADES is in the process of observing 136 square arcminutes of sky to search for high redshift galaxies, with significantly deeper sensitivity in both F444W and F356W (down to $\sim$30th magnitude). The JADES NIRCam photometry catalog for the GOODS-S deep field [163, 164] represents a subsection of the full survey with the deepest limiting magnitude and covering an area of 27 square arcminutes. In Figure 2.12 we show the F444W magnitude and F356W-F444W color of the JADES detections in black, as compared to the F444W magnitude and F356W-F444W color limits of the GTO 1184 dropout sources in purple (with a triangle at the 3σ limit and a vertical bar at the 1σ limit). We count the number of sources in the catalog that have a F444W magnitude less than or equal to to the upper limit of a given GTO 1184 dropout source, as well as a F356W magnitude greater than the F356W magnitude limit for the GTO 1184 source, as in the brown dwarf false positive calculation. We then

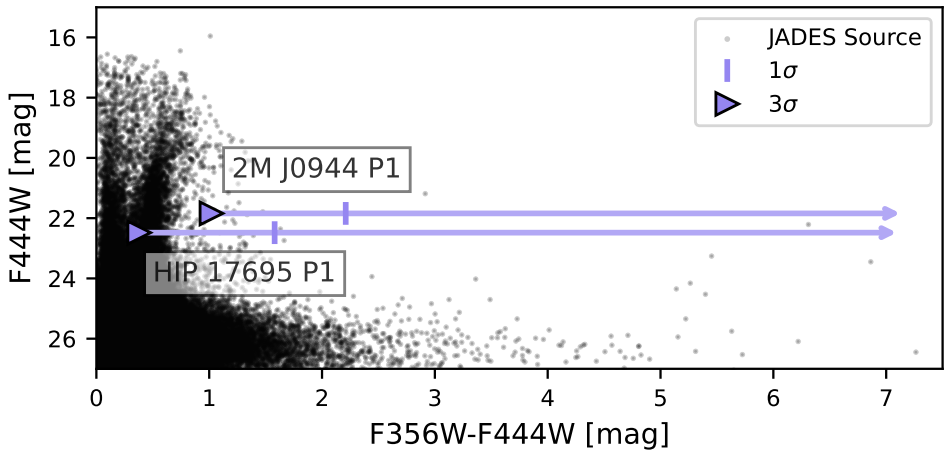

Figure 2.12: Color-magnitude diagram of the 2 dropout candidates (in purple) as compared to the sources in the JADES GOODS-S deep field catalog (in black), demonstrating the rarity of extragalactic sources with F444W magnitude < 24 and F356W-F444W color > 1. We show the 3σ and 1σ color limit of the dropout candidates with a triangle and verical bar, respectively. 2M J0944 P1 has the strongest color limit and a correspondingly low likelihood of being a background galaxy.

scale by the sky coverage of the GOODS-S deep field compared to the GTO 1184 survey field-of-view (0.11 square arcminutes per target), and determine the expected number of JADES sources that would mimic the dropout source in its field of view. As shown in the rightmost column of Table 2.4, the expected number of contaminants for source 2M J0944 P1 is a scant 0.021, and we gain confidence in ruling out background galaxy contaminants as the source of this signal. However, HIP 17695 P1 has a 3σ color limit consistent with more frequently occurring galaxies, therefore background contamination is more likely. We note that while the results for HIP 17695 imply that we should see several dropout galaxies in that FOV (the expected number is 3.667), the vast majority of planet-mimicking galaxies in the JADES data lie right near the 3σ detection limit in F444W for GTO 1184. Thus our detection of only a few dropout candidates with an SNRE of 4 or more is consistent with the expectation.

2.5 Discussion

This work represents the first probe of the sub-Saturn-mass exoplanet population via direct imaging, thus we have a responsibility to explore even marginal detections which are potentially consistent with low-mass planetary companions. The first dropout candidate, HIP 17695 P1, was initially detected with an SNRE of 4.84 in F444W. This was calculated by comparing the flux within the FWHM of a given point to the noise level averaged on an annulus surrounding the star at that separation. However after fitting a PSF model to the source and comparing the resulting flux to the local noise level, we found that that the SNR is only 1.64. This, in combination with the higher likelihood of contamination by extragalactic sources as shown in Table 2.4, makes it less compelling and leads us to demote it from consideration as an exoplanet candidate.

The remaining dropout source, 2M J0944 P1, with a marginally significant PSF fit SNR of 3.91 in F444W per Table 2.3 and an expected number of contaminating background sources of 0.023 objects with 3σ confidence, remains an intriguing candidate. The simplest course of action to confirm or reject the exoplanet nature of this source is to re-observe the system, re-detect the source at higher SNR, and verify common proper motion with the host star. Each of our target stars has a proper motion on the order of 100s of mas yr^{-1} or more, and common motion would be straight forward to detect after only one year given the astrometric accuracy for faint sources of $\lesssim$20 mas with NIRCam as demonstrated in this work.

Follow-up observations of the 2M J0944 system were recently executed in JWST Cycle 2 Guest Observer Program 3840 and the results of those analyses will be published in a future paper (Bogat et al., in prep). We note that the original candidate for this followup program was a 5σ source in the vicinity of G 7-34, however it was revealed to be an artifact due to imperfect cosmic-

ray correction with re-reduction of the full dataset using updated versions of the JWST pipeline and `spaceKLIP` (see Section 2.3.1). We were able to swap G 7-34 with 2M J0944 through a target change request, as 2M J0944 hosted our second-best dropout point source candidate at that time.

We also note that no objects consistent with Jupiter-mass, super-Jupiter-mass, or BD companions were detected in the survey. This is loosely in keeping with previous results showing low occurrence rates for giant planets orbiting M dwarfs [165], and we provide quantitative context for these results in the following subsection.

2.5.1 Implications for Population Statistics

The existing observational constraints for giant M dwarf planets with masses 1-10 M_{Jup} are consistent with a single underlying planet population, however several possible functional forms may accurately describe the planet surface-density distribution. Clanton et al. 2016a [93] adopted a power-law with a sharp outer cutoff radius around 10 AU to match imaging upper limits at the widest separations. Meyer et al. 2018 [166] included newer imaging constraints and found that a log-normal distribution with a peak around 3 AU fit the extant observations. However, due to the limited mass sensitivity of the previously available high-contrast imaging observations, the population of sub-Jupiter-mass planets at wide separation lacks constraint.

To explore the population in this newly accessible mass regime, we perform yield simulations based on a recent parametric demographics model for M dwarf companions (Meyer et al. 2025, in prep) and our sensitivity constraints from the 5σ sensitivity curves for each target (see Section 2.7.2). We simulate the yield for brown dwarf binary companions, as well as for

planets in two different planetary mass regimes, dividing the planet population into sub-Jupiters and super-Jupiters with the transition defined at 1 M_{Jup}. Each population is represented by a log-normal orbital distribution (peaking at ∼4 AU for sub- and super-Jupiters, and ∼30 AU for brown dwarfs) and a power-law mass ratio distribution (index of ∼-1.43 for planets and ∼0.3 for brown dwarfs). The super-Jupiter model is constrained by empirical evidence from previous exoplanet demographics surveys, including the HARPS radial velocity survey [167], SPHERE SHINE survey [31], and GPIES [168]. We set the lower mass limit for planets at 0.03 M_{Jup} (or 10 $M_{\oplus}$), as this is below the median detection threshold for the survey. The upper mass limit for planets is defined as 10% of the stellar mass, instead of the deuterium-burning limit of 13 M_{Jup}, as M dwarf disks are not expected to be massive enough to create 13-Jupiter-mass objects via a planet-like formation pathway. For companion generation, we draw 10^5 random sets of orbital parameters using the following priors: uniform priors for the longitude of the ascending node and the longitude of periapse, cosine priors for inclination, and Gaussian priors for eccentricity ($\mu = 0$, $\sigma = 0.3$; [169]), and consider a given planet "detected" if it appears above the 5-σ contrast curve for its host star. We calculate the expected number of planets to be detected around each star individually, assuming a total frequency (objects per star between 0 and 200 AU) of 0.02 for BDs, 0.09 for super-Jupiters, and 0.18 for sub-Jupiters, then sum the results to achieve an expected yield for the entire program. This results in an estimated yield for GTO 1184 of 0.45 ± 0.13 sub-Jupiters, 0.1 ± 0.012 super-Jupiters, and 0.085 ± 0.05 brown dwarfs.

We also explore an alternative sub-Jupiter model, which follows the same mass ratio distribution as the gas giants but features a modified separation model. This model assumes the same log-normal distribution of semimajor axis as that of the super-Jupiters within 10 AU [27], but transitions to a log-flat distribution beyond 10 AU. The extension is motivated by the presence of

the Solar System outer planets and by recent mm-wave ALMA disk gap observations (e.g. Garufi et al. 2024) [170]. Under this assumption, the expected program yield of sub-Jupiters increased to 1.36 ± 0.18, effectively tripling the previous expectation.

In the super-Jupiter and BD regimes, our predictions are consistent both with the lack of detections in GTO 1184 and with the low yields from previous, less-sensitive M-dwarf observations from the ground (e.g. Bowler et al. 2015 [171]). For sub-Jupiters, a log-flat distribution of objects beyond 10 AU leads to a significant boost in the yield prediction at wide separation compared to the higher mass companions, and our identification of the marginal sub-Jupiter candidate 2M J0944 P1 is intriguing in this context. However, the small sample size of the survey, in combination with parametric degeneracies in the occurrence model, prevents us from definitively determining whether the log-normal or log-flat distribution of sub-Jupiters beyond 10 AU more accurately represents the underlying population via these observations alone.

Assuming conservatively that 2M J0944 P1 is not a planet, we can place an upper limit on the frequency of planetary companions in the mass and separation range covered by GTO 1184. We simulate 10,000 surveys with varying amplitudes of the planet and BD occurrence distribution, using the log-flat distribution of sub-Jupiters, and compare the simulated populations with the detection probability curves to determine the maximum possible planet and brown dwarf frequency (a.k.a. the intrinsic number of objects per star) that still results in an expectation of 0 detections in our observations. We adopt the 68%, 95%, and 99.7% detection probability contours respectively (shown in Figure 2.9) and find that the frequency of planets with masses between 0.3-1.0 M_{Jup} and semimajor axes between 10-200 AU (reflecting our sensitivity limits) is < 0.10 with 1σ confidence, < 0.14 with 2σ confidence, and < 0.17 with 3σ confidence. When we repeat the analysis assuming the log-normal distribution of sub-Jupiters beyond 10 AU, we find

Category	Mass Range	SMA Range	Frequency Upper Limit (1σ)	(2σ)	(3σ)
Sub-Jupiters (log-norm)	0.1-1 M_{Jup}	10-200 AU	< 0.10	< 0.13	< 0.16
Sub-Jupiters (log-flat)	0.1-1 M_{Jup}	10-200 AU	< 0.10	< 0.14	< 0.17
Super-Jupiters	1 M_{Jup} - 0.1 M_*	10-200 AU	< 0.12	< 0.15	< 0.21
Brown Dwarfs	3-75 M_{Jup}	10-200 AU	< 0.16	< 0.18	< 0.23

Table 2.5: Occurrence constraints (objects per star) for substellar companions in different mass categories with semimajor axes between 10-200 AU that would result in the expectation of 0 detections in the survey. The sub-Jupiter results are shown for both the case where the underlying separation distribution is a log-normal distribution centered at 4 AU (denoted "log-norm" in the table), and the case where it is represented by the same log-normal distribution within 10 AU but transitions to log-flat beyond 10 AU (denoted "log-flat" in the table). The estimates are generated by simulating the substellar companion population described by Meyer et al. 2025 (in prep) and comparing with the 68%, 95%, and 99.7% detection probability contours (see Fig. 2.9) for the 1-, 2-, and 3-σ confidence estimates respectively. The super-Jupiter and brown dwarf constraints are loose but consistent with previous direct-imaging surveys. The results for sub-Jupiters are the first occurrence constraints produced in this mass-separation regime, and are not significantly sensitive to the underlying separation models given the small sample size.

very similar limits of < 0.10 with 1σ confidence, < 0.13 with 2σ confidence, and < 0.16 with 3σ confidence, showing that the occurrence constraints are not significantly model-dependent. These results, as well as the occurrence constraints for the super-Jupiter and BD populations, are summarized in Table 2.5. Given the small sample size of our survey, the constraints are necessarily loose. However, continued imaging of nearby, young M dwarf systems will build up the statistical power of our early observations to provide a clearer picture of wide-orbit giant planet occurrence around M stars.

2.5.2 Lessons Learned for JWST NIRCam Coronagraphic Imaging

In GTO 1184, we achieved a flux contrast roughly similar to the results of the Direct Imaging ERS observations (F444W 5σ contrast of 1.5×10^{-5} at 1" in this work as compared to 1.0×10^{-5} at 1" in Carter et al. 2022 [50]), but our choice of cooler target stars results in deeper

companion mass sensitivities for individual targets by up to a factor of 10. Notably, we achieve this without the use of dedicated reference stars, thereby maximizing the survey efficiency and the total observation time used for science targets.

We also opted not to use the small-grid dither approach [172], which is commonly employed when using dedicated PSF reference stars to increase the PSF sample variety. However, dithering on a science target is not recommended as it would result in the majority of the exposures having a sub-optimal star-coronagraph alignment. As noted in Figure 2.3, we found that RDI without dithering can outperform the sensitivity of the pure ADI reduction within the IWA even with only a single reference star used, but that this depends on the star-mask alignment of the reference observation being closer to that of a given science observation than the two science roll images are to each other. In the background-limited regime, we find that the inclusion of additional science targets as PSF references further improves the sensitivity. We note that the masking applied to prepare the science observations for use as PSF references (described in Section 2.3.1.2) was critical to allow the maximum number of references to be useful without generating subtraction artifacts. Further contrast sensitivity improvements may be possible by incorporating PSFs into the reference library from other NIRCam coronagraphic surveys, including JWST GOs 4050 and 5835 (PI Carter) and GO 6005 (PI Biller), however these data were not publicly available at the time of our analysis.

We note that we chose to have larger slews between adjacent observations (occasionally $\gtrsim 50°$) in order to group target observation sequences by similar spectral type. Due to the exceptional thermal stability of the observatory, these slew distances did not have a significant effect on the WFE drift between adjacent observations [147], and therefore did not adversely affect the PSF subtraction quality.

2.5.3 Caveats & Limitations

There are several as-yet undiscussed factors which add uncertainty to our results. The first is that we rely on a single, cloud-free model grid (`BEX-petitCODE` [58]) for predicting the photometry of planets below 2 M_{Jup}, which may not accurately reflect their physical conditions. Comparisons to models which include clouds (e.g. `BT-SETTL` [173]) and/or disequilibrium chemistry ([e.g. `ATMO 2020-NEQ` [152]) would provide a more complete picture of the possible planet parameters compatible with a given detected source. However, no atmospheric models currently exist which include self-consistent prescriptions for both clouds and disequilibrium chemistry simultaneously, especially near or below effective temperatures of 150 K.

Furthermore, the `BEX-petitCODE` model grid has a low temperature limit of 150 K, while we demonstrate that JWST NIRCam coronagraphy is sensitive to planets significantly fainter, thus lower mass and presumably colder than can currently be modeled. We have performed a basic extrapolation (linear in log space) to be able to visualize the most likely accessible planet masses in our survey (see Figure 2.9). Around the faintest and youngest target in the GTO 1184 sample (2MJ 0443), we achieve model predicted sensitivity to planets comparable in mass and separation to Neptune in our Solar System. These results reveal that extensions to exoplanet evolution and atmosphere model grids that include the relevant physics for ice-giant like planets at temperatures $<$150 K are needed to fully interpret NIRCam's sensitivity.

We also note that our differentiation between point-like and extended sources was performed by inspecting PSF fit residuals by eye, rather than by an explicit quantitative metric. The ability to quantify the "extendedness" of a given source is being implemented into `spaceKLIP` at the time of writing, and will be useful to better rule out extended sources in the future.

We reiterate that we reduced our SNRE threshold to yield the detection of several F356W dropout sources. As our background noise is approximately gaussian, one would expect 1 in 15800 pixels to produce a noise fluctuation above a 4σ level. The field of view of the entire survey is 799313 pixels, so we expect that ~ 50 individual pixels would achieve an SNRE of 4. However, we convolve the data with a tophat filter of the size of the PSF (FWHM of 2.3 pixels for F444W) before calculating the SNRE. This has the effect of suppressing signals with a spatial correlation narrower than the FWHM of the PSF. As the spatial correlation of the background noise corresponds to a gaussian FWHM of 0.55 pixels, these statistical fluctuations are narrower than the PSF and thus unlikely to contaminate our SNRE calculations or be visually confused with PSFs. Furthermore, we have cross-checked each dropout source to ensure the signal remains above SNRE 4 across multiple reduction strategies, we believe this chance is further reduced (indeed several initial dropout candidates were ruled out this way) however nonzero. Given our 4σ F444W SNRE cutoff for these sources, lower limits on the F356W-F444W colors, and the lack of diagnostic follow-up, we do not claim a definitive detection of a sub-Saturn-mass exoplanet. However, these results indicate that deeper observations of 2M J0944 would provide a more significant detection as well as better color limits, and they have been pursued in the aforementioned GO 3840 follow-up observations.

As alluded to in Section 2.5.1, both the small sample size of the GTO 1184 survey and the presence of parametric degeneracies in the occurrence model prevent us from definitively determining whether the separation distribution of sub-Jupiters at wide orbits (beyond 10 AU) follows a log-normal or log-flat distribution. The effect of the small sample size is self-evident, and we note explicitly that even if the sub-Jupiter candidate 2M J0944 were confirmed, we would still need more high-contrast imaging observations to meaningfully constrain the occurrence rate

of sub-Jupiters beyond 10 AU. Regarding degeneracies in the model, currently both the peak amplitude of sub-Jupiter frequency (at 4 AU in either case) and the shape of the separation distribution's wide-orbit tail are ill-constrained by observations. The frequency for the log-normal distribution is predicted to be 0.18 objects per star across separations from 1-100 AU. Assuming the same frequency within 10 AU but transitioning to a log-flat distribution beyond 10 AU results in approximately triple the expected sub-Jupiters at wide orbits. Thus, if we measure a frequency of wide-orbit sub-Jupiters to be significantly higher than expected from the log-normal distribution case, we might deduce that the underlying population must indeed have some extended tail. However it could also be explained by the sub-Jupiter population at all separations being elevated, but still having a log-normal separation distribution. [97] summarizes $\sim$20 years of microlensing data from the Optical Gravitational Lensing Experiment (OGLE), finding that each microlensing star hosts $1.4^{+0.9}_{-0.6}$ ice giants (with semimajor axis 5-15 AU and planet-star mass ratios ranging from 10^{-4} to 3.3×10^{-2}) on average. To confidently differentiate between the two wide-orbit demographic models, we will need stronger constraints on the sub-Jupiter population in the inner (1-10 AU) separation region around M dwarfs, which are expected to be provided by exoplanet discoveries from the Roman Galactic Bulge Time Domain Survey [174, 175] and *Gaia* astrometry in the next several years [106].

2.6 Summary & Conclusions

We present results from JWST Cycle 1 GTO Program 1184, designed to survey a carefully selected sample of very nearby, young, M dwarfs with JWST NIRCam Coronagraphy at 3 - 5 μm wavelengths to search for sub-Jupiter mass planets on wide orbits. The key approaches and

results of the survey are as follows:

- We chose very nearby, young, low-luminosity M dwarfs as targets to access planets and disks at Solar System-like separations and achieve very deep planet mass sensitivity in contrast limited observations;

- We used the standard high-contrast imaging post-processing approach of KLIP RDI and the open source software package `spaceKLIP` to construct optimized PSF references using the science target observations (a self-referenced survey). This approach allowed us to perform an efficient survey while reaching contrasts consistent with other JWST NIRCam observations that observed dedicated PSF references;

- Our observations and post-processing approach result in reduced images with typical model derived sensitivities to Saturn-mass planets at Saturn like projected separations (9.5 AU). For some targets, the sensitivities push down to approximately the mass of Neptune at $\gtrsim$10 AU, based on the extrapolation of existing model grids. We are able to rule out companions with masses $\gtrsim 0.3$ M_{Jup} in the 10s of AU region around each of the 9 target stars;

- While our model derived mass sensitivities are the deepest yet achieved via direct imaging observations, we note that the GTO 1184 observations are sensitive to masses below the lower limits of the available planet evolution model grids at the young ages of the targets. The models need to be extended to lower masses (cooler temperatures) to fully explore the available parameter space without extrapolation;

- We tentatively identify a marginally detected source, 2M J0944 P1, that has a 3-5 μm photometric color limit consistent with the expectation for a $\sim$Saturn-mass planet. For this

source, we estimate low probabilities of background contamination by stars, field brown dwarfs, or galaxies. In a future publication, we will present a proper-motion analysis of recently collected follow-up NIRCam coronagraphic imaging data to either confirm or refute the association of 2M J0944 P1 with 2M J0944.

- We also place the survey results in context with planet population models in three different mass regimes. In particular, we place the first occurrence rate constraints on wide-orbit, sub-Jupiter (semimajor axes 10-200 AU, masses 0.3-1 M_{Jup}) exoplanets around M dwarfs to be < 0.10 and < 0.16 objects per star with 1- and 3-σ confidence respectively, assuming the Meyer 2025 (in prep) population model;

- Finally, GTO 1184 allowed for the first detection of the well studied AU Mic debris disk at 3-5 μm [137] and the first reflected light detection of the faint disk associated with Fomalhaut C [138].

The execution and analysis of GTO 1184 survey data has further demonstrated the unprecedented sensitivity of JWST NIRCam coronagraphy and its potential to advance exoplanet science. The search for wide-separation planets in young M dwarf systems provides insight into the broad population of their exoplanets from the inner regions to outer reaches of these systems. The deep, wide-orbit constraints provided by GTO 1184 also provide context for the orbital and thermal evolution of the inner and potentially habitable planets of these systems. With several larger JWST surveys currently planned to search for planetary companions of young, low-mass stars, e.g. GO 4050/5835 (PI Carter), GO 6005 (PI Biller), GO 6122 (PI Bowens-Ruben), GO 8826 (PI Lawson), we have entered a new regime of direct sub-Jupiter imaging with JWST.

2.7 Ancillary Information

2.7.1 Flux Maps

In our primary analysis, we use the SNRE maps as the key diagnostic tool, however the measurement of per-pixel noise and individual source photometry is done in units of flux (MJy/steradian). In Figure 2.13 we show the images of each target in the F444W filter for reference, and the SNRE maps of each target can be found in Section 2.4.

In Figure 2.14, we show the images of each target in the F356W filter (in flux units) for reference. The SNRE maps of each target can be found in Section 2.4.

2.7.2 Individual Sensitivity Curves

For brevity, we displayed the survey median contrast sensitivity curves in Section 2.4.1, and here in Figure 2.15 we show the results for each target individually. We achieve the background limited sensitivity at a separation of approximately 2.5" for each target, with the exceptions of AU Mic (due to its bright disk) and TYC 5899 (due to a bright off-axis source at $\sim$3"). The background-limited contrast is shallowest for the latest-type M dwarfs, as their intrinsic luminosities are the lowest while the background level is roughly constant across the targets.

In Figure 2.16 we show the 5σ sensitivity limits in units of apparent magnitude for each target. We achieve a typical background-limited flux sensitivity of $\sim$ 21.5 in F444W and $\sim$ 22.5 in F356W. However the sensitivity is shallower for AU Mic due the use of the SHALLOW2 detector readout pattern for that target, as opposed to the MEDIUM8 pattern which was used for the rest of the targets.

2.7.3 Candidate Photometry

In Section 2.4.2, we show the best-fit parameters for each source in each filter using either the `spaceKLIP` or semi-independent least-squares PSF fitting methods, as occasionally the `spaceKLIP` method failed to converge or produced erroneous results. Here in Tables 2.6 and 2.7 we show the results for each method in filters F444W and F356W respectively, for reference.

2.7.4 Extended Source Catalog

In Table 2.8 we show the list of extended sources identified in the GTO 1184 survey, with their approximate location and peak SNRE in each filter. While most of the sources are clearly visibly extended in the data, some were identified as extended only after the observation of a halo-like or extended structure in the residuals when fitting a point-like PSF.

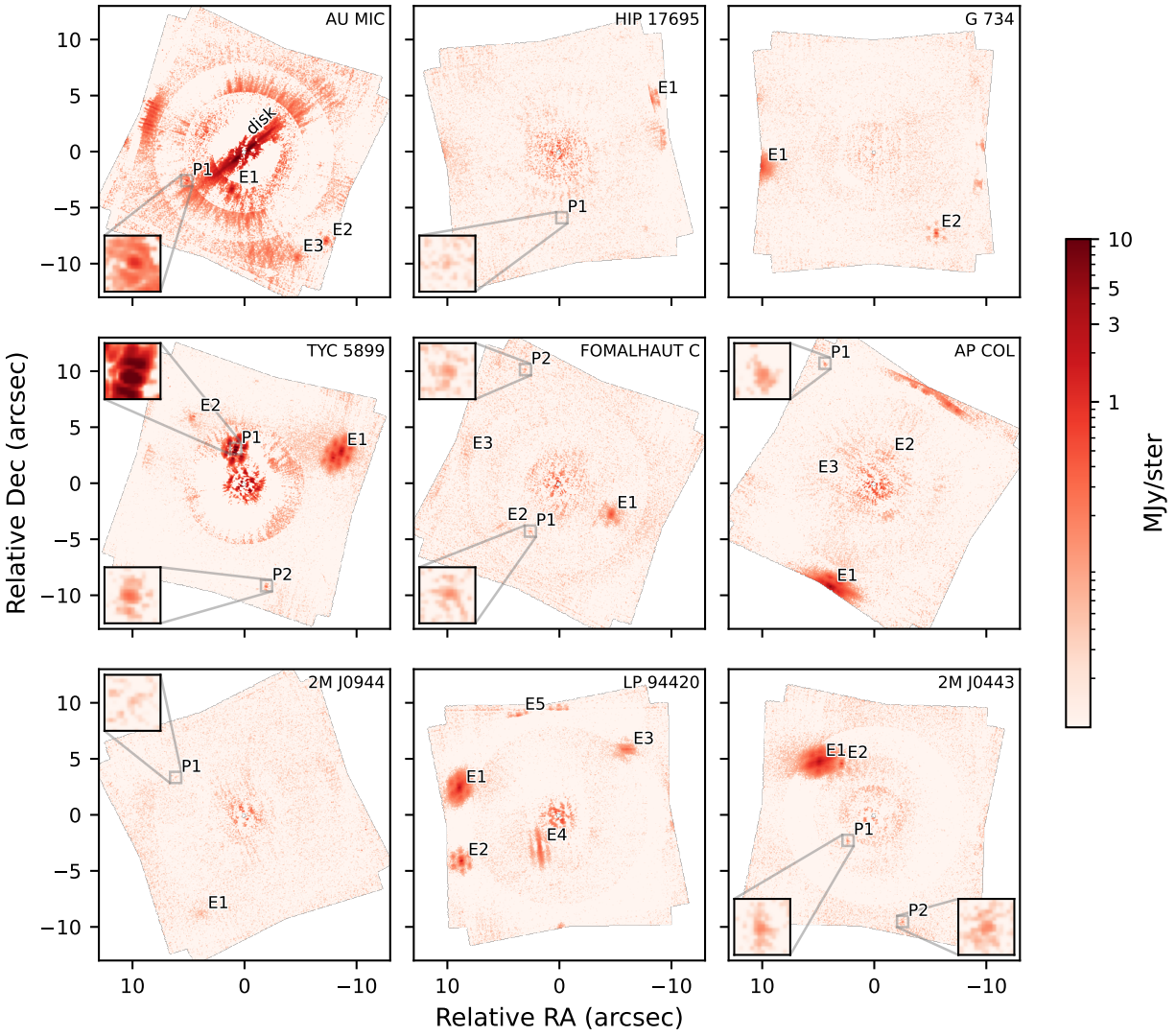

Figure 2.13: Flux maps of all targets in GTO 1184, in the F444W filter. All observations were reduced with RDI using the full library of reference PSFs. Point-like and extended sources are labeled in the images (with names beginning with "P" and "E" respectively), and the point-like sources are magnified in the image insets. Extended background sources are abundant in the survey, and the edge-on disk of AU Mic is clearly detected.

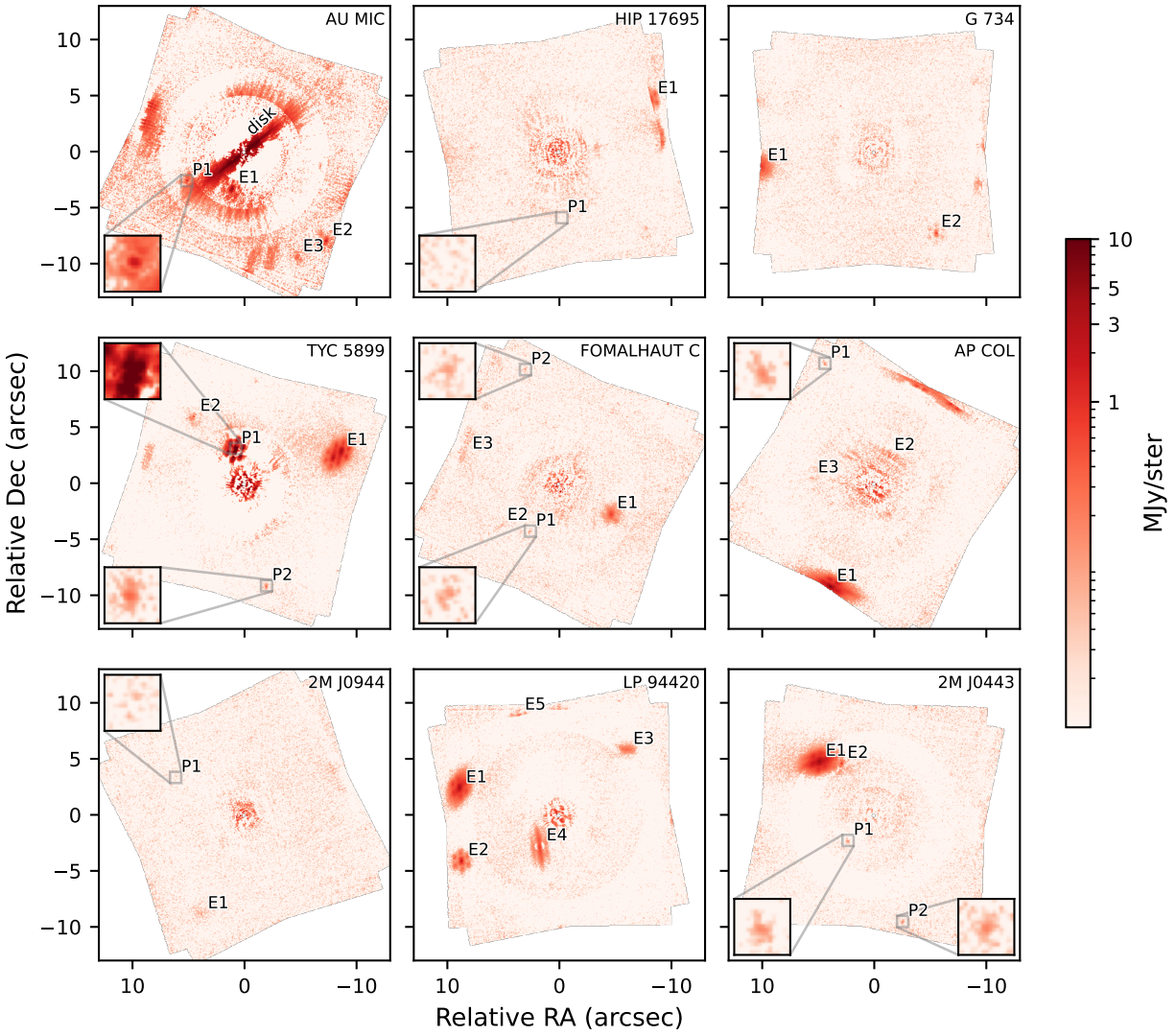

Figure 2.14: Flux maps of all targets in GTO 1184, in the F356W filter. All observations were reduced with RDI using the full library of reference PSFs. Point-like and extended sources are labeled in the images (with names beginning with "P" and "E" respectively), and the point-like sources are magnified in the image insets. Extended background sources are abundant in the survey, and the edge-on disk of AU Mic is clearly detected.

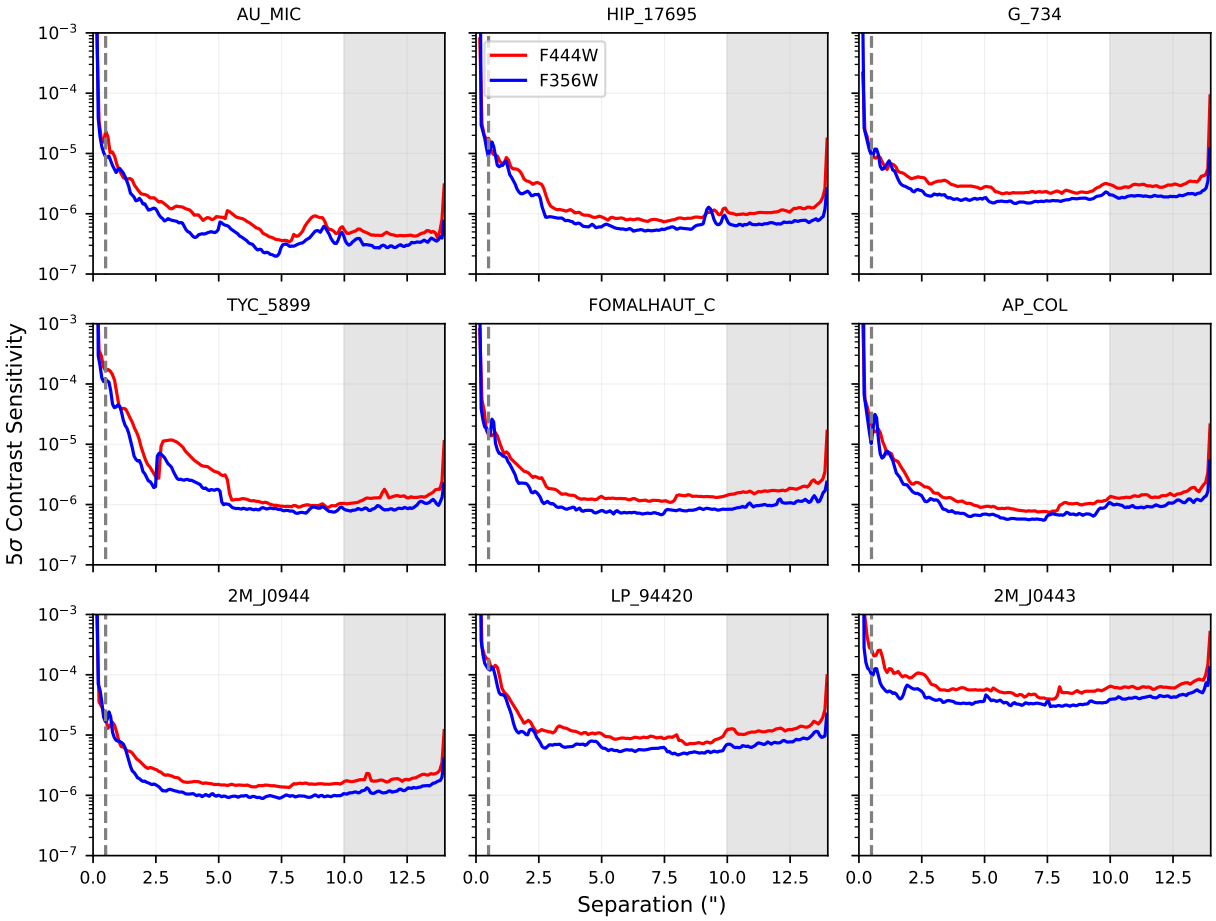

Figure 2.15: 5σ sensitivity curves for each target star in the F444W filter (red lines) and F356W filter (blue lines). The sensitivity is given in units of flux contrast in the lower panel. The coronagraph inner working angle (IWA) is shown in the gray dashed line, and the separations where only partial coverage exists due square framed observations at multiple roll angles is shown by the gray shaded region. We demonstrate extremely deep limits in absolute flux at close angular separations.

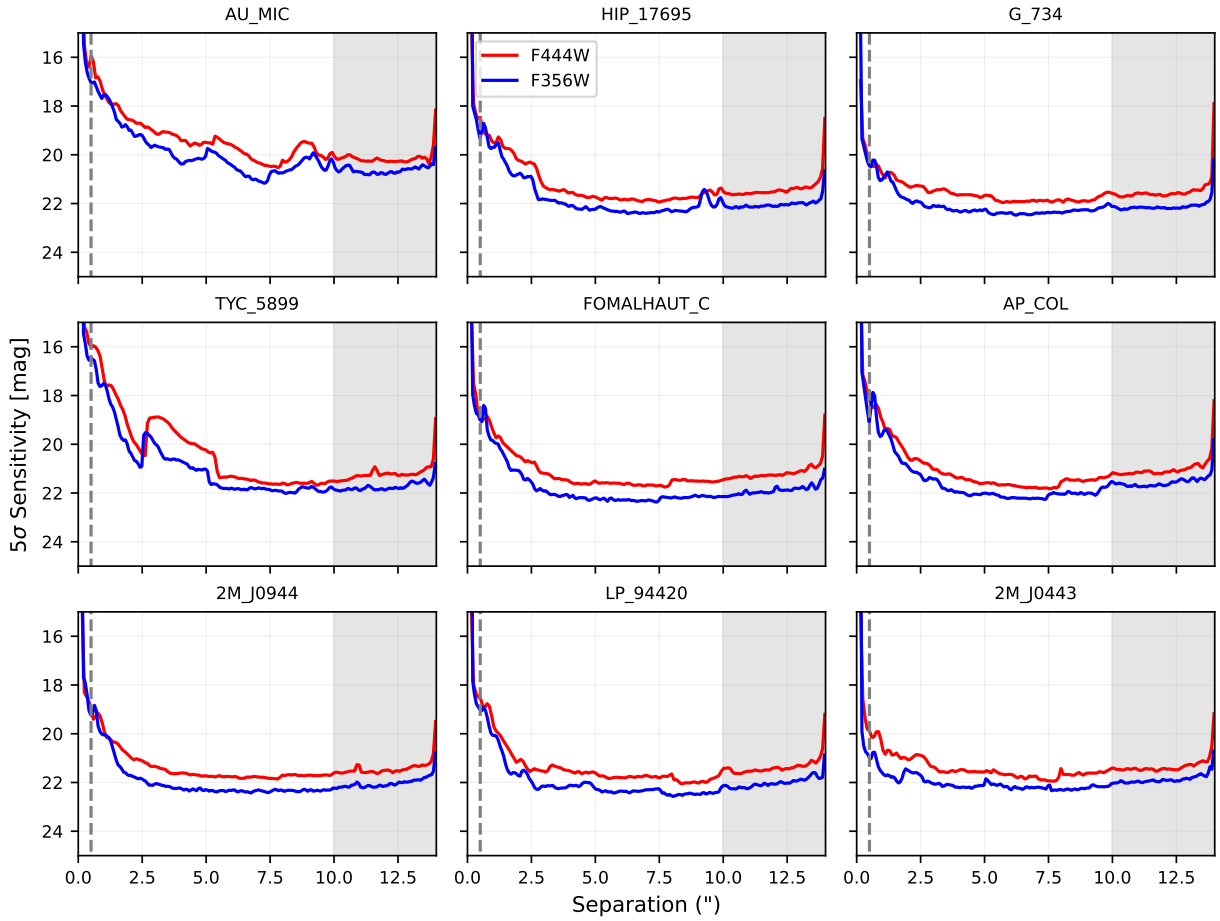

Figure 2.16: 5σ sensitivity curves for each target star in the F444W filter (red lines) and F356W filter (blue lines). The sensitivity is given in units of apparent magnitude in the lower panel. The coronagraph inner working angle (IWA) is shown in the gray dashed line, and the separations where only partial coverage exists due square framed observations at multiple roll angles is shown by the gray shaded region. We demonstrate extremely deep limits in absolute flux at close angular separations.

F444W			spaceKLIP			
Target	Source	SNRE	RA	Dec	Flux [mag]	SNR
AU Mic	P1	7.21	$5.057^{+0.014}_{-0.014}$	$-2.51^{+0.011}_{-0.011}$	$18.947^{+0.144}_{-0.144}$	7.68
HIP 17695	P1	4.84	-	-	-	-
TYC 5899	P1	68.69	$0.745^{+0.007}_{-0.007}$	$3.031^{+0.007}_{-0.007}$	$14.634^{+0.004}_{-0.004}$	75.11
	P2	17.12	-	-	-	-
Fomalhaut C	P1	9.03	$2.521^{+0.058}_{-0.058}$	$-4.219^{+0.112}_{-0.112}$	$20.98^{+0.174}_{-0.174}$	6.83
	P2	5.76	$2.992^{+0.042}_{-0.042}$	$10.216^{+0.014}_{-0.014}$	$21.153^{+0.108}_{-0.108}$	5.76
AP Col	P1	5.81	$4.385^{+0.037}_{-0.037}$	$10.692^{+0.013}_{-0.013}$	$21.042^{+0.125}_{-0.125}$	4.04
2M J0944	P1	4.02	$6.098^{+0.018}_{-0.018}$	$3.423^{+0.022}_{-0.022}$	$21.842^{+0.093}_{-0.093}$	3.91
2M J0443	P1	9.28	$2.314^{+0.016}_{-0.016}$	$-2.264^{+0.011}_{-0.011}$	$21.282^{+0.196}_{-0.196}$	4.08
	P2	8.44	$-2.537^{+0.056}_{-0.056}$	$-9.475^{+0.009}_{-0.009}$	$20.865^{+0.095}_{-0.095}$	5.96

F444W (cont'd)		LSQ				
Target	Source	RA	Dec	Flux [mag]	SNR	Method
AU Mic	P1	$5.052^{+0.009}_{-0.009}$	$-2.511^{+0.008}_{-0.008}$	$18.765^{+0.049}_{-0.049}$	7.59	sklip
HIP 17695	P1	$-0.281^{+0.007}_{-0.007}$	$-5.837^{+0.009}_{-0.009}$	$22.481^{+0.282}_{-0.282}$	1.64	lsq
TYC 5899	P1	$0.748^{+0.007}_{-0.007}$	$3.034^{+0.007}_{-0.007}$	$14.644^{+0.007}_{-0.007}$	50.95	sklip
	P2	$-1.979^{+0.008}_{-0.008}$	$-9.107^{+0.007}_{-0.007}$	$19.54^{+0.032}_{-0.032}$	12.97	lsq
Fomalhaut C	P1	$2.489^{+0.032}_{-0.032}$	$-4.197^{+0.009}_{-0.009}$	$21.082^{+0.084}_{-0.084}$	4.98	sklip
	P2	$2.951^{+0.042}_{-0.042}$	$10.203^{+0.014}_{-0.014}$	$21.114^{+0.086}_{-0.086}$	4.67	sklip
AP Col	P1	$4.349^{+0.037}_{-0.037}$	$10.7^{+0.068}_{-0.068}$	$20.673^{+0.153}_{-0.153}$	4.85	sklip
2M J0944	P1	$6.086^{+0.016}_{-0.016}$	$3.402^{+0.022}_{-0.022}$	$22.044^{+0.191}_{-0.191}$	2.47	sklip
2M J0443	P1	$2.311^{+0.011}_{-0.011}$	$-2.259^{+0.011}_{-0.011}$	$20.678^{+0.085}_{-0.085}$	5.94	lsq
	P2	$-2.593^{+0.056}_{-0.056}$	$-9.481^{+0.009}_{-0.009}$	$20.882^{+0.066}_{-0.066}$	6.66	sklip

Table 2.6: Photometric and astrometric results for each off-axis source in the F444W filter, using both the spaceKLIP and LSQ PSF fitting methods as described in Section 2.3.2. We show the peak SNRE and preferred fitting method, as well as the best-fit relative right ascension, relative declination, flux, and PSF fit SNR using each method. In cases where a PSF fit failed, or was not performed for F356W dropout sources, a dash is displayed.

F356W			spaceKLIP			
Target	Source	SNRE	RA	Dec	Flux [mag]	SNR
AU Mic	P1	9.26	$5.065^{+0.013}_{-0.013}$	$-2.503^{+0.008}_{-0.008}$	$19.203^{+0.118}_{-0.118}$	7.89
HIP 17695	P1	-0.39	-	-	-	-
TYC 5899	P1	68.46	$0.742^{+0.007}_{-0.007}$	$3.033^{+0.007}_{-0.007}$	$14.804^{+0.006}_{-0.006}$	68.02
	P2	12.17	-	-	-	-
Fomalhaut C	P1	5.41	$2.483^{+0.018}_{-0.018}$	$-4.184^{+0.013}_{-0.013}$	$21.688^{+0.111}_{-0.111}$	5.84
	P2	4.59	$2.996^{+0.031}_{-0.031}$	$10.235^{+0.029}_{-0.029}$	$21.997^{+0.157}_{-0.157}$	4.1
AP Col	P1	5.39	$4.345^{+0.019}_{-0.019}$	$10.714^{+0.025}_{-0.025}$	$21.828^{+0.215}_{-0.215}$	3.72
2M J0944	P1	2.98	-	-	-	-
2M J0443	P1	6.45	-	-	-	-
	P2	7.99	$-2.548^{+0.041}_{-0.041}$	$-9.477^{+0.014}_{-0.014}$	$21.444^{+0.083}_{-0.083}$	7.09

F356W (cont'd)		LSQ				
Target	Source	RA	Dec	Flux [mag]	SNR	Method
AU Mic	P1	$5.054^{+0.013}_{-0.013}$	$-2.503^{+0.008}_{-0.008}$	$19.006^{+0.051}_{-0.051}$	8.96	sklip
HIP 17695	P1	-	-	-	-	-
TYC 5899	P1	$0.745^{+0.007}_{-0.007}$	$3.036^{+0.007}_{-0.007}$	$14.735^{+0.01}_{-0.01}$	48.57	sklip
	P2	$-1.982^{+0.008}_{-0.008}$	$-9.102^{+0.008}_{-0.008}$	$20.003^{+0.041}_{-0.041}$	11.38	lsq
Fomalhaut C	P1	$2.506^{+0.013}_{-0.013}$	$-4.182^{+0.012}_{-0.012}$	$21.789^{+0.103}_{-0.103}$	4.59	sklip
	P2	$2.965^{+0.031}_{-0.031}$	$10.206^{+0.029}_{-0.029}$	$21.798^{+0.114}_{-0.114}$	4.38	sklip
AP Col	P1	$4.346^{+0.01}_{-0.01}$	$10.74^{+0.028}_{-0.028}$	$21.126^{+0.108}_{-0.108}$	4.60	sklip
2M J0944	P1	-	-	-	-	-
2M J0443	P1	$2.299^{+0.092}_{-0.092}$	$-2.262^{+0.047}_{-0.047}$	$21.334^{+0.142}_{-0.142}$	5.84	lsq
	P2	$-2.589^{+0.041}_{-0.041}$	$-9.49^{+0.014}_{-0.014}$	$21.439^{+0.082}_{-0.082}$	5.99	sklip

Table 2.7: Photometric and astrometric results for each off-axis source in the F356W filter, using both the spaceKLIP and LSQ PSF fitting methods as described in Section 2.3.2. We show the peak SNRE and preferred fitting method, as well as the best-fit relative right ascension, relative declination, flux, and PSF fit SNR using each method. In cases where a PSF fit failed, or was not performed for F356W dropout sources, a dash is displayed.

Target	Source	Separation ["]		Peak SNRE	
		RA	Dec	F356W	F444W
AU MIC	E1	1.038	-3.241	25.62	21.38
	E2	-7.394	-7.960	19.47	16.16
	E3	-4.751	-9.408	4.00	6.85
HIP 17695	E1*	-8.338	4.814	21.74	15.22
G 734	E1	10.100	-1.227	37.42	42.88
	E2	-5.632	-7.268	36.43	50.65
TYC 5899	E1	-8.716	2.989	172.44	197.97
	E2	4.499	6.073	11.88	17.25
FOMALHAUT C	E1	-4.688	-2.674	39.28	40.45
	E2	5.192	-3.744	4.95	5.91
	E3	8.275	2.674	1.92	7.35
AP COL	E1	3.870	-9.219	66.09	69.82
	E2	-1.227	2.612	8.13	3.70
	E3	5.506	0.535	5.04	-0.02
2M J0944	E1	3.807	-8.841	5.80	6.75
LP 94420	E1	8.904	2.486	164.04	168.94
	E2	8.716	-4.059	90.56	65.23
	E3	-6.136	5.947	17.77	28.42
	E4	1.668	-2.737	26.83	20.63
	E5*	3.618	9.030	9.92	13.36
2M J0443	E1	4.877	4.877	195.68	189.98
	E2	2.863	4.688	28.97	36.78

Table 2.8: We detected 22 extended sources across the 9 targets in the GTO 1184 survey, as labeled in Figures 2.5, 2.6, 2.13 and 2.14. As our study is focused on point sources likely to be substellar companions, here we report only the approximate relative position to the target star and peak SNRE in F356W and F444W. The starred sources (HIP 17695 E1 and LP94420 E5) are affected by data wrapping at the edge of the field of view, and thus the relative position is likely erroneous.

Chapter 3: JWST NIRCam Follow-Up of a Directly Imaged Planet Candidate Associated with the Young M Dwarf 2M J0944

3.1 Introduction

Giant planets contain the largest repositories of mass, angular momentum, and volatile materials in their host planetary systems, aside from the host stars themselves. As a result, they are key to understanding the formation and dynamical histories of planetary systems. In our own Solar System, numerical simulations have demonstrated the key role of Jupiter in sculpting the early protosolar environment, reshaping the protoplanetary disk, triggering multiple epochs of planetesimal formation [176], and possibly explaining the low mass of the terrestrial planets [9]. The discovery of the first exoplanet, a 0.46 Jupiter-mass planet orbiting a Sun-like star with a period of 4.23 days [3], raised myriad questions about planet migration and formation mechanisms which continue to be explored via the analysis of exoplanet occurrence rates and atmospheric composition [177].

[178] identified a positive correlation between the presence of super-Earths and gas giants in high metallicity FGK systems, but not in low metallicity FGK systems. In [179], they extended this study to include M dwarf systems, again finding more giant planets generally in metal-rich systems, but no correlation with the presence of super-Earths, suggesting that the simultaneous

formation of super-Earths and giant planets is suppressed in low-mass disks. Occurrence rate analyses from [180] showed that systems with small planets are more likely to have distant (beyond 3 AU) or less massive (less than 120 Earth masses) companions than to have nearby or more massive companions, implying that the presence of Jovian planets between 0.3-3 AU could suppress the formation of small planets.

Planet formation models fall generally into the category of either core accretion [17] or direct gravitational collapse [22], which produce different predictions for the formation temperature of planets as a function of mass [86]. The observation of planetary systems across a range of ages, most notably as the planets cool over the first billion years [85], would provide critical constraints on the dominant formation mechanisms present [26,32,84,87]. The masses and atmospheric compositions of many mature (> 1 Gyr) planets and brown dwarfs have been measured by transit spectroscopy combined with radial velocity measurements [181–185].

The study of giant exoplanets via direct imaging provides unique advantages for the characterization of their orbits and atmospheres. The detection of photons originating directly from the planet significantly mitigates dependence on the host star modeling, and the increase in sensitivity with planet-star separation provides access to the widest outskirts of exoplanet systems, where the atmospheric evolution is less perturbed by stellar irradiation [186–188]. In addition, the technique is more sensitive to planets with "face-on" orbits (corresponding to an orbital inclination near 0 degrees), which are missed entirely by transit surveys and difficult to detect via the radial velocity method (as the signal amplitude is proportional to the sine of the inclination). While ground-based direct-imaging surveys such as SHINE and GPIES have typically been limited in sensitivity to planet masses greater than that of Jupiter [31, 168], coronagraphic observations with JWST NIRCam and MIRI have routinely demonstrated sub-Jupiter-mass sensitivity

in young (< 1 Gyr) systems [189, 190].

At the time of writing, 45 young exoplanets have been discovered via direct imaging [7], and all have masses above 2 M_{Jup}. The exoplanet candidate TWA 7b stands as the single directly imaged companion with a mass below 1 M_{Jup} [190, 191], providing a possible missing link in the data needed to ground atmospheric evolution models. Thus, the detection and characterization of benchmark young sub-Jupiters is a high priority for current observers.

In previous work ([1] hereafter "B25"), we surveyed nine nearby, young M dwarf systems with JWST NIRCam coronagraphy during JWST Cycle 1. These observations achieved a median 5σ contrast sensitivity deeper than 10^{-5} at a separation of $1''$, corresponding to 0.20 MJup in F444W and 1.30 MJup in F356W at planet–star separations of 10 au. Furthermore, we reported the marginal detection of a point source (hereafter "P1") in the vicinity of the M dwarf 2MASS J09445422-1220544 (hereafter 2M J0944, other catalog names include G 161-71 and NLTT 22503). The star's age has been determined from likely association with the Argus comoving group [123, 192] to be 50^{+5}_{-10} Myr [121, 133], and its distance from Gaia Data Release 3 (DR3) to be 13.150 ± 0.006 pc [131]. Assuming that bound companions have the same age and distance as the host star, we referred to the cloud-free model grid (`BEX-petitCODE`, [58]) to determine the expected flux of a young exoplanet associated with 2M J0944. We thus found that the measured flux of P1 in F444W ($21.842^{+0.093}_{-0.085}$ mag) and the F356W-F444W color limit (> 1.02 and > 2.21 with 3σ and 1σ confidence respectively) were consistent with the predictions for a sub-Jupiter-mass companion with a projected separation of 93 au. If confirmed, this object would be a critical benchmark planet for atmospheric studies, thus time was awarded in Cycle 2 to re-observe 2M J0944 along with the M star AP Columbae (hereafter "AP Col") as a reference.

This paper presents the follow-up observations of 2M J0944 with the aim of confirming

or refuting P1 as a bona fide exoplanet. § 3.2 summarizes the original observations taken in Cycle 1 and the follow-up observations executed in Cycle 2. § 3.3 describes the methods used to reduce and analyze the data. § 3.4 presents the reduced images, a summary of all sources detected in the vicinity of 2M J0944 in both epochs, and an analysis of the relative motion of any sources detected in both epochs. § 3.5 discusses the possible artifactual or astrophysical nature of the various sources detected and presents lessons learned for future direct imaging searches for exoplanets. Finally, § 3.6 summarizes our findings.

3.2 Observations

The initial observations of 2MJ0944 were completed on November 27, 2022 (hereafter referred to as "Epoch 1"), consisting of JWST NIRCam images with an exposure time of 30 minutes (17 integrations per exposure) in F444W and 15 minutes (8 integrations per exposure) in F356W using the M335R coronagraphic mask, 10 groups per integration, and the MEDIUM8 readout pattern as defined in the NIRCam Detector Readout Patterns page of the JWST User Documentation. The exposures were repeated for two roll angles in each filter separated by 10 degrees. As P1 was marginally detected with a signal-to-noise ratio per resolution element (SNRE) of 4.02 in F444W, we re-observed 2M J0944 in Cycle 2 with double the exposure time (34 integrations per exposure in F444W and 17 integrations per exposure in F356W) again repeated at two roll angles separated by 10 degrees, using the M335R coronagraphic mask, 10 groups per integration, and the MEDIUM8 readout pattern. Based on the previous detection and the increase in exposure time, we expect to detect P1 in this dataset with an SNRE of 5.69 in F444W. We also observe AP Col with a nine-point small-grid dither [172] for use as a reference during stellar point-spread

function (PSF) subtraction. The Epoch 1 data was reduced using a library of 6 reference PSFs, however because the source of interest is separated from the target star by 5.837 arcseconds, the signal is not within the region dominated by stellar PSF speckles and thus a wide diversity of PSF references is not expected to be needed to recover the signal.

For both the science and reference observations, we make use of the simultaneous long- and short-wavelength observation mode which was not available in Cycle 1, thus we also receive data in the F200W filter with a total exposure time of 3 hours (102 integrations with 10 groups each in the MEDIUM8 detector readout pattern) split across the two roll angles. As the field of view (FOV) of the short wavelength detector extends only to 5 arcseconds, we do not expect P1 to be observable in the F200W data, however it is possible that a circumstellar disk may be detectable at this wavelength, if one is present, as such disks are typically much brighter at F200W than at F444W [189, 193]. The possibility of serendipitous disk detection thus provides significant scientific benefit with no exposure time "cost" to the observatory. All follow-up observations were executed successfully on January 9, 2024 (hereafter "Epoch 2"), providing a temporal baseline of 408 days between the Cycle 1 and Cycle 2 programs.

3.3 Data Reduction & Analysis Methods

We follow in general the procedure for calibration, PSF subtraction, and off-axis source analysis used in B25 with some differences detailed below.

3.3.1 Preprocessing

As in the B25 data analysis, we use the community-developed python package `spaceKLIP` [149] for the "preprocessing" steps, which include wrappers for the official `jwst` pipeline detector-level (stage 1) and instrument-level (stage 2) calibration steps [148], as well as additional steps for bad pixel correction and frame alignment. However, several updates to `spaceKLIP` and to the pipeline configuration were made in between data reductions which affect the preprocessing.

During stage 1 processing, the data quality (DQ) flags are initialized to track which pixels are saturated, hot, or otherwise unfit for use. Approximately one in 1000 NIRCam pixels are known to exhibit exponential rather than linear responses to incident photons, and are flagged as resistor-capacitor (RC) pixels [194]. In this reduction, we opted to flag those RC pixels which also have high dark current as "saturated" pixels using the `flag_rcsat` keyword in the stage 1 pipeline step, which provided a noticeable improvement in the flagging of several patches of bad pixels missed by the previous pipeline version.

Also in stage 1, the measurement of pixel count rates is enabled by the NIRCam detector's non-destructive readouts. The counts in each pixel, containing the sum of the astrophysical signal, read noise, and photon noise, are read multiple times "up the ramp" as photons are collected in an integration, and a slope describing the average count rate can be fit to this curve. In the B25 data reduction, we used the optimal weighting least-squares fit (OLS) by default [195, 196]. The OLS algorithm weighs each point along the ramp based on the relative amount of read noise versus photon noise in that point. However in the new reduction we use the likelihood algorithm recently added to the `jwst` pipeline and detailed in [197]. This algorithm operates on the differences between each subsequent point rather than on the points themselves, and calculates a

covariance matrix for the sequence of readouts to determine the maximum likelihood ramp slope with higher precision than possible with OLS. The likelihood algorithm is also applied to the "jump detection" step to determine which readouts are contaminated by cosmic rays (CRs) or other acute noise events [198]. This is done by comparing the χ^2 value of ramp fits with every readout included to those with individual readouts excluded from the fit. If the exclusion of a particular readout results in a significantly improved χ^2, that readout is flagged as a jump location and the ramp slope is calculated without it.

Stage 2 processing, which includes background subtraction, flat field corrections, WCS coordinate calculation, outlier detection, and the unit conversion from detector counts to astrophysical flux, was performed using the default pipeline settings identical to the B25 data reduction.

As in the B25 data reduction, we used a combination of the pipeline-generated DQ array, custom bad pixel maps containing manually flagged CR hits, and sigma clipping to identify which pixels to mask and replace before PSF subtraction. However in this data reduction we implemented the cleaning iteratively, flagging and subsequently cleaning pixels using a single identification method, rather than flagging pixels using each of the methods and then replacing them all at the end (as in the B25 data reduction). This reduced the size of individual patches of bad pixels that needed replacement values to be generated by 2D interpolation, thus improving the quality of pixel replacement. During each cleaning iteration, we first identified pixels which were only bad in some integrations within an exposure, and we replaced those pixels with the median value of the good quality integrations in the associated pixel location. We then used 2D interpolation with a window size of 9x9 pixels to replace pixels that were bad in every integration of an exposure.

The version of `spaceKLIP`[1] used in our final data reduction pipeline contains improved modules for locating the position of the target star and coronagraph centers in each frame. There was also an update to allow the realignment of the data, such that the stellar PSF is in the same pixel location in each frame, without data wrapping around the edges of the array during shifting.

3.3.2 PSF Subtraction

To remove the starlight that is not suppressed by the coronagraphic masks, we employ Karhunen-Loève Image Processing (KLIP, [199]), an implementation of principal component analysis provided in `pyKLIP` [150] and wrapped by `spaceKLIP`. In principle, this method reconstructs an empirical model of the stellar PSF using a finite number of basis images referred to as "KL modes". We use both reference differential imaging (RDI, [69]) in which observations of similar stars are used to model and subtract the stellar PSF, and angular differential imaging (ADI, [65]) where exposures of the science target at multiple roll angles are used to differentiate astrophysical sources from the stellar PSF. The combined approach, denoted "ADI+RDI", is achieved by reducing each roll angle of the science data separately, including both the reference observations and the alternate science roll image in a library of reference PSFs. Then the two PSF-subtracted images are derotated and averaged together to produce the final result. In the B25 data reduction, we used the RDI-only PSF subtraction method with a library of 6 reference stars (HIP 17695, G 7-34, AP Col, LP 944-20, and 2MASSI J0443376+000205) and 6 KL modes, as this provided the best sensitivity in the small-separation ($\lesssim$ 3 arcseconds) region. In Epoch 2 however, we used only the dedicated reference target AP Col, which was observed using a small grid dither to obtain a diversity of PSFs. As our source of interest is widely separated ($> 5''$)

[1] Specific code version is linked in the acknowledgments.

from the target star, we found that ADI+RDI with 50 KL modes resulted in the best performance for the purpose of this study.

3.3.3 Contrast Analysis and Source Fitting

Due to the complex PSF subtraction process, the sensitivity of the observation must be determined by the injection and recovery of simulated sources. We calculate the flux contrast of an off-axis source relative to the star that could be detected with a signal-to-noise ratio (SNR) of five, equivalent to a false alarm probability of 2.9 $\times 10^{-7}$. We refer to this metric as the 5σ flux contrast sensitivity, and calculate it as a function of angular separation from the target star using the modules provided by `spaceKLIP` as described in B25.

The photometry and astrometry of off-axis point sources are also determined by the injection and recovery methods contained in `spaceKLIP`. As in the B25 data reduction process, an off-axis PSF model is generated at the approximate planet-star separation of the source of interest, modified by the same KLIP subtraction algorithm applied to the observation, and fit to the data using a Markov-Chain Monte Carlo (MCMC) approach. A new feature in `spaceKLIP` affecting this step in the new reduction pipeline is the capability to fit extended sources. The "extendedness" of a source is approximated by convolving the point source PSF with a 2D Gaussian. The standard deviation of the Gaussian distribution along the major and minor axis (σ_x and σ_y) of the ellipse, as well as the angle of the major axis in the plane of the sky, are added as additional parameters which can be forward-modeled and fit by the MCMC process. As low SNR sources or sources with high background variation tend to bias the fit towards erroneously large σ_x and σ_y, we opt only to allow extended PSF fitting in cases where the source is well-detected.

We quantify the uncertainty on the astrometric measurements by repeating the MCMC fit 10 times. If the standard deviation of the best-fit astrometry is less than the error reported by the MCMC fit itself, we assume the reported error is accurate. However if this is not the case, we adopt the scatter of the best-fit astrometry as a more accurate description of the uncertainty. To this uncertainty we also add in quadrature a factor of 3 mas to represent the error in our knowledge of the star position behind the coronagraph mask and 20 mas as an approximation of errors due to plate scale distortion at wide ($> 5''$) separations.

As the photometric fits for extended sources tend to be overestimated by the MCMC chain, and the extended sources we detect in these observations are widely separated from the target star, we measure the flux of these objects instead using an aperture photometry method based on that described in Section 3.5 of [117]. We use the python package `STPSF` (formerly `WebbPSF`, [200]) to generate an off-axis point-source PSF model and measure the multiplicative correction factor needed for a given finite aperture radius. We add a second correction factor to account for changes in flux due to the KLIP algorithm by applying the KLIP throughput calculated during the flux contrast sensitivity analysis at the separation of the source. We measure the flux within the aperture and multiply by both the aperture correction factor and KLIP throughput factor to get the total flux from the source and background. We then measure a sample of background fluxes in an array of non-overlapping apertures with the same radius arranged in an annulus surrounding the source with a radius of three times the aperture radius, and correct for aperture size and KLIP throughput. Finally, we take the mean of the background fluxes as the background flux which is subtracted from the source flux, and take the standard deviation of the fluxes as the 1σ noise level. In the case of point-source non-detections, we use this noise level to represent the 1σ upper limit on the flux of the source, and we use triple that flux value as the 3σ upper limit. In calculating

the noise level from aperture photometry for the various non-detection cases, we find that they generally agree with the expectations from the contrast sensitivity at the same separations. For each of the extended sources, we measure the photometry using a range of aperture radii (0.1, 0.2, 0.3, 0.4, 0.5, 0.6, and $1.0''$), and report the results for the smallest radius at which the measured flux stops increasing with radius size.

3.3.4 Rereduction of Epoch 1 Data

As several aspects of the reduction process have changed between the initial analysis of the Epoch 1 data and that of the follow-up data, we have rereduced the Epoch 1 observation of 2M J0944 with the Epoch 1 reference library and the updated pipeline to ensure that any detected photometric or astrometric variation between the two epochs is astrophysical in origin.

The key change between the two reductions of the Epoch 1 data is in the selection and treatment of reference observations. In B25 we used the stars HIP 17695, G 7-34, AP Col, LP 94420, and 2M J0443 as a library of references for 2M J0944, and we masked off-axis sources in the reference images by replacing the affected pixels in a given image with the median value of those pixel locations in the unaffected reference images. However, this did occasionally result in artifacts due to the varying brightness of the stellar PSF in different reference observations. In the new reduction of the Epoch 1 data, we opt not to mask sources, and instead remove LP 94420 from the reference library due to its high number of bright contaminating off-axis sources especially in the region of the field of view near source P1.

3.4 Results

The primary result of our analysis is the non-detection of source P1 in either wavelength in Epoch 2, and the removal of this source from consideration as a candidate exoplanet. In Figures 3.1 and 3.2, we show the results of the PSF subtraction for filters F444W and F356W respectively. The top row shows the original reduction of the Epoch 1 observation presented in B25, the middle row shows the new reduction of the Epoch 1 observation as described in § 3.3, and the bottom row shows the Epoch 2 observation. Figure 3.3 shows the PSF subtraction results for the F200W filter, which was only executed in Epoch 2. Due to the narrower field of view in this observation ($10''$ in diameter), we do not expect to detect P1 in F200W.

Each observation is shown in units of SNRE (calculated as described in B25) in the left column, and in megajanskys per steradian in the right column. Each detected off-axis source is labeled with a circle centered on the position in Epoch 1, and the target star location is marked with a white star. The relative position, flux, SNR from PSF fitting, and SNRE for each source in each filter at each epoch are reported in Table 3.1. Where only limits on the flux have been reported, we show the 3σ upper limit on the flux with the 1σ upper limit in parentheses. As in B25, we generally consider a point source with SNRE > 5 to be "robustly" detected, and a source with SNRE between 4 and 5 to be "marginally" detected. The detections (or lack thereof) of each labeled source are detailed below.

3.4.1 Source P1

The off-axis source P1 was originally flagged as a source of interest due to a marginal detection with SNRE 4.02 in F444W and a non-detection in F356W, shown in the top row of

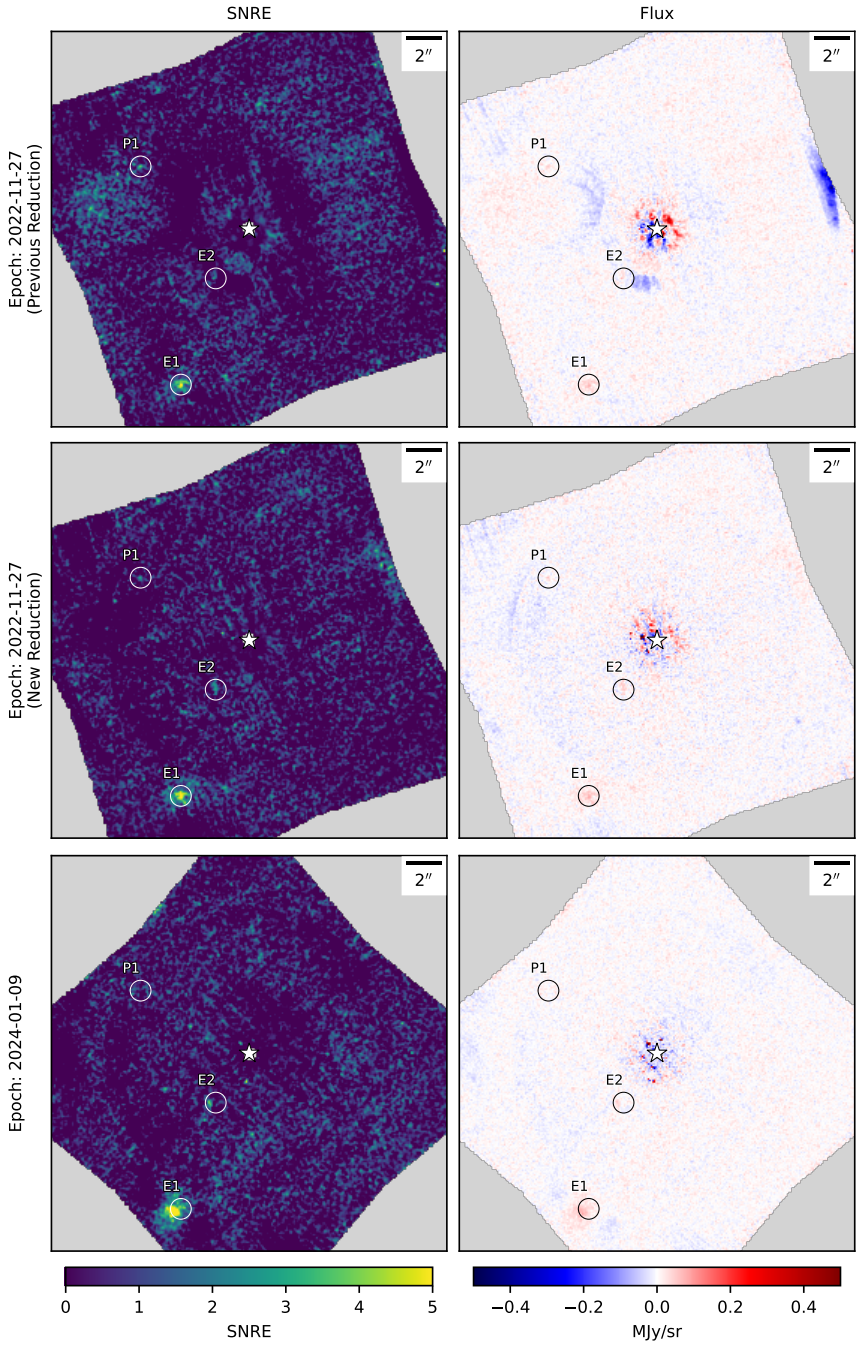

Figure 3.1: PSF Subtraction results in the F444W filter. The top row shows the original reduction of the Epoch 1 observation presented in B25, the middle row shows the new reduction of the Epoch 1 observation described in § 3.3, and the bottom row shows the Epoch 2 observation. Each observation is shown in units of SNRE in the left column, and megajanskys per steradian in the right column. Each source observed in the Epoch 1 data is labeled with a circle centered on the Epoch 1 position, and the target star location is marked with a white star. The source of interest P1 is marginally detected in the original reduction with an SNRE of 4.02, which decreased to 3.37 in the new reduction, and was not redetected in Epoch 2. The extended sources E1 and E2 show clear motion relative to the target star, indicating likely background sources.

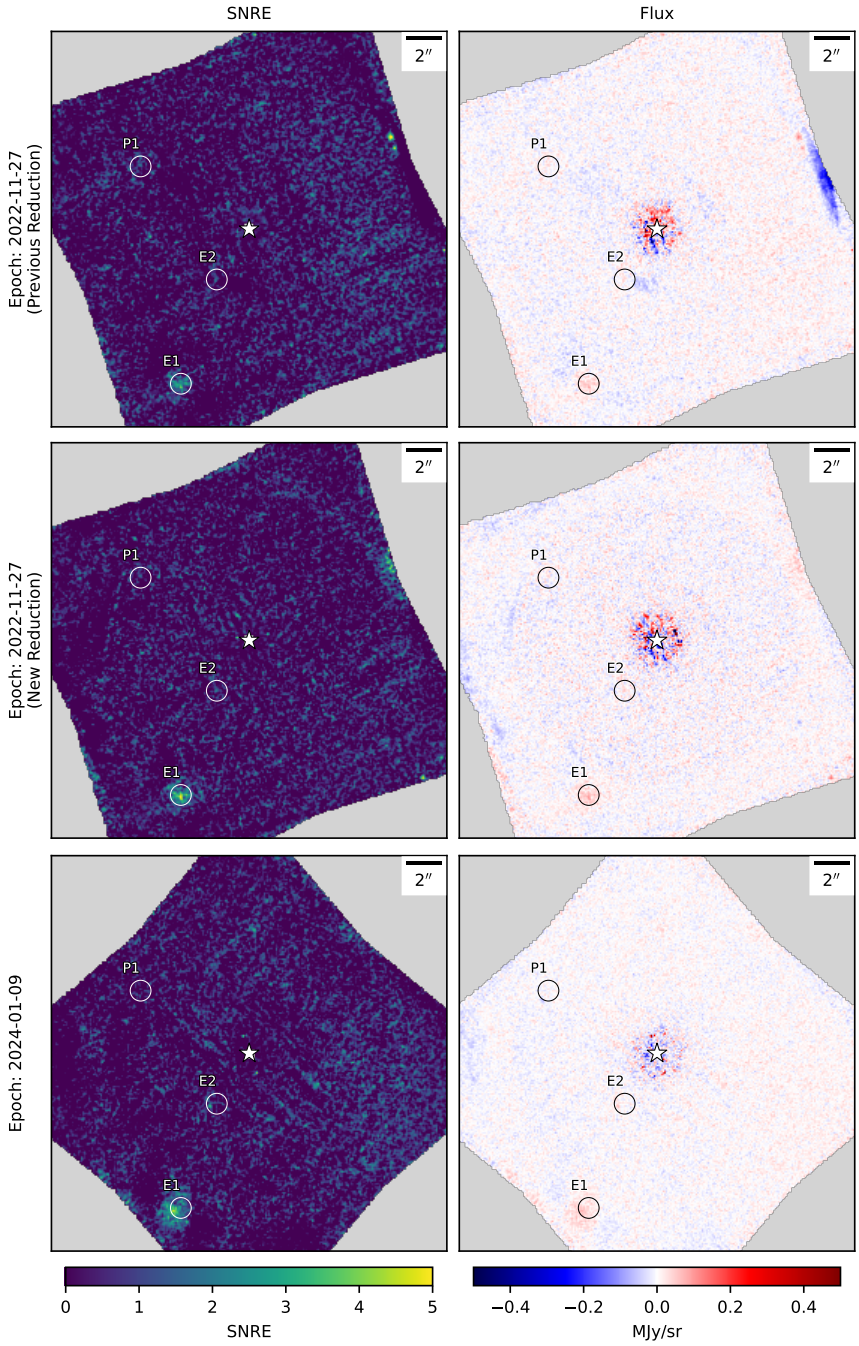

Figure 3.2: PSF Subtraction results in the F356W filter. The top row shows the original reduction of the Epoch 1 observation presented in B25, the middle row shows the new reduction of the Epoch 1 observation described in § 3.3, and the bottom row shows the Epoch 2 observation. Each observation is shown in units of SNRE in the left column, and megajanskys per steradian in the right column. Each source observed in the Epoch 1 data is labeled with a circle centered on the Epoch 1 position, and the target star location is marked with a white star. The source of interest P1 is not detected at this wavelength in either epoch. The extended source E1 shows clear motion relative to the target star, indicating a likely background source. Source E2 is faintly present at this wavelength, and shows similar relative motion.

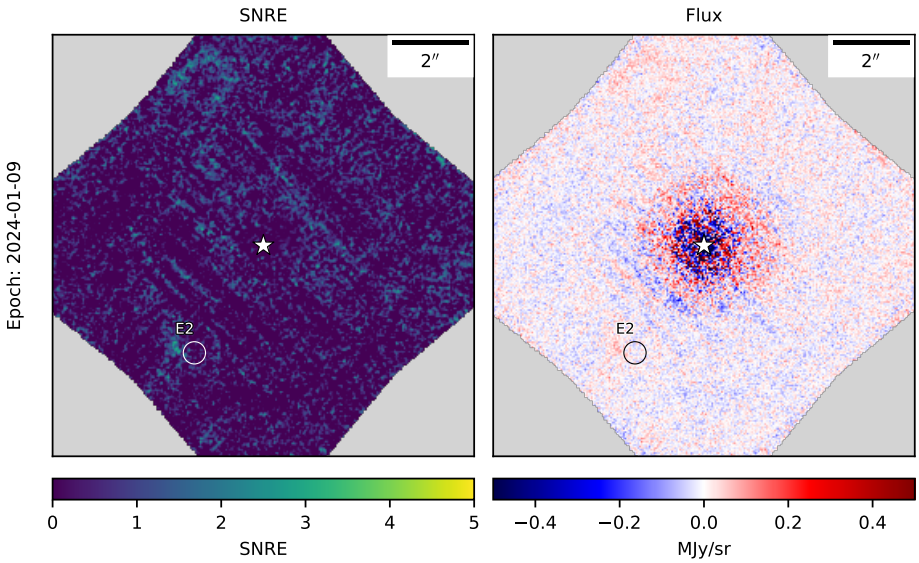

Figure 3.3: PSF Subtraction results in the F200W filter at Epoch 2. The observation is shown in units of SNRE in the left panel, and in megajanskys per steradian in the right panel. Source E2 is labeled with a circle centered on the Epoch 1 position in F444W, and the target star location is marked with a white star. The source of interest P1, and the bright extended source E1 are outside of the field of view. Source E2 is clearly extended at this wavelength, and shows motion relative to the position of peak flux in Epoch 1. We note that the FOV of this observation is half of the width of the F444W and F356W observations.

Src.	Epoch	Filter	Δ RA [mas]	Δ Dec [mas]	Flux [mag]	SNR	Peak SNRE
P1	2022-11-27	F356W	...	...	> 22.432 (> 23.625)	1.85	1.38
		F444W	6.045 ± 0.037	3.478 ± 0.035	$22.223^{+0.251}_{-0.251}$	2.08	3.37
	2024-01-09	F356W	...	...	> 22.608 (> 23.801)	0.09	0.06
		F444W	...	...	> 22.423 (> 23.616)	0.54	0.38
E1	2022-11-27	F356W	3.780 ± 0.032	-8.687 ± 0.064	$20.075^{+0.192}_{-0.163}$	6.17	5.94
		F444W	3.758 ± 0.030	-8.729 ± 0.030	$20.048^{+0.252}_{-0.204}$	4.83	7.44
	2024-01-09	F356W	4.246 ± 0.030	-8.712 ± 0.030	$20.190^{+0.175}_{-0.151}$	6.71	5.18
		F444W	4.163 ± 0.029	-8.851 ± 0.030	$19.656^{+0.187}_{-0.160}$	6.31	8.08
E2	2022-11-27	F356W	1.796 ± 0.051	-2.840 ± 0.044	$22.488^{+0.987}_{-0.508}$	1.68	2.26
		F444W	1.858 ± 0.032	-2.739 ± 0.032	$21.343^{+0.253}_{-0.205}$	4.82	3.05
	2024-01-09	F200W	2.217 ± 0.029	-2.772 ± 0.030	$22.924^{+0.357}_{-0.268}$	3.57	3.93
		F356W	2.205 ± 0.039	-2.905 ± 0.035	$22.425^{+0.270}_{-0.216}$	4.56	4.29
		F444W	2.277 ± 0.039	-2.594 ± 0.044	$21.623^{+0.437}_{-0.311}$	3.02	4.56

Table 3.1: Source Catalog. We report the astrometry, photometry, SNR of the photometric fit, and peak SNRE measured for each source identified in Figure 3.1, in the latest reduction of each epoch and each filter. In the case of non-detections we show the 3σ flux limit with the 1σ limit in parentheses. Source P1 was originally marginally detected with an SNRE of 4.02 in B25, however in the latest reduction of the Epoch 1 data the SNRE decreased to 3.37, which is below the threshold of what would be considered a source of interest. The source is not redetected at all in Epoch 2. Source E2 was not originally reported in B25, however in Epoch 2 the source is visible in all three filters, and some extended flux has been identified near the expected location for a background object in Epoch 1.

figures 3.1 and 3.2. This resulted in a F444W flux measurement of $21.842^{+0.093}_{-0.085}$ mag and a 3σ F356W-F444W color limit of 1.02 mag, which ruled out most stars and background galaxies as possible contaminants. Assuming the same age (50^{+5}_{-10} Myr) and distance (13.30 ± 0.15 pc) as the host star, these flux measurements also placed the source in a broad region of color-magnitude space consistent with young sub-Jupiter mass exoplanets in the cloud-free `BEX-petitcode` [58] atmospheric models. In the new reductions of the Epoch 1 data, shown in the middle row of figures 3.1 and 3.2, we find that the SNRE of P1 is decreased from 4.02 to 3.37, which falls

below the threshold of what we consider a reportable marginal detection. Furthermore, if P1 were an astrophysical source, we would expect a redetection in Epoch 2 with an SNRE of 5.7 due to the increased integration time. However, we report a complete non-detection with an SNRE of 0.38 and 0.06, corresponding to a 3σ upper limit of 22.423 and 22.608 magnitudes in flux, at the expected source location in F444W and F356W respectively. We must therefore conclude that P1 was not bound companion, but was an artifact, noise speckle, or astrophysical transient of some kind. Possible sources of P1, as well as potential explanations for the reduction in signal between the old and new reductions of the Epoch 1 data, are explored in § 3.5.

3.4.2 Source E1

Source E1 is a highly extended source robustly detected in both wavelengths, in both epochs, and in both the old and new reductions of the Epoch 1 data. It was originally reported in B25 with a peak SNRE of 6.75 in F444W and 5.80 in F356W. In the new reduction, the SNRE is increased to 7.44 in F444W and 5.94 in F356W, and we measure a flux of $21.623^{+0.437}_{-0.311}$ mag in F444W and $20.075^{+0.192}_{-0.163}$ mag in F356W using an aperture size of $0.6''$. In Epoch 2, the source is redetected and measured to have a flux across the two epochs that is consistent within error bars in F356W ($20.190^{+0.175}_{-0.151}$ mag). In F444W, the source is measured to be brighter in Epoch 2 ($19.656^{+0.187}_{-0.160}$ mag), however this is likely due to the close proximity of the source in Epoch 1 to the flux-attenuating neutral density (ND) square filter located in the bottom right corner of the NIRCam detector subarray used for coronagraphic imaging. The suppression of flux in this region would cause the source to appear dimmer in Epoch 1 than in Epoch 2, when the roll angle of the observation results in a wider separation between the source and the ND square, and the

PSF being wider at longer wavelengths would cause the effect to be greater at F444W and possibly negligible at F356W. The source position relative to the star is significantly offset to the east between the two epochs, indicating that it is likely a background object. Therefore we perform an astrometric analysis in § 3.4.5 to determine if the relative motion is consistent with that expected of an extremely distant object (i.e. with no detectable parallax). Finally, we note that while the SNR of the flux measurement increased as expected in F444W (from 4.83 in Epoch 1 to 6.31 in Epoch 2), the SNR increased only slightly in F356W (from 6.17 in Epoch 1 to 6.71 in Epoch 2) and the SNRE in fact decreased slightly from 5.94 in Epoch 1 to 5.18 in Epoch 2. We suspect that this is due to a contaminating background object just outside the field of view to the southeast. The contamination is brighter in F356W, and the source E1 is closer to the edge of the field of view in Epoch 2, thus creating a higher noise background which affects the SNR calculations in the Epoch 2 observation at F356W specifically.

3.4.3 Source E2

Source E2 was not originally reported in B25, as it had an SNRE <4 in both filters, and displayed possible extended structure. However, in the Epoch 2 data, we detect a source at a similar location with flux $21.808^{+0.187}_{-0.187}$ mag (SNRE 4.56) in F444W and $22.425^{+0.270}_{-0.216}$ mag (SNRE 4.29) in F356W. This prompts a reevaluation of the Epoch 1 data to determine if the faint flux observed is possibly astrophysical in nature. Between the original and the re-reduction of the Epoch 1 data, we find the SNRE of E2 is decreased slightly from 3.39 to 3.05 in F444W and from 2.33 to 2.26 in F356W. The increase in SNRE from Epoch 1 to 2 (from 3.05 to 4.56 in F444W and from 2.26 to 4.56 in F356W) is however consistent with the expectation from the doubled

integration time, the flux measurements in both filters are consistent between the two epochs, and the astrometric offset between the two epochs is similar to that of source E1. Furthermore, the source is visible (and visibly extended) at the expected location in the Epoch 2 F200W data (see Fig. 3.3), with peak SNRE of 3.93 and flux from aperture photometry of $22.924^{+0.357}_{-0.268}$ mag. While the detections of this source are only marginally significant, the fact that the source is visible in every filter in Epoch 2 leads us to consider it a bona fide astrophysical source. We therefore elect to use the centroid location of the flux observed in Epoch 1 to analyze the astrometry of E2 and determine its consistency with a background object in § 3.4.5. We report the full results in Table 3.1.

3.4.4 Contrast Analysis

We compute the 5σ contrast sensitivity as described in § 3.3.3, finding a contrast limit in Epoch 2 of 7.16×10^{-6} at $1''$ and 2.39×10^{-6} beyond $3''$ in F444W and 4.63×10^{-6} at $1''$ and 1.33×10^{-6} beyond $3''$ in F356W as shown in the top and middle panels of Figure 3.4 respectively. We demonstrate improvement between epochs 1 and 2 in the background limited regime ($\gtrsim 3''$) on the order of $\sqrt{2}$, as expected due to the doubled integration time in Epoch 2. The improvement is more significant in the F356W filter, which is possibly due to lower sky backgrounds (0.11 MJy/sr in F356W compared to 0.28 MJy/sr in F444W during Epoch 2) as measured using the JWST Backgrounds Tool [201]. These contrast curves further support the interpretation of sources E1 and E2 as astrophysical in nature, given their increase in SNRE in both filters between the two epochs. Furthermore, the contrast limits support the dismissal of source P1 as an exoplanet candidate, given our increase in sensitivity at the separation of P1

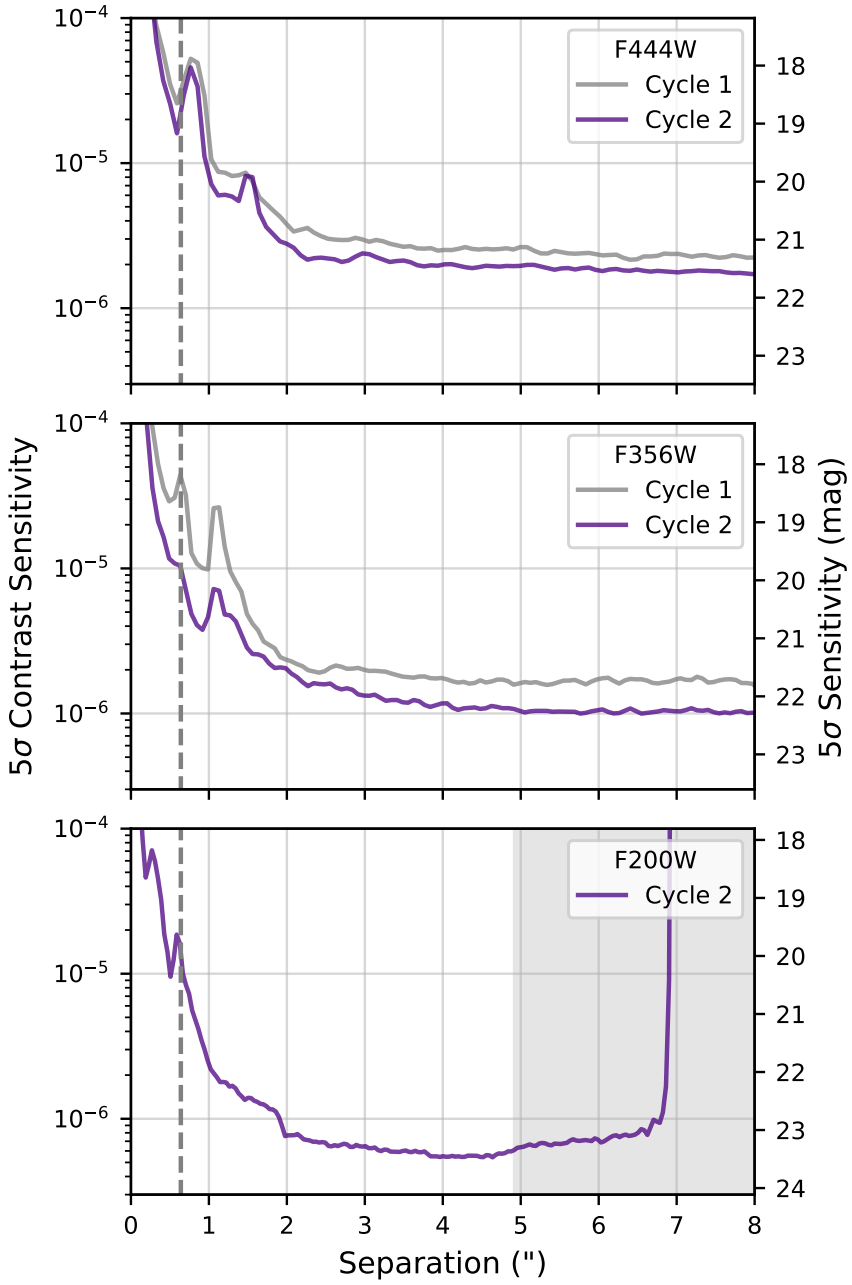

Figure 3.4: Here we show the 5σ contrast curves in the F444W, F356W, and F200W filters (top, middle, and bottom rows respectively). The inner working angle is shown by the vertical dashed line. The grey line shows the contrast achieved in the Epoch 1 observation, and the purple line shows that achieved in the Epoch 2 observation. We can see a $\sim\sqrt{2}$ improvement between Epoch 1 and 2 in the contrast achieved in the background limited regime as expected for both F444W and F356W. The deepest contrast is achieved in F200W due to the doubled effective integration time as compared to the Epoch 2 F444W and F356W observations. The peaks in the contrast curves within $2''$ are due to residuals located at the peaks of the stellar PSF lobes. We note

($5.8''$) and lack of detection.

In the F200W filter, we achieve a contrast limit of 2.51×10^{-6} at $1''$ and 6.47×10^{-7} beyond $3''$ (corresponding to 21.8 and 23.3 magnitudes respectively) as shown in the bottom panel of Figure 3.4. The deeper contrast limit is due to the total exposure time of three hours in this filter, as compared to the 1.5 hour exposures for the Epoch 2 observations in F356W and F444W.

3.4.5 Astrometric Analysis

The astrometric measurements of sources E1 and E2 are analyzed by comparing to the stationary background object model in `backtracks` [202]. This model interprets the parallax (76.0509 ± 0.0336 mas) and proper motion ($-331.327 \pm 0.034, 40.177 \pm 0.037$ mas/yr in RA and Dec) of the target star provided by Gaia DR3 and calculates the expected relative path of an object with no observable parallax or proper motion (i.e. a extragalactic stationary object). Though E1 and E2 are extended sources and thus not considered possible planet candidates, to have a point of comparison we also calculate the maximum expected displacement of the source due to orbital motion. This is found by taking the projected separation to be the minimum physical separation of the object and the target star, and calculating the orbital speed of a satellite at that separation from the target. For this calculation we use a stellar mass based on the [203] evolutionary model for pre-main sequence stars. We performed a linear interpolation of the model grid to find the stellar mass to be 0.180 ± 0.003 $M_\odot$, based on the age of 50 Myr, and the 2MASS J-, H-, and K-band apparent magnitudes of 8.496, 7.919, and 7.601 respectively [204]. We thus derived a maximum displacement due to orbital motion of 20 mas for E1 and 34 mas for E2.

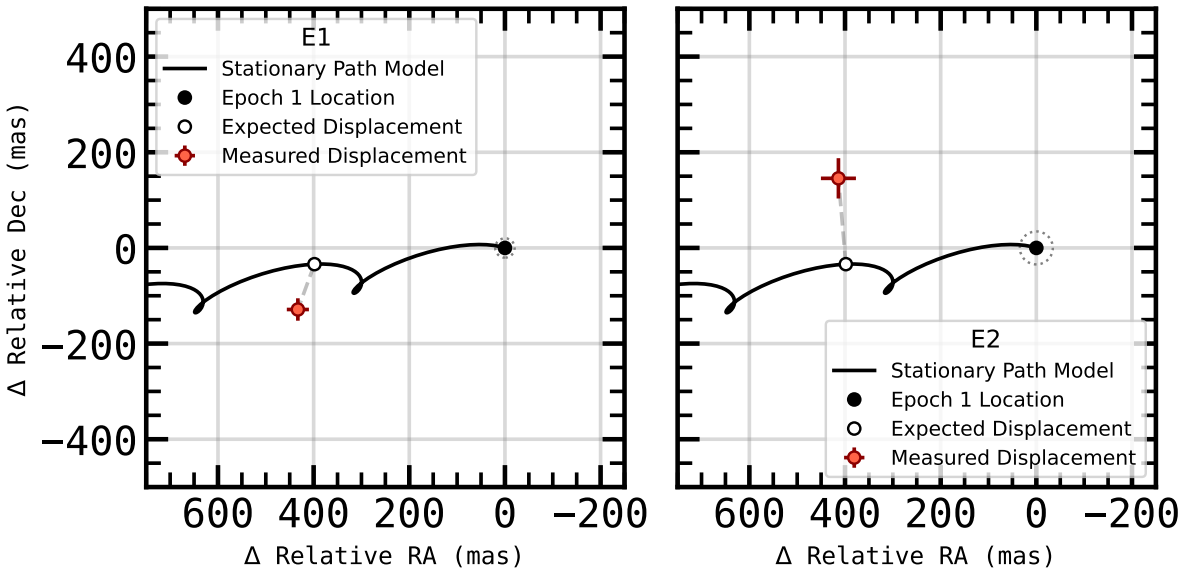

Figure 3.5: Astrometric analysis of source E1 and E2 in the left and right panels respectively, showing the change in relative right ascension (RA) and declination (Dec) between Epochs 1 and 2. The position of the source in Epoch 1 is shown by the black dot at position (0,0), the expected position of the source in Epoch 2 is shown by the white dot, and the measured position of the source in Epoch 2 is shown by the red dot. The solid black line shows the expected path of a stationary background object at infinite distance, and the dotted gray circle shows the maximum displacement of a point source expected from orbital motion (though for source E1 this circle is approximately the same size as the Epoch 1 marker). We can see that both sources exhibit displacement between the two epochs which is much more than possible from orbital motion. We note that the change in RA for both objects is consistent with a background source, but there is significant scatter in the change of declination.

Figure 3.5 shows the expected relative motion of a stationary background object via the black lines for sources E1 and E2 in the left and right panels respectively, using the average position across the F356W and F444W filters to account for possible systematic offsets between the measurements in each filter. The position of the source in Epoch 1 is shown by the black dot at (0,0), the expected relative displacement of the source in Epoch 2 is shown by the white dot, and the measured position of the source in Epoch 2 is shown by the red dot. We also show the maximum possible displacement of the source due to orbital motion by the dotted gray circle, though for source E1 this circle is nearly the same size as the Epoch 1 marker.

In Epoch 2, the measured displacement in RA of each source is consistent with that expected for the stationary background source, however there is high scatter in the declination compared to the expectation.

The measured displacement of source E1 is separated from the expected position for a stationary source by 101 mas, corresponding approximately to a 3σ deviation from the model. The displacement of source E2 from the expectation for a stationary source is more significant (180 mas, corresponding to a 5σ deviation), however the low SNR of signal at Epoch 1 leads to this deviation being less credible. Both sources are displaced from the expectation from the bound object model by over 400 mas (417 mas for E1 and 412 mas for E2) in the most favorable case that the planet is traveling at the maximum on-sky velocity in the direction that minimizes the discrepancy, which corresponds to a $> 10\sigma$ deviation. While this clearly demonstrates that E1 and E2 are not bound objects in the 2M J0944 system, the astrometric measurements are somewhat inconsistent with the background model as well, and possible explanations for this are discussed in § 3.5.

3.5 Discussion

3.5.1 On the Possible Nature of P1

In the B25 reduction of the Epoch 1 data, we measured the flux of P1 to be $21.842^{+0.093}_{-0.085}$ mag in F444W with SNR 3.91, and we measured the F356W-F444W color limit to be > 1.02 mag with 3σ confidence (> 2.21 with 1σ confidence). However, in the rereduction of the Epoch 1 data performed in this work we find the flux in F444W to be reduced to $22.223^{+0.251}_{-0.251}$ mag with an SNR of only 2.08 and a F356W-F444W color limit to be > 0.21 mag with 3σ confidence

(> 1.40 with 1σ confidence). Furthermore, we find a complete non-detection of P1 in Epoch 2, with associated 3σ flux limits of 22.423 mag in F444W and 22.608 mag in F356W, and we formally dismiss it as a planet candidate. Here we consider possible explanations for the source identified in the B25 reduction of the Epoch 1 data.

Several astrophysical processes may contribute to the observed signal in Epoch 1 and the non-detection in Epoch 2. We have ruled out contamination by cosmic rays (CRs) via a manual inspection of each integration in the pre-PSF-subtracted images, as CRs affect only a subset of integrations in a given exposure. Alternatively, an extragalactic transient source with decreasing flux over time could explain the observations. The flux measurements provided in this work imply a reduction in F444W flux of at least 0.20 mag with 3σ confidence (1.39 mag with 1σ confidence) over a period of 408 days. While the most common supernovae (type 1a) are expected to decline by at least this rate following the time of maximum light [205], the JWST spectrum of type 1a supernova 2021aefx in the nebular phase (> 200 days past maximum light) suggests that these objects should be brighter at F356W than at F444W [206]. As we measure a F356W 3σ flux limit of 22.432 and 22.608 in Epochs 1 and 2 respectively, the type 1a supernova explanation is considered unlikely. Alternatively, some exotic transients (e.g. kilonovae, [207]) are known to be redder at these wavelengths, however these phenomena are so intrinsically rare as not to be considered within the scope of this study. We also considered the possibility that P1 was an off-axis source in one of the reference images which was injected into the science image during PSF subtraction. We performed an ADI-only reduction of the Epoch 1 data and recovered the source with a similar marginal SNRE, thus ruling out contamination by any reference observations.

Artifacts originating from NIRCam itself (such as warm or otherwise bad pixels) may have contributed to the elevated flux, though it is difficult to diagnose the exact cause due to the faint-

ness of the signal. Cumulative wavefront error (WFE) drift, as well as the periodic realignments of the primary mirror to correct for it, may also induce changes to the optical path of the system which affect sensitivity to faint sources over time [147]. The root-mean-square (RMS) WFE was approximately 68 nm at the time of both observing epochs, however the second observation epoch (January 9th, 2024) was just after three consecutive 'tilt events' causing RMS WFE spikes above 100 nm and subsequent corrections which occurred in December 2023 (inspected using `STPSF` [200]). While this results in a similar RMS WFE across the two epochs, the distribution of the errors across the detector, and thus the pattern of noise fluctuations, is altered. As the original detection itself was marginal (SNRE of 4.02 in F444W), we noted in B25 that the signal may be a high amplitude background noise fluctuation. Given the survey size, including all nine M stars, of 799,313 pixels, we calculated that one would expect 50 individual pixels to reach a spurious SNR of 4 of greater. However, our SNRE calculations were tuned to suppress noise spikes which are spatially narrower than the PSF in a given observation in order to reduce the confusion of noise fluctuations with faint PSFs. Regardless, the case of a high background fluctuation masquerading as a faint point source remained a possibility. We can see in Figure 3.1 that there is a region of elevated background in the B25 reduction of the Epoch 1 data near the original detection of P1 which may have amplified the flux of a noise peak to a marginally significant level. The new reduction of the Epoch 1 data resulted in both a smoother background in this region of the image, and a lower SNRE of P1 (3.37 in F444W), suggesting that the local background level in the original reduction may have contributed to an erroneous detection.

3.5.2 On the Possible Natures of E1 and E2

As the extended source E1 is robustly detected in both F444W and F356W, and in both epochs, we confidently categorize it as a background galaxy. As noted in § 3.4.3, source E2 is extended and visible in all three filters in Epoch 2, particularly in F444W and F200W. There is also emission in the approximate location expected for a background object in Epoch 1, particularly in the F444W re-reduction. Considering the marginal detections of consistently extended emission in multiple epochs and filters, along with the apparent relative motion, we also consider E2 to be a background galaxy. To support these classifications, we compare the measured aperture photometry of E1 and E2 with the NIRCam photometric catalog of extragalactic sources from the GOODS-S deep field subsection of the JWST Advanced Deep Extragalactic Survey (JADES) survey (K. N. Hainline et al. 2020; M. Curtis-Lake et al. 2024; B. E. Robertson et al. 2023)(D. J. Eisenstein et al. 2023; M. J. Rieke et al. 2023). While in Table 3.1 we show the aperture photometry results using an aperture radius of $0.6''$ for E1 and $0.3''$ for E2, in Figure 3.6 we display the photometric results for E1, E2, and all of the JADES sources using the $0.3''$ radius aperture for direct comparison. We thus demonstrate that both E1 and E2 (the purple diamond and square, respectively) are consistent with the red arm of the bright population of JADES galaxies (black points) in each of the color-magnitude diagrams generated from our observed filters.

Assuming from the spatial extent and photometric analysis that both E1 and E2 are galaxies, we would expect the relative astrometry to be consistent with that of a stationary object at infinite distance as modeled by the solid black lines in Figure 3.5. However, we noted in § 3.4.5 that the relative astrometry of E1 and E2 show a deviation from the expected path of 101 and 180 mas respectively. There are several factors relating to the intrinsic nature of the sources and to the

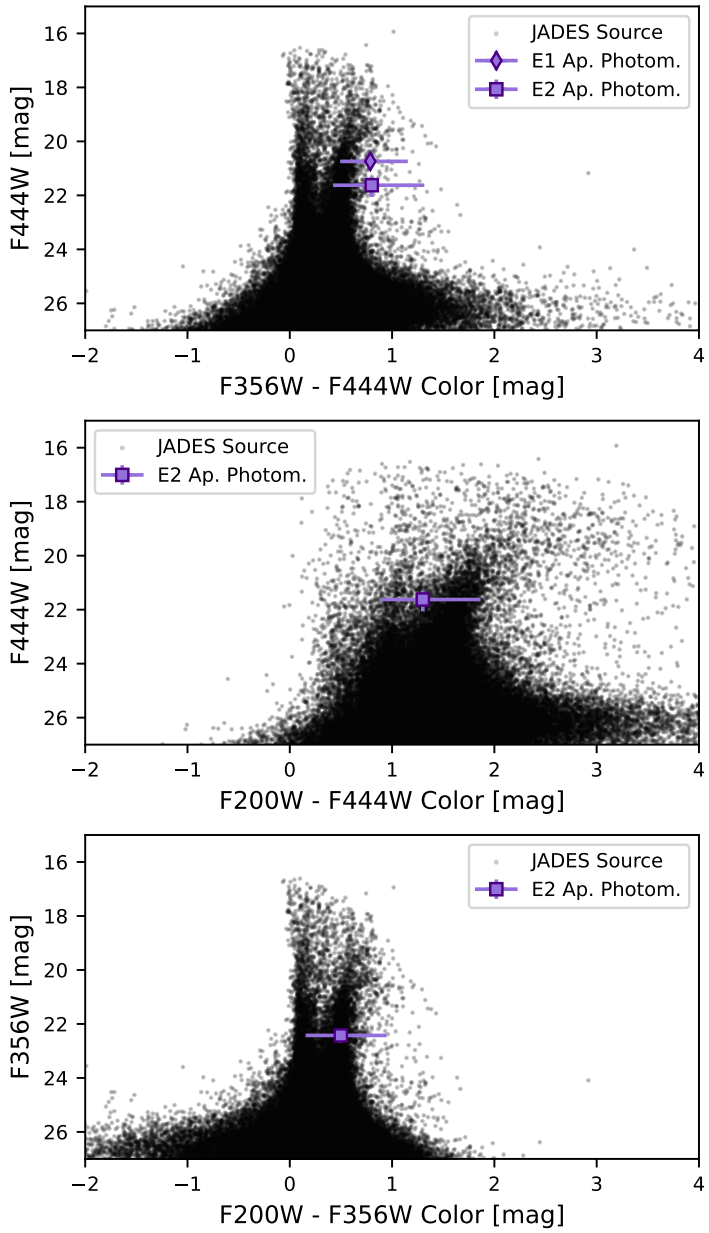

Figure 3.6: Here we compare the photometry of the extended sources E1 and E2 (shown by the purple markers) with that of the extragalactic sources published in the JADES catalog (shown by the black dots), demonstrating that both objects are consistent with the major population of JADES galaxies. The photometric error bars are shown in both the color and magnitude axes, but are sometimes smaller than the marker size. The top panel shows the F356W-F444W color-magnitude diagram, the middle panel shows F200W-F444W, and the bottom panel shows F200W-F356W; and as the source E1 lies outside the field of view of the F200W observations, it is only shown in the top panel.

applied image processing technique which may contribute to the observed discrepancy.

In the case of E1, the high angular extent of the galaxy may cause increased difficulty in locating the precise centroid of the object. The PSF fitting routine in `spaceKLIP` that we employ is primarily designed to fit point sources, as that is the form we expect for an exoplanet. Thus, our astrometric results may be influenced by fluctuations on the spatial scale of the PSF width and increase the astrometric error in a galaxy exhibiting spatial non-uniformities. Additionally, the precise location of E1 in the field of view in Epoch 1 is just north of the ND square as mentioned in § 3.4.2. As the flux in this corner is attenuated by the ND square by a factor of ~ 7.5 mag, some flux in the southern region of the galaxy may be suppressed and result in a northward bias of the measured centroid. In this case, we would then erroneously expect the galaxy in Epoch 2 to appear north of the true location, resulting in the apparent southward offset which we observe. In the case of E2, which is both spatially extended and intrinsically faint, we suspect that measurement error simply be underestimated. The direction of the astrometry deviation also aligns with the major axis of E2's angular extent, supporting this hypothesis.

An additional factor which would apply to both sources is the effect of detector plate scale distortion, i.e. that the conversion from distance in pixels to angular separation is not perfectly constant across the detector. In standard imaging observations, a pre-computed distortion map provided by the JWST Calibration References Data System (CRDS) is applied directly to the image, and each pixel is re-interpolated to assign the detected flux to the correct on-sky location. However, the noise added by this interpolation before PSF subtraction can significantly impact sensitivity of coronagraphic observations, especially in the speckle-dominated regime (separations $\lesssim 3''$). Therefore we elected to skip this step and applied a constant astrometric error component of 20 mas.

Several options exist to mitigate these possible contributions to the astrometric discrepancy in future work. To account for astrometric error associated with high angular extent and/or low SNR, injection-recovery tests of simulated sources with similar properties can be performed to measure the astrometric uncertainty empirically and determine if our current reported error is in fact underestimated. If this test reveals that the current method returns unsuitably high error in astrometric measurements of extended sources, we will explore alternate methods to recover the astrometry more accurately. To explore the effect of plate scale distortion, we can attempt several ways to incorporate the CRDS distortion solution. As E1 is very widely separated from the target star at $9.7''$, it would be simultaneously the easiest to recover without stellar PSF subtraction and the most affected by plate scale distortion. Therefore we would first apply the distortion correction to the pre-PSF-subtracted data, and attempt to recover the signal of E1 without any PSF subtraction. This would give us the most direct measurement of the astrometry and photometry of E1 without having to propagate signal changes due to the KLIP algorithm. If the source is not visible without PSF subtraction, we will apply the KLIP algorithm and attempt to recover both E1 and E2 with the knowledge that the background noise may be higher due to the distortion correction. Finally, it may be possible to generate a mapping function from the provided distortion solution to convert from a given pixel location in the uncorrected image to the distortion-corrected on-sky position. This would have some complications as the use of multiple roll-angle observations means that every location in the final PSF-subtracted image is the superposition of two detector locations and thus contains two different distortion components. However such a tool would be highly useful for attaining accurate astrometry in coronagraphic observations without suffering the noise increase from re-interpolation of the pixels.

Regardless of the tension between the measured astrometry of E1 and E2 in Epoch 2 and the

expected location of a stationary background object, we find the astrometric accuracy sufficient to rule out E1 and E2 as bound companions of 2M J0944, which is the primary purpose of this work.

3.5.3 Limits on Circumstellar Flux around 2M J0944

While our study has focused on the attempted recovery of the point source P1 in the F444W filter, the collection of simultaneous data at F200W provides an excellent opportunity to explore the possibility of circumstellar emission due to a debris disk. Recent searches for exoplanets around M dwarfs with JWST have resulted in the serendipitous discovery of debris disks at F200W [208], and observations of known M dwarf disks have demonstrated that their grain size distribution results in higher surface brightness at F200W as compared to F444W [190].

As seen in Figure 3.3, there is no obvious extended emission that could be attributed to a disk. There are some large scale, structured variations in the background flux. These are largely attributed to "$1/f$ noise", a temporally-correlated readout noise source which is well-described by a $1/f$ power spectrum that causes parallel striping in the detector frame [209]. These stripes are especially apparent in the left panel of Figure 3.3. Thus, the search for faint, circumstellar flux remains inconclusive based on the current reduction strategy.

In future work, limits on the presence of a disk can be better assessed using several strategies. First, advanced $1/f$ noise correction techniques (e.g. [209]) could significantly reduce the presence of the striping artifacts that limit sensitivity. In addition, PSF subtraction via RDI only (not ADI+RDI as we have employed for the purpose of point source detection), and with no annular divisions in the KLIP subtraction, would mitigate self-subtraction and preserve relative

background flux levels as a function of angular separation from the target star. The use of Model-Constrained RDI (MCRDI, [210]) would further preserve disk flux through the KLIP subtraction process. Using this reduction process, surface brightness limits on potential disk emission could be assessed, however the lack of constraints on possible disk inclinations would still pose inherent degeneracies between the observed surface brightness limit and the deprojected surface brightness of a disk. Should the $1/f$ noise originate primarily from the reference observation, the inclusion of additional references either from publicly available JWST observations or from synthetic references produced using `STPSF` could provide a significant boost in sensitivity.

3.5.4 Lessons Learned

Our primary takeaway from this follow-up program is that while NIRCam is demonstrably sensitive to faint, directly imaged sources (e.g. the extended source E2), low SNR sources have risk of being non-astrophysical in origin. In B25, we examined the possibility that P1 may turn out to be a high-amplitude noise fluctuation. We determined that the spatial correlation of the background noise fluctuations in the F444W data correspond to a Gaussian full-width at half-max (FWHM) of 0.55 pixels, which is narrower than the F444W PSF FHWM of 2.3 pixels and that these fluctuations are thus unlikely to contaminate our SNRE calculations or be visually confused with PSFs. However we did acknowledge that this source of contamination remained a possibility. We advise caution when considering sources with SNR below 5 for dedicated follow-up observations.

As stated in § 3.3.4, we have re-reduced the Epoch 1 data in order to have an apples-to-apples comparison between epochs and to ensure that any changes in flux and astrometry are

astrophysical rather than due to changes in the data reduction pipeline. We showed in Figure 3.4 that the contrast sensitivity increased as expected due to the increased exposure times. However we note here that in the re-reduction of the Epoch 1 data, the measured contrast sensitivity was degraded by a factor of~ 0.3 mag beyond $1''$ in both F356W and F444W as compared to the B25 reduction. We also note the appearance of residual spikes associated with the stellar PSF lobes which were not present in the first reduction, but are visible both in the PSF subtracted images and in the new contrast curves. We understand the change in reduction quality to be due to a combination of changes in the spaceKLIP pipeline, likely those regarding frame alignment and bad pixel flagging and replacement. Regardless, the non-detection of P1 in Epoch 2 is definitive and would not be affected by a 0.3 magnitude change in flux sensitivity.

3.6 Summary and Conclusions

The primary purpose of this work was to follow up the marginal exoplanet candidate P1 in the vicinity of the M dwarf 2M J0944, which was originally measured in [1] (B25) to have a flux of $21.842^{+0.093}_{-0.085}$ mag in F444W with SNR 3.91, and a F356W-F444W color limit of > 1.02 mag with 3σ confidence (> 2.21 with 1σ confidence). Here we definitively show that P1 is not a bound companion by re-observing the system 408 days later, demonstrating a non-detection of the source, and placing 3σ flux limits of 22.423 mag in F444W and 22.608 mag in F356W in the expected location of the source assuming co-motion with the host star. We conclude that the source observed in B25 was likely a noise fluctuation or other artifact amplified by the reduction strategy used at the time.

Given the lack of confirmation of a bound companion to 2M J0944, and the minor increase

in contrast sensitivity achieved, we do not have sufficient new information to warrant updating the occurrence rates calculated in B25. However, we intend for the archival data from this program (JWST GO 3840, P.I. Bogat) and from the original survey of 9 M dwarfs (JWST GTO 1184, P.I. Schlieder) to be incorporated in future holistic studies of exoplanet occurrence rates around M dwarfs.

While the source of interest P1 was not redetected, we did redetect a similarly faint source (E2) as well as a brighter and more extended source (E1). We demonstrated via astrometric analysis that neither E1 nor E2 are bound to the target star 2M J0944, and via photometric analysis we showed that both sources are consistent with the population of red galaxies observed in the JADES GOODS-S deep field. While the relative astrometry does not match perfectly with the expected path of a stationary background galaxy, we have identified several possible explanations for the deviation including plate scale distortion, the spatial coincidence of E1 with a flux-attenuating neutral density filter square, the low SNR of E2, and the extended flux distributions of both sources.

Through these observations we have demonstrated NIRCam's routine sensitivity to very faint objects in the near-infrared, achieving a flux contrast of 7.16×10^{-6} at $1''$ (2.39×10^{-6} beyond $3''$) in F444W, 4.63×10^{-6} at $1''$ (1.33×10^{-6} beyond $3''$) in F356W, and 2.51×10^{-6} at $1''$ (6.47×10^{-7} beyond $3''$) in F200W.

We anticipate near-term future work to include further efforts to resolve the tension between the astrometric measurements of sources E1 and E2 as compared to the expected path of an extragalactic source as outlined in § 3.5.2, as well as a more detailed analysis to search for extended disk emission in the Epoch 2 F200W data as outlined in § 3.5.3.

Finally, we look forward to the continued exploration of wide-orbit giant planets around

M stars in the effort to disentangle the contributions of planet-like and binary-like formation pathways in these systems. The inherent scarcity of wide-orbit giant planets necessitates large sample sizes for unbiased surveys to have either a reasonable likelihood of discovering a new companion or to be able to place useful constraints on the occurrence rate of such companions. The ground-based direct-imaging survey SHINE has placed constraints on massive companions (1-75 M_{Jup}) with semimajor axes 5-300 AU around M dwarfs to be $5.4^{+8.7}_{-4.4}\%$ for the brown dwarf binary component and $< 9.7\%$ for the planetary companion component, based on a sub-sample of 20 M dwarfs [31]. More recently, in B25 we measured the occurrence rate of sub-Jupiter-mass exoplanets (0.3-1 M_{Jup}) on wide orbits (10-100 AU) around M dwarfs to be < 0.10 and < 0.16 objects per star with 1σ and 3σ confidence respectively, using a sample of only 9 stars. Ongoing efforts to expand the sample size of observations with sub-Jupiter-mass sensitivity, such as JWST GO 4050 (PI: Carter, including 23 M dwarfs), GO 5835 (PI: Carter, including 60 M dwarfs), GO 6122 (PI: Bowens-Rubin, including 6 M dwarfs), and GO 8826 (PI: Lawson, including 22 M dwarfs) will be critical to further constrain the occurrence of giant planets around the lowest mass stars. These observations are already yielding promising preliminary results, in particular with the follow-up observation of TWA 7b during GO 4050 [190] which adds evidence for its status as the first directly-imaged sub-Jupiter-mass candidate.

Chapter 4: Supporting Roman Space Telescope Coronagraphy

4.1 Introduction

To date, every direct detection of an exoplanet has been executed in infrared (IR) wavelengths or Hα emission, using facilities both on the ground (e.g. VLT/SPHERE [211], Gemini/GPI [49], Keck/KPIC [212]) and in space (e.g. HST/NICMOS [213], JWST/NIRCam [50]). Using state-of-the-art facilities and post-processing techniques, such observations have achieved flux contrasts of 10^{-7} at near-IR wavelengths at a separation of 2 arcseconds [116]. However, the ultimate goal of direct imaging is to detect an Earth-like planet orbiting a Sun-like star, which will require flux contrast sensitivity on the order of 10^{-10} at visible wavelengths. The Habitable Worlds Observatory (HWO) mission is being developed for this purpose, along with a suite of new instrumentation technology, observation scheduling strategies, and post-processing algorithms.

The Nancy Grace Roman Space Telescope (Roman) Coronagraph Instrument, expected to launch in late 2026, will serve as a critical technology demonstration in preparation for the future HWO. The Roman Coronagraph will implement active wavefront control with deformable mirrors for the first time in space, achieving flux contrast sensitivities better than 10^{-8} for separations from $150 - 450$ mas [76]. While this falls short of the requirement to image an Earth analog, it will enable observations of giant planets in visible, reflected light for the first time. With access

to giant planets much older and colder than can be detected with IR imaging, the direct imaging community will be able to characterize giant planet atmospheres in both young and mature states and explore the full time evolution of Jovian analogs.

As the HWO will be targeting systems with known planets discovered by radial velocity (RV) and/or stellar astrometry, we must develop observation strategies for scheduling follow-up imaging of indirectly discovered planets [82]. The Roman Coronagraph thus provides a critical opportunity in advance of the HWO to plan and execute reflected-light direct imaging of objects which have only been detected indirectly.

From a scientific perspective, the statistical characterization of the mass versus semi-major axis, mass versus radius, and mass versus luminosity relationships is the primary observational method used to uncover the dominant processes that drive planetary formation and evolution [214]. RV planets have a very well-defined orbital period, eccentricity, time of conjunction (when the planet passes in front of the star and changes from negative to positive radial velocity), and $m \sin i$ (a parameter proportional to the RV semi-amplitude containing both the planet mass m and orbital inclination i). However, i itself is completely unconstrained, and thus the true planet mass remains unknown. With direct imaging, the orbital inclination and therefore the true mass of a planet can be constrained dynamically. The planet mass is thus a critical parameter which, for a few favorable RV systems, the Roman Coronagraph may be able to measure directly for the first time.

The challenge of directly imaging RV planets with Roman was first assessed by Traub et al. in 2014 and 2016 for the purpose of estimating the science yield of possible Roman (then named WFIRST-AFTA) coronagraph designs [215, 216]. They found that 12 RV planets as described in the Exoplanet Orbit Database at Penn State University [217] could be accessible to

imaging with the instrument design which would eventually become the Roman Coronagraph. Greco & Burrows (2015) [218] found the volume-averaged observability (i.e. the fraction of a randomly oriented planet's orbit for which it is detectable) of Jupiter-like planets orbiting host stars within 10 pc of Earth to be $\sim 12\%$, suggesting that randomly timed observations are extremely unlikely to be successful. Adding to the difficulty, Brown et al. (2015) [219] assessed the ability of direct imaging observations to constrain the masses of RV planets, finding that the ability to measure the true planet mass was primarily limited by uncertainties in the orbit fit parameters. In 2021, Carrión-Conzález et al. [220] performed a holistic study of the 4300 confirmed exoplanets on the NASA Exoplanet Archive [7] at the time and identified 26 planets which have a $> 25\%$ chance of being detected at some point in their orbits in the optimistic scenario for Roman Coronagraph performance. However the coupling of uncertainties between different orbital parameters (such as the time and argument of periapse) was lost due to the nature of the input catalog, which increased the scatter in predicted planet flux and separation. Spohn et al. (2022) [82] have since described best practices for propagating orbit fits from RV data for the purpose of scheduling direct imaging observations, recommending the propagation of each possible orbit fitting the RV data independently to conserve the correlation of particular orbital parameters in the RV fit posterior distribution.

In the following sections, I describe the programmatic context for this work (§ 4.2), the methods used to propagate RV orbit uncertainties and quantify the detection probability of known planets (§ 4.3), and the resulting time-resolved detectability of possible target planets (§ 4.4). I then discuss the prioritization of the targets and provide recommendations on observation scheduling to maximize detection probability and orbital characterization (§ 4.5). Finally, I provide a summary of our findings and anticipated future work (§ 4.6).

4.2 Prior Work by the Roman Coronagraph CPP

The Coronagraph Community Participation Program (CPP) is an international collaboration of scientific teams selected by NASA to develop target databases, observation plans, and data analysis tools in support of the Roman Coronagraph mission [221]. Given my involvement in simulation development beginning with the Roman Coronagraph Community Exoplanet Imaging Data Challenge in 2020 [222], I joined the CPP during its inaugural phase in 2022. My work for the team since then has included data reduction pipeline development (namely leading the PSF subtraction step), the definition of team-standard coordinate and orbital basis conventions, the co-leading of a CPP white paper on reflected-light planet imaging strategies, and extensive preparation for observation planning.

With the launch of Roman currently scheduled for Fall 2026, the mission provided a deadline of January 15, 2026 for the initial observation plans associated with the primary coronagraphic observing programs. This chapter will therefore focus on my primary task for observation planning: to produce a prioritized list of known RV planets which are favorable for a first direct, reflected-light detection with the Roman Coronagraph.

Through the CPP, significant though unpublished prior work has been accomplished to enable my timely contributions to the team. Dr. Dmitry Savransky and his group have developed a tool and associated database `plandb`[1] which estimates the orbit-averaged detection probability (a.k.a. "completeness" [223, 224]) of the planets in the NASA Exoplanet Archive. These calculations are based on published orbit fits, which often decouple the uncertainties of correlated orbital parameters such as the time and argument of periapse. As a result, planet properties are difficult

[1] https://plandb.sioslab.com/ ; hosted by the Space Imaging and Optical Systems Lab at Cornell University

to predict as a function of time without refitting the original RV dataset, but averaging over the full orbit still produces a useful first prioritization. Savransky's group identified 26 planets with non-zero completeness and host star V-band flux brighter than 8 magnitudes. Of these planets, two (HD 142 c and psi 1 Dra B b) were deemed unobservable due to nearby binary stars. An additional two (beta Pictoris b, and HD 100546 b) were removed from consideration as they have been imaged previously [225, 226]. Five targets (HD 219134 h, HD 95735 c, tau Ceti e, tau Ceti f, and HD 114613 b) were dismissed as their RV detections were deemed contentious, possibly associated with stellar activity, or otherwise unreliable. Finally, the planet 14 Herculis b is in consideration as a target for Roman imaging, however it is not investigated as an RV-only planet in this study due to recent JWST imaging of the system [227] and an ongoing investigation of astrometric data from the Hipparcos-Gaia Catalog of Accelerations [228] which is outside the scope of this work.

As noted in both Brown (2015) and Spohn et al. (2022), the orbital uncertainties from RV fitting combined with the time delay between the RV observations and the intended direct imaging observations can massively exacerbate the uncertainty in the detection probability of a given planet at a given time. A subset of the CPP team led by Dr. Sarah Blunt has therefore dedicated effort to finding the most recent RV data available for the remaining 15 targets of interest (shown in Table 4.1) and refitting the RV data with the open source code `RadVel` [229].

Following their work, I was provided with updated RV fits for each planet to consider as a possible target for the first reflected light observation attempts with the Roman Coronagraph. The format of these data is essentially the posterior distribution of orbital parameters from an MCMC chain. More practically, it can be thought of as a "point cloud", where each point contains (1) a set of parameters that describes one possible orbit and (2) a likelihood value which describes

Target	C	m sin(i) [M_{Jup}]	a [AU]	P [day]	e	Host Sp. Type	d [pc]	Ref.
47 UMa b	0.053	2.44	2.059	1076.6	0.016	G1	13.7967	[230]
47 UMa c	0.512	0.497	3.404	2287	0.179	”	”	[230]
47 UMa d	0.036	1.51	13.8	19000	0.38	”	”	[230]
55 Cnc d	0.438	3.82	5.6	4799	0.0913	K0	12.5855	[231]
eps Eri b	0.036	0.651	3.5	2650	0.044	K2	3.2026	[230]
HD 114783 c	0.137	0.659	4.97	4340	0.114	K1	21.0628	[230]
HD 134987 c	0.001	0.935	6.62	5960	0.154	G6	26.1804	[230]
HD 154345 b	0.368	0.905	4.272	3420	0.038	G9	18.284	[230]
HD 160691 c	0.432	2.423	5.543	4472.967	0.027	G3	15.5981	[232]
HD 190360 b	0.476	1.492	3.955	2892.2	0.3274	G7	16.0069	[230]
HD 192310 c	0.008	0.076	1.18	525.8	0.32	K2	8.7968	[233]
HD 217107 c	0.167	4.31	5.942	5141	0.3928	G8	20.0619	[230]
HD 87883 b	0.038	2.292	4.072	3303	0.7121	K0	18.2912	[230]
HD 39091 b[2]	0.146	10.02	3.1	2093.07	0.637	G0	18.2702	[234]
ups And d	0.185	4.1	2.517	1282.41	0.294	F9	13.4054	[230]

Table 4.1: A summary of the RV planets considered in this work for imaging with the Roman Coronagraph. We show the observational completeness (C) calculated by the Savransky group, which corresponds to the detection probability of a randomly timed observation. We also show the minimum mass (m sin(i)), semimajor axis (a), eccentricity (e), host star spectral type, and system distance (d) as published in the literature. The last column specifies the reference used for the displayed orbital parameter set.

how well that orbit fits the available data. My task, as detailed in the following subsections, was thus to propagate each of the possible orbits over time, describe the expected planet-star separation and flux ratio over time with accurate uncertainties, and predict the time-resolved detection probability of each planet.

4.3 Methods

To determine the detection probability of a given planet at a given time, we must first model what is currently known about the planet. We first define the coordinate system and orbital element basis in § 4.3.1. We convert the RV fit posterior basis to a basis of orbital elements more useful for imaging, and then add a distribution of the elements unconstrained by the RV

fit, as described in § 4.3.2. We then propagate each orbit in the point cloud through time using the formulae described in § 4.3.3. Finally, we compare the likelihood-weighted distribution of planet-star separation and flux ratio at a range of observation times to the predicted sensitivity of the Roman Coronagraph as shown in § 4.3.4.

4.3.1 Definition of Coordinate System and Orbital Elements

To orient ourselves in astronomical observations, we define a coordinate system following the conventions laid out in Hilditch (2001) *An Introduction to Close Binary Stars* [235]. Figure 4.1, adapted from W. Thompson et al. (2023) [236], provides an illustration of the conventions described in this section. The coordinate vectors $\hat{x}$, $\hat{y}$, and $\hat{z}$ are defined such that the origin is located at the position of the host star and $\hat{z}$ is the direction pointing directly away from the earth. Then $\hat{x}$ is the cardinal East direction in the plane of the sky, and $\hat{y}$ is the direction rotated $90°$ clockwise in the plane of the sky (cardinal North). We can then define the position of the star $\vec{x}_*$ and observer $\vec{x}_\mathrm{o}$ as:

$$\vec{x}_* = (0, 0, 0), \tag{4.1}$$

$$\vec{x}_\mathrm{o} = (0, 0, -d), \tag{4.2}$$

where d is the distance from the earth to the exoplanet system, and the time-dependent position of the planet as

$$\vec{x}_\mathrm{p}(t) = (x, y, z), \tag{4.3}$$

where the components x, y, z can be calculated as a function of time based on the orbital description described below.

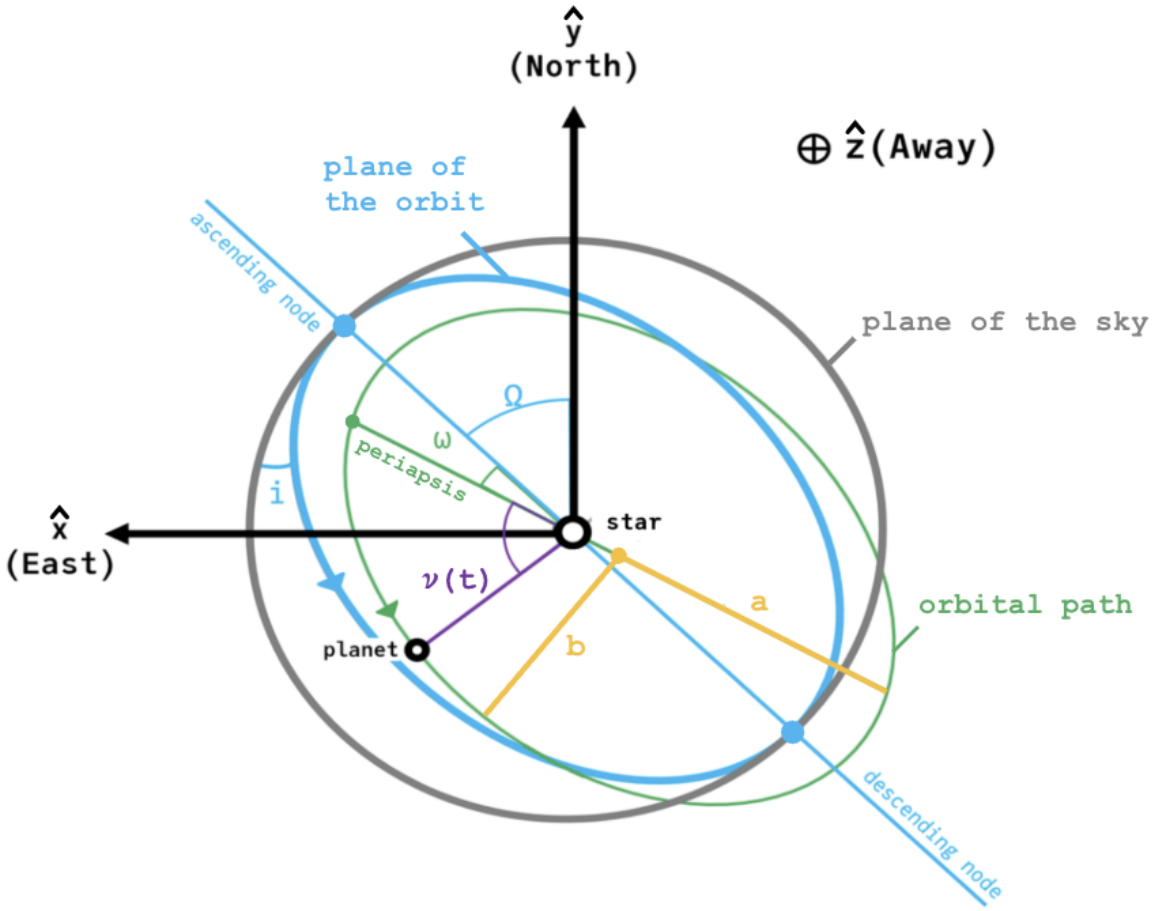

Figure 4.1: Schematic of coordinate system and orbital elements, modified from W. Thompson (2023) [236]. We show the coordinate basis vectors $\hat{x}$, $\hat{y}$, and $\hat{z}$ in black. Ellipses show the plane of the sky in grey, the plane of the orbit in blue, and the orbital path in green. We label the key orbital parameters: the semimajor axis a, semiminor axis b, longitude of the ascending node Ω, argument of periapse ω, orbital inclination i, and mean anomaly $\nu(t)$.

To define a unique planet orbit, a minimum of six parameters are required. The size of the orbit can be described by the semimajor axis a (half the length of the major axis of the orbital ellipse, equivalent to the mean planet-star distance) or the orbital period P (the time required to complete one orbit). The shape of the orbit is typically specified by the eccentricity e, which can be calculated from the semimajor axis a and semiminor axis b (half the length of the minor axis

of the orbital ellipse) by the following equation:

$$e = \sqrt{1 - \frac{b^2}{a^2}} \tag{4.4}$$

such that e can range from 0 to 1, and $e = 0$ describes a circular orbit.

Three angles then define the orientation of the orbit in 3D space. The inclination i describes the rotation about the major axis, where $i = 0$ corresponds to a "face-on" orbit parallel with the plane of the sky, and $i = 90^\circ$ corresponds to an "edge-on" orbit perpendicular to the plane of the sky. The longitude of the ascending node Ω describes the rotation of the orbit in the plane of the sky, and is measured from cardinal North ($\hat{y}$) eastward to the the "ascending node", where the planet's orbit intersects the plane of the sky and the planet passes from negative to positive z coordinates. The argument of periapse ω then represents the rotation of the orbit in the plane of the orbit, and is measured from the longitude of the ascending node to the location of periapse (minimum planet-star distance) of the planet, along the direction of the planet's orbit[3].

Finally, a parameter is needed to describe the location of the planet in time. We use the time of periapse $t_{\rm p}$, which is the time when the planet is located at periapse. While for circular orbits the argument (and thus time) of periapse is ill-defined, a particular combination of the two parameters can still define the orbit uniquely.

With the orbit itself defined, we can describe the position of the planet at any given time by the true anomaly $\nu(t)$, which is the stellocentric angle measured from the argument of periapse to the position of the planet at a given time t, along the plane of the orbit in the direction of the planet's orbit. The location of the planet $\vec{x}_{\rm p}(t)$ can then be found by the following expression

[3]A note of caution that in some cases the orbit is described using the argument of periapse from the perspective of the star rather than the planet, which introduces a 180° offset and must be accounted for.

derived in Appendix 1 of Thompson et al. (2023) [236]:

$$\vec{x}_{\mathrm{p}}(t) = \frac{a(1-e^2)}{1+e\cos(\nu(t))} \times \begin{bmatrix} \cos(\nu(t)+\omega)\cos\Omega - \sin(\nu(t)+\omega)\cos(i)\sin(\Omega) \\ \cos(\nu(t)+\omega)\cos\Omega + \sin(\nu(t)+\omega)\cos(i)\sin(\Omega) \\ \sin(\nu(t)+\omega)\sin(i) \end{bmatrix} \tag{4.5}$$

However, the calculation of $\nu(t)$ from the orbital elements (referred to as orbit propagation), and thus the calculation of the precise planet location $\vec{x}_{\mathrm{p}}$, is not possible with pure algebra in cases where $e \neq 0$. This complication is due to the nature in which an eccentric planet's speed varies along its orbit, which prohibits the closed-form expression of $\nu(t)$. Numerical methods are commonly used to bypass this limitation, and are introduced in § 4.3.3.

4.3.2 Planet Modeling

In the RV posterior for each planet, the possible orbits are described using a basis of the orbital elements P (orbital period), t_p (time of periapse), e (orbital eccentricity), ω' (argument of periapse from the perspective of the star), and k (RV semiamplitude in km/s). The first step is then to convert to the orbital basis described in § 4.3.1 and illustrated in Figure 4.1, which uses the orbital elements a (semimajor axis), t_p (time of periapse), e (orbital eccentricity), i (orbital inclination), ω (argument of periapse from the perspective of the planet), and Ω (longitude of the ascending node). Each of the following computations is performed for every orbit realization in the RV posterior point cloud in order to maintain the correlation between related parameters.

The simplest conversion is that from ω' to ω, where switching from the star to planet per-

spective is a matter of rotating by 180°. Thus we use the below equation:

$$\omega = \omega' + \pi \tag{4.6}$$

where ω and ω' are measured in radians.

The inclination itself is unconstrained by the RV data, as RV is sensitive only to the component of the stars motion which is perpendicular to the plane of the sky. However the semiamplitude k is related to both the planet mass and inclination by the below relation [237]:

$$\frac{k}{\text{ms}^{-1}} = 203 \left(\frac{P}{\text{days}}\right)^{-1/3} \cdot \frac{(m_\text{p}/\text{M}_\text{Jup}) \sin i}{(M_\text{tot}/\text{M}_\odot)} \cdot \frac{1}{\sqrt{1-e^2}} \tag{4.7}$$

where m_p is the planet mass, M_tot is the total system mass, M_Jup is the mass of Jupiter, and $\text{M}_\odot$ is the mass of the Sun. Under the assumption that $m_\text{p} \ll M_\text{tot}$, or more specifically that $m_\text{p} < 0.1 M_\text{tot}$ which holds for each of our planets, this simplifies to

$$m_\text{p} \sin i \approx \frac{k}{28.4329 \text{ ms}^{-1}} \cdot \sqrt{1-e^2} \left(\frac{M_*}{\text{M}_\odot}\right)^{2/3} \left(\frac{P}{1 \text{ year}}\right)^{1/3} \tag{4.8}$$

where M_* is the host star mass (collected from the `plandb` database) and the value 28.4329 ms^{-1} is the RV semiamplitude of a Jupiter mass planet orbiting a Solar mass star with a period of 1 year. To assign an inclination and mass to each orbit in the point cloud, we first calculate the critical inclination i_crit which would result in the companion having a mass of $0.08\text{M}_\odot$, a.k.a. the minimum mass of a hydrogen-fusing star [238]. We can rule out inclinations more face-on than i_crit as these correspond to stellar companions, and spectroscopy binary surveys typically have sensitivity down to the minimum stellar mass [239]. We thus draw the inclination from

a distribution proportional to $\sin i$ for i between i_{crit} and $\pi - i_{\text{crit}}$. This represents a uniform distribution of orbital plane orientations in 3D space, as there are more unique orbital orientations corresponding to an edge-on inclination ($i = \pi/2$) than corresponding to a face-on inclination ($i = 0, \pi$), and simultaneously rejects too-massive companions without skewing the distribution. Then the planet mass is determined simply by division, as by definition $m_{\text{p}} = (m_{\text{p}} \sin i)/\sin i$.

We find the semimajor axis a using Kepler's Third Law, as described in § 4.3.1 using both the planet mass and the stellar mass to calculate the total mass of the system. Though we used the approximation of $M_{\text{tot}} \approx M_*$ during the calculation of $m_{\text{p}} \sin i$ for computational simplicity, we do not approximate here as there is no computational cost. Additionally, any error in the predicted separation due to this approximation is such that the separation may be slightly underestimated, typically resulting in a more conservative detection probability estimate.

The final orbital parameter is the longitude of the ascending node Ω which defines the rotation of the orbit within the plane of the sky, and is completely unconstrained by RV measurements. As the contrast sensitivity of the primary imaging mode of the Roman Coronagraph is radially symmetric, that is, it depends only on the planet-star separation and not on the position angle in the FOV, we adopt a constant value of $\Omega = 0$ for every orbit. This has the added benefit of simplifying plots of the orbital path predictions by removing the "smearing" effect of a randomized Ω.

The above parameters allow us to make quantitative predictions of the planet-star separation over time, however some additional assumptions are required to predict the planet-star flux ratio. As introduced in § 1.2.1, the flux ratio is given by

$$\frac{F_{\text{p}}}{F_*} = \left(\frac{R_{\text{p}}}{r(t)}\right)^2 A_{\text{g}}(\lambda)\Phi(\alpha(t), \lambda) \tag{4.9}$$

where $R_{\rm p}$ is the planet radius, $r(t)$ is the time-dependent orbital radius, $A_{\rm g}$ is the geometrical albedo as a function of wavelength λ, and Φ is the normalized scattering law as a function of both λ and the time-dependent planetocentric star-observer phase angle $\alpha(t)$.

We first use the planet mass to estimate a planetary radius $R_{\rm p}$ based on a modified Forecaster mass-radius relation [240]. The Forecaster relation is an empirical relation composed of segments in several mass regimes which are linear in log-log space. As the published version includes inflated Hot Jupiters in the input dataset, the predicted radii of more widely separated Jupiter-mass exoplanets are often overestimated. We therefore use a modified mass-radius relation for cold planets which is described in Section 10 of the `plandb` Known Planets Table documentation page[4] and provides a constant prediction of 1 Jupiter radius for objects with masses between that of Jupiter and 0.08 $M_\odot$.

For the phase curve Φ we assume a Lambertian phase curve which is independent of λ given in Equation 1.9 and repeated here for reference:

$$\Phi(\alpha) = \frac{\sin\alpha + (\pi - \alpha)\cos\alpha}{\pi}. \tag{4.10}$$

In the limit that the distance between Earth and the host star is much greater than the planet-star separation (true for all exoplanets), the phase angle α is given by

$$\alpha = \cos^{-1}\left(\frac{z_{\rm p}}{\sqrt{x_{\rm p}^2 + y_{\rm p}^2}}\right), \tag{4.11}$$

where $x_{\rm p}$, $y_{\rm p}$, and $z_{\rm p}$ are the components of the planet location $\vec{x}_{\rm p}$ in the coordinate system as

[4] https://plandb.sioslab.com/docs/html/index.html#knownplanets-table

defined in § 4.3.1.

The albedo is chosen based on previously observed spectra of Jupiter [241] to be 0.465 in Band 1 (a 10% bandpass centered on 575 nm). This is possibly an overestimate, and one of the least constrained parameters needed to make the predictions sought in this work [242]. While the absolute flux ratio predicted may change with updated albedo assumptions, we assume that a constant value will provide the necessary baseline to make a comparative assessment of the possible target planets.

Finally, the 3D planet location $\vec{x}_{\mathrm{p}}$ is determined as a function of time by propagating the RV orbit fit as described in the following section.

4.3.3 Orbit Propagation

Given the necessary set of parameters to describe the planetary orbit for each point in the point cloud, we then propagate each possible orbit over time to generate a distribution of possible physical locations in space ($\vec{x}_{\mathrm{p}} = [x_{\mathrm{p}}, y_{\mathrm{p}}, z_{\mathrm{p}}]$ in the coordinate system described in § 4.3.1). As mentioned in that section, there is no closed-form expression to determine the position of an eccentric planet over time. We thus adopt the use of several intermediate values as tools to determine $\vec{x}_{\mathrm{p}}(t)$.

The eccentric anomaly $E(t)$ describes the angle from the location of periapse to the position of the planet, but is centered on the center of the orbital ellipse rather than on the star. Using this

value, the planet position can be calculated as

$$\vec{x}_{\mathrm{p}}(t) = \begin{bmatrix} B(\cos E - e) + G(\sqrt{1-e^2}\sin E) \\ A(\cos E - e) + F(\sqrt{1-e^2}\sin E) \\ C(\cos E - e) + H(\sqrt{1-e^2}\sin E) \end{bmatrix} \tag{4.12}$$

where the Thiele-Innes geometrical constants A, B, C, F, G, and H [235] are defined below:

$$\begin{aligned} A &= a\cos\omega\cos\Omega - a\sin\omega\sin\Omega\cos i \\ B &= a\cos\omega\sin\Omega + a\sin\omega\cos\Omega\cos i \\ C &= a\sin\omega\sin i \\ F &= -a\sin\omega\cos\Omega - a\cos\omega\sin\Omega\cos i \\ G &= -a\sin\omega\sin\Omega + a\cos\omega\cos\Omega\cos i \\ H &= a\cos\omega\sin i \end{aligned} \tag{4.13}$$

To calculate the eccentric anomaly itself, we go through mean anomaly $\mu(t)$, which describes the angle centered on the center of the orbital ellipse, from the location of periapse to the position of the planet *as if it were traveling at a constant rate*. This value is simply given by

$$\mu(t) = \frac{2\pi(t - t_p)}{P}, \tag{4.14}$$

and the eccentric anomaly can then be found by solving the below equation for E using numerical

methods, as no analytical solution exists.

$$\mu(t) = E(t) - esin(E(t)) \tag{4.15}$$

We use an iterative numerical approach, calculating the first guess of the eccentric anomaly $E(t)_0$ as

$$E(t)_0 = \mu(t) + e\sin(\mu(t)) + \frac{e^2\sin(2\mu(t))}{2} \tag{4.16}$$

and defining the error ϵ in the ith approximation as

$$\epsilon_i = E(t)_i - e\sin E(t)_i - \mu. \tag{4.17}$$

We then repeatedly update the guess of $E(t)$ such that

$$E(t)_i = E(t)_{i-1} - \frac{\epsilon_{i-1}}{(1 - e\cos(E(t)_{i-1})} \tag{4.18}$$

until either $\epsilon_i < 10^{-15}$ or 20 iterations have been completed.

We perform the above calculation for each orbit in the point cloud and for time stamps ranging from January 1, 2027 to June 30, 2028 on a 5 day interval, which correspond to the anticipated first 18 months of Roman science observations. Figure 4.2 shows an example of the orbit propagation for 47 Uma c, where the effect of the unconstrained inclination is clearly visible.

At each time stamp, we assess the distribution of planet-star angular separations and flux

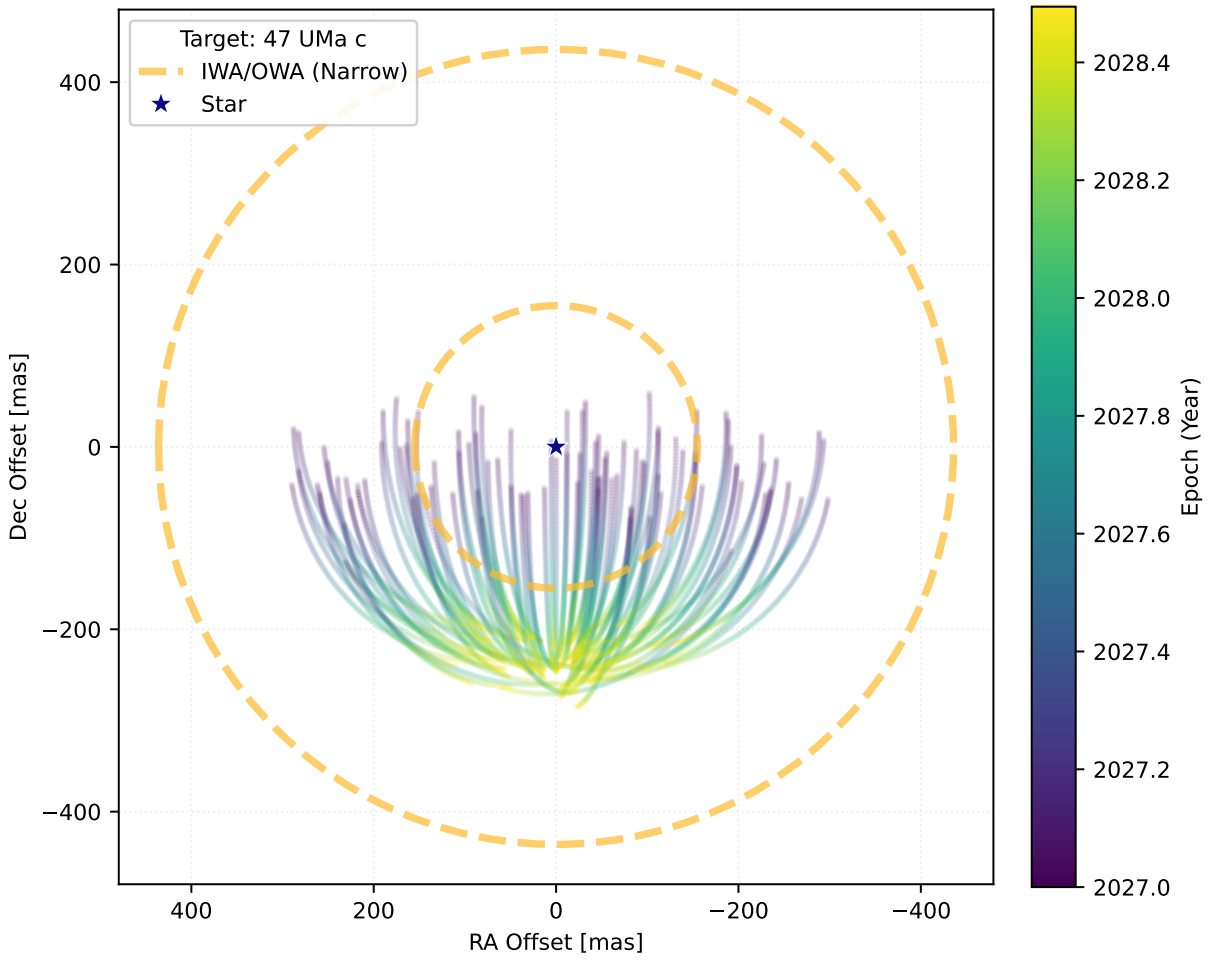

Figure 4.2: An example of orbit propagation from the RV posterior fit for the target 47 UMa c. We show the relative RA and Dec (on the x and y axis respectively) of a subsample of possible orbits from the time period of Jan 1, 2027 to June 30, 2028. The time is shown by the color of the line, and the inner and outer working angles of the primary Roman Coronagraph imaging mode (Band 1, narrow FOV) are shown by the two dashed orange circles. Due to the unknown inclination, the planet-star separation is best constrained near the position of the descending node which occurs in mid 2028.

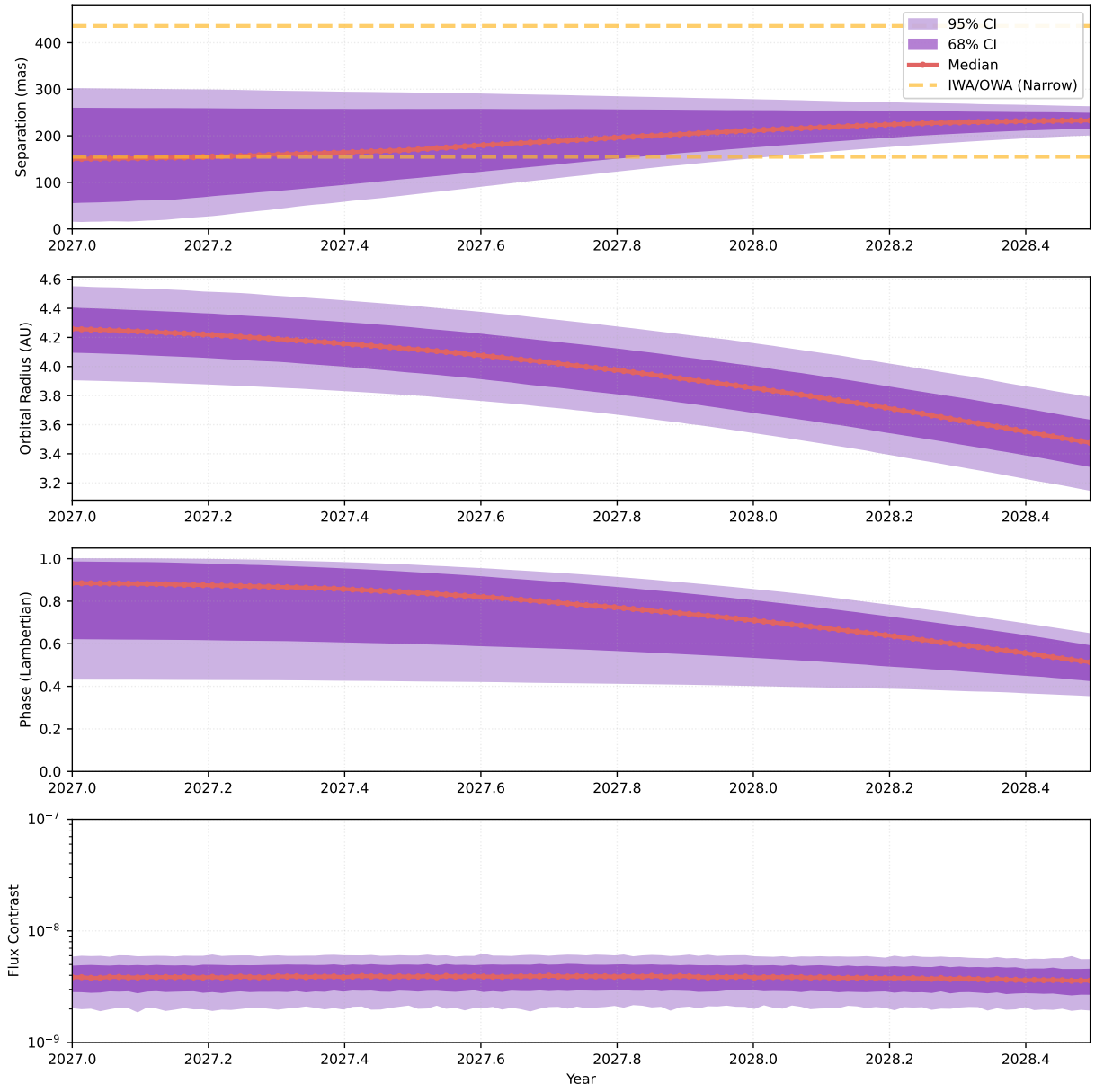

Figure 4.3: An example calculation of the separation and flux contrast for 47 Uma c. The top panel shows the predicted planet-star angular separation in mas, the second panel shows the orbital radius in AU, the third panel shows the phase assuming a Lambertian phase curve, and the bottom panel shows the resulting planet-star flux contrast. For each parameter we show the median with the red line, the 68% confidence interval with the dark purple region, and the 95% confidence interval with the light purple region. In the top panel we also show the OWA and IWA with the upper and lower dashed orange lines respectively.

contrasts. The angular separation in arcseconds is given by

$$\theta = \frac{\sqrt{x_{\rm p}^2 + y_{\rm p}^2}}{d} \times 206265'', \tag{4.19}$$

where d is the distance to the host star in parsecs. The flux ratio is calculated using Equations 4.10 and 4.11. We calculate the 2.5th, 16th, 50th, 84th, and 97.5th percentile values of each parameter at each timestamp weighted by the RV posterior likelihood of each orbit in the point cloud, following the prescription in Spohn et al. (2022) [82] to capture the uncertainty accurately. In Figure 4.3, we provide an example calculation for 47 Uma c, where the top panel shows the predicted planet-star angular separation in mas, the second panel shows the orbital radius in AU ($r(t)$ in Eq. 4.9), the third panel shows the phase assuming a Lambertian phase curve, and the bottom panel shows the planet-star flux contrast. For each parameter we show the median with the red line, the 68% confidence interval with the dark purple region, and the 95% confidence interval with the light purple region. In the top panel we also show the OWA and IWA with the upper and lower dashed orange lines respectively. In the unique case of 47 UMa c, we can see that while in early 2027 the planet is at a fuller phase, it is also more distant from the star due to its eccentricity. Thus the predicted flux contrast is approximately constant for the 18 month window from January 2027 to June 2028.

4.3.4 Calculating Detection Probability

We determine the time-resolved detection probability following the recommendations in Spohn et al. (2022) [82]. We compute the percentage of orbits in the point cloud which predict a detectable flux contrast and angular separation, weighted by the likelihood, at each time stamp.

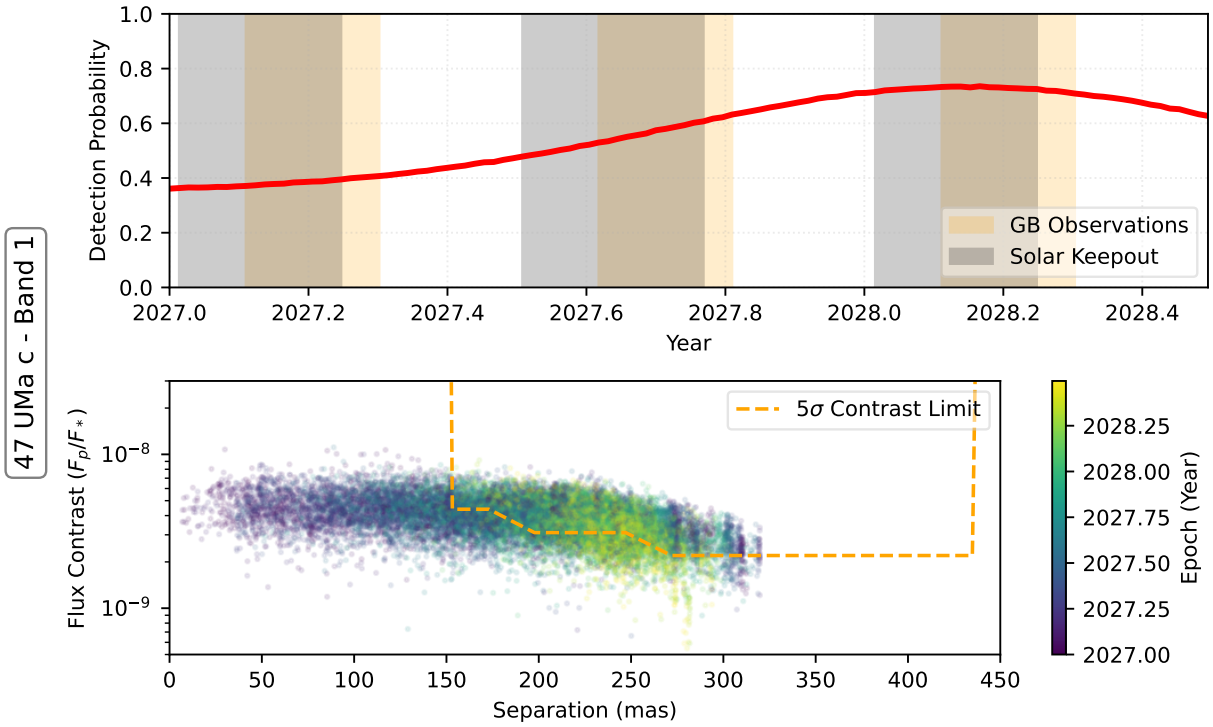

Figure 4.4: An example calculation of the detection probability for 47 Uma c. The top panel shows the detection probability in the red line, as well as the windows when the target star is unobservable due to galactic bulge (GB) observations in orange or solar keepout restrictions in grey. In the bottom panel we show the predicted separation and flux contrast (on the x and y axis respectively) as a function of time (encoded by the color of the points), as they compare to the contrast curve (orange dashed line, assuming optimistic performance and 10 hours of exposure).

A given point in contrast-separation space is deemed detectable if the predicted flux contrast is shallower than the the flux contrast required for a 5σ detection at the predicted separation. We use a simulated contrast curve which assumes an optimistic instrument performance scenario and 10 hours of exposure time [76], as shown by the orange dashed curve in the bottom panel of Figure 4.4. The points in this panel show the distribution of separation and flux contrast (on the x and y axis respectively) as a function of time (encoded by the color of the points) for 47 UMa c as an example. The time-dependent detection probability computed from these data is shown by the red line in the top panel. We can see from the plot that the detection probability in early 2027 is limited primarily by the uncertainty in planet-star separation, while in 2028 it is limited more by

the uncertainty in the albedo of the planet.

For the purpose of observation planning, we must also consider whether the science target is in fact observable according to programmatic constraints. Roman cannot point within 56° of the solar or anti-solar direction, so any epochs where the target star appears too close to the sun or to the anti-solar direction are not viable. This is referred to as the "solar avoidance constraint", or sometimes as "solar keepout". Additionally, the execution of the Roman Wide Field Instrument (WFI) Galactic Bulge (GB) Time Domain Survey (TDS) requires prioritized use of the observatory during two annual windows. To approximate these, we assume that any time the GB is observable within solar avoidance constraints, Roman will be used for GB observations and thus coronagraphic observations will be prohibited. We adopt the Gaia DR3 [131] ICRS coordinates for each potential target star, and we use the location of radio source Sagittarius A$*$ published in Petrov et al. (2011) [243] as a proxy for the GB location. We then use the CPP-developed python tool `roman-pointing`[5] to calculate the time windows within which a given target is unobservable due to solar keepout or GB observations, as shown by the grey and orange regions respectively in the top panel of Figure 4.4.

4.4 Results

The targets explored in this work can be separated into four broad categories: Good Targets, Uncertain Separation Targets, Narrow Targets, and Dim Targets. The "Good Targets," are defined as having a detection probability which surpasses 0.5 at some point in the first 18 months of the mission. There are three targets in this category, each discussed in § 4.4.1. We then show targets which are bad because either the separation is ill-constrained (a.k.a. "Uncertain Separation

[5]https://github.com/roman-corgi/roman_pointing

Targets" in § 4.4.2), they are within the IWA (a.k.a. "Narrow Targets" in § 4.4.3), or they are below the flux limit (a.k.a "Dim Targets" in § 4.4.4) for the entire 18-month time window.

4.4.1 Good Targets

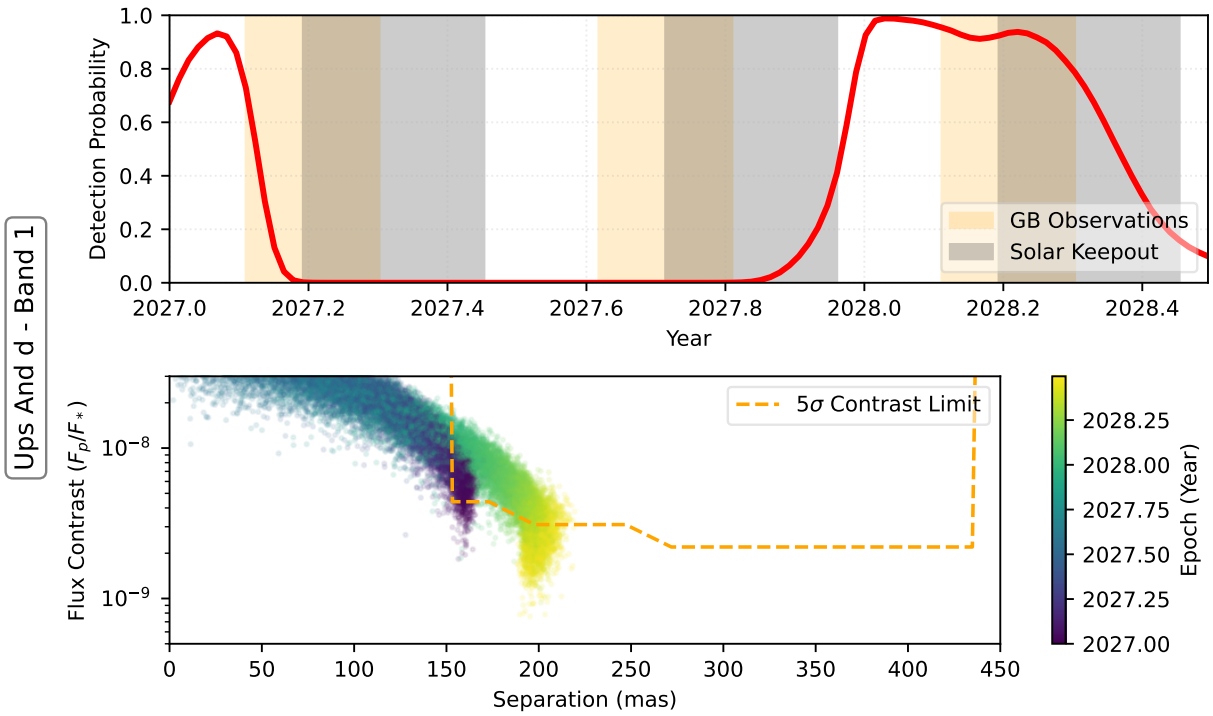

Figure 4.5: Detection probability results for upsilon Andromedae (ups And) d.

The good targets for observation are presented in decreasing order of peak detection probability. The first object is upsilon Andromedae (ups And) d, a $4.1 M_{Jup}$ minimum-mass object orbiting 2.517 AU from an F9 type star 13.4 pc away [230]. This configuration corresponds to an angular separation of 188 mas and expected flux contrast of 8.38×10^{-9} at quadrature (90° phase angle). The timing of the planet's passage through the ascending/descending nodes is such that the planet will be most detectable (with a peak detection probability of 0.93) in the first window for science operations in 2027, and then will be detectable again with a peak probability of 0.99 on January 11, 2028, as shown in the above figure.

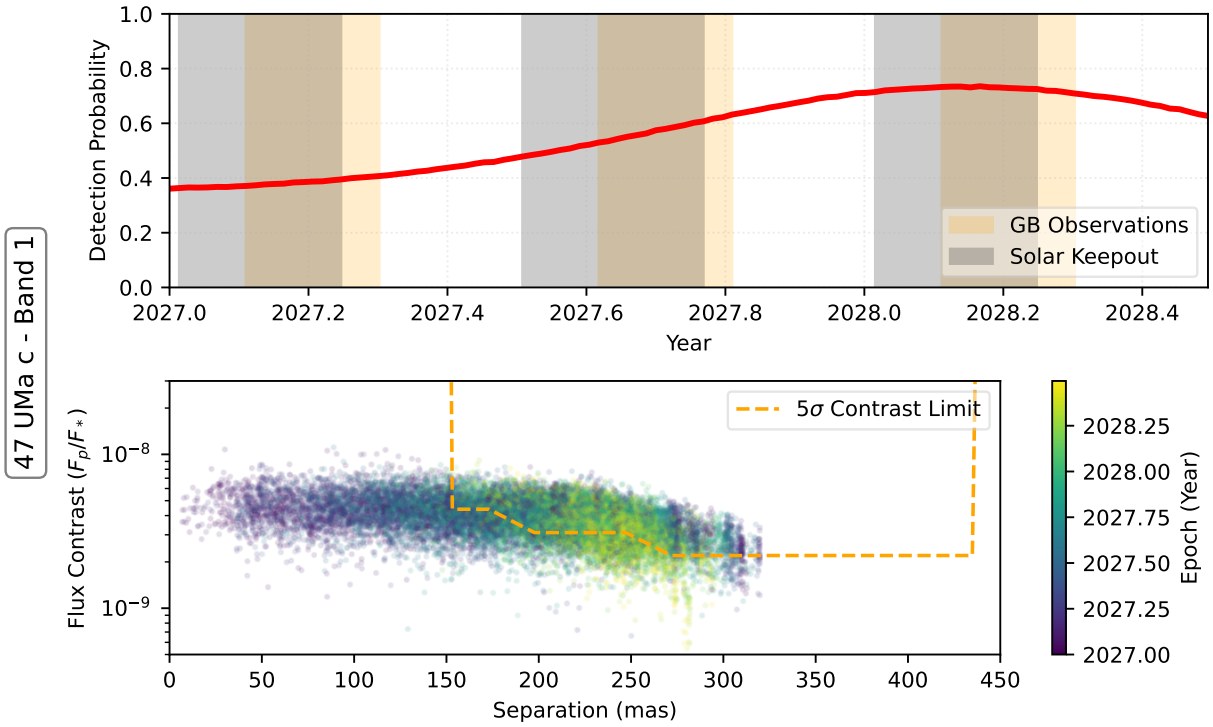

Figure 4.6: Detection probability results for 47 Ursa Majoris (47 UMa) c.

Next, the planet 47 Ursa Majoris (UMa) c has a peak detection probability of 0.74 on March 1, 2028, as shown above. 47 UMa c is a $0.50 M_{Jup}$ minimum-mass object orbiting at 3.4 AU from a G1 type star 13.8 pc away [230]. This corresponds to an angular separation of 247 mas and an expected flux contrast of 3.46×10^{-9} at quadrature. While constraints on the orbital inclination could result in a larger mean predicted separation during mid-2027, the predicted flux contrast is still very near the detection limit. Thus, only marginal increases in the detection probability would be expected even if the separation were known to be favorable. In 2028, the detection probability is primarily limited by the flux contrast and is therefore sensitive to assumptions about the planet albedo and phase curve.

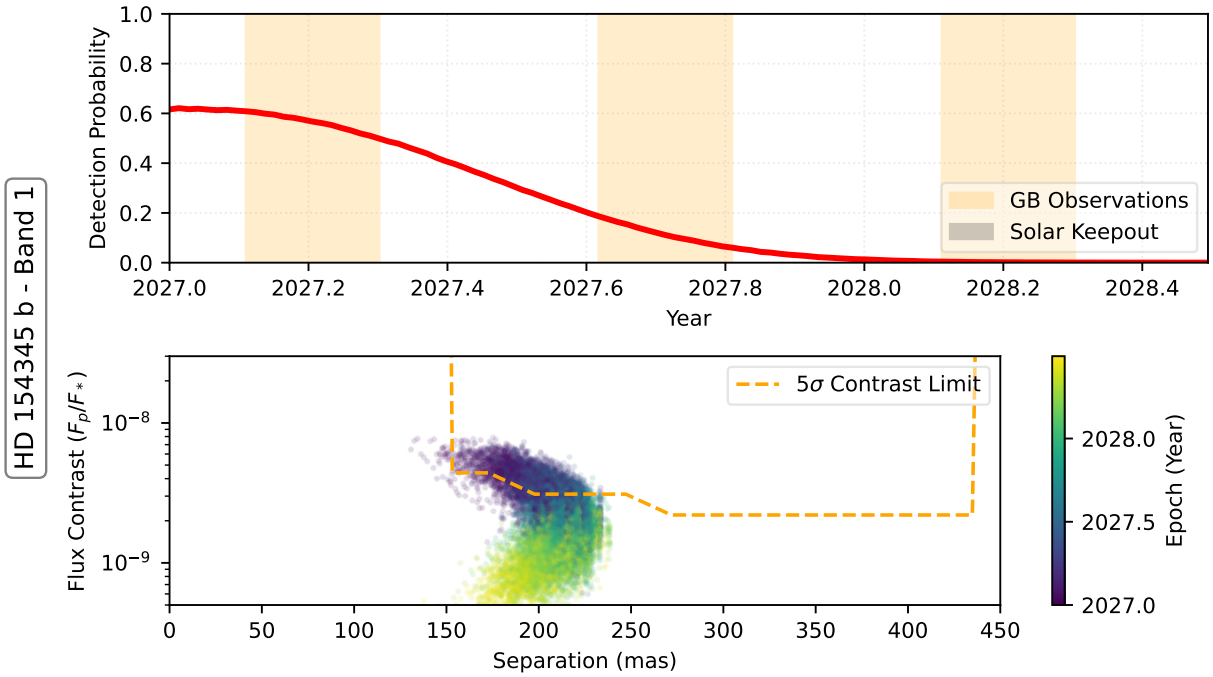

Figure 4.7: Detection probability results for HD 154345 b.

The final "good target" is HD 154345 b, shown above, with a peak detection probability of 0.62 on January 1, 2027. HD 154345 is a 0.90 M_{Jup} minimum-mass object orbiting 4.27 AU from a G9 type star 18.3 pc away [230]. This corresponds to a maximum angular separation of 234 mas, and an expected flux contrast at quadrature of 2.91×10^{-9}. The planet is expected to have a favorable separation during the entire 18-month window, however it is predicted to be monotonically decreasing in flux contrast and thus also in detection probability.

4.4.2 Bad Targets: Uncertain Separation

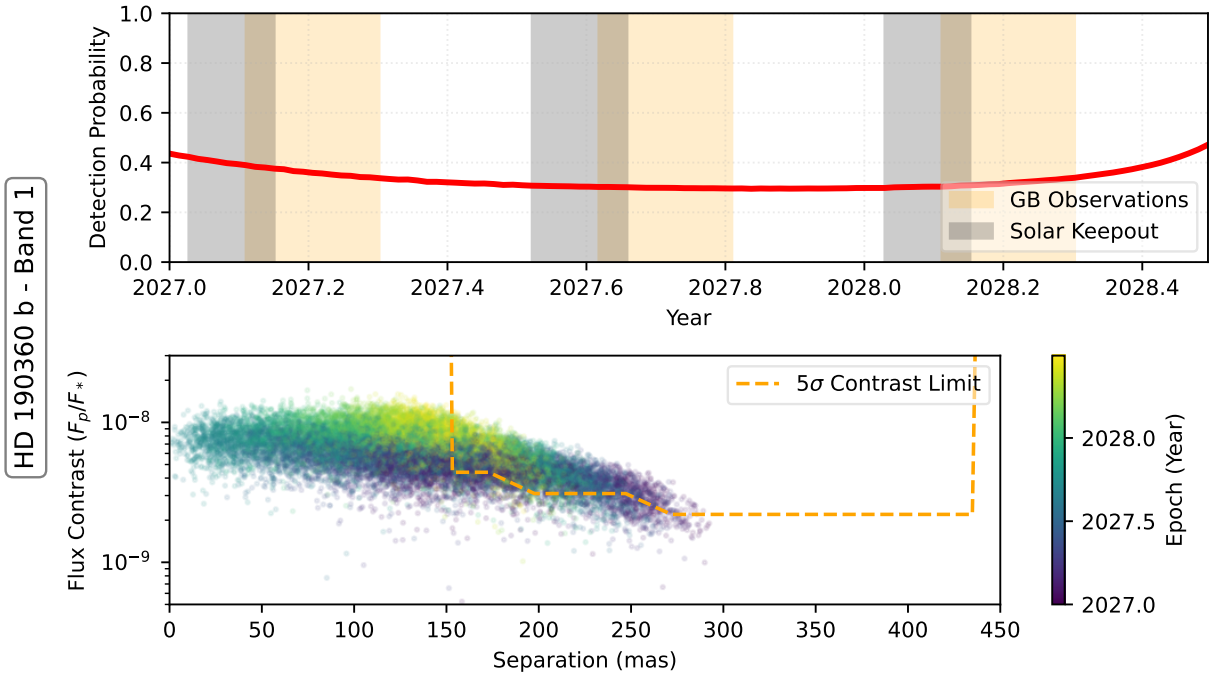

Figure 4.8: Detection probability results for HD 190360 b.

Two of the targets have predicted flux contrasts which are feasible to observe, however the unknown inclination renders the planet-star separation ill-constrained during the 18-month time window considered in this work. HD 190360 b, shown above, is expected to have a flux contrast $\geq 3.69 \times 10^{-9}$ after mid 2027, however half or more of the orbits result in separations narrower than the IWA. The timing of quadrature is such that this object is not expected to have a well-constrained separation beyond the IWA until October 2028. The other planet in this category is epsilon Eridani (eps Eri) b, whose detection summary plot can be found in § 4.7. This object suffers the opposite problem, as many of the modeled orbits suggest a planet-star separation beyond the OWA. If additional information such as stellar astrometry can constrain their orbital inclinations, the expected detection probability of these planets may change significantly.

4.4.3 Bad Targets: Narrow

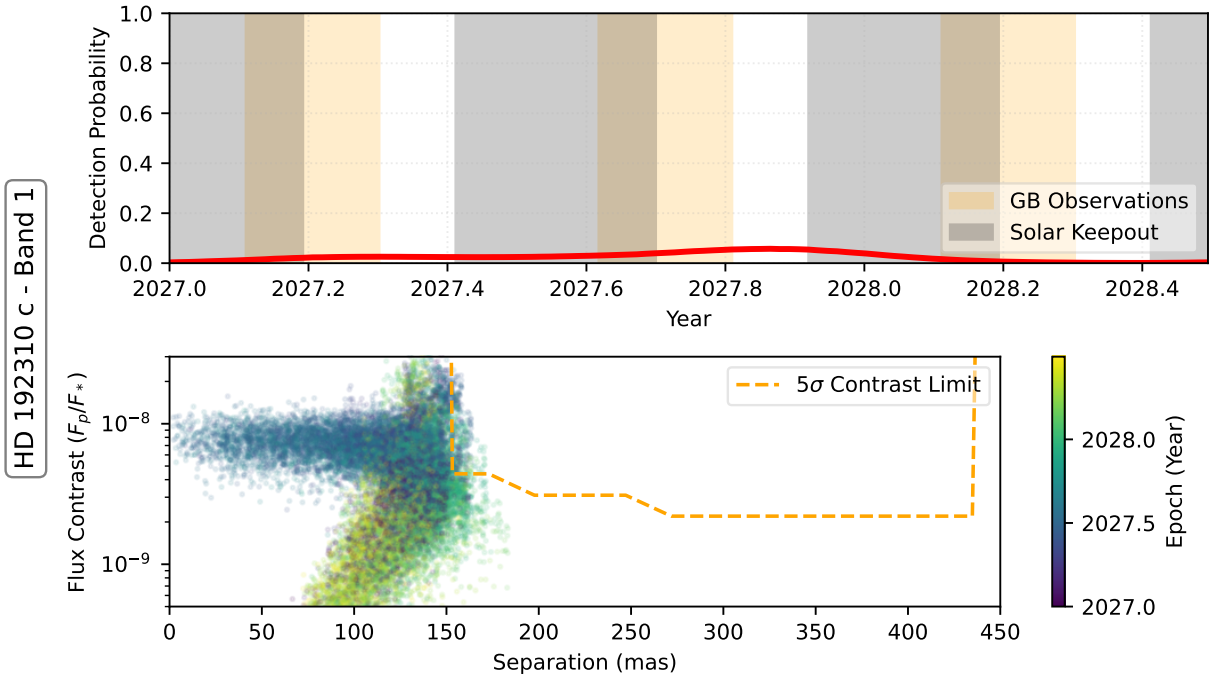

Figure 4.9: Detection probability results for HD 192310 c.

The targets in this category, HD 192320 c and 47 UMa b, are undetectable as they orbit entirely within the coronagraph IWA. We show the detectability summary for HD 192310 c above as an example. Based on the orbital description in the literature, this planet has a semimajor axis of 3.96 AU, and it orbits a G7 type star 16.0 pc away [233]. Due to its high eccentricity (0.32) this corresponds to an angular separation at quadrature between 91 and 177 mas, which may be observable if the argument of periapse is favorable. However the propagation of the RV fit posteriors from the CPP show separations greater than 150 mas to be unlikely. Similarly, the orbit of 47 UMa b corresponds to a maximum angular separation of $\sim$ 150 mas. While the low angular separation of this planet was known, we explored it due to its shared host star with 47 UMa c. The detection probability summary plot for 47 UMa b can be found in § 4.7.

4.4.4 Bad Targets: Dim

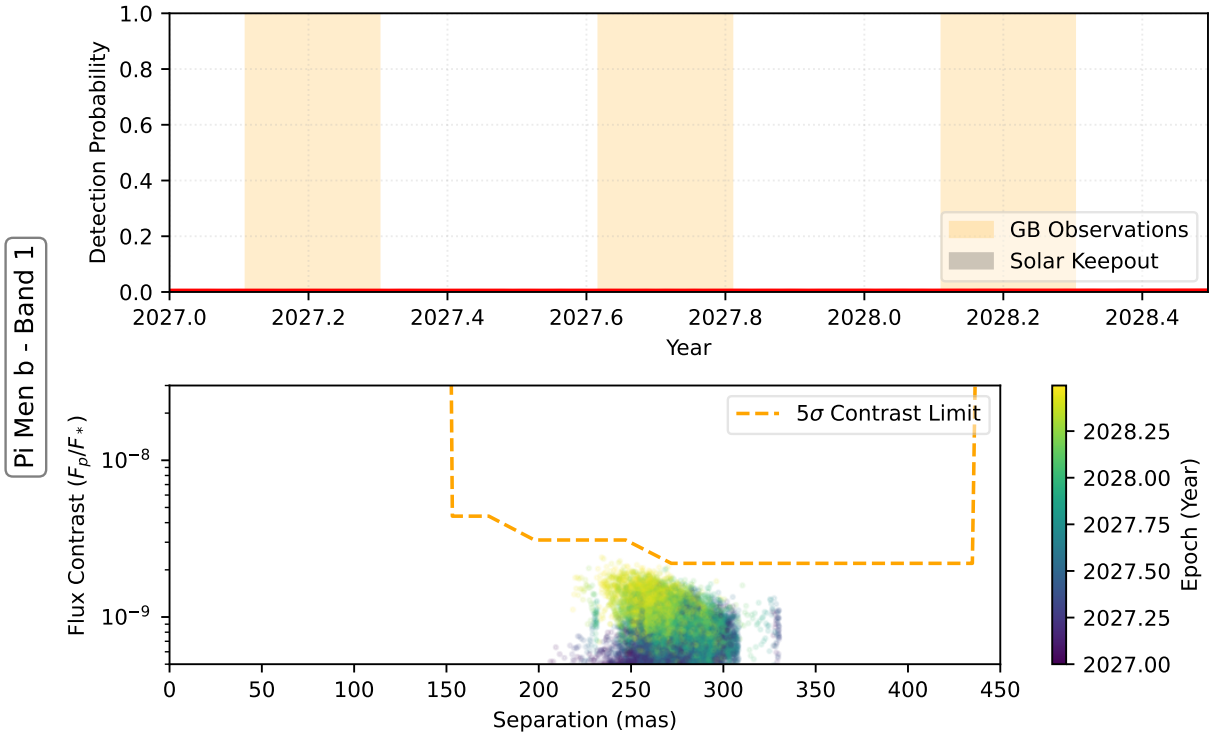

Figure 4.10: Detection probability results for pi Mensae (pi Men) b.

The remaining 8 targets may have favorable separations during the primary mission, however they are expected to be undetectable due to low flux contrasts. Above, we show the detection probability summary for pi Mensae (pi Men) b as an example. This planet is a $10.02 M_{Jup}$ minimum-mass object orbiting 3.1 AU from a G0 type star 18.3 pc away [234]. Its high eccentricity (0.637) results in an angular separation of 62-278 mas and a mean expected flux contrast of 5.53×10^{-9} at quadrature. However the predicted flux contrasts during the 18-month window are below 1.5×10^{-9} due to the planet being in an unfavorable phase.

The additional targets in this category are 47 UMa d, 55 Cancri (55 Cnc) d, HD 87883 b, HD 114783 c, HD 134987 c, HD 160691 c, and HD 217107 c, and their detection probability

summary plots can be found in § 4.7. As their detectability is primarily limited by the predicted flux contrast, any updates to the modeling which increase the predicted albedo of these planets may render them more likely to be observable.

4.5 Discussion

The primary purpose of this study is to provide a prioritized list of objects for observations in reflected light with the Roman Coronagraph, and the primary metric used for ranking is the detection probability (P_{det}) calculated in the previous section. To provide time for potential follow-up observation and further characterization, we prioritize planets with high P_{det} in the first six months of the mission (Jan 1, 2027 to June 30, 2027). Of the 15 targets explored, 6 were found to have $P_{\text{det}} \geq 0.10$ in this time window, and are shown in Table 4.2 below.

Target	**Peak P_{det}**	**Date**
ups And d	0.93	2027-01-31
HD 154345 b	0.62	2027-01-11
47 UMa c	0.46	2027-06-25
HD 190360 b	0.43	2027-01-06
eps Eri b	0.28	2027-01-31
HD 217107 c	0.10	2027-01-06

Table 4.2: The best targets for observation with the Roman Coronagraph, ranked in order of peak detection probability (P_{det}) in the first six months. We show the best observation date.

Based solely on the ranking by P_{det}, we can identify ups And d as the clear leader for the best reflected-light observation target. It is predicted to have a separation of 156 ± 2 mas and a flux contrast of $(6.87 \pm 1.49) \times 10^{-9}$, which corresponds to a detection probability of 0.93 assuming 10 hours of integration time and an optimistic instrument performance. Achieving the optimistic contrast level required for this observation in the first month of science operations will require considerable effort, as there are many uncertainties in the instrument performance which

affect the final sensitivity level. It is also likely that observations of brighter self-luminous targets will be observed first to exercise and characterize the Band 1 HLC mode, resulting in additional scheduling constraints. However, ups And d is also the ideal target for follow-up characterization. As shown in Figure 4.5, the RV orbit propagation suggests that there will be an ideal window for a second observation with a peak P_{det} of 0.99 on January 11, 2028. Conveniently, the planet is expected to be brighter (flux contrast $(9.06 \pm 2.16) \times 10^{-9}$) and more widely separated (163 ± 4 mas) at this time compared to the first observation epoch, which may enable a follow-up detection with the SNR needed to accomplish critical goals for characterization.

These goals are generally (1) to fully constrain the planet orbit and thus enable a dynamical mass calculation, (2) to measure changes in the planet photometry due to orbital motion and thus constrain the shape of the phase curve, and (3) to complete a spectroscopic observation and thus investigate the planet's atmospheric composition.

Regarding the first goal (the primary interest of this work), we can consider the problem from the perspective of degrees of freedom. As the RV data constrains all of the orbital parameters except two (longitude of ascending node Ω and inclination i), we can conclude that at least two additional data points are required to constrain the orbit fully. Observing the planet near quadrature, which is when it is passing through the ascending or descending node, is the best time to constrain Ω. This part of the orbit is also typically when the detection probability is highest for an RV planet with no inclination constraints, and is thus ideal for the first detection attempt. Following a successful detection, the photometry of the planet is much more easily predictable, and we can be more confident in the planet's flux ratio by planning a second observation where the planet is expected to be at a similar or fuller phase. This implies that the planning of a second observation to constrain the planet's inclination could be arranged such that information

is gained from both a detection and a non-detection. Essentially a detection might be expected for low (more face-on) inclinations, but a high inclination might result in the planet being behind the coronagraph mask, and thus a non-detection would provide a lower limit on the inclination and corresponding upper limit on the planet mass. This type of deduction would not be possible during the first observation attempt, as it would be extremely difficult to determine whether a non-detection was due to obscuration by the coronagraphic IWA or by the planet having a lower flux than expected. Therefore, we broadly recommend an observing strategy such that Ω and the flux contrast are first constrained by imaging the planet near quadrature, and that a second observation is used to constrain the inclination.

The second and third goals also benefit from the observation technique described above. Measuring changes in the planet photometry naturally requires multiple observations, and the first detection provides the grounding point to which future detections are compared. For planning spectroscopic observations, we need both a good understanding of the planet photometry (to plan the exposure time for a desired SNR) as well as an ability to predict both the separation and position angle of the planet (to align the spectroscopic slit with the planet location). This means both the longitude of the ascending node and the inclination need to be characterized before a spectroscopic observation is scheduled.

4.5.1 Caveats and Limitations

As discussed in the previous section, uncertainties on the albedo and phase curve shape are a major limitation on our ability to predict the flux contrast over time of an RV planet in reflected light. We adopt a constant, Jupiter-like albedo (0.465 ± 0.1) and a Lambert phase

function for the initial predictions made in this work, however this neglects a number of physical processes. In reality, both the albedo and phase curve are dependent on atmospheric properties such as cloud composition, which are in turn dependent on time-dependent parameters such as the orbital radius. Furthermore, the phase function based on Rayleigh scattering developed by Madhusudhan and Burrows (2012) [77] predicts lower flux contrasts than the Lambert phase function near quadrature by up to a factor of 2. Thus our simplified approach for the purpose of comparing possible targets may systematically over-predict the planet flux near quadrature.

In this study we have restricted our sources of prior orbital constraints to RV data for the purpose of a uniform exploration, however additional orbital information may be available from astrometric data (e.g. Hipparcos/Gaia). Some of the planets presented have published constrains on the inclination, such as pi Men b with $i = 54.436^{+5.945}_{-3.719}$ deg from Feng et al. (2022) [244]. Given the predicted low flux contrast of pi Men b due to the unfavorable phase of the planet between 2027 and 2028, it is unlikely that this constraint would increase the detection probability. However, the P_{det} of targets HD 190360 b and eps Eri b is primarily limited by the inclination uncertainty, thus a detailed study of any astrometric anomalies in these host stars could make a meaningful difference.

Finally, we acknowledge that the results of this study are very sensitive to assumptions about the performance of the Roman Coronagraph optical system and corresponding contrast sensitivity. Conservative performance estimates result in a contrast floor of $\sim 1 \times 10^{-8}$ at a separation of 200 mas and $\sim 6 \times 10^{-9}$ beyond 250 mas, which would prevent the successful detection even our best candidate, ups And d. Thus the execution of any reflected-light planet observations is dependent on achieving optimum performance with the instrument.

4.6 Conclusions

The purpose of this study has been to prioritize exoplanets discovered by radial velocity (RV) monitoring for the first direct, reflected-light observations with the Nancy Grace Roman Coronagraph Instrument. We have computed the time-resolved detection probability P_{det} of each planet by independently propagating each of the possible orbits generated by the RV Markov Chain Monte-Carlo (MCMC) fitting process, which maintains the correlation of mutually dependent orbital parameters. Finally, we have identified three exoplanets with a $P_{\text{det}} > 0.5$ in the first 18 months of the Roman mission: upsilon Andromedae d (ups And d, $P_{\text{det}} = 0.99$ on January 11, 2028), 47 Ursa Majoris c (47 UMa c, $P_{\text{det}} = 0.74$ on March 1, 2028), and HD 154345 ($P_{\text{det}} = 0.62$ on Jan. 1, 2027).

Based on the peak detection probability, as well as the presence of multiple detection windows for follow-up observations, we currently recommend ups And d as the best target for reflected-light imaging with the Roman Coronagraph. In particular, we recommend the first observation attempt on January 31, 2027 when the planet is near quadrature and the longitude of the ascending node can be constrained. We then recommend early 2028 as the best time to attempt to constrain the inclination and complete spectroscopic follow-up.

We anticipate several next steps to increase the fidelity of the predictions presented in this work. First, we plan to implement a more physically motivated treatment of the planet albedo and phase curves. We will implement the recently published cloud model for substellar atmospheres (`Virga` [245]), which includes calculations of scattering properties and variable sedimentation efficiency, and adopt the formalism described in Madhusudhan and Burrows (2012) [77] to generate the flux contrast predictions. We will also complete sensitivity studies to quantify the influ-

ence of these uncertainties. Computing the detection probability of each planet using the physically improbable maximum albedo would reveal which planets are unobservable even under ideal conditions due to orbital geometry. We can also compare the detection probability results for a range of phase functions (Lambert, isotropic, and Rayleigh), and for a variety of albedo priors (uniform vs. Gaussian).

Second, we will investigate the application of data from the Hipparcos-Gaia Catalog of Accelerations (HGCA, [228]) to constrain the orbital inclination of the possible targets. The complex systematics involved in this dataset may render this step a challenge, however it would be particularly useful for the few targets whose detection probability is currently dominated by the inclination uncertainty (47 UMa c, HD 190360 b, and eps Eri b).

Finally, we will assess the ability to constrain the longitude of the ascending node, the inclination, and the planet mass with a limited number of simulated reflected light detections. This investigation will help us determine the ideal imaging strategy for the most detectable planets, and will feed forward to imaging strategies for the future Habitable Worlds Observatory as well.

The successful direct imaging of an exoplanet in reflected light will be a major advancement in exoplanet science. With access to field-age systems, we can enable studies of the atmospheres of widely separated exoplanets across Gigayear timescales. In addition, we can measure the dynamical masses of RV exoplanets, further grounding the interpretation of their dynamical histories and atmospheric compositions. The observation strategies developed by the Roman Coronagraph mission will be paramount to achieving the goal of directly imaging an Earth-like planet around a Sun-like star with the HWO, and will usher in a new era of science high-contrast imaging.

4.7 Appendix: Additional Planet Detection Probability Summaries

The following plots summarize the detection probability P_{det} for the additional planets mentioned in § 4.4.

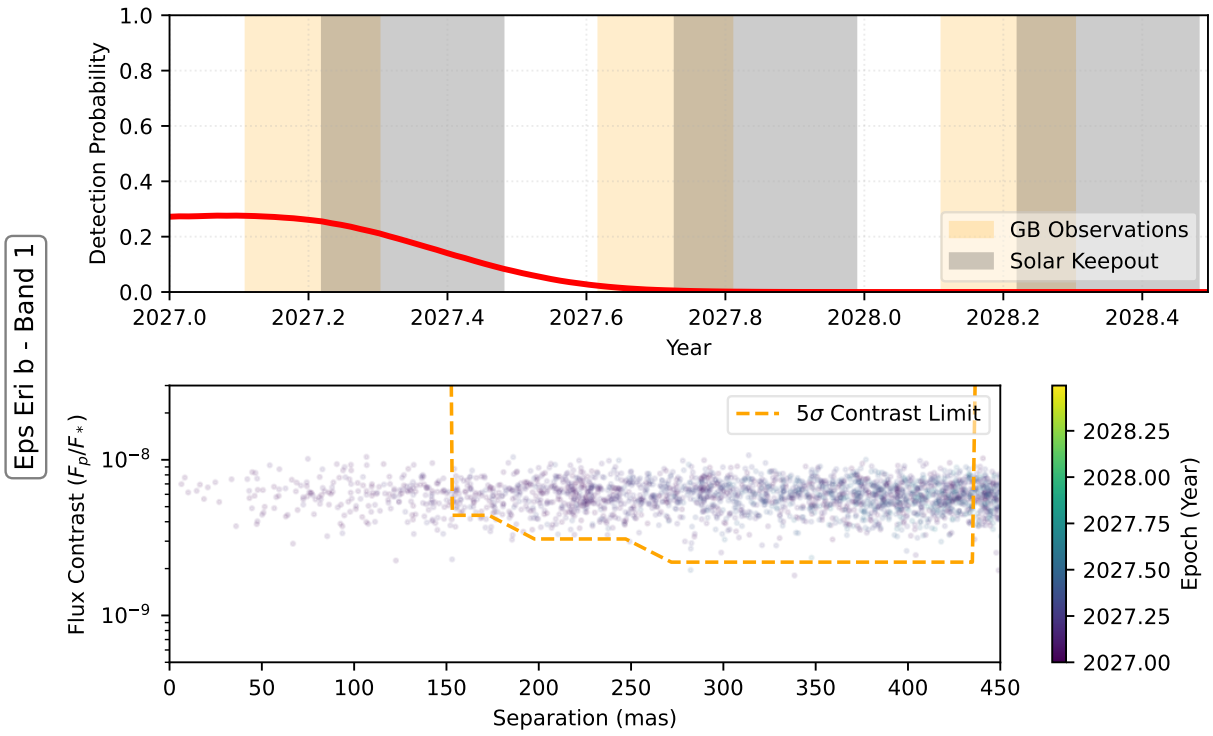

Figure 4.11: Detection probability results for epsilon Eridani b.

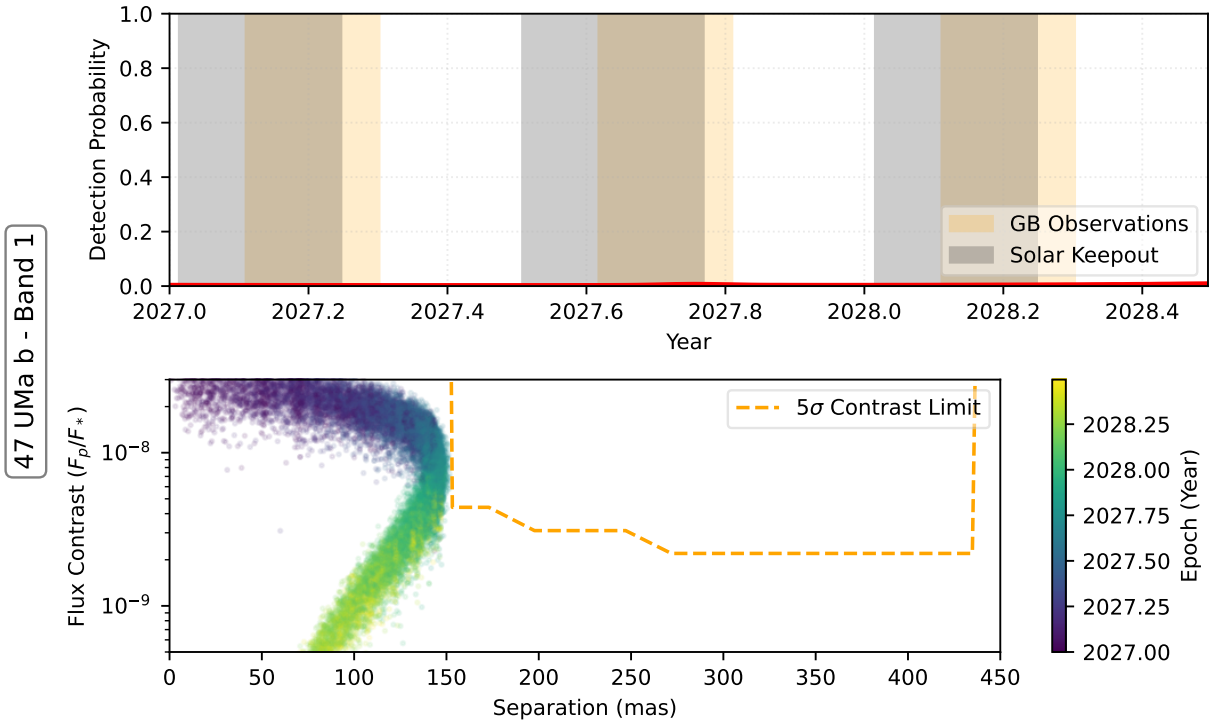

Figure 4.12: Detection probability results for 47 UMa b.

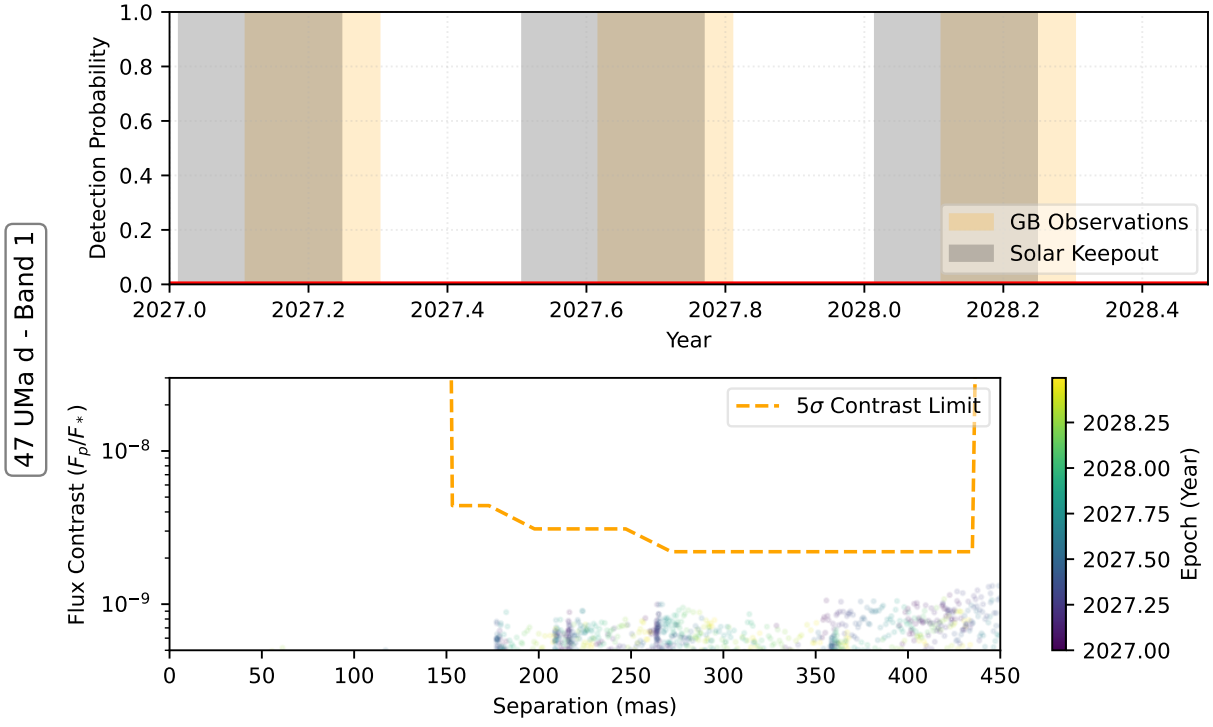

Figure 4.13: Detection probability results for 47 UMa d.

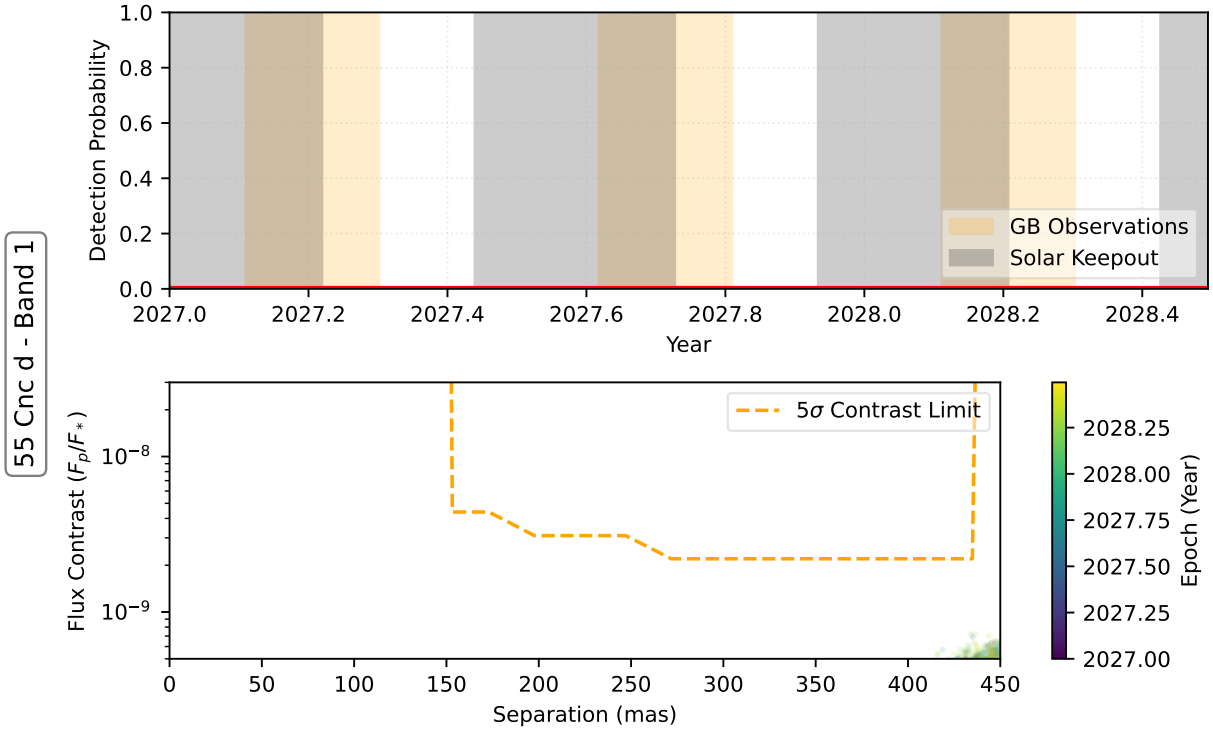

Figure 4.14: Detection probability results for 55 Cancri d.

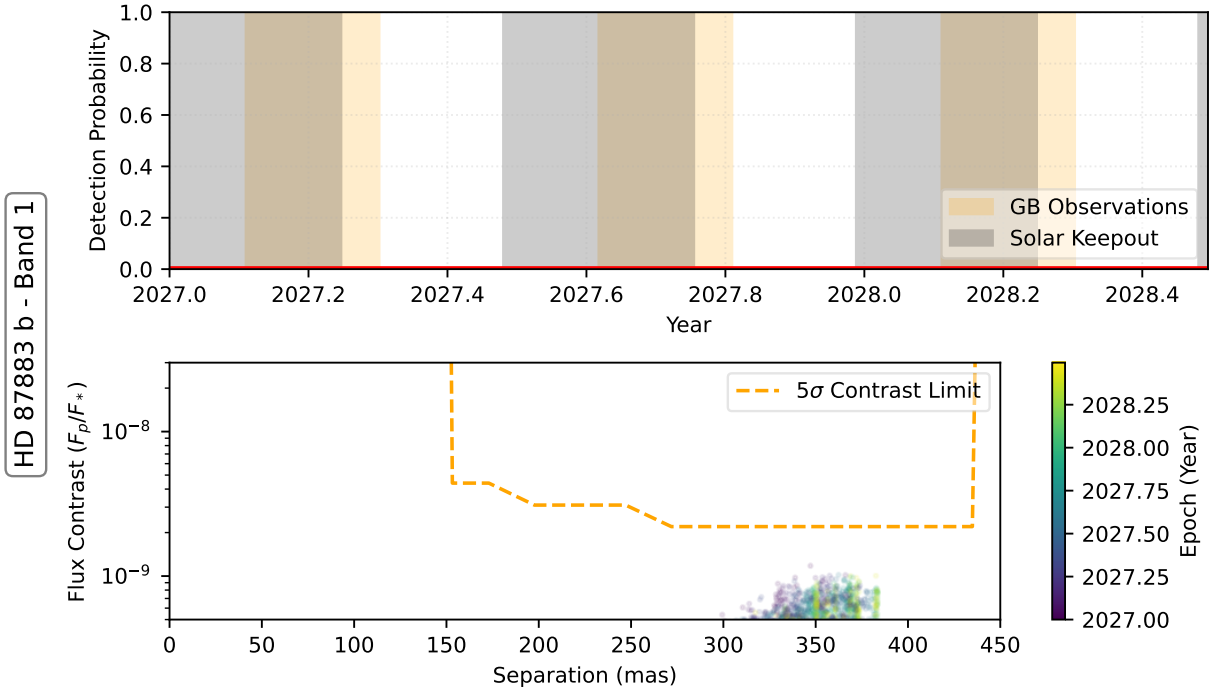

Figure 4.15: Detection probability results for HD 87883 b.

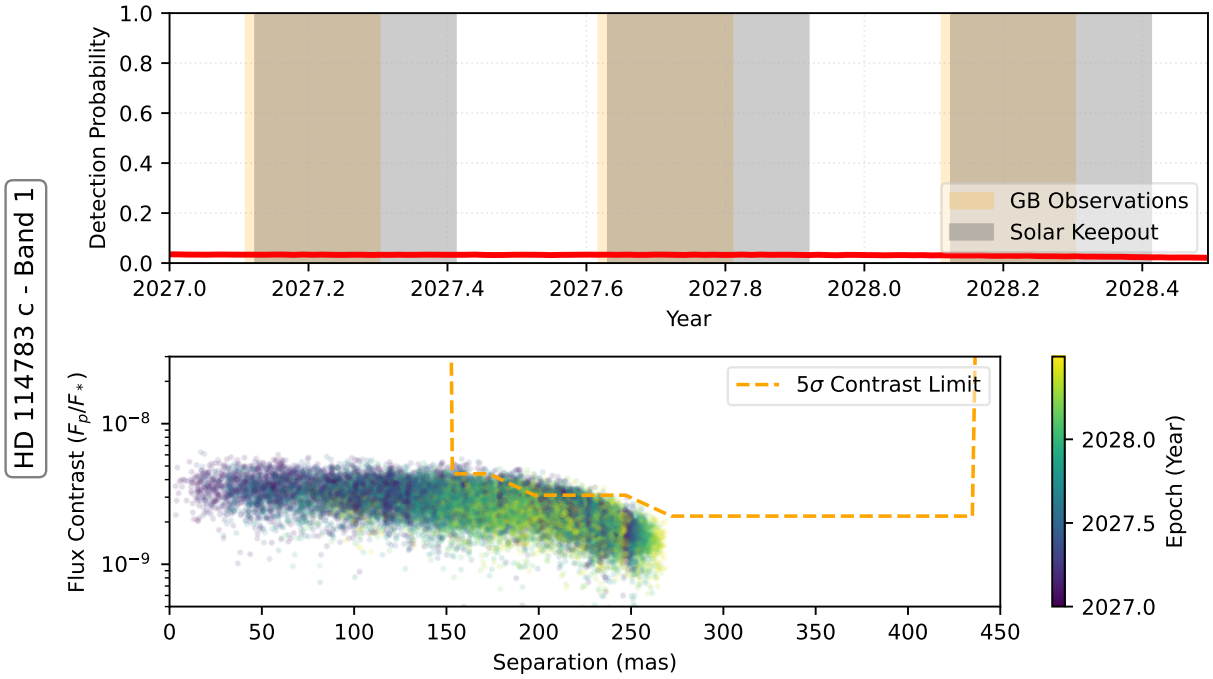

Figure 4.16: Detection probability results for HD 114783 c.

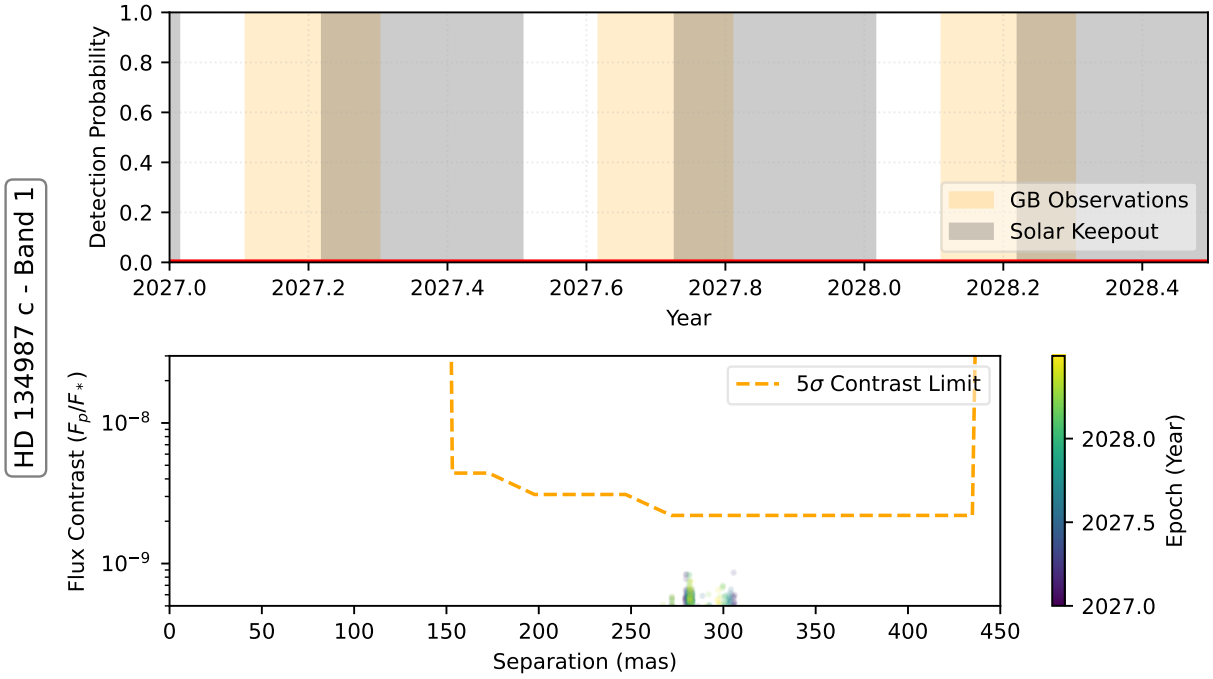

Figure 4.17: Detection probability results for HD 134987 c.

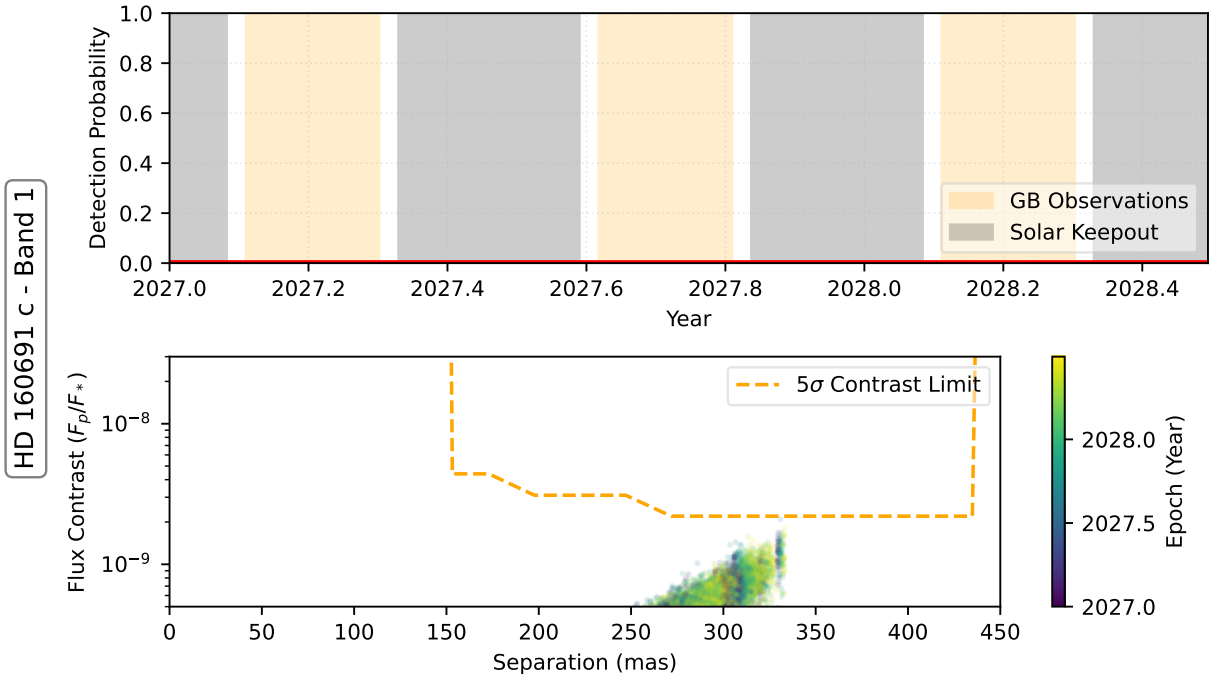

Figure 4.18: Detection probability results for HD 160691 c.

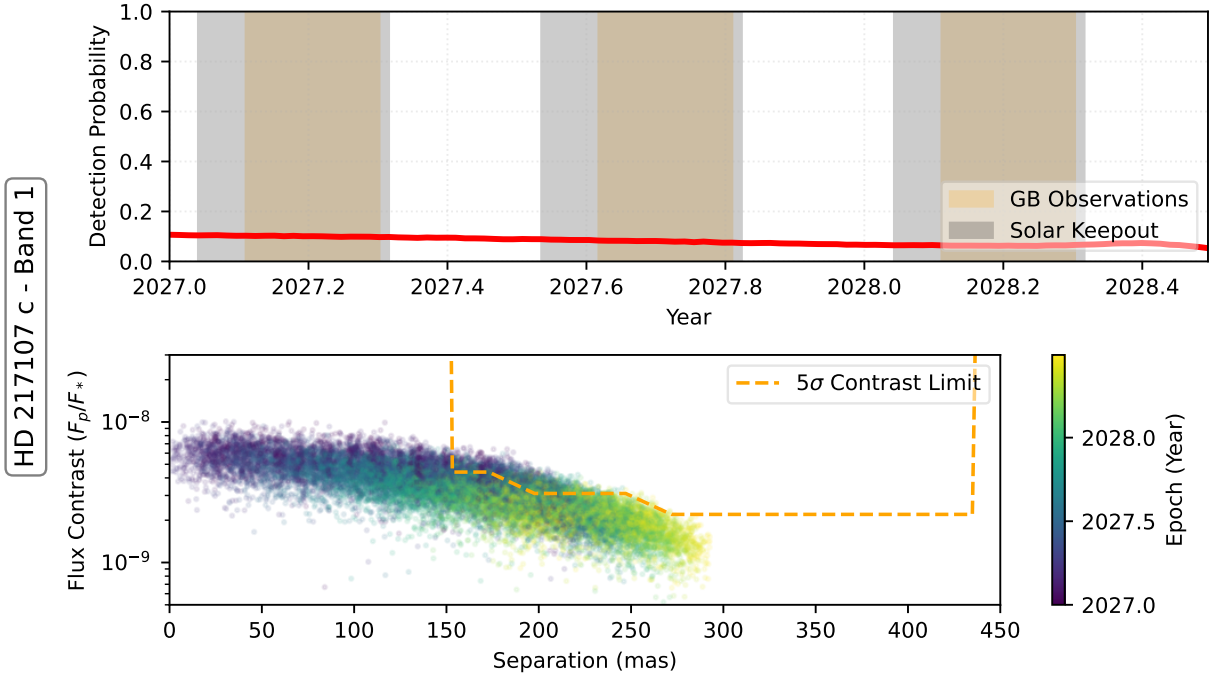

Figure 4.19: Detection probability results for HD 217107 c.

Chapter 5: Conclusions

The studies completed in this thesis have explored the capability of new and upcoming observatories to detect wide-orbit giant planets via direct imaging. As the occurrence rate of GPs is known to correlate with both orbital semimajor axis and host star mass [27, 28], observations of the exterior regions (beyond 10 au) around the lowest-mass stars (M dwarfs) provide necessary constraints on the giant planet distribution and thus insight into the dominant formation mechanisms. Additionally, the atmospheric properties of GPs change as they cool over Myr to Gyr timescales, such that observations of both young self-luminous planets and mature reflected-light planets are needed to constrain atmospheric evolution models [26].

In Chapter 2 I presented the results of a JWST NIRCam Cycle 1 coronagraphic survey of nine nearby, young M dwarfs (GTO 1184, PI Schlieder). We observed each system at $3-5$ μm wavelengths and achieved sensitivity to planets with Saturn-like masses and semimajor axes, allowing us to place the first occurrence rate limits on wide-orbit sub-Jupiter-mass exoplanets. We found the frequency of planets with masses $0.3-1.0$ M_{Jup} and semimajor axes $10-200$ au of to be < 0.10 and < 0.16 objects per star with 1- and 3-σ confidence respectively, which is in agreement with the low rates of wide-orbit GPs expected for low mass host stars in both the core accretion and gravitational instability scenario [16, 22]. While the low sample size of the survey presented in this chapter render the occurrence rate limits necessarily loose, GTO 1184 has

provided the foundation for ongoing large-scale, self-referenced surveys with sub-Jupiter-mass sensitivity including GO 4050/5835 (PI Carter), GO 6005 (PI Biller), GO 6122 (PI Bowens-Ruben), and GO 8826 (PI Lawson). In addition, we detected debris disks around the M dwarfs AU Microscopii and Fomalhaut C. These detections are detailed in Lawson et al. (2023) [137] and Lawson et al. (2024) [138], to which I contributed as a co-author.

GTO 1184 also revealed a marginally significant exoplanet candidate source (P1) in the vicinity of the M dwarf 2M J0944, which we investigated further in Chapter 3. I led a follow-up JWST observation program (GO 3840, PI Bogat) to re-observe 2M J0944 with a longer integration time and with simultaneous F200W imaging, in which P1 was not redetected. This outcome, in combination with a reanalysis of the original data from GTO 1184, suggested that the original signal reported in Chapter 2 was likely not astrophysical, but was rather a high magnitude noise speckle or artifact amplified by the data reduction pipeline at the time. We did however re-detect two extended sources (one of which had magnitude similar to P1 in the F444W filter) and we demonstrated via astrometric and photometric analysis that they are likely background galaxies. Finally, we achieved deep contrast limits in the F200W filter of 2.51×10^{-6} at $1''$ and 6.47×10^{-7} beyond $3''$. This observing program highlighted the extreme sensitivity of NIRCam to faint objects, as well as the perils of investigating low-SNR sources in direct-imaging data.

Finally, in Chapter 4 I explored the feasibility of observing mature (age > 1 Gyr) giant planets in reflected, visible light with the Roman Coronagraph. In this study, we adopted a short list of giant exoplanets discovered via radial velocity measurements, propagated a distribution of best-fit orbits over the primary mission of Roman, and generated quantitative predictions for the detection probability of each potential target planet as a function of time. This analysis predicted the giant planet upsilon Andromedae d to be the most detectable planet with the Roman

Coronagraph (assuming a Lambertian phase curve, geometric albedo of 0.465 ± 0.1, and an optimistic instrument performance), provided a framework for observation scheduling with the Roman Coronagraph, and allowed the CPP to produce initial observation plans for reflected light imaging.

5.1 Collaborative Contributions to Space-Based Direct Imaging

In concert with the particular studies that I led, as described previously in this thesis, I have made contributions to the direct imaging community in the form of collaborations on large ongoing JWST imaging surveys as well as open source software development for both JWST and Roman coronagraphy.

I am actively participating as a co-investigator in several ongoing JWST programs (GO 6005, PI Biller; GO 4050 & 5835, PI Carter; and GO 7651, PI Kammerer) which will observe a total of 225 target stars and enable demographic studies analogous to Vigan et al. (2021) [31]. As part of this work I have become a contributor to `spaceKLIP`, the open-source python package for JWST coronagraphic data reduction which implements the Karhunen-Loève Image Processing (KLIP) algorithm to subtract the stellar PSF. In particular, I added a module to manage a large library of stellar PSF references and improved the tracking of star-coronagraph alignment offsets, which is critical for reducing large, self-referenced survey datasets.

I also formally support the Roman Coronagraph as part of the `corgiDRP` development team. I have led the development of several key modules of the data reduction pipeline, including the steps which perform PSF subtraction via an implementation of pyKLIP, and which calibrate the flux throughput of the PSF subtraction algorithm via the injection and recovery of synthetic

off-axis PSFs.

5.2 Future Work

Fundamentally, my research goals are centered on understanding the formation of giant exoplanets. I approach this problem by searching for new benchmark objects and constraining planet occurrence rates via direct imaging surveys, and thus I am particularly interested in improving high-contrast imaging techniques and developing next generation instruments.

My immediate future goal, as part of a postdoctoral research contract with the Laboratoire d'Astrophysique de Marseille, is to facilitate the success of the Roman Coronagraph by continuing to support the baseline Hybrid Lyot Coronagraph (HLC) imaging mode. I will build on my foundational work with the CPP to improve the quality of PSF subtraction (and thus the final sensitivity of the observations) as well as the accuracy of photometric and astrometric retrieval. The `corgiDRP` pipeline currently uses an implementation of KLIP to perform PSF subtraction, assuming a single reference star PSF sampled immediately before and after the science target. Recent JWST observations have shown the efficacy of reducing data with simulated PSF references [246], and the ESCAPE team under the guidance of Dr. Élodie Choquet is exploring the application of high-order dithering strategies for reference differential imaging (RDI). In collaboration with the ESCAPE team, I plan to explore the effect of augmenting traditional RDI PSF observations with a library of simulated PSF images which contain the effects of high-order dithering. To accomplish this, I would facilitate the integration of the advanced Roman Coronagraph PSF simulator CAPyBARA [247] with the CPP simulation and data reduction environment and then optimize the performance of `corgiDRP` on the set of simulated data.

My work towards prioritizing particular systems for follow-up observation with the Roman Coronagraph has focused on propagating the current orbital constraints achieved with RV monitoring. I intend to improve on the current predictions by integrating astrometric constraints from the Hipparcos-Gaia Catalog of Accelerations [228]. I will then update the predictions for the time-resolved detection probability of each planet to provide observation planning guidance with the maximum amount of a priori information. I plan to use the resulting orbit fits to assess the precision of mass measurements possible for each of the planets found to be detectable with the Roman Coronagraph.

I will also continue to support JWST observations through the ongoing survey collaborations mentioned previously in order to further constrain the occurrence of wide orbit, low-mass giant planets around a broad range of host star masses. M dwarfs were chosen as the initial targets for sub-Jupiter surveys, as they provide the most intrinsically favorable environment to achieve deep mass sensitivity. However, understanding the correlation of wide-orbit GP occurrence with host star mass would provide further key insights into the processes that govern planet formation and evolution, especially if it differs from that of the inner planets.

As we continue to learn the intricacies of false-positive vetting, companion astrometry prediction, and advanced post-processing techniques with JWST data, I intend to implement emergent direct imaging strategies within the Roman Coronagraph mission. Such strategies will feed forward to the Habitable Worlds Observatory, inching us closer to the goal of directly imaging an Earth-like planet orbiting a Sun-like star.

Appendix A: Facilities and Software Used in this Thesis

A.1 Facilities

1. JWST Near-InfraRed Camera (NIRCam) [70]

2. Barbara A. Mikulski Archive for Space Telescopes (JWST GO 1184, JWST GO 3840)

A.2 Software

1. `astropy` [248]

2. `astroquery` [249]

3. `backtracks` [202]

4. `jwst` [148]

5. `matplotlib` [250]

6. `numpy` [251]

7. `orbitize` [252]

8. `pandas` [253, 254]

9. `photutils` [255]

10. `pyKLIP` [150]

11. `radvel` [229]

12. `roman_pointing` [GitHub Link]

13. `roman_table` [GitHub Link]

14. `scipy` [256]

15. `skimage` [257]

16. `spaceKLIP` [149]

17. `STPSF` [146, 200]

Bibliography

[1] Ellis Bogat, Joshua E. Schlieder, Kellen D. Lawson, Yiting Li, Jarron M. Leisenring, Michael R. Meyer, William Balmer, Thomas Barclay, Charles A. Beichman, Geoffrey Bryden, Per Calissendorff, Aarynn L. Carter, Matthew De Furio, Julien H. Girard, Thomas P. Greene, Tyler D. Groff, Jens Kammerer, Jorge Llop-Sayson, Michael W. McElwain, Marcia J. Rieke, and Marie Ygouf. Probing the outskirts of m dwarf planetary systems with a cycle 1 jwst nircam coronagraphy survey. *The Astronomical Journal*, 170(4):225, sep 2025.

[2] A. Wolszczan and D. A. Frail. A planetary system around the millisecond pulsar PSR1257 + 12. *Nature*, 355(6356):145–147, January 1992.

[3] Michel Mayor and Didier Queloz. A Jupiter-mass companion to a solar-type star. *Nature*, 378(6555):355–359, November 1995.

[4] W. P. Hirst. Theories of the Origin of the Solar System. *Monthly Notes of the Astronomical Society of South Africa*, 5:10, January 1946.

[5] Wilbur K. Brown. A solar system formation model based on supernova shell fragmentation. *Icarus*, 15(1):120,IN3,123–122,IN3,134, August 1971.

[6] A. G. W. Cameron. Origin of the solar system. *ARA&A*, 26:441–472, January 1988.

[7] R. L. Akeson, X. Chen, D. Ciardi, M. Crane, J. Good, M. Harbut, E. Jackson, S. R. Kane, A. C. Laity, S. Leifer, M. Lynn, D. L. McElroy, M. Papin, P. Plavchan, S. V. Ramírez, R. Rey, K. von Braun, M. Wittman, M. Abajian, B. Ali, C. Beichman, A. Beekley, G. B. Berriman, S. Berukoff, G. Bryden, B. Chan, S. Groom, C. Lau, A. N. Payne, M. Regelson, M. Saucedo, M. Schmitz, J. Stauffer, P. Wyatt, and A. Zhang. The NASA Exoplanet Archive: Data and Tools for Exoplanet Research. *Publications of the Astronomical Society of the Pacific*, 125(930):989, July 2013.

[8] Alessandro Morbidelli and Aurélien Crida. The dynamics of jupiter and saturn in the gaseous protoplanetary disk. *Icarus*, 191(1):158–171, 2007.

[9] Konstantin Batygin and Greg Laughlin. Jupiter's decisive role in the inner solar system's early evolution. *Proceedings of the National Academy of Sciences*, 112(14):4214–4217, 2015.

[10] Kevin J. Walsh, Alessandro Morbidelli, Sean N. Raymond, David P. O'Brien, and Avi M. Mandell. A low mass for Mars from Jupiter's early gas-driven migration. *Nature*, 475(7355):206–209, July 2011.

[11] Sean N. Raymond and Alessandro Morbidelli. The Grand Tack model: a critical review. In *Complex Planetary Systems, Proceedings of the International Astronomical Union*, volume 310 of *IAU Symposium*, pages 194–203, July 2014.

[12] R. Brasser, S. Matsumura, S. Ida, S. J. Mojzsis, and S. C. Werner. Analysis of Terrestrial Planet Formation by the Grand Tack Model: System Architecture and Tack Location. *ApJ*, 821(2):75, April 2016.

[13] Matthew S. Clement, Nathan A. Kaib, Sean N. Raymond, and Kevin J. Walsh. Mars' growth stunted by an early giant planet instability. *Icarus*, 311:340–356, September 2018.

[14] W. B. Hubbard. Thermal structure of Jupiter. *ApJ*, 152:745–754, June 1968.

[15] Karl E. Haisch, Jr., Elizabeth A. Lada, and Charles J. Lada. Disk frequencies and lifetimes in young clusters. *The Astrophysical Journal*, 553(2):L153, may 2001.

[16] H. Mizuno. Formation of the Giant Planets. *Progress of Theoretical Physics*, 64(2):544–557, August 1980.

[17] James B. Pollack, Olenka Hubickyj, Peter Bodenheimer, Jack J. Lissauer, Morris Podolak, and Yuval Greenzweig. Formation of the Giant Planets by Concurrent Accretion of Solids and Gas. *Icarus*, 124(1):62–85, November 1996.

[18] Harold F. Levison, Edward Thommes, and Martin J. Duncan. Modeling the Formation of Giant Planet Cores. I. Evaluating Key Processes. *AJ*, 139(4):1297–1314, April 2010.

[19] A. Fortier, Y. Alibert, F. Carron, W. Benz, and K.-M. Dittkrist. Planet formation models: the interplay with the planetesimal disc. *A&A*, 549:A44, January 2013.

[20] Anders Johansen and Bertram Bitsch. Exploring the conditions for forming cold gas giants through planetesimal accretion. *A&A*, 631:A70, November 2019.

[21] Alexandre Emsenhuber, Christoph Mordasini, Remo Burn, Yann Alibert, Willy Benz, and Erik Asphaug. The New Generation Planetary Population Synthesis (NGPPS). II. Planetary population of solar-like stars and overview of statistical results. *A&A*, 656:A70, December 2021.

[22] A. P. Boss. Giant planet formation by gravitational instability. *Science*, 276:1836–1839, January 1997.

[23] Lucio Mayer, Thomas Quinn, James Wadsley, and Joachim Stadel. Formation of Giant Planets by Fragmentation of Protoplanetary Disks. *Science*, 298(5599):1756–1759, November 2002.

[24] Kevin C. Schlaufman. Evidence of an Upper Bound on the Masses of Planets and Its Implications for Giant Planet Formation. *ApJ*, 853(1):37, January 2018.

[25] Mark S. Marley, Jonathan J. Fortney, Olenka Hubickyj, Peter Bodenheimer, and Jack J. Lissauer. On the Luminosity of Young Jupiters. *The Astrophysical Journal*, 655(1):541–549, January 2007.

[26] Gabriel-Dominique Marleau and Andrew Cumming. Constraining the initial entropy of directly-detected exoplanets. *Monthly Notices of the Royal Astronomical Society*, 437(2):1378–1399, January 2014. arXiv:1302.1517 [astro-ph].

[27] Benjamin J. Fulton, Lee J. Rosenthal, Lea A. Hirsch, Howard Isaacson, Andrew W. Howard, Cayla M. Dedrick, Ilya A. Sherstyuk, Sarah C. Blunt, Erik A. Petigura, Heather A. Knutson, Aida Behmard, Ashley Chontos, Justin R. Crepp, Ian J. M. Crossfield, Paul A. Dalba, Debra A. Fischer, Gregory W. Henry, Stephen R. Kane, Molly Kosiarek, Geoffrey W. Marcy, Ryan A. Rubenzahl, Lauren M. Weiss, and Jason T. Wright. California Legacy Survey. II. Occurrence of Giant Planets beyond the Ice Line. *ApJS*, 255(1):14, July 2021.

[28] Rachel B. Fernandes, Gijs D. Mulders, Ilaria Pascucci, Christoph Mordasini, and Alexandre Emsenhuber. Hints for a Turnover at the Snow Line in the Giant Planet Occurrence Rate. *ApJ*, 874(1):81, March 2019.

[29] Christian Clanton and B. Scott Gaudi. Synthesizing Exoplanet Demographics: A Single Population of Long-Period Planetary Companions to M Dwarfs Consistent with Microlensing, Radial Velocity, and Direct Imaging Surveys. *The Astrophysical Journal*, 819(2):125, March 2016. arXiv:1508.04434 [astro-ph].

[30] D. Suzuki, D. P. Bennett, T. Sumi, I. A. Bond, L. A. Rogers, F. Abe, Y. Asakura, A. Bhattacharya, M. Donachie, M. Freeman, A. Fukui, Y. Hirao, Y. Itow, N. Koshimoto, M. C. A. Li, C. H. Ling, K. Masuda, Y. Matsubara, Y. Muraki, M. Nagakane, K. Onishi, H. Oyokawa, N. Rattenbury, To. Saito, A. Sharan, H. Shibai, D. J. Sullivan, P. J. Tristram, A. Yonehara, and the MOA collaboration. THE EXOPLANET MASS-RATIO FUNCTION FROM THE MOA-II SURVEY: DISCOVERY OF A BREAK AND LIKELY PEAK AT A NEPTUNE MASS. *The Astrophysical Journal*, 833(2):145, December 2016.

[31] A. Vigan, C. Fontanive, M. Meyer, B. Biller, M. Bonavita, M. Feldt, S. Desidera, G. -D. Marleau, A. Emsenhuber, R. Galicher, K. Rice, D. Forgan, C. Mordasini, R. Gratton, H. Le Coroller, A. -L. Maire, F. Cantalloube, G. Chauvin, A. Cheetham, J. Hagelberg, A. -M. Lagrange, M. Langlois, M. Bonnefoy, J. -L. Beuzit, A. Boccaletti, V. D'Orazi, P. Delorme, C. Dominik, Th Henning, M. Janson, E. Lagadec, C. Lazzoni, R. Ligi, F. Menard, D. Mesa, S. Messina, C. Moutou, A. Müller, C. Perrot, M. Samland, H. M. Schmid, T. Schmidt, E. Sissa, M. Turatto, S. Udry, A. Zurlo, L. Abe, J. Antichi, R. Asensio-Torres, A. Baruffolo, P. Baudoz, J. Baudrand, A. Bazzon, P. Blanchard, A. J. Bohn, S. Brown Sevilla, M. Carbillet, M. Carle, E. Cascone, J. Charton, R. Claudi, A. Costille, V. De Caprio, A. Delboulbé, K. Dohlen, N. Engler, D. Fantinel, P. Feautrier, T. Fusco, P. Gigan, J. H. Girard, E. Giro, D. Gisler, L. Gluck, C. Gry, N. Hubin, E. Hugot, M. Jaquet, M. Kasper, D. Le Mignant, M. Llored, F. Madec, Y. Magnard, P. Martinez, D. Maurel, O. Möller-Nilsson, D. Mouillet, T. Moulin, A. Origné, A. Pavlov, D. Perret, C. Petit, J. Pragt, P. Puget, P. Rabou, J. Ramos, E. L. Rickman, F. Rigal, S. Rochat, R. Roelfsema, G. Rousset, A. Roux, B. Salasnich, J. -F.

Sauvage, A. Sevin, C. Soenke, E. Stadler, M. Suarez, Z. Wahhaj, L. Weber, and F. Wildi. The sphere infrared survey for exoplanets (shine). iii. the demographics of young giant exoplanets below 300 au with sphere. *Astronomy and Astrophysics*, 651:1–22, July 2021. 24 pages, 14 figures, 3 tables. Accepted for publication in A&A.

[32] Brendan P. Bowler. Imaging Extrasolar Giant Planets. *Publications of the Astronomical Society of the Pacific*, 128(968):102001, October 2016. arXiv:1605.02731 [astro-ph].

[33] M. Lecar, M. Podolak, D. Sasselov, and E. Chiang. On the Location of the Snow Line in a Protoplanetary Disk. *ApJ*, 640(2):1115–1118, April 2006.

[34] Grant M. Kennedy and Scott J. Kenyon. Planet Formation around Stars of Various Masses: The Snow Line and the Frequency of Giant Planets. *ApJ*, 673(1):502–512, January 2008.

[35] N. C. Santos, G. Israelian, and M. Mayor. Spectroscopic [Fe/H] for 98 extra-solar planet-host stars. Exploring the probability of planet formation. *A&A*, 415:1153–1166, March 2004.

[36] Debra A. Fischer and Jeff Valenti. The Planet-Metallicity Correlation. *ApJ*, 622(2):1102–1117, April 2005.

[37] John J. Bochanski, Suzanne L. Hawley, Kevin R. Covey, Andrew A. West, I. Neill Reid, David A. Golimowski, and Željko Ivezić. The Luminosity and Mass Functions of Low-mass Stars in the Galactic Disk. II. The Field. *AJ*, 139(6):2679–2699, June 2010.

[38] Andrew W. Howard, Geoffrey W. Marcy, Stephen T. Bryson, Jon M. Jenkins, Jason F. Rowe, Natalie M. Batalha, William J. Borucki, David G. Koch, Edward W. Dunham, Thomas N. Gautier, III, and et al. Planet Occurrence within 0.25 AU of Solar-type Stars from Kepler. *ApJS*, 201(2):15, August 2012.

[39] Gijs D. Mulders, Ilaria Pascucci, and Dániel Apai. A Stellar-mass-dependent Drop in Planet Occurrence Rates. *ApJ*, 798(2):112, January 2015.

[40] Jia-Yi Yang, Ji-Wei Xie, and Ji-Lin Zhou. Occurrence and Architecture of Kepler Planetary Systems as Functions of Stellar Mass and Effective Temperature. *AJ*, 159(4):164, April 2020.

[41] Danley C. Hsu, Eric B. Ford, and Ryan Terrien. Occurrence rates of planets orbiting M Stars: applying ABC to Kepler DR25, Gaia DR2, and 2MASS data. *MNRAS*, 498(2):2249–2262, October 2020.

[42] S. Sabotta, M. Schlecker, P. Chaturvedi, E. W. Guenther, I. Muñoz Rodríguez, J. C. Muñoz Sánchez, J. A. Caballero, Y. Shan, S. Reffert, I. Ribas, and et al. The CARMENES search for exoplanets around M dwarfs. Planet occurrence rates from a subsample of 71 stars. *A&A*, 653:A114, September 2021.

[43] A. Kaminski, S. Sabotta, J. Kemmer, P. Chaturvedi, R. Burn, J. C. Morales, J. A. Caballero, I. Ribas, A. Reiners, A. Quirrenbach, and et al. The CARMENES search for exoplanets around M dwarfs: Occurrence rates of Earth-like planets around very low-mass stars. *A&A*, 696:A101, April 2025.

[44] L. Mignon, X. Delfosse, N. Meunier, G. Chaverot, R. Burn, X. Bonfils, F. Bouchy, N. Astudillo-Defru, G. Lo Curto, G. Gaisne, S. Udry, T. Forveille, D. Segransan, C. Lovis, N. C. Santos, and M. Mayor. Radial velocity homogeneous analysis of M dwarfs observed with HARPS. II. Detection limits and planetary occurrence statistics. *arXiv e-prints*, page arXiv:2502.06553, February 2025.

[45] Daniel Foreman-Mackey, David W. Hogg, and Timothy D. Morton. EXOPLANET POPULATION INFERENCE AND THE ABUNDANCE OF EARTH ANALOGS FROM NOISY, INCOMPLETE CATALOGS. *The Astrophysical Journal*, 795(1):64, October 2014.

[46] Vladislava Ananyeva, Anastasiia Ivanova, Inna Shashkova, Oleg Yakovlev, Alexander Tavrov, Oleg Korablev, and Jean-Loup Bertaux. Exoplanets Catalogue Analysis: The Distribution of Exoplanets at FGK Stars by Mass and Orbital Period Accounting for the Observational Selection in the Radial Velocity Method. *Atmosphere*, 14(2):353, February 2023.

[47] Michael Perryman, Joel Hartman, Gáspár Á. Bakos, and Lennart Lindegren. Astrometric Exoplanet Detection with Gaia. *ApJ*, 797(1):14, December 2014.

[48] Aparna Bhattacharya, Rachel Akeson, Jay Anderson, Etienne Bachelet, Jean-Phillipe Beaulieu, Andrea Bellini, David P. Bennett, Alan Boss, Valerio Bozza, Geoffrey Bryden, and et al. Masses and Distances of Planetary Microlens Systems with High Angular Resolution Imaging. *BAAS*, 51(3):520, May 2019.

[49] Bruce Macintosh, James R. Graham, Patrick Ingraham, Quinn Konopacky, Christian Marois, Marshall Perrin, Lisa Poyneer, Brian Bauman, Travis Barman, Adam S. Burrows, Andrew Cardwell, Jeffrey Chilcote, Robert J. De Rosa, Daren Dillon, Rene Doyon, Jennifer Dunn, Darren Erikson, Michael P. Fitzgerald, Donald Gavel, Stephen Goodsell, Markus Hartung, Pascale Hibon, Paul Kalas, James Larkin, Jerome Maire, Franck Marchis, Mark S. Marley, James McBride, Max Millar-Blanchaer, Katie Morzinski, Andrew Norton, B. R. Oppenheimer, David Palmer, Jennifer Patience, Laurent Pueyo, Fredrik Rantakyro, Naru Sadakuni, Leslie Saddlemyer, Dmitry Savransky, Andrew Serio, Remi Soummer, Anand Sivaramakrishnan, Inseok Song, Sandrine Thomas, J. Kent Wallace, Sloane Wiktorowicz, and Schuyler Wolff. First light of the Gemini Planet Imager. *Proceedings of the National Academy of Science*, 111(35):12661–12666, September 2014.

[50] Aarynn L. Carter, Sasha Hinkley, Jens Kammerer, Andrew Skemer, Beth A. Biller, Jarron M. Leisenring, Maxwell A. Millar-Blanchaer, Simon Petrus, Jordan M. Stone, Kimberly Ward-Duong, Jason J. Wang, Julien H. Girard, Dean C. Hines, Marshall D. Perrin, Laurent Pueyo, William O. Balmer, Mariangela Bonavita, Mickael Bonnefoy, Gael Chauvin, Elodie Choquet, Valentin Christiaens, Camilla Danielski, Grant M. Kennedy, Elisabeth C. Matthews, Brittany E. Miles, Polychronis Patapis, Shrishmoy Ray, Emily Rickman, Steph Sallum, Karl R. Stapelfeldt, Niall Whiteford, Yifan Zhou, Olivier Absil, Anthony Boccaletti, Mark Booth, Brendan P. Bowler, Christine H. Chen, Thayne Currie, Jonathan J. Fortney, Carol A. Grady, Alexandra Z. Greebaum, Thomas Henning, Kielan K. W. Hoch, Markus Janson, Paul Kalas, Matthew A. Kenworthy, Pierre

Kervella, Adam L. Kraus, Pierre-Olivier Lagage, Michael C. Liu, Bruce Macintosh, Sebastian Marino, Mark S. Marley, Christian Marois, Brenda C. Matthews, Dimitri Mawet, Michael W. McElwain, Stanimir Metchev, Michael R. Meyer, Paul Molliere, Sarah E. Moran, Caroline V. Morley, Sagnick Mukherjee, Eric Pantin, Andreas Quirrenbach, Isabel Rebollido, Bin B. Ren, Glenn Schneider, Malavika Vasist, Kadin Worthen, Mark C. Wyatt, Zackery W. Briesemeister, Marta L. Bryan, Per Calissendorff, Faustine Cantalloube, Gabriele Cugno, Matthew De Furio, Trent J. Dupuy, Samuel M. Factor, Jacqueline K. Faherty, Michael P. Fitzgerald, Kyle Franson, Eileen C. Gonzales, Callie E. Hood, Alex R. Howe, Masayuki Kuzuhara, Anne-Marie Lagrange, Kellen Lawson, Cecilia Lazzoni, Ben W. P. Lew, Pengyu Liu, Jorge Llop-Sayson, James P. Lloyd, Raquel A. Martinez, Johan Mazoyer, Paulina Palma-Bifani, Sascha P. Quanz, Jea Adams Redai, Matthias Samland, Joshua E. Schlieder, Motohide Tamura, Xianyu Tan, Taichi Uyama, Arthur Vigan, Johanna M. Vos, Kevin Wagner, Schuyler G. Wolff, Marie Ygouf, Xi Zhang, Keming Zhang, and Zhoujian Zhang. The JWST Early Release Science Program for Direct Observations of Exoplanetary Systems I: High-contrast Imaging of the Exoplanet HIP 65426 b from 2 to 16 μm. *ApJL*, 951(1):L20, July 2023.

[51] Yifan Zhou, Brendan P. Bowler, Kevin R. Wagner, Glenn Schneider, Dániel Apai, Adam L. Kraus, Laird M. Close, Gregory J. Herczeg, and Min Fang. Hubble Space Telescope UV and Hα Measurements of the Accretion Excess Emission from the Young Giant Planet PDS 70 b. *AJ*, 161(5):244, May 2021.

[52] Direct Imaging & Spectroscopy of Extrasolar Planets. Astronomical Society of the Pacific, 2022.

[53] Charles A. Beichman, John Krist, John T. Trauger, Tom Greene, Ben Oppenheimer, Anand Sivaramakrishnan, René Doyon, Anthony Boccaletti, Travis S. Barman, and Marcia Rieke. Imaging Young Giant Planets From Ground and Space. *Publications of the Astronomical Society of the Pacific*, 122(888):162–200, February 2010.

[54] A. Grandjean, A.-M. Lagrange, M. Keppler, N. Meunier, L. Mignon, S. Borgniet, G. Chauvin, S. Desidera, F. Galland, S. Messina, and et al. A HARPS RV search for planets around young nearby stars. *A&A*, 633:A44, January 2020.

[55] E. Palle, M. Oshagh, N. Casasayas-Barris, T. Hirano, M. Stangret, R. Luque, J. Strachan, E. Gaidos, G. Anglada-Escude, P. Plavchan, and et al. Transmission spectroscopy and Rossiter-McLaughlin measurements of the young Neptune orbiting AU Mic. *A&A*, 643:A25, November 2020.

[56] A. E. Roy and D. Clarke. *Astronomy: principles and practice*. Institute of Physics Pub, Bristol ; Philadelphia, 4th ed edition, 2003.

[57] R. Hanel, B. Conrath, L. Herath, V. Kunde, and J. Pirraglia. Albedo, internal heat, and energy balance of Jupiter: preliminary results of the voyager infrared investigation. *J. Geophys. Res.*, 86(A10):8705–8712, September 1981.

[58] Esther F. Linder, Christoph Mordasini, Paul Mollière, Gabriel-Dominique Marleau, Matej Malik, Sascha P. Quanz, and Michael R. Meyer. Evolutionary models of cold and low-mass

planets: Cooling curves, magnitudes, and detectability, March 2019. arXiv:1812.02027 [astro-ph].

[59] David Berardo, Andrew Cumming, and Gabriel-Dominique Marleau. The Evolution of Gas Giant Entropy During Formation by Runaway Accretion. *ApJ*, 834(2):149, January 2017.

[60] Subrahmanyan Chandrasekhar. *Radiative transfer*. New York: Dover, 1960.

[61] Mamadou N'Diaye, Elodie Choquet, Sylvain Egron, Laurent Pueyo, Lucie Leboulleux, Olivier Levecq, Marshall D. Perrin, Erin Elliot, J. Kent Wallace, Emmanuel Hugot, Michel Marcos, Marc Ferrari, Chris A. Long, Rachel Anderson, Audrey DiFelice, and Rémi Soummer. High-contrast Imager for Complex Aperture Telescopes (HICAT): II. Design overview and first light results. page 914327, Montréal, Quebec, Canada, August 2014.

[62] Meiji M. Nguyen, Bryony F. Nickson, Emiel H. Por, Remi Soummer, John G. Hagopian, Bruce Macintosh, Jeffrey Chilcote, Laurent Pueyo, Marshall Perrin, and Quinn Konopacky. GPI 2.0: Optical Designs for the Upgrade of the Gemini Planet Imager Coronagraphic system, September 2022. arXiv:2209.12955 [astro-ph].

[63] Bernard Lyot. Étude de la couronne solaire en dehors des éclipses. Avec 16 figures dans le texte. *ZA*, 5:73, January 1932.

[64] Erik M. Johansson, Marcos A. van Dam, Paul J. Stomski, James M. Bell, Jason C. Chin, Roger C. Sumner, Peter L. Wizinowich, Roberto Biasi, Mario Andrighettoni, and Dietrich Pescoller. Upgrading the Keck AO wavefront controllers. In Norbert Hubin, Claire E. Max, and Peter L. Wizinowich, editors, *Adaptive Optics Systems*, volume 7015 of *Society of Photo-Optical Instrumentation Engineers (SPIE) Conference Series*, page 70153E, July 2008.

[65] Christian Marois, David Lafreniere, Rene Doyon, Bruce Macintosh, and Daniel Nadeau. Angular Differential Imaging: A Powerful High-Contrast Imaging Technique. *The Astrophysical Journal*, 641(1):556–564, April 2006.

[66] David Lafrenière, Christian Marois, René Doyon, and Travis Barman. HST/NICMOS detection of HR 8799 b in 1998. *The Astrophysical Journal*, 694(2):L148–L152, April 2009. arXiv:0902.3247 [astro-ph].

[67] Rémi Soummer, Laurent Pueyo, and James Larkin. Detection and Characterization of Exoplanets and Disks Using Projections on Karhunen-Loève Eigenimages. *The Astrophysical Journal*, 755(2):L28, August 2012.

[68] Benjamin L. Gerard and Christian Marois. Planet detection down to a few lambda/D: an RSDI/TLOCI approach to PSF subtraction. In *Adaptive Optics Systems V*, volume 9909, pages 1544–1556. SPIE, July 2016.

[69] David Lafreniere, Christian Marois, Rene Doyon, Daniel Nadeau, and Etienne Artigau. A new algorithm for point spread function subtraction in high-contrast imaging: a demonstration with angular differential imaging. *The Astrophysical Journal*, 660(1):770–780, May 2007. arXiv:astro-ph/0702697.

[70] Marcia J. Rieke, Douglas M. Kelly, Karl Misselt, John Stansberry, Martha Boyer, Thomas Beatty, Eiichi Egami, Michael Florian, Thomas P. Greene, Kevin Hainline, Jarron Leisenring, Thomas Roellig, Everett Schlawin, Fengwu Sun, Lee Tinnin, Christina C. Williams, Christopher N. A. Willmer, Debra Wilson, Charles R. Clark, Scott Rohrbach, Brian Brooks, Alicia Canipe, Matteo Correnti, Audrey DiFelice, Mario Gennaro, Julian Girard, George Hartig, Bryan Hilbert, Anton M. Koekemoer, Nikolay K. Nikolov, Norbert Pirzkal, Armin Rest, Massimo Robberto, Ben Sunnquist, Randal Telfer, Chi Rai Wu, Malcolm Ferry, Dan Lewis, Stefi Baum, Charles Beichman, René Doyon, Alan Dressler, Daniel J. Eisenstein, Laura Ferrarese, Klaus Hodapp, Scott Horner, Daniel T. Jaffe, Doug Johnstone, John Krist, Peter Martin, Donald W. McCarthy, Michael Meyer, George H. Rieke, John Trauger, and Erick T. Young. Performance of NIRCam on JWST in Flight. *Publications of the Astronomical Society of the Pacific*, 135(1044):028001, February 2023.

[71] Space Telescope Science Institute. JWST User Documentation, 2023.

[72] Aarynn L. Carter, Andrew J. I. Skemer, Camilla Danielski, Jarron Leisenring, Jason J. Wang, Kyle Van Gorkom, Brian York, Jea Adams, Beth Biller, Julien H. Girard, Sasha Hinkley, Bryony Nickson, Marshall Perrin, and Laurent Pueyo. Simulating JWST high contrast observations with PanCAKE. In *Techniques and Instrumentation for Detection of Exoplanets X*, volume 11823, pages 162–178. SPIE, September 2021.

[73] Julien H. Girard, Jarron Leisenring, Jens Kammerer, Mario Gennaro, Marcia Rieke, John Stansberry, Armin Rest, Eiichi Egami, Ben Sunnquist, Martha Boyer, Alicia Canipe, Matteo Correnti, Bryan Hilbert, Marshall D. Perrin, Laurent Pueyo, Remi Soummer, Marsha Allen, Howard Bushouse, Jonathan Aguilar, Brian Brooks, Dan Coe, Audrey DiFelice, David Golimowski, George Hartig, Dean C. Hines, Anton Koekemoer, Bryony Nickson, Nikolay Nikolov, Vera Kozhurina-Platais, Nor Pirzkal, Massimo Robberto, Anand Sivaramakrishnan, Sangmo Tony Sohn, Randal Telfer, Chi Rai Wu, Thomas Beatty, Michael Florian, Kevin Hainline, Doug Kelly, Karl Misselt, Everett Schlawin, Fengwu Sun, Christina Williams, Christopher Willmer, Christopher Stark, Marie Ygouf, Aarynn Carter, Charles Beichman, Thomas P. Greene, Thomas Roellig, John Krist, Jéa Adams Redai, Jason Wang, Charles R. Clark, Dan Lewis, and Malcolm Ferry. JWST/NIRCam Coronagraphy: Commissioning and First On-Sky Results, August 2022. arXiv:2208.00998 [astro-ph, physics:physics].

[74] N. Jeremy Kasdin, Vanessa P. Bailey, Bertrand Mennesson, Robert T. Zellem, Marie Ygouf, Jason Rhodes, Thomas Luchik, Feng Zhao, A. J. Eldorado Riggs, Byoung-Joon Seo, and et al. The Nancy Grace Roman Space Telescope Coronagraph Instrument (CGI) technology demonstration. In Makenzie Lystrup and Marshall D. Perrin, editors, *Space Telescopes and Instrumentation 2020: Optical, Infrared, and Millimeter Wave*, volume 11443 of *Society of Photo-Optical Instrumentation Engineers (SPIE) Conference Series*, page 114431U, December 2020.

[75] John W. Hardy and Laird Thompson. Adaptive Optics for Astronomical Telescopes. *Physics Today*, 53(4):69, April 2000.

[76] Vanessa P. Bailey, Eduardo Bendek, Brian Monacelli, Caleb Baker, Gasia Bedrosian, Eric Cady, Ewan S. Douglas, Tyler Groff, Sergi R. Hildebrandt, N. Jeremy Kasdin, and et al. Nancy Grace Roman Space Telescope coronagraph instrument overview and status. In *Society of Photo-Optical Instrumentation Engineers (SPIE) Conference Series*, volume 12680 of *Society of Photo-Optical Instrumentation Engineers (SPIE) Conference Series*, page 126800T, October 2023.

[77] Nikku Madhusudhan and Adam Burrows. Analytic Models for Albedos, Phase Curves, and Polarization of Reflected Light from Exoplanets. *ApJ*, 747(1):25, March 2012.

[78] Dimitri Mawet, Lea Hirsch, Eve J. Lee, Jean-Baptiste Ruffio, Michael Bottom, Benjamin J. Fulton, Olivier Absil, Charles Beichman, Brendan Bowler, Marta Bryan, and et al. Deep Exploration of eps Eridani with Keck Ms-band Vortex Coronagraphy and Radial Velocities: Mass and Orbital Parameters of the Giant Exoplanet. *AJ*, 157(1):33, January 2019.

[79] A.-L. Maire, A. Leclerc, W. O. Balmer, S. Desidera, S. Lacour, V. D'Orazi, M. Samland, M. Langlois, E. Matthews, C. Babusiaux, and et al. Direct imaging and dynamical mass of a benchmark T-type brown dwarf companion to HD 167665. *A&A*, 691:A263, November 2024.

[80] Brianna Lacy and Adam Burrows. Prospects for Directly Imaging Young Giant Planets at Optical Wavelengths. *The Astrophysical Journal*, 892(2):151, April 2020.

[81] Medicine National Academies of Sciences and Engineering. *Pathways to Discovery in Astronomy and Astrophysics for the 2020s*. 2021.

[82] Corey Spohn, Dmitry Savransky, and Rhonda Morgan. Scheduling direct imaging observations based on radial velocity orbital fits: Best practices for translating orbits and failure modes. *The Astronomical Journal*, 163(4):163, mar 2022.

[83] B. Scott Gaudi. Microlensing Surveys for Exoplanets. *ARA&A*, 50:411–453, September 2012.

[84] Tiffany Meshkat, Dimitri Mawet, Marta L. Bryan, Sasha Hinkley, Brendan P. Bowler, Karl R. Stapelfeldt, Konstantin Batygin, Deborah Padgett, Farisa Y. Morales, Eugene Serabyn, Valentin Christiaens, Timothy D. Brandt, and Zahed Wahhaj. A Direct Imaging Survey of Spitzer-detected Debris Disks: Occurrence of Giant Planets in Dusty Systems*. *The Astronomical Journal*, 154(6):245, November 2017.

[85] Gilles Chabrier, Jérémy Leconte, and Isabelle Baraffe. Understanding exoplanet formation, structure and evolution in 2010. *Proceedings of the International Astronomical Union*, 6(S276):171–180, October 2010.

[86] David S. Spiegel and Adam Burrows. Spectral and Photometric Diagnostics of Giant Planet Formation Scenarios. *ApJ*, 745(2):174, February 2012.

[87] James G Rogers and James E Owen. Unveiling the planet population at birth. *Monthly Notices of the Royal Astronomical Society*, 503(1):1526–1542, March 2021.

[88] Todd J. Henry and Wei-Chun Jao. The Character of M Dwarfs. *ARA&A*, 62(1):593–633, September 2024.

[89] Courtney D. Dressing and David Charbonneau. The Occurrence of Potentially Habitable Planets Orbiting M Dwarfs Estimated from the Full Kepler Dataset and an Empirical Measurement of the Detection Sensitivity. *ApJ*, 807(1):45, July 2015.

[90] Kevin K. Hardegree-Ullman, Michael C. Cushing, Philip S. Muirhead, and Jessie L. Christiansen. Kepler Planet Occurrence Rates for Mid-type M Dwarfs as a Function of Spectral Type. *AJ*, 158(2):75, August 2019.

[91] X. Bonfils, X. Delfosse, S. Udry, T. Forveille, M. Mayor, C. Perrier, F. Bouchy, M. Gillon, C. Lovis, F. Pepe, D. Queloz, N. C. Santos, D. Ségransan, and J. L. Bertaux. The HARPS search for southern extra-solar planets. XXXI. The M-dwarf sample. *A&A*, 549:A109, January 2013.

[92] Benjamin T. Montet, Justin R. Crepp, John Asher Johnson, Andrew W. Howard, and Geoffrey W. Marcy. The TRENDS High-contrast Imaging Survey. IV. The Occurrence Rate of Giant Planets around M Dwarfs. *ApJ*, 781(1):28, January 2014.

[93] Christian Clanton and B. Scott Gaudi. Synthesizing Exoplanet Demographics: A Single Population of Long-period Planetary Companions to M Dwarfs Consistent with Microlensing, Radial Velocity, and Direct Imaging Surveys. *ApJ*, 819(2):125, March 2016.

[94] A. Cassan, D. Kubas, J. P. Beaulieu, M. Dominik, K. Horne, J. Greenhill, J. Wambsganss, J. Menzies, A. Williams, U. G. Jørgensen, A. Udalski, D. P. Bennett, M. D. Albrow, V. Batista, S. Brillant, J. A. R. Caldwell, A. Cole, Ch. Coutures, K. H. Cook, S. Dieters, D. Dominis Prester, J. Donatowicz, P. Fouqué, K. Hill, N. Kains, S. Kane, J. B. Marquette, R. Martin, K. R. Pollard, K. C. Sahu, C. Vinter, D. Warren, B. Watson, M. Zub, T. Sumi, M. K. Szymański, M. Kubiak, R. Poleski, I. Soszynski, K. Ulaczyk, G. Pietrzyński, and Ł. Wyrzykowski. One or more bound planets per Milky Way star from microlensing observations. *Nature*, 481(7380):167–169, January 2012.

[95] P. Mroz and R. Poleski. Exoplanet Occurrence Rates from Microlensing Surveys. *arXiv e-prints*, page arXiv:2310.07502, October 2023.

[96] Y. Shvartzvald, D. Maoz, A. Udalski, T. Sumi, M. Friedmann, S. Kaspi, R. Poleski, M. K. Szymański, J. Skowron, S. Kozłowski, Ł. Wyrzykowski, P. Mróz, P. Pietrukowicz, G. Pietrzyński, I. Soszyński, K. Ulaczyk, F. Abe, R. K. Barry, D. P. Bennett, A. Bhattacharya, I. A. Bond, M. Freeman, K. Inayama, Y. Itow, N. Koshimoto, C. H. Ling, K. Masuda, A. Fukui, Y. Matsubara, Y. Muraki, K. Ohnishi, N. J. Rattenbury, To. Saito, D. J. Sullivan, D. Suzuki, P. J. Tristram, Y. Wakiyama, and A. Yonehara. The frequency of snowline-region planets from four years of OGLE-MOA-Wise second-generation microlensing. *MNRAS*, 457(4):4089–4113, April 2016.

[97] R. Poleski, J. Skowron, P. Mróz, A. Udalski, M. K. Szymański, P. Pietrukowicz, K. Ulaczyk, K. Rybicki, P. Iwanek, M. Wrona, and M. Gromadzki. Wide-Orbit Exoplanets are Common. Analysis of Nearly 20 Years of OGLE Microlensing Survey Data. *AcA*, 71(1):1–23, March 2021.

[98] Weicheng Zang, Hongjing Yang, Cheongho Han, Chung-Uk Lee, Andrzej Udalski, Andrew Gould, Shude Mao, Xiangyu Zhang, Wei Zhu, Michael D. Albrow, Sun-Ju Chung, Kyu-Ha Hwang, Youn Kil Jung, Yoon-Hyun Ryu, In-Gu Shin, Yossi Shvartzvald, Jennifer C. Yee, Sang-Mok Cha, Dong-Jin Kim, Hyoun-Woo Kim, Seung-Lee Kim, Dong-Joo Lee, Yongseok Lee, Byeong-Gon Park, Richard W. Pogge, Przemek Mróz, Jan Skowron, Radoslaw Poleski, Michał K. Szymański, Igor Soszyński, Paweł Pietrukowicz, Szymon Kozłowski, Krzysztof Ulaczyk, Krzysztof A. Rybicki, Patryk Iwanek, Marcin Wrona, and Mariusz Gromadzki. Systematic KMTNet planetary anomaly search. IV. Complete sample of 2019 prime-field. *MNRAS*, 515(1):928–939, September 2022.

[99] Takahiro Sumi, Naoki Koshimoto, David P. Bennett, Nicholas J. Rattenbury, Fumio Abe, Richard Barry, Aparna Bhattacharya, Ian A. Bond, Hirosane Fujii, Akihiko Fukui, Ryusei Hamada, Yuki Hirao, Stela Ishitani Silva, Yoshitaka Itow, Rintaro Kirikawa, Iona Kondo, Yutaka Matsubara, Shota Miyazaki, Yasushi Muraki, Greg Olmschenk, Clément Ranc, Yuki Satoh, Daisuke Suzuki, Mio Tomoyoshi, Paul. J. Tristram, Aikaterini Vandorou, Hibiki Yama, and Kansuke Yamashita. Free-floating Planet Mass Function from MOA-II 9 yr Survey toward the Galactic Bulge. *AJ*, 166(3):108, September 2023.

[100] Weicheng Zang, Youn Kil Jung, Jennifer C. Yee, Kyu-Ha Hwang, Hongjing Yang, Andrzej Udalski, Takahiro Sumi, Andrew Gould, Shude Mao, Michael D. Albrow, Sun-Ju Chung, Cheongho Han, Yoon-Hyun Ryu, In-Gu Shin, Yossi Shvartzvald, Sang-Mok Cha, Dong-Jin Kim, Hyoun-Woo Kim, Seung-Lee Kim, Chung-Uk Lee, Dong-Joo Lee, Yongseok Lee, Byeong-Gon Park, Richard W. Pogge, Xiangyu Zhang, Renkun Kuang, Hanyue Wang, Jiyuan Zhang, Zhecheng Hu, Wei Zhu, Przemek Mróz, Jan Skowron, Radosław Poleski, Michał K. Szymański, Igor Soszyński, Paweł Pietrukowicz, Szymon Kozłowski, Krzysztof Ulaczyk, Krzysztof A. Rybicki, Patryk Iwanek, Marcin Wrona, Mariusz Gromadzki, Fumio Abe, Richard Barry, David P. Bennett, Aparna Bhattacharya, Ian A. Bond, Hirosane Fujii, Akihiko Fukui, Ryusei Hamada, Yuki Hirao, Stela Ishitani Silva, Yoshitaka Itow, Rintaro Kirikawa, Naoki Koshimoto, Yutaka Matsubara, Shota Miyazaki, Yasushi Muraki, Greg Olmschenk, Clément Ranc, Nicholas J. Rattenbury, Yuki Satoh, Daisuke Suzuki, Mio Tomoyoshi, Paul J. Tristram, Aikaterini Vandorou, Hibiki Yama, and Kansuke Yamashita. Microlensing events indicate that super-earth exoplanets are common in jupiter-like orbits. *Science*, 388(6745):400–404, 2025.

[101] Satoshi Okuzumi, Munetake Momose, Sin-iti Sirono, Hiroshi Kobayashi, and Hidekazu Tanaka. Sintering-induced Dust Ring Formation in Protoplanetary Disks: Application to the HL Tau Disk. *ApJ*, 821(2):82, April 2016.

[102] Sean M. Andrews, David J. Wilner, Zhaohuan Zhu, Tilman Birnstiel, John M. Carpenter, Laura M. Pérez, Xue-Ning Bai, Karin I. Öberg, A. Meredith Hughes, Andrea Isella, and Luca Ricci. Ringed Substructure and a Gap at 1 au in the Nearest Protoplanetary Disk. *ApJL*, 820(2):L40, April 2016.

[103] Rebecca G. Martin and Mario Livio. On the Evolution of the CO Snow Line in Protoplanetary Disks. *ApJL*, 783(2):L28, March 2014.

[104] J. Lannier, P. Delorme, A. M. Lagrange, S. Borgniet, J. Rameau, J. E. Schlieder, J. Gagné, M. A. Bonavita, L. Malo, G. Chauvin, M. Bonnefoy, and J. H. Girard. MASSIVE: A Bayesian analysis of giant planet populations around low-mass stars. *A&A*, 596:A83, December 2016.

[105] GRAVITY Collaboration, Abuter, R., Amorim, A., Benisty, M., Berger, J. P., Bonnet, H., Bourdarot, G., Bourget, P., Brandner, W., Clénet, Y., Davies, R., Delplancke-Ströbele, F., Dembet, R., Drescher, A., Eckart, A., Eisenhauer, F., Feuchtgruber, H., Finger, G., Förster Schreiber, N. M., Garcia, P., Garcia-Lopez, R., Gao, F., Gendron, E., Genzel, R., Gillessen, S., Hartl, M., Haubois, X., Haussmann, F., Henning, T., Hippler, S., Horrobin, M., Jochum, L., Jocou, L., Kaufer, A., Kervella, P., Lacour, S., Lapeyrère, V., Le Bouquin, J.-B., Ledoux, C., Léna, P., Lutz, D., Mang, F., Mérand, A., More, N., Nowak, M., Ott, T., Paumard, T., Perraut, K., Perrin, G., Pfuhl, O., Rabien, S., Ribeiro, D. C., Sadun Bordoni, M., Shangguan, J., Shimizu, T., Stadler, J., Straub, O., Straubmeier, C., Sturm, E., Tacconi, L. J., Tristram, K. R. W., Vincent, F., von Fellenberg, S., Widmann, F., Wieprecht, E., Woillez, J., Yazici, S., and Zins, G. Astrometric detection of a neptune-mass candidate planet in the nearest m-dwarf binary system gj65 with vlti/gravity. *A&A*, 685:L9, 2024.

[106] A. Sozzetti, P. Giacobbe, M. G. Lattanzi, G. Micela, R. Morbidelli, and G. Tinetti. Astrometric detection of giant planets around nearby M dwarfs: the Gaia potential. *MNRAS*, 437(1):497–509, January 2014.

[107] B. Holl, A. Sozzetti, J. Sahlmann, P. Giacobbe, D. Ségransan, N. Unger, J. B. Delisle, D. Barbato, M. G. Lattanzi, R. Morbidelli, and D. Sosnowska. Gaia Data Release 3. Astrometric orbit determination with Markov chain Monte Carlo and genetic algorithms: Systems with stellar, sub-stellar, and planetary mass companions. *A&A*, 674:A10, June 2023.

[108] Kyle Franson, William O. Balmer, Brendan P. Bowler, Laurent Pueyo, Yifan Zhou, Emily Rickman, Zhoujian Zhang, Sagnick Mukherjee, Tim D. Pearce, Daniella C. Bardalez Gagliuffi, Lauren I. Biddle, Timothy D. Brandt, Rachel Bowens-Rubin, Justin R. Crepp, James W. Davidson, Jacqueline Faherty, Christian Ginski, Elliott P. Horch, Marvin Morgan, Caroline V. Morley, Marshall D. Perrin, Aniket Sanghi, Maïssa Salama, Christopher A. Theissen, Quang H. Tran, and Trevor N. Wolf. JWST/NIRCam 4–5 μm Imaging of the Giant Planet AF Lep b. *ApJL*, 974(1):L11, October 2024.

[109] Flavien Kiefer, Anne-Marie Lagrange, Pascal Rubini, and Florian Philipot. Searching for substellar companion candidates with Gaia. II. A catalog of 9,698 planet candidate solar-type hosts. *arXiv e-prints*, page arXiv:2409.16993, September 2024.

[110] Jonathan Brande, Thomas Barclay, Joshua E. Schlieder, Eric D. Lopez, and Elisa V. Quintana. The Feasibility of Directly Imaging Nearby Cold Jovian Planets with MIRI/JWST. *AJ*, 159(1):18, January 2020.

[111] Aarynn L. Carter, Sasha Hinkley, Mariangela Bonavita, Mark W. Phillips, Julien H. Girard, Marshall Perrin, Laurent Pueyo, Arthur Vigan, Jonathan Gagné, and Andrew J. I. Skemer. Direct imaging of sub-Jupiter mass exoplanets with James Webb Space Telescope coronagraphy. *MNRAS*, 501(2):1999–2016, February 2021.

[112] Jonathan P. Gardner, John C. Mather, Randy Abbott, James S. Abell, Mark Abernathy, Faith E. Abney, John G. Abraham, Roberto Abraham, Yasin M. Abul-Huda, Scott Acton, Cynthia K. Adams, Evan Adams, David S. Adler, Maarten Adriaensen, Jonathan Albert Aguilar, Mansoor Ahmed, Nasif S. Ahmed, Tanjira Ahmed, Rüdeger Albat, Loïc Albert, Stacey Alberts, David Aldridge, Mary Marsha Allen, Shaune S. Allen, Martin Altenburg, Serhat Altunc, Jose Lorenzo Alvarez, Javier Álvarez-Márquez, Catarina Alves de Oliveira, Leslie L. Ambrose, Satya M. Anandakrishnan, Gregory C. Andersen, Harry James Anderson, Jay Anderson, Kristen Anderson, Sara M. Anderson, Julio Aprea, Benita J. Archer, Jonathan W. Arenberg, Ioannis Argyriou, Santiago Arribas, Étienne Artigau, Amanda Rose Arvai, Paul Atcheson, Charles B. Atkinson, Jesse Averbukh, Cagatay Aymergen, John J. Bacinski, Wayne E. Baggett, Giorgio Bagnasco, Lynn L. Baker, Vicki Ann Balzano, Kimberly A. Banks, David A. Baran, Elizabeth A. Barker, Larry K. Barrett, Bruce O. Barringer, Allison Barto, William Bast, Pierre Baudoz, Stefi Baum, Thomas G. Beatty, Mathilde Beaulieu, Kathryn Bechtold, Tracy Beck, Megan M. Beddard, Charles Beichman, Larry Bellagama, Pierre Bely, Timothy W. Berger, Louis E. Bergeron, Antoine-Darveau Bernier, Maria D. Bertch, Charlotte Beskow, Laura E. Betz, Carl P. Biagetti, Stephan Birkmann, Kurt F. Bjorklund, James D. Blackwood, Ronald Paul Blazek, Stephen Blossfeld, Marcel Bluth, Anthony Boccaletti, Jr. Boegner, Martin E., Ralph C. Bohlin, John Joseph Boia, Torsten Böker, N. Bonaventura, Nicholas A. Bond, Kari Ann Bosley, Rene A. Boucarut, Patrice Bouchet, Jeroen Bouwman, Gary Bower, Ariel S. Bowers, Charles W. Bowers, Leslye A. Boyce, Christine T. Boyer, Martha L. Boyer, Michael Boyer, Robert Boyer, Larry D. Bradley, Gregory R. Brady, Bernhard R. Brandl, Judith L. Brannen, David Breda, Harold G. Bremmer, David Brennan, Pamela A. Bresnahan, Stacey N. Bright, Brian J. Broiles, Asa Bromenschenkel, Brian H. Brooks, Keira J. Brooks, Bob Brown, Bruce Brown, Thomas M. Brown, Barry W. Bruce, Jonathan G. Bryson, Edwin D. Bujanda, Blake M. Bullock, A. J. Bunker, Rafael Bureo, Irving J. Burt, James Aaron Bush, Howard A. Bushouse, Marie C. Bussman, Olivier Cabaud, Steven Cale, Charles D. Calhoon, Humberto Calvani, Alicia M. Canipe, Francis M. Caputo, Mihai Cara, Larkin Carey, Michael Eli Case, Thaddeus Cesari, Lee D. Cetorelli, Don R. Chance, Lynn Chandler, Dave Chaney, George N. Chapman, S. Charlot, Pierre Chayer, Jeffrey I. Cheezum, Bin Chen, Christine H. Chen, Brian Cherinka, Sarah C. Chichester, Zachary S. Chilton, Dharini Chittiraibalan, Mark Clampin, Charles R. Clark, Kerry W. Clark, Stephanie M. Clark, Edward E. Claybrooks, Keith A. Cleveland, Andrew L. Cohen, Lester M. Cohen, Knicole D. Colón, Benee L. Coleman, Luis Colina, Brian J. Comber, Thomas M. Comeau, Thomas Comer, Alain Conde Reis, Dennis C. Connolly, Kyle E. Conroy, Adam R. Contos, James Contreras, Neil J. Cook, James L. Cooper, Rachel Aviva Cooper, Michael F. Correia, Matteo Correnti, Christophe Cossou, Brian F. Costanza, Alain Coulais, Colin R. Cox, Ray T. Coyle, Misty M. Cracraft, Keith A. Crew, Gary J. Curtis, Bianca Cusveller, Cleyciane Da Costa Maciel, Christopher T. Dailey, Frédéric Daugeron, Greg S. Davidson, James E. Davies, Katherine Anne Davis, Michael S. Davis, Ratna Day,

Daniel de Chambure, Pauline de Jong, Guido De Marchi, Bruce H. Dean, John E. Decker, Amy S. Delisa, Lawrence C. Dell, Gail Dellagatta, Franciszka Dembinska, Sandor Demosthenes, Nadezhda M. Dencheva, Philippe Deneu, William W. DePriest, Jeremy Deschenes, Nathalie Dethienne, Örs Hunor Detre, Rosa Izela Diaz, Daniel Dicken, Audrey S. DiFelice, Matthew Dillman, Maureen O. Disharoon, William V. Dixon, Jesse B. Doggett, Keisha L. Dominguez, Thomas S. Donaldson, Cristina M. Doria-Warner, Tony Dos Santos, Heather Doty, Jr. Douglas, Robert E., René Doyon, Alan Dressler, Jennifer Driggers, Phillip A. Driggers, Jamie L. Dunn, Kimberly C. DuPrie, Jean Dupuis, John Durning, Sanghamitra B. Dutta, Nicholas M. Earl, Paul Eccleston, Pascal Ecobichon, Eiichi Egami, Ralf Ehrenwinkler, Jonathan D. Eisenhamer, Michael Eisenhower, Daniel J. Eisenstein, Zaky El Hamel, Michelle L. Elie, James Elliott, Kyle Wesley Elliott, Michael Engesser, Néstor Espinoza, Odessa Etienne, Mireya Etxaluze, Leah Evans, Luce Fabreguettes, Massimo Falcolini, Patrick R. Falini, Curtis Fatig, Matthew Feeney, Lee D. Feinberg, Raymond Fels, Nazma Ferdous, Henry C. Ferguson, Laura Ferrarese, Marie-Héléne Ferreira, Pierre Ferruit, Malcolm Ferry, Joseph Charles Filippazzo, Daniel Firre, Mees Fix, Nicolas Flagey, Kathryn A. Flanagan, Scott W. Fleming, Michael Florian, James R. Flynn, Luca Foiadelli, Mark R. Fontaine, Erin Marie Fontanella, Peter Randolph Forshay, Elizabeth A. Fortner, Ori D. Fox, Alexandro P. Framarini, John I. Francisco, Randy Franck, Marijn Franx, David E. Franz, Scott D. Friedman, Katheryn E. Friend, James R. Frost, Henry Fu, Alexander W. Fullerton, Lionel Gaillard, Sergey Galkin, Ben Gallagher, Anthony D. Galyer, Macarena García Marín, Lisa E. Gardner, Dennis Garland, Bruce Albert Garrett, Danny Gasman, András Gáspár, René Gastaud, Daniel Gaudreau, Peter Timothy Gauthier, Vincent Geers, Paul H. Geithner, Mario Gennaro, John Gerber, John C. Gereau, Robert Giampaoli, Giovanna Giardino, Paul C. Gibbons, Karoline Gilbert, Larry Gilman, Julien H. Girard, Mark E. Giuliano, Konstantinos Gkountis, Alistair Glasse, Kirk Zachary Glassmire, Adrian Michael Glauser, Stuart D. Glazer, Joshua Goldberg, David A. Golimowski, Shireen P. Gonzaga, Karl D. Gordon, Shawn J. Gordon, Paul Goudfrooij, Michael J. Gough, Adrian J. Graham, Christopher M. Grau, Joel David Green, Gretchen R. Greene, Thomas P. Greene, Perry E. Greenfield, Matthew A. Greenhouse, Thomas R. Greve, Edgar M. Greville, Stefano Grimaldi, Frank E. Groe, Andrew Groebner, David M. Grumm, Timothy Grundy, Manuel Güdel, Pierre Guillard, John Guldalian, Christopher A. Gunn, Anthony Gurule, Irvin Meyer Gutman, Paul D. Guy, Benjamin Guyot, Warren J. Hack, Peter Haderlein, James B. Hagan, Andria Hagedorn, Kevin Hainline, Craig Haley, Maryam Hami, Forrest Clifford Hamilton, Jeffrey Hammann, Heidi B. Hammel, Christopher J. Hanley, Carl August Hansen, Bruce Hardy, Bernd Harnisch, Michael Hunter Harr, Pamela Harris, Jessica Ann Hart, George F. Hartig, Hashima Hasan, Kathleen Marie Hashim, Ryan Hashimoto, Sujee J. Haskins, Robert Edward Hawkins, Brian Hayden, William L. Hayden, Mike Healy, Karen Hecht, Vince J. Heeg, Reem Hejal, Kristopher A. Helm, Nicholas J. Hengemihle, Thomas Henning, Alaina Henry, Ronald L. Henry, Katherine Henshaw, Scarlin Hernandez, Donald C. Herrington, Astrid Heske, Brigette Emily Hesman, David L. Hickey, Bryan N. Hilbert, Dean C. Hines, Michael R. Hinz, Michael Hirsch, Robert S. Hitcho, Klaus Hodapp, Philip E. Hodge, Melissa Hoffman, Sherie T. Holfeltz, Bryan Jason Holler, Jennifer Rose Hoppa, Scott Horner, Joseph M. Howard, Richard J. Howard, Jean M. Huber, Joseph S. Hunkeler, Alexander Hunter, David Gavin Hunter, Spencer W. Hurd, Brendan J. Hurst, John B. Hutchings, Jason E. Hylan, Lu-

minita Ilinca Ignat, Garth Illingworth, Sandra M. Irish, III Isaacs, John C., Jr. Jackson, Wallace C., Daniel T. Jaffe, Jasmin Jahic, Amir Jahromi, Peter Jakobsen, Bryan James, John C. James, LeAndrea Rae James, William Brian Jamieson, Raymond D. Jandra, Ray Jayawardhana, Robert Jedrzejewski, Basil S. Jeffers, Peter Jensen, Egges Joanne, Alan T. Johns, Carl A. Johnson, Eric L. Johnson, Patricia Johnson, Phillip Stephen Johnson, Thomas K. Johnson, Timothy W. Johnson, Doug Johnstone, Delphine Jollet, Danny P. Jones, Gregory S. Jones, Olivia C. Jones, Ronald A. Jones, Vicki Jones, Ian J. Jordan, Margaret E. Jordan, Reginald Jue, Mark H. Jurkowski, Grant Justis, Kay Justtanont, Catherine C. Kaleida, Jason S. Kalirai, Phillip Cabrales Kalmanson, Lisa Kaltenegger, Jens Kammerer, Samuel K. Kan, Graham Childs Kanarek, Shaw-Hong Kao, Diane M. Karakla, Hermann Karl, Susan A. Kassin, David D. Kauffman, Patrick Kavanagh, Leigh L. Kelley, Douglas M. Kelly, Sarah Kendrew, Herbert V. Kennedy, Deborah A. Kenny, Ritva A. Keski-Kuha, Charles D. Keyes, Ali Khan, Richard C. Kidwell, Randy A. Kimble, James S. King, Richard C. King, Wayne M. Kinzel, Jeffrey R. Kirk, Marc E. Kirkpatrick, Pamela Klaassen, Lana Klingemann, Paul U. Klintworth, Bryan Adam Knapp, Scott Knight, Perry J. Knollenberg, Daniel Mark Knutsen, Robert Koehler, Anton M. Koekemoer, Earl T. Kofler, Vicki L. Kontson, Aiden Rose Kovacs, Vera Kozhurina-Platais, Oliver Krause, Gerard A. Kriss, John Krist, Monica R. Kristoffersen, Claudia Krogel, Anthony P. Krueger, Bernard A. Kulp, Nimisha Kumari, Sandy W. Kwan, Mark Kyprianou, Aurora Gadiano Labador, Álvaro Labiano, David Lafrenière, Pierre-Olivier Lagage, Victoria G. Laidler, Benoit Laine, Simon Laird, Charles-Philippe Lajoie, Matthew D. Lallo, May Yen Lam, Stephanie Marie LaMassa, Scott D. Lambros, Richard Joseph Lampenfield, Matthew Ed Lander, James Hutton Langston, Kirsten Larson, Melora Larson, Robert Joseph LaVerghetta, David R. Law, Jon F. Lawrence, David W. Lee, Janice Lee, Yat-Ning Paul Lee, Jarron Leisenring, Michael Dunlap Leveille, Nancy A. Levenson, Joshua S. Levi, Marie B. Levine, Dan Lewis, Jake Lewis, Nikole Lewis, Mattia Libralato, Norbert Lidon, Paula Louisa Liebrecht, Paul Lightsey, Simon Lilly, Frederick C. Lim, Pey Lian Lim, Sai-Kwong Ling, Lisa J. Link, Miranda Nicole Link, Jamie L. Lipinski, XiaoLi Liu, Amy S. Lo, Lynette Lobmeyer, Ryan M. Logue, Chris A. Long, Douglas R. Long, Ilana D. Long, Knox S. Long, Marcos López-Caniego, Jennifer M. Lotz, Jennifer M. Love-Pruitt, Michael Lubskiy, Edward B. Luers, Robert A. Luetgens, Annetta J. Luevano, Sarah Marie G. Flores Lui, III Lund, James M., Ray A. Lundquist, Jonathan Lunine, Nora Lützgendorf, Richard J. Lynch, Alex J. MacDonald, Kenneth MacDonald, Matthew J. Macias, Keith I. Macklis, Peiman Maghami, Rishabh Y. Maharaja, Roberto Maiolino, Konstantinos G. Makrygiannis, Sunita Giri Malla, Eliot M. Malumuth, Elena Manjavacas, Andrea Marini, Amanda Marrione, Anthony Marston, André R. Martel, Didier Martin, Peter G. Martin, Kristin L. Martinez, Marc Maschmann, Gregory L. Masci, Margaret E. Masetti, Michael Maszkiewicz, Gary Matthews, Jacob E. Matuskey, Glen A. McBrayer, Donald W. McCarthy, Mark J. McCaughrean, Leslie A. McClare, Michael D. McClare, John C. McCloskey, Taylore D. McClurg, Martin McCoy, Michael W. McElwain, Roy D. McGregor, Douglas B. McGuffey, Andrew G. McKay, William K. McKenzie, Brian McLean, Matthew McMaster, Warren McNeil, Wim De Meester, Kimberly L. Mehalick, Margaret Meixner, Marcio Meléndez, Michael P. Menzel, Michael T. Menzel, Matthew Merz, David D. Mesterharm, Michael R. Meyer, Michele L. Meyett, Luis E. Meza, Calvin Midwinter, Stefanie N. Milam, Jay Todd Miller, William C. Miller, Cherie L. Miskey, Karl

Misselt, Eileen P. Mitchell, Martin Mohan, Emily E. Montoya, Michael J. Moran, Takahiro Morishita, Amaya Moro-Martín, Debra L. Morrison, Jane Morrison, Ernie C. Morse, Michael Moschos, S. H. Moseley, Gary E. Mosier, Peter Mosner, Matt Mountain, Jason S. Muckenthaler, Donald G. Mueller, Migo Mueller, Daniella Muhiem, Prisca Mühlmann, Susan Elizabeth Mullally, Stephanie M. Mullen, Alan J. Munger, Jess Murphy, Katherine T. Murray, James C. Muzerolle, Matthew Mycroft, Andrew Myers, Carey R. Myers, Fred Richard R. Myers, Richard Myers, Kaila Myrick, IV Nagle, Adrian F., Omnarayani Nayak, Bret Naylor, Susan G. Neff, Edmund P. Nelan, John Nella, Duy Tuong Nguyen, Michael N. Nguyen, Bryony Nickson, John Joseph Nidhiry, Malcolm B. Niedner, Maria Nieto-Santisteban, Nikolay K. Nikolov, Mary Ann Nishisaka, Alberto Noriega-Crespo, Antonella Nota, Robyn C. O'Mara, Michael Oboryshko, Marcus B. O'Brien, William R. Ochs, Joel D. Offenberg, Patrick Michael Ogle, Raymond G. Ohl, Joseph Hamden Olmsted, Shannon Barbara Osborne, Brian Patrick O'Shaughnessy, Göran Östlin, Brian O'Sullivan, O. Justin Otor, Richard Ottens, Nathalie N. Q. Ouellette, Daria J. Outlaw, Beverly A. Owens, Camilla Pacifici, James Christophe Page, James G. Paranilam, Sang Park, Keith A. Parrish, Laura Paschal, Polychronis Patapis, Jignasha Patel, Keith Patrick, Jr. Pattishall, Robert A., Douglas William Paul, Shirley J. Paul, Tyler Andrew Pauly, Cheryl M. Pavlovsky, Maria Peña-Guerrero, Andrew H. Pedder, Matthew Weldon Peek, Patricia A. Pelham, Konstantin Penanen, Beth A. Perriello, Marshall D. Perrin, Richard F. Perrine, Chuck Perrygo, Muriel Peslier, Michael Petach, Karla A. Peterson, Tom Pfarr, James M. Pierson, Martin Pietraszkiewicz, Guy Pilchen, Judy L. Pipher, Norbert Pirzkal, Joseph T. Pitman, Danielle M. Player, Rachel Plesha, Anja Plitzke, John A. Pohner, Karyn Konstantin Poletis, Joseph A. Pollizzi, Ethan Polster, James T. Pontius, Klaus Pontoppidan, Susana C. Porges, Gregg D. Potter, Stephen Prescott, Charles R. Proffitt, Laurent Pueyo, Irma Aracely Quispe Neira, Armando Radich, Reiko T. Rager, Julien Rameau, Deborah D. Ramey, Rafael Ramos Alarcon, Riccardo Rampini, Robert Rapp, Robert A. Rashford, Bernard J. Rauscher, Swara Ravindranath, Timothy Rawle, Tynika N. Rawlings, Tom Ray, Michael W. Regan, Brian Rehm, Kenneth D. Rehm, Neill Reid, Carl A. Reis, Florian Renk, Tom B. Reoch, Michael Ressler, Armin W. Rest, Paul J. Reynolds, Joel G. Richon, Karen V. Richon, Michael Ridgaway, Adric Richard Riedel, George H. Rieke, Marcia J. Rieke, Richard E. Rifelli, Jane R. Rigby, Catherine S. Riggs, Nancy J. Ringel, Christine E. Ritchie, Hans-Walter Rix, Massimo Robberto, Gregory L. Robinson, Michael S. Robinson, Orion Robinson, Frank W. Rock, David R. Rodriguez, Bruno Rodríguez del Pino, Thomas Roellig, Scott O. Rohrbach, Anthony J. Roman, Frederick J. Romelfanger, Jr. Romo, Felipe P., Jose J. Rosales, Perry Rose, Anthony F. Roteliuk, Marc N. Roth, Braden Quinn Rothwell, Sylvain Rouzaud, Jason Rowe, Neil Rowlands, Arpita Roy, Pierre Royer, Chunlei Rui, Peter Rumler, William Rumpl, Melissa L. Russ, Michael B. Ryan, Richard M. Ryan, Karl Saad, Modhumita Sabata, Rick Sabatino, Elena Sabbi, Phillip A. Sabelhaus, Stephen Sabia, Kailash C. Sahu, Babak N. Saif, Jean-Christophe Salvignol, Piyal Samara-Ratna, Bridget S. Samuelson, Felicia A. Sanders, Bradley Sappington, B. A. Sargent, Arne Sauer, Bruce J. Savadkin, Marcin Sawicki, Tina M. Schappell, Caroline Scheffer, Silvia Scheithauer, Ron Scherer, Conrad Schiff, Everett Schlawin, Olivier Schmeitzky, Tyler S. Schmitz, Donald J. Schmude, Analyn Schneider, Jürgen Schreiber, Hilde Schroeven-Deceuninck, John J. Schultz, Ryan Schwab, Curtis H. Schwartz, Dario Scoccimarro, John F. Scott, Michelle B. Scott, Bonita L. Seaton, Bruce S. Seely, Bernard

Seery, Mark Seidleck, Kenneth Sembach, Clare Elizabeth Shanahan, Bryan Shaughnessy, Richard A. Shaw, Christopher Michael Shay, Even Sheehan, Kartik Sheth, Hsin-Yi Shih, Irene Shivaei, Noah Siegel, Matthew G. Sienkiewicz, Debra D. Simmons, Bernard P. Simon, Marco Sirianni, Anand Sivaramakrishnan, Jeffrey E. Slade, G. C. Sloan, Christine E. Slocum, Steven E. Slowinski, Corbett T. Smith, Eric P. Smith, Erin C. Smith, Koby Smith, Robert Smith, Stephanie J. Smith, John L. Smolik, David R. Soderblom, Sangmo Tony Sohn, Jeff Sokol, George Sonneborn, Christopher D. Sontag, Peter R. Sooy, Remi Soummer, Dana M. Southwood, Kay Spain, Joseph Sparmo, David T. Speer, Richard Spencer, Joseph D. Sprofera, Scott S. Stallcup, Marcia K. Stanley, John A. Stansberry, Christopher C. Stark, Carl W. Starr, Diane Y. Stassi, Jane A. Steck, Christine D. Steeley, Matthew A. Stephens, Ralph J. Stephenson, Alphonso C. Stewart, Massimo Stiavelli, Hervey Jr. , Stockman, Paolo Strada, Amber N. Straughn, Scott Streetman, David Kendal Strickland, Jingping F. Strobele, Martin Stuhlinger, Jeffrey Edward Stys, Miguel Such, Kalyani Sukhatme, Joseph F. Sullivan, Pamela C. Sullivan, Sandra M. Sumner, Fengwu Sun, Benjamin Dale Sunnquist, Daryl Allen Swade, Michael S. Swam, Diane F. Swenton, Robby A. Swoish, Oi In Tam Litten, Laszlo Tamas, Andrew Tao, David K. Taylor, Joanna M. Taylor, Maurice te Plate, Mason Van Tea, Kelly K. Teague, Randal C. Telfer, Tea Temim, Scott C. Texter, Deepashri G. Thatte, Christopher Lee Thompson, Linda M. Thompson, Shaun R. Thomson, Harley Thronson, C. M. Tierney, Tuomo Tikkanen, Lee Tinnin, William Thomas Tippet, Connor William Todd, Hien D. Tran, John Trauger, Edwin Gregorio Trejo, Justin Hoang Vinh Truong, Christine L. Tsukamoto, Yasir Tufail, Jason Tumlinson, Samuel Tustain, Harrison Tyra, Leonardo Ubeda, Kelli Underwood, Michael A. Uzzo, Steven Vaclavik, Frida Valenduc, Jeff A. Valenti, Julie Van Campen, Inge van de Wetering, Roeland P. Van Der Marel, Remy van Haarlem, Bart Vandenbussche, Ewine F. van Dishoeck, Dona D. Vanterpool, Michael R. Vernoy, Maria Begoña Vila Costas, Kevin Volk, Piet Voorzaat, Mark F. Voyton, Ekaterina Vydra, Darryl J. Waddy, Christoffel Waelkens, Glenn Michael Wahlgren, Jr. Walker, Frederick E., Michel Wander, Christine K. Warfield, Gerald Warner, Francis C. Wasiak, Matthew F. Wasiak, James Wehner, Kevin R. Weiler, Mark Weilert, Stanley B. Weiss, Martyn Wells, Alan D. Welty, Lauren Wheate, Thomas P. Wheeler, Christy L. White, Paul Whitehouse, Jennifer Margaret Whiteleather, William Russell Whitman, Christina C. Williams, Christopher N. A. Willmer, Chris J. Willott, Scott P. Willoughby, Andrew Wilson, Debra Wilson, Donna V. Wilson, Rogier Windhorst, Emily Christine Wislowski, David J. Wolfe, Michael A. Wolfe, Schuyler Wolff, Amancio Wondel, Cindy Woo, Robert T. Woods, Elaine Worden, William Workman, Gillian S. Wright, Carl Wu, Chi-Rai Wu, Dakin D. Wun, Kristen B. Wymer, Thomas Yadetie, Isabelle C. Yan, Keith C. Yang, Kayla L. Yates, Christopher R. Yeager, Ethan John Yerger, Erick T. Young, Gary Young, Gene Yu, Susan Yu, Dean S. Zak, Peter Zeidler, Robert Zepp, Julia Zhou, Christian A. Zincke, Stephanie Zonak, and Elisabeth Zondag. The James Webb Space Telescope Mission. *PASP*, 135(1048):068001, June 2023.

[113] Joshua E. Schlieder, Charles A. Beichman, Michael R. Meyer, and Thomas Greene. Toward Direct Imaging of Low-Mass Gas-Giants with the *James Webb Space Telescope*. *arXiv e-prints*, page arXiv:1512.00053, October 2015.

[114] Caroline V. Morley, Mark S. Marley, Jonathan J. Fortney, Roxana Lupu, Didier Saumon,

Tom Greene, and Katharina Lodders. Water Clouds in Y Dwarfs and Exoplanets. *ApJ*, 787(1):78, May 2014.

[115] Sasha Hinkley, Aarynn L. Carter, Shrishmoy Ray, Andrew Skemer, Beth Biller, Elodie Choquet, Maxwell A. Millar-Blanchaer, Stephanie Sallum, Brittany Miles, Niall Whiteford, Polychronis Patapis, Marshall Perrin, Laurent Pueyo, Glenn Schneider, Karl Stapelfeldt, Jason Wang, Kimberly Ward-Duong, Brendan P. Bowler, Anthony Boccaletti, Julien H. Girard, Dean Hines, Paul Kalas, Jens Kammerer, Pierre Kervella, Jarron Leisenring, Eric Pantin, Yifan Zhou, Michael Meyer, Michael C. Liu, Mickael Bonnefoy, Thayne Currie, Michael McElwain, Stanimir Metchev, Mark Wyatt, Olivier Absil, Jea Adams, Travis Barman, Isabelle Baraffe, Mariangela Bonavita, Mark Booth, Marta Bryan, Gael Chauvin, Christine Chen, Camilla Danielski, Matthew De Furio, Samuel M. Factor, Michael P. Fitzgerald, Jonathan J. Fortney, Carol Grady, Alexandra Greenbaum, Thomas Henning, Kielan K. W. Hoch, Markus Janson, Grant Kennedy, Matthew Kenworthy, Adam Kraus, Masayuki Kuzuhara, Pierre-Olivier Lagage, Anne-Marie Lagrange, Ralf Launhardt, Cecilia Lazzoni, James Lloyd, Sebastian Marino, Mark Marley, Raquel Martinez, Christian Marois, Brenda Matthews, Elisabeth C. Matthews, Dimitri Mawet, Johan Mazoyer, Mark Phillips, Simon Petrus, Sascha P. Quanz, Andreas Quirrenbach, Julien Rameau, Isabel Rebollido, Emily Rickman, Matthias Samland, B. Sargent, Joshua E. Schlieder, Anand Sivaramakrishnan, Jordan M. Stone, Motohide Tamura, Pascal Tremblin, Taichi Uyama, Malavika Vasist, Arthur Vigan, Kevin Wagner, and Marie Ygouf. The jwst early release science program for the direct imaging and spectroscopy of exoplanetary systems. *Publications of the Astronomical Society of the Pacific*, 134(1039):095003, sep 2022.

[116] Jens Kammerer, Kellen Lawson, Marshall D. Perrin, Isabel Rebollido, Christopher C. Stark, Tomas Stolker, Julien H. Girard, Laurent Pueyo, William O. Balmer, Kadin Worthen, Christine Chen, Roeland P. van der Marel, Nikole K. Lewis, Kimberly Ward-Duong, Jeff A. Valenti, Mark Clampin, and C. Matt Mountain. JWST-TST High Contrast: JWST/NIRCam Observations of the Young Giant Planet β Pic b. *AJ*, 168(2):51, August 2024.

[117] Marie Ygouf, Charles A. Beichman, Jorge Llop-Sayson, Geoffrey Bryden, Jarron M. Leisenring, András Gáspár, John E. Krist, Marcia J. Rieke, George H. Rieke, Schuyler Grace Wolff, Thomas L. Roellig, Kate Su, Kevin N. Hainline, Klaus W. Hodapp, Thomas P. Greene, Michael R. Meyer, Douglas M. Kelly, Karl Misselt, John Stansberry, Martha Boyer, Doug Johnstone, Scott Horner, and Alexandra Z. Greenbaum. Searching for Planets Orbiting Fomalhaut with JWST/NIRCam. *AJ*, 167(1):26, January 2024.

[118] Gabriele Cugno, Jarron Leisenring, Kevin R. Wagner, Camryn Mullin, Roubing Dong, Thomas Greene, Doug Johnstone, Michael R. Meyer, Schuyler G. Wolff, Charles Beichman, Martha Boyer, Scott Horner, Klaus Hodapp, Doug Kelly, Don McCarthy, Thomas Roellig, George Rieke, Marcia Rieke, John Stansberry, and Erick Young. JWST/NIRCam Imaging of Young Stellar Objects. II. Deep Constraints on Giant Planets and a Planet Candidate Outside of the Spiral Disk Around SAO 206462. *AJ*, 167(4):182, April 2024.

[119] Jonathan Gagné, Eric E. Mamajek, Lison Malo, Adric Riedel, David Rodriguez, David Lafrenière, Jacqueline K. Faherty, Olivier Roy-Loubier, Laurent Pueyo, Annie C. Robin, and René Doyon. BANYAN. XI. The BANYAN Σ Multivariate Bayesian Algorithm to Identify Members of Young Associations with 150 pc. *ApJ*, 856(1):23, March 2018.

[120] B. Zuckerman and Inseok Song. Young Stars Near the Sun. *ARA&A*, 42(1):685–721, September 2004.

[121] C. A. O. Torres, G. R. Quast, C. H. F. Melo, and M. F. Sterzik. Young Nearby Loose Associations. In B. Reipurth, editor, *Handbook of Star Forming Regions, Volume II*, volume 5, page 757. Astronomical Society of the Pacific, 2008.

[122] Evgenya L. Shkolnik, Guillem Anglada-Escudé, Michael C. Liu, Brendan P. Bowler, Alycia J. Weinberger, Alan P. Boss, I. Neill Reid, and Motohide Tamura. Identifying the Young Low-mass Stars within 25 pc. II. Distances, Kinematics, and Group Membership. *ApJ*, 758(1):56, October 2012.

[123] Lison Malo, Étienne Artigau, René Doyon, David Lafrenière, Loïc Albert, and Jonathan Gagné. BANYAN. III. Radial Velocity, Rotation, and X-Ray Emission of Low-mass Star Candidates in Nearby Young Kinematic Groups. *ApJ*, 788(1):81, June 2014.

[124] Adam L. Kraus, Evgenya L. Shkolnik, Katelyn N. Allers, and Michael C. Liu. A Stellar Census of the Tucana-Horologium Moving Group. *AJ*, 147(6):146, June 2014.

[125] Eric E. Mamajek. ON THE AGE AND BINARITY OF FOMALHAUT. *The Astrophysical Journal*, 754(2):L20, August 2012.

[126] Eric E. Mamajek, Jennifer L. Bartlett, Andreas Seifahrt, Todd J. Henry, Sergio B. Dieterich, John C. Lurie, Matthew A. Kenworthy, Wei-Chun Jao, Adric R. Riedel, John P. Subasavage, Jennifer G. Winters, Charlie T. Finch, Philip A. Ianna, and Jacob Bean. The Solar Neighborhood. XXX. Fomalhaut C. *AJ*, 146(6):154, December 2013.

[127] Ch. E. Worley and G. G. Douglass. *The Washington Visual Double Star Catalogue, 1984*. 1984.

[128] Gary L. Wycoff, Brian D. Mason, and Sean E. Urban. Data Mining for Double Stars in Astrometric Catalogs. *AJ*, 132(1):50–60, July 2006.

[129] Markus Janson, Felix Hormuth, Carolina Bergfors, Wolfgang Brandner, Stefan Hippler, Sebastian Daemgen, Natalia Kudryavtseva, Eva Schmalzl, Carolin Schnupp, and Thomas Henning. The AstraLux Large M-dwarf Multiplicity Survey. *ApJ*, 754(1):44, July 2012.

[130] Markus Janson, Carolina Bergfors, Wolfgang Brandner, Natalia Kudryavtseva, Felix Hormuth, Stefan Hippler, and Thomas Henning. The AstraLux Multiplicity Survey: Extension to Late M-dwarfs. *ApJ*, 789(2):102, July 2014.

[131] Gaia Collaboration, F. Arenou, C. Babusiaux, M. A. Barstow, S. Faigler, A. Jorissen, P. Kervella, T. Mazeh, N. Mowlavi, P. Panuzzo, J. Sahlmann, S. Shahaf, A. Sozzetti, N. Bauchet, Y. Damerdji, P. Gavras, P. Giacobbe, E. Gosset, J.-L. Halbwachs, B. Holl,

M. G. Lattanzi, N. Leclerc, T. Morel, D. Pourbaix, P. Re Fiorentin, G. Sadowski, D. Ségransan, C. Siopis, D. Teyssier, T. Zwitter, L. Planquart, A. G. A. Brown, A. Vallenari, T. Prusti, J. H. J. de Bruijne, M. Biermann, O. L. Creevey, C. Ducourant, D. W. Evans, L. Eyer, R. Guerra, A. Hutton, C. Jordi, S. A. Klioner, U. L. Lammers, L. Lindegren, X. Luri, F. Mignard, C. Panem, S. Randich, P. Sartoretti, C. Soubiran, P. Tanga, N. A. Walton, C. A. L. Bailer-Jones, U. Bastian, R. Drimmel, F. Jansen, D. Katz, F. van Leeuwen, J. Bakker, C. Cacciari, J. Castañeda, F. De Angeli, C. Fabricius, M. Fouesneau, Y. Frémat, L. Galluccio, A. Guerrier, U. Heiter, E. Masana, R. Messineo, C. Nicolas, K. Nienartowicz, F. Pailler, F. Riclet, W. Roux, G. M. Seabroke, R. Sordo, F. Thévenin, G. Gracia-Abril, J. Portell, M. Altmann, R. Andrae, M. Audard, I. Bellas-Velidis, K. Benson, J. Berthier, R. Blomme, P. W. Burgess, D. Busonero, G. Busso, H. Cánovas, B. Carry, A. Cellino, N. Cheek, G. Clementini, M. Davidson, P. de Teodoro, M. Nuñez Campos, L. Delchambre, A. Dell'Oro, P. Esquej, J. Fernández-Hernández, E. Fraile, D. Garabato, P. García-Lario, R. Haigron, N. C. Hambly, D. L. Harrison, J. Hernández, D. Hestroffer, S. T. Hodgkin, K. Janßen, G. Jevardat de Fombelle, S. Jordan, A. Krone-Martins, A. C. Lanzafame, W. Löffler, O. Marchal, P. M. Marrese, A. Moitinho, K. Muinonen, P. Osborne, E. Pancino, T. Pauwels, A. Recio-Blanco, C. Reylé, M. Riello, L. Rimoldini, T. Roegiers, J. Rybizki, L. M. Sarro, M. Smith, E. Utrilla, M. van Leeuwen, U. Abbas, P. Ábrahám, A. Abreu Aramburu, C. Aerts, J. J. Aguado, M. Ajaj, F. Aldea-Montero, G. Altavilla, M. A. Álvarez, J. Alves, F. Anders, R. I. Anderson, E. Anglada Varela, T. Antoja, D. Baines, S. G. Baker, L. Balaguer-Núñez, E. Balbinot, Z. Balog, C. Barache, D. Barbato, M. Barros, S. Bartolomé, J.-L. Bassilana, U. Becciani, M. Bellazzini, A. Berihuete, M. Bernet, S. Bertone, L. Bianchi, A. Binnenfeld, S. Blanco-Cuaresma, A. Blazere, T. Boch, A. Bombrun, D. Bossini, S. Bouquillon, A. Bragaglia, L. Bramante, E. Breedt, A. Bressan, N. Brouillet, E. Brugaletta, B. Bucciarelli, A. Burlacu, A. G. Butkevich, R. Buzzi, E. Caffau, R. Cancelliere, T. Cantat-Gaudin, R. Carballo, T. Carlucci, M. I. Carnerero, J. M. Carrasco, L. Casamiquela, M. Castellani, A. Castro-Ginard, L. Chaoul, P. Charlot, L. Chemin, V. Chiaramida, A. Chiavassa, N. Chornay, G. Comoretto, G. Contursi, W. J. Cooper, T. Cornez, S. Cowell, F. Crifo, M. Cropper, M. Crosta, C. Crowley, C. Dafonte, A. Dapergolas, P. David, P. de Laverny, F. De Luise, R. De March, J. De Ridder, R. de Souza, A. de Torres, E. F. del Peloso, E. del Pozo, M. Delbo, A. Delgado, J.-B. Delisle, C. Demouchy, T. E. Dharmawardena, S. Diakite, C. Diener, E. Distefano, C. Dolding, H. Enke, C. Fabre, M. Fabrizio, G. Fedorets, P. Fernique, F. Figueras, Y. Fournier, C. Fouron, F. Fragkoudi, M. Gai, A. Garcia-Gutierrez, M. Garcia-Reinaldos, M. García-Torres, A. Garofalo, A. Gavel, E. Gerlach, R. Geyer, G. Gilmore, S. Girona, G. Giuffrida, R. Gomel, A. Gomez, J. González-Núñez, I. González-Santamaría, J. J. González-Vidal, M. Granvik, P. Guillout, J. Guiraud, R. Gutiérrez-Sánchez, L. P. Guy, D. Hatzidimitriou, M. Hauser, M. Haywood, A. Helmer, A. Helmi, M. H. Sarmiento, S. L. Hidalgo, N. Hładczuk, D. Hobbs, G. Holland, H. E. Huckle, K. Jardine, G. Jasniewicz, A. Jean-Antoine Piccolo, Ó Jiménez-Arranz, J. Juaristi Campillo, F. Julbe, L. Karbevska, S. Khanna, G. Kordopatis, A. J. Korn, Á Kóspál, Z. Kostrzewa-Rutkowska, K. Kruszyńska, M. Kun, P. Laizeau, S. Lambert, A. F. Lanza, Y. Lasne, J.-F. Le Campion, Y. Lebreton, T. Lebzelter, S. Leccia, I. Lecoeur-Taibi, S. Liao, E. L. Licata, H. E. P. Lindstrøm, T. A. Lister, E. Livanou, A. Lobel, A. Lorca, C. Loup, P. Madrero Pardo, A. Magdaleno Romeo, S. Managau, R. G. Mann, M. Manteiga, J. M. Marchant, M. Marconi, J. Marcos, M. M.

S. Marcos Santos, D. Marín Pina, S. Marinoni, F. Marocco, D. J. Marshall, L. Martin Polo, J. M. Martín-Fleitas, G. Marton, N. Mary, A. Masip, D. Massari, A. Mastrobuono-Battisti, P. J. McMillan, S. Messina, D. Michalik, N. R. Millar, A. Mints, D. Molina, R. Molinaro, L. Molnár, G. Monari, M. Monguió, P. Montegriffo, A. Montero, R. Mor, A. Mora, R. Morbidelli, D. Morris, T. Muraveva, C. P. Murphy, I. Musella, Z. Nagy, L. Noval, F. Ocaña, A. Ogden, C. Ordenovic, J. O. Osinde, C. Pagani, I. Pagano, L. Palaversa, P. A. Palicio, L. Pallas-Quintela, A. Panahi, S. Payne-Wardenaar, X. Peñalosa Esteller, A. Penttilä, B. Pichon, A. M. Piersimoni, F.-X. Pineau, E. Plachy, G. Plum, E. Poggio, A. Prša, L. Pulone, E. Racero, S. Ragaini, M. Rainer, C. M. Raiteri, P. Ramos, M. Ramos-Lerate, S. Regibo, P. J. Richards, C. Rios Diaz, V. Ripepi, A. Riva, H.-W. Rix, G. Rixon, N. Robichon, A. C. Robin, C. Robin, M. Roelens, H. R. O. Rogues, L. Rohrbasser, M. Romero-Gómez, N. Rowell, F. Royer, D. Ruz Mieres, K. A. Rybicki, A. Sáez Núñez, A. Sagristà Sellés, E. Salguero, N. Samaras, V. Sanchez Gimenez, N. Sanna, R. Santoveña, M. Sarasso, M. S. Schultheis, E. Sciacca, M. Segol, J. C. Segovia, D. Semeux, H. I. Siddiqui, A. Siebert, L. Siltala, A. Silvelo, E. Slezak, I. Slezak, R. L. Smart, O. N. Snaith, E. Solano, F. Solitro, D. Souami, J. Souchay, A. Spagna, L. Spina, F. Spoto, I. A. Steele, H. Steidelmüller, C. A. Stephenson, M. Süveges, J. Surdej, L. Szabados, E. Szegedi-Elek, F. Taris, M. B. Taylor, R. Teixeira, L. Tolomei, N. Tonello, F. Torra, J. Torra, G. Torralba Elipe, M. Trabucchi, A. T. Tsounis, C. Turon, A. Ulla, N. Unger, M. V. Vaillant, E. van Dillen, W. van Reeven, O. Vanel, A. Vecchiato, Y. Viala, D. Vicente, S. Voutsinas, M. Weiler, T. Wevers, Ł Wyrzykowski, A. Yoldas, P. Yvard, H. Zhao, J. Zorec, and S. Zucker. Gaia Data Release 3: Stellar multiplicity, a teaser for the hidden treasure, June 2022. arXiv:2206.05595 [astro-ph].

[132] Cameron P. M. Bell, Eric E. Mamajek, and Tim Naylor. A self-consistent, absolute isochronal age scale for young moving groups in the solar neighbourhood. *Monthly Notices of the Royal Astronomical Society*, 454:593–614, November 2015. ADS Bibcode: 2015MNRAS.454..593B.

[133] B. Zuckerman. The Nearby, Young, Argus Association: Membership, Age, and Dusty Debris Disks. *ApJ*, 870(1):27, January 2019.

[134] Ya. V. Pavlenko, H. R. A. Jones, E. L. Martín, E. Guenther, M. A. Kenworthy, and M. R. Zapatero Osorio. Lithium in LP944-20. *Monthly Notices of the Royal Astronomical Society*, 380:1285–1296, September 2007. ADS Bibcode: 2007MNRAS.380.1285P.

[135] Paul Kalas, Michael C. Liu, and Brenda C. Matthews. Discovery of a large dust disk around the nearby star AU Microscopium. *Science*, 303(5666):1990–1992, March 2004. arXiv:astro-ph/0403132.

[136] G. M. Kennedy, M. C. Wyatt, P. Kalas, G. Duchêne, B. Sibthorpe, J.-F. Lestrade, B. C. Matthews, and J. S. Greaves. Discovery of the Fomalhaut C debris disc. *Monthly Notices of the Royal Astronomical Society: Letters*, 438(1):L96–L100, February 2014. arXiv:1312.5315 [astro-ph].

[137] Kellen Lawson, Joshua E. Schlieder, Jarron M. Leisenring, Ell Bogat, Charles A. Beichman, Geoffrey Bryden, András Gáspár, Tyler D. Groff, Michael W. McElwain, Michael R.

Meyer, Thomas Barclay, Per Calissendorff, Matthew De Furio, Marie Ygouf, Anthony Boccaletti, Thomas P. Greene, John Krist, Peter Plavchan, Marcia J. Rieke, Thomas L. Roellig, John Stansberry, John P. Wisniewski, and Erick T. Young. JWST/NIRCam Coronagraphy of the Young Planet-hosting Debris Disk AU Microscopii. *AJ*, 166(4):150, October 2023.

[138] Kellen Lawson, Joshua E. Schlieder, Jarron M. Leisenring, Ell Bogat, Charles A. Beichman, Geoffrey Bryden, András Gáspár, Tyler D. Groff, Michael W. McElwain, Michael R. Meyer, Thomas Barclay, Per Calissendorff, Matthew De Furio, Yiting Li, Marcia J. Rieke, Marie Ygouf, Thomas P. Greene, Julien H. Girard, Mario Gennaro, Jens Kammerer, Armin Rest, Thomas L. Roellig, and Ben Sunnquist. JWST/NIRCam Detection of the Fomalhaut C Debris Disk in Scattered Light. *ApJL*, 967(1):L8, May 2024.

[139] Peter Plavchan, Thomas Barclay, Jonathan Gagné, Peter Gao, Bryson Cale, William Matzko, Diana Dragomir, Sam Quinn, Dax Feliz, Keivan Stassun, Ian J. M. Crossfield, David A. Berardo, David W. Latham, Ben Tieu, Guillem Anglada-Escudé, George Ricker, Roland Vanderspek, Sara Seager, Joshua N. Winn, Jon M. Jenkins, Stephen Rinehart, Akshata Krishnamurthy, Scott Dynes, John Doty, Fred Adams, Dennis A. Afanasev, Chas Beichman, Mike Bottom, Brendan P. Bowler, Carolyn Brinkworth, Carolyn J. Brown, Andrew Cancino, David R. Ciardi, Mark Clampin, Jake T. Clark, Karen Collins, Cassy Davison, Daniel Foreman-Mackey, Elise Furlan, Eric J. Gaidos, Claire Geneser, Frank Giddens, Emily Gilbert, Ryan Hall, Coel Hellier, Todd Henry, Jonathan Horner, Andrew W. Howard, Chelsea Huang, Joseph Huber, Stephen R. Kane, Matthew Kenworthy, John Kielkopf, David Kipping, Chris Klenke, Ethan Kruse, Natasha Latouf, Patrick Lowrance, Bertrand Mennesson, Matthew Mengel, Sean M. Mills, Tim Morton, Norio Narita, Elisabeth Newton, America Nishimoto, Jack Okumura, Enric Palle, Joshua Pepper, Elisa V. Quintana, Aki Roberge, Veronica Roccatagliata, Joshua E. Schlieder, Angelle Tanner, Johanna Teske, C. G. Tinney, Andrew Vanderburg, Kaspar von Braun, Bernie Walp, Jason Wang, Sharon Xuesong Wang, Denise Weigand, Russel White, Robert A. Wittenmyer, Duncan J. Wright, Allison Youngblood, Hui Zhang, and Perri Zilberman. A planet within the debris disk around the pre-main-sequence star AU Microscopii. *Nature*, 582(7813):497–500, June 2020. arXiv:2006.13248 [astro-ph].

[140] E. Martioli, G. Hébrard, A. C. M. Correia, J. Laskar, and A. Lecavelier des Etangs. New constraints on the planetary system around the young active star AU Mic: Two transiting warm Neptunes near mean-motion resonance. *Astronomy & Astrophysics*, 649:A177, May 2021.

[141] G. H. Schaefer, R. J. White, E. K. Baines, T. S. Boyajian, T. A. ten Brummelaar, C. D. Farrington, J. Sturmann, L. Sturmann, and N. H. Turner. AB Dor Moving Group Stars Resolved with the CHARA Array. *ApJ*, 858(2):71, May 2018.

[142] A. Reiners and G. Basri. A Volume-Limited Sample of 63 M7-M9.5 Dwarfs. I. Space Motion, Kinematic Age, and Lithium. *ApJ*, 705(2):1416–1424, November 2009.

[143] K. N. Allers and Michael C. Liu. A Near-infrared Spectroscopic Study of Young Field Ultracool Dwarfs. *ApJ*, 772(2):79, August 2013.

[144] Christian Marois, David Lafrenière, René Doyon, Bruce Macintosh, and Daniel Nadeau. Angular Differential Imaging: A Powerful High-Contrast Imaging Technique. *ApJ*, 641(1):556–564, April 2006.

[145] John E. Krist, Kunjithapatham Balasubramanian, Richard E. Muller, Stuart B. Shaklan, Douglas M. Kelly, Daniel W. Wilson, Charles A. Beichman, Eugene Serabyn, Yalan Mao, Pierre M. Echternach, John T. Trauger, and Kurt M. Liewer. The JWST/NIRCam coronagraph flight occulters. In Jr. Oschmann, Jacobus M., Mark C. Clampin, and Howard A. MacEwen, editors, *Space Telescopes and Instrumentation 2010: Optical, Infrared, and Millimeter Wave*, volume 7731 of *Society of Photo-Optical Instrumentation Engineers (SPIE) Conference Series*, page 77313J, July 2010.

[146] Marshall D. Perrin, Rémi Soummer, Erin M. Elliott, Matthew D. Lallo, and Anand Sivaramakrishnan. Simulating point spread functions for the James Webb Space Telescope with WebbPSF. *Proceedings of the SPIE*, 8442:84423D, September 2012.

[147] Michael W. McElwain, Lee D. Feinberg, Marshall D. Perrin, Mark Clampin, C. Matt Mountain, Matthew D. Lallo, Charles-Philippe Lajoie, Randy A. Kimble, Charles W. Bowers, Christopher C. Stark, D. Scott Acton, Charles Atkinson, Beth Barinek, Allison Barto, Scott Basinger, Tracy Beck, Matthew D. Bergkoetter, Marcel Bluth, Rene A. Boucarut, Gregory R. Brady, Keira J. Brooks, Bob Brown, John Byard, Larkin Carey, Maria Carrasquilla, Dan Chae, David Chaney, Pierre Chayer, Taylor Chonis, Lester Cohen, Helen J. Cole, Thomas M. Comeau, Matthew Coon, Eric Coppock, Laura Coyle, Bruce H. Dean, Kenneth J. Dziak, Michael Eisenhower, Nicolas Flagey, Randy Franck, Benjamin Gallagher, Larry Gilman, Tiffany Glassman, Joseph J. Green, John Grieco, Shari Haase, Theodore J. Hadjimichael, John G. Hagopian, Walter G. Hahn, George F. Hartig, Keith A. Havey, William L. Hayden, Robert Hellekson, Brian Hicks, Sherie T. Holfeltz, Joseph M. Howard, Jesse A. Huguet, Brian Jahne, Leslie A. Johnson, John D. Johnston, Alden S. Jurling, Jeffrey R. Kegley, Scott Kennard, Ritva A. Keski-Kuha, J. Scott Knight, Bernard A. Kulp, Joshua S. Levi, Marie B. Levine, Paul Lightsey, Robert A. Luetgens, John C. Mather, Gary W. Matthews, Andrew G. McKay, Kimberly I. Mehalick, Marcio Meléndez, Gary E. Mosier, Jess Murphy, Edmund P. Nelan, Malcolm B. Niedner, Darin M. Nol, Catherine M. Ohara, Raymond G. Ohl, Eugene Olczak, Shannon B. Osborne, Sang Park, Charles Perrygo, Laurent Pueyo, David C. Redding, Michael W. Regan, Paul Reynolds, Rich Rifelli, Jane R. Rigby, Derek Sabatke, Babak N. Saif, Thomas R. Scorse, Byoung-Joon Seo, Fang Shi, Norbert Sigrist, Koby Smith, J. Scott Smith, Erin C. Smith, Sangmo Tony Sohn, H. Philip Stahl, Randal Telfer, Todd Terlecki, Scott C. Texter, David Van Buren, Julie M. Van Campen, Begoña Vila, Mark F. Voyton, Mark Waldman, Chanda B. Walker, Nick Weiser, Conrad Wells, Garrett West, Tony L. Whitman, Erin Wolf, and Thomas P. Zielinski. The James Webb Space Telescope Mission: Optical Telescope Element Design, Development, and Performance. *PASP*, 135(1047):058001, May 2023.

[148] Howard Bushouse, Jonathan Eisenhamer, Nadia Dencheva, James Davies, Perry Greenfield, Jane Morrison, Phil Hodge, Bernie Simon, David Grumm, Michael Droettboom, Edward Slavich, Megan Sosey, Tyler Pauly, Todd Miller, Robert Jedrzejewski, Warren Hack, David Davis, Steven Crawford, David Law, Karl Gordon, Michael Regan, Mihai Cara,

Ken MacDonald, Larry Bradley, Clare Shanahan, William Jamieson, Mairan Teodoro, and Thomas Williams. JWST Calibration Pipeline, April 2023.

[149] Jens Kammerer, Julien Girard, Aarynn L. Carter, Marshall D. Perrin, Rachel Cooper, Deepashri Thatte, Thomas Vandal, Jarron Leisenring, Jason Wang, William O. Balmer, Anand Sivaramakrishnan, Laurent Pueyo, Kimberly Ward-Duong, Ben Sunnquist, and Jéa Adams Redai. Performance of near-infrared high-contrast imaging methods with JWST from commissioning, September 2022. arXiv:2208.00996 [astro-ph].

[150] Jason J. Wang, Jean-Baptise Ruffio, Robert J. De Rosa, Jonathan Aguilar, Schuyler G. Wolff, and Laurent Pueyo. pyKLIP: PSF Subtraction for Exoplanets and Disks. *Astrophysics Source Code Library*, page ascl:1506.001, June 2015. ADS Bibcode: 2015ascl.soft06001W.

[151] D. Mawet, J. Milli, Z. Wahhaj, D. Pelat, O. Absil, C. Delacroix, A. Boccaletti, M. Kasper, M. Kenworthy, C. Marois, B. Mennesson, and L. Pueyo. Fundamental Limitations of High Contrast Imaging Set by Small Sample Statistics. *The Astrophysical Journal*, 792:97, September 2014. ADS Bibcode: 2014ApJ...792...97M.

[152] M. W. Phillips, P. Tremblin, I. Baraffe, G. Chabrier, N. F. Allard, F. Spiegelman, J. M. Goyal, B. Drummond, and E. Hébrard. A new set of atmosphere and evolution models for cool T–Y brown dwarfs and giant exoplanets. *Astronomy & Astrophysics*, 637:A38, May 2020.

[153] France Allard, Peter H. Hauschildt, David R. Alexander, Akemi Tamanai, and Andreas Schweitzer. The Limiting Effects of Dust in Brown Dwarf Model Atmospheres. *ApJ*, 556(1):357–372, July 2001.

[154] J. Davy Kirkpatrick, Federico Marocco, Christopher R. Gelino, Yadukrishna Raghu, Jacqueline K. Faherty, Daniella C. Bardalez Gagliuffi, Steven D. Schurr, Kevin Apps, Adam C. Schneider, Aaron M. Meisner, Marc J. Kuchner, Dan Caselden, R. L. Smart, S. L. Casewell, Roberto Raddi, Aurora Kesseli, Nikolaj Stevnbak Andersen, Edoardo Antonini, Paul Beaulieu, Thomas P. Bickle, Martin Bilsing, Raymond Chieng, Guillaume Colin, Sam Deen, Alexandru Dereveanco, Katharina Doll, Hugo A. Durantini Luca, Anya Frazer, Jean Marc Gantier, Léopold Gramaize, Kristin Grant, Leslie K. Hamlet, Hiro Higashimura, Michiharu Hyogo, Peter A. Jałowiczor, Alexander Jonkeren, Martin Kabatnik, Frank Kiwy, David W. Martin, Marianne N. Michaels, William Pendrill, Celso Pessanha Machado, Benjamin Pumphrey, Austin Rothermich, Rebekah Russwurm, Arttu Sainio, John Sanchez, Fyodor Theo Sapelkin-Tambling, Jörg Schümann, Karl Selg-Mann, Harshdeep Singh, Andres Stenner, Guoyou Sun, Christopher Tanner, Melina Thévenot, Maurizio Ventura, Nikita V. Voloshin, Jim Walla, Zbigniew Wedracki, Jose I. Adorno, Christian Aganze, Katelyn N. Allers, Hunter Brooks, Adam J. Burgasser, Emily Calamari, Thomas Connor, Edgardo Costa, Peter R. Eisenhardt, Jonathan Gagné, Roman Gerasimov, Eileen C. Gonzales, Chih-Chun Hsu, Rocio Kiman, Guodong Li, Ryan Low, Eric Mamajek, Blake M. Pantoja, Mark Popinchalk, Jon M. Rees, Daniel Stern, Genaro Suárez, Christopher Theissen, Chao-Wei Tsai, Johanna M. Vos, David Zurek, and The Backyard

Worlds: Planet 9 Collaboration. The Initial Mass Function Based on the Full-sky 20 pc Census of ∼3600 Stars and Brown Dwarfs. *ApJS*, 271(2):55, April 2024.

[155] L. Girardi, M. A. T. Groenewegen, E. Hatziminaoglou, and L. da Costa. Star counts in the Galaxy. Simulating from very deep to very shallow photometric surveys with the TRILEGAL code. *A&A*, 436(3):895–915, June 2005.

[156] Matthew De Furio, Michael R. Meyer, Thomas Greene, Klaus Hodapp, Doug Johnstone, Jarron Leisenring, Marcia Rieke, Massimo Robberto, Thomas Roellig, Gabriele Cugno, Eleonora Fiorellino, Carlo F. Manara, Roberta Raileanu, and Sierk van Terwisga. Identification of a Turnover in the Initial Mass Function of a Young Stellar Cluster Down to 0.5 M_J. *ApJL*, 981(2):L34, March 2025.

[157] Edward L. Wright, Peter R. M. Eisenhardt, Amy K. Mainzer, Michael E. Ressler, Roc M. Cutri, Thomas Jarrett, J. Davy Kirkpatrick, Deborah Padgett, Robert S. McMillan, Michael Skrutskie, S. A. Stanford, Martin Cohen, Russell G. Walker, John C. Mather, David Leisawitz, Thomas N. Gautier, III, Ian McLean, Dominic Benford, Carol J. Lonsdale, Andrew Blain, Bryan Mendez, William R. Irace, Valerie Duval, Fengchuan Liu, Don Royer, Ingolf Heinrichsen, Joan Howard, Mark Shannon, Martha Kendall, Amy L. Walsh, Mark Larsen, Joel G. Cardon, Scott Schick, Mark Schwalm, Mohamed Abid, Beth Fabinsky, Larry Naes, and Chao-Wei Tsai. The Wide-field Infrared Survey Explorer (WISE): Mission Description and Initial On-orbit Performance. *AJ*, 140(6):1868–1881, December 2010.

[158] Shelley A. Wright, James E. Larkin, James R. Graham, and Chung-Pei Ma. The Presence of Weak Active Galactic Nuclei in High Redshift Star-forming Galaxies. *The Astrophysical Journal*, 711:1291–1296, March 2010. ADS Bibcode: 2010ApJ...711.1291W.

[159] Lin Yan, E. Donoso, Chao-Wei Tsai, D. Stern, R. J. Assef, P. Eisenhardt, A. W. Blain, R. Cutri, T. Jarrett, S. A. Stanford, E. Wright, C. Bridge, and D. A. Riechers. CHARACTERIZING THE MID-INFRARED EXTRAGALACTIC SKY WITH *WISE* AND SDSS. *The Astronomical Journal*, 145(3):55, January 2013.

[160] B. E. Robertson, S. Tacchella, B. D. Johnson, K. Hainline, L. Whitler, D. J. Eisenstein, R. Endsley, M. Rieke, D. P. Stark, S. Alberts, A. Dressler, E. Egami, R. Hausen, G. Rieke, I. Shivaei, C. C. Williams, C. N. A. Willmer, S. Arribas, N. Bonaventura, A. Bunker, A. J. Cameron, S. Carniani, S. Charlot, J. Chevallard, M. Curti, E. Curtis-Lake, F. D'Eugenio, P. Jakobsen, T. J. Looser, N. Lützgendorf, R. Maiolino, M. V. Maseda, T. Rawle, H.-W. Rix, R. Smit, H. Übler, C. Willott, J. Witstok, S. Baum, R. Bhatawdekar, K. Boyett, Z. Chen, A. de Graaff, M. Florian, J. M. Helton, R. E. Hviding, Z. Ji, N. Kumari, J. Lyu, E. Nelson, L. Sandles, A. Saxena, K. A. Suess, F. Sun, M. Topping, and I. E. B. Wallace. Identification and properties of intense star-forming galaxies at redshifts z>10. *Nature Astronomy*, April 2023. arXiv:2212.04480 [astro-ph].

[161] Mirko Curtis-Lake, Roberto Maiolino, Stefano Carniani, Francesco D'Eugenio, Jacopo Chevallard, Emma Curtis-Lake, Tobias J. Looser, Jan Scholtz, Hannah Übler, Joris Witstok, Alex Cameron, Stephane Charlot, Isaac Laseter, Lester Sandles, Santiago Arribas, Andrew Bunker, Giovanna Giardino, Michael V. Maseda, Tim Rawle, Bruno Rodríguez

Del Pino, Renske Smit, Chris J. Willott, Daniel J. Eisenstein, Ryan Hausen, Benjamin Johnson, Marcia Rieke, Brant Robertson, Sandro Tacchella, Christina C. Williams, Christopher Willmer, William M. Baker, Rachana Bhatawdekar, Kristian Boyett, Eiichi Egami, Jakob M. Helton, Zhiyuan Ji, Nimisha Kumari, Irene Shivaei, and Fengwu Sun. JADES: Insights on the low-mass end of the mass–metallicity–star-formation rate relation at $3 < z < 10$ from deep JWST/NIRSpec spectroscopy, April 2023. arXiv:2304.08516 [astro-ph].

[162] Kevin N. Hainline, Raphael E. Hviding, Marcia Rieke, Irene Shivaei, Ryan Endsley, Emma Curtis-Lake, Renske Smit, Christina C. Williams, Stacey Alberts, Kristan N. K Boyett, Andrew J. Bunker, Eiichi Egami, Michael V. Maseda, Sandro Tacchella, and Christopher N. A. Willmer. Simulating JWST/NIRCam Color Selection of High-redshift Galaxies. *ApJ*, 892(2):125, April 2020.

[163] Daniel J. Eisenstein, Benjamin D. Johnson, Brant Robertson, Sandro Tacchella, Kevin Hainline, Peter Jakobsen, Roberto Maiolino, Nina Bonaventura, Andrew J. Bunker, Alex J. Cameron, Phillip A. Cargile, Emma Curtis-Lake, Ryan Hausen, Dávid Puskás, Marcia Rieke, Fengwu Sun, Christopher N. A. Willmer, Chris Willott, Stacey Alberts, Santiago Arribas, William M. Baker, Stefi Baum, Rachana Bhatawdekar, Stefano Carniani, Stephane Charlot, Zuyi Chen, Jacopo Chevallard, Mirko Curti, Christa DeCoursey, Francesco D'Eugenio, Anna de Graaff, Eiichi Egami, Jakob M. Helton, Zhiyuan Ji, Gareth C. Jones, Nimisha Kumari, Nora Lützgendorf, Isaac Laseter, Tobias J. Looser, Jianwei Lyu, Michael V. Maseda, Erica Nelson, Eleonora Parlanti, Bernard J. Rauscher, Tim Rawle, George Rieke, Hans-Walter Rix, Wiphu Rujopakarn, Lester Sandles, Aayush Saxena, Jan Scholtz, Katherine Sharpe, Irene Shivaei, Charlotte Simmonds, Renske Smit, Michael W. Topping, Hannah Übler, Giacomo Venturi, Christina C. Williams, Joris Witstok, and Charity Woodrum. The JADES Origins Field: A New JWST Deep Field in the JADES Second NIRCam Data Release. *arXiv e-prints*, page arXiv:2310.12340, October 2023.

[164] Marcia J. Rieke, Brant Robertson, Sandro Tacchella, Kevin Hainline, Benjamin D. Johnson, Ryan Hausen, Zhiyuan Ji, Christopher N. A. Willmer, Daniel J. Eisenstein, Dávid Puskás, Stacey Alberts, Santiago Arribas, William M. Baker, Stefi Baum, Rachana Bhatawdekar, Nina Bonaventura, Kristan Boyett, Andrew J. Bunker, Alex J. Cameron, Stefano Carniani, Stephane Charlot, Jacopo Chevallard, Zuyi Chen, Mirko Curti, Emma Curtis-Lake, A. Lola Danhaive, Christa DeCoursey, Alan Dressler, Eiichi Egami, Ryan Endsley, Jakob M. Helton, Raphael E. Hviding, Nimisha Kumari, Tobias J. Looser, Jianwei Lyu, Roberto Maiolino, Michael V. Maseda, Erica J. Nelson, George Rieke, Hans-Walter Rix, Lester Sandles, Aayush Saxena, Katherine Sharpe, Irene Shivaei, Maya Skarbinski, Renske Smit, Daniel P. Stark, Meredith Stone, Katherine A. Suess, Fengwu Sun, Michael Topping, Hannah Übler, Natalia C. Villanueva, Imaan E. B. Wallace, Christina C. Williams, Chris Willott, Lily Whitler, Joris Witstok, and Charity Woodrum. JADES Initial Data Release for the Hubble Ultra Deep Field: Revealing the Faint Infrared Sky with Deep JWST NIRCam Imaging. *ApJS*, 269(1):16, November 2023.

[165] I. Ribas, A. Reiners, M. Zechmeister, J. A. Caballero, J. C. Morales, S. Sabotta, D. Baroch, P. J. Amado, A. Quirrenbach, M. Abril, J. Aceituno, G. Anglada-Escudé, M. Azzaro, D. Barrado, V. J. S. Béjar, D. Benítez de Haro, G. Bergond, P. Bluhm, R. Calvo Ortega, C. Cardona Guillén, P. Chaturvedi, C. Cifuentes, J. Colomé, D. Cont, M. Cortés-Contreras, S. Czesla, E. Díez-Alonso, S. Dreizler, C. Duque-Arribas, N. Espinoza, M. Fernández, B. Fuhrmeister, D. Galadí-Enríquez, A. García-López, E. González-Álvarez, J. I. González Hernández, E. W. Guenther, E. de Guindos, A. P. Hatzes, Th. Henning, E. Herrero, D. Hintz, Á. L. Huelmo, S. V. Jeffers, E. N. Johnson, E. de Juan, A. Kaminski, J. Kemmer, J. Khaimova, S. Khalafinejad, D. Kossakowski, M. Kürster, F. Labarga, M. Lafarga, S. Lalitha, M. Lampón, J. Lillo-Box, N. Lodieu, M. J. López González, M. López-Puertas, R. Luque, H. Magán, L. Mancini, E. Marfil, E. L. Martín, S. Martín-Ruiz, K. Molaverdikhani, D. Montes, E. Nagel, L. Nortmann, G. Nowak, E. Pallé, V. M. Passegger, A. Pavlov, S. Pedraz, V. Perdelwitz, M. Perger, A. Ramón-Ballesta, S. Reffert, D. Revilla, E. Rodríguez, C. Rodríguez-López, S. Sadegi, M. Á. Sánchez Carrasco, A. Sánchez-López, J. Sanz-Forcada, S. Schäfer, M. Schlecker, J. H. M. M. Schmitt, P. Schöfer, A. Schweitzer, W. Seifert, Y. Shan, S. L. Skrzypinski, E. Solano, O. Stahl, M. Stangret, S. Stock, J. Stürmer, H. M. Tabernero, L. Tal-Or, T. Trifonov, S. Vanaverbeke, F. Yan, and M. R. Zapatero Osorio. The CARMENES search for exoplanets around M dwarfs. Guaranteed time observations Data Release 1 (2016-2020). *A&A*, 670:A139, February 2023.

[166] Michael R. Meyer, Adam Amara, Maddalena Reggiani, and Sascha P. Quanz. M-dwarf exoplanet surface density distribution. A log-normal fit from 0.07 to 400 AU. *A&A*, 612:L3, April 2018.

[167] A. Grandjean, A. M. Lagrange, N. Meunier, G. Chauvin, S. Borgniet, S. Desidera, F. Galland, F. Kiefer, S. Messina, D. Iglesias, B. Nicholson, B. Pantoja, P. Rubini, E. Sedaghati, M. Sterzik, and N. Zicher. HARPS radial velocity search for planets in the Scorpius-Centaurus association. A combination with the HARPS and SOPHIE young nearby stars (YNS) surveys. *A&A*, 669:A12, January 2023.

[168] Eric L. Nielsen, Robert J. De Rosa, Bruce Macintosh, Jason J. Wang, Jean-Baptiste Ruffio, Eugene Chiang, Mark S. Marley, Didier Saumon, Dmitry Savransky, S. Mark Ammons, Vanessa P. Bailey, Travis Barman, Célia Blain, Joanna Bulger, Adam Burrows, Jeffrey Chilcote, Tara Cotten, Ian Czekala, Rene Doyon, Gaspard Duchêne, Thomas M. Esposito, Daniel Fabrycky, Michael P. Fitzgerald, Katherine B. Follette, Jonathan J. Fortney, Benjamin L. Gerard, Stephen J. Goodsell, James R. Graham, Alexandra Z. Greenbaum, Pascale Hibon, Sasha Hinkley, Lea A. Hirsch, Justin Hom, Li-Wei Hung, Rebekah Ilene Dawson, Patrick Ingraham, Paul Kalas, Quinn Konopacky, James E. Larkin, Eve J. Lee, Jonathan W. Lin, Jérôme Maire, Franck Marchis, Christian Marois, Stanimir Metchev, Maxwell A. Millar-Blanchaer, Katie M. Morzinski, Rebecca Oppenheimer, David Palmer, Jennifer Patience, Marshall Perrin, Lisa Poyneer, Laurent Pueyo, Roman R. Rafikov, Abhijith Rajan, Julien Rameau, Fredrik T. Rantakyrö, Bin Ren, Adam C. Schneider, Anand Sivaramakrishnan, Inseok Song, Remi Soummer, Melisa Tallis, Sandrine Thomas, Kimberly Ward-Duong, and Schuyler Wolff. The Gemini Planet Imager Exoplanet Survey:

Giant Planet and Brown Dwarf Demographics from 10 to 100 au. *The Astronomical Journal*, 158(1):13, June 2019.

[169] David W. Hogg, Adam D. Myers, and Jo Bovy. Inferring the Eccentricity Distribution. *ApJ*, 725(2):2166–2175, December 2010.

[170] A. Garufi, C. Ginski, R. G. van Holstein, M. Benisty, C. F. Manara, S. Pérez, P. Pinilla, Á. Ribas, P. Weber, J. Williams, L. Cieza, C. Dominik, S. Facchini, J. Huang, A. Zurlo, J. Bae, J. Hagelberg, Th. Henning, M. R. Hogerheijde, M. Janson, F. Ménard, S. Messina, M. R. Meyer, C. Pinte, S. P. Quanz, E. Rigliaco, V. Roccatagliata, H. M. Schmid, J. Szulágyi, R. van Boekel, Z. Wahhaj, J. Antichi, A. Baruffolo, and T. Moulin. The SPHERE view of the Taurus star-forming region. The full census of planet-forming disks with GTO and DESTINYS programs. *A&A*, 685:A53, May 2024.

[171] Brendan P. Bowler, Michael C. Liu, Evgenya L. Shkolnik, and Motohide Tamura. Planets around Low-mass Stars (PALMS). IV. The Outer Architecture of M Dwarf Planetary Systems. *ApJS*, 216(1):7, January 2015.

[172] Charles-Philippe Lajoie, Rémi Soummer, Laurent Pueyo, Dean C. Hines, Edmund P. Nelan, Marshall Perrin, Mark Clampin, and John C. Isaacs. Small-grid dithers for the JWST coronagraphs. In Howard A. MacEwen, Giovanni G. Fazio, Makenzie Lystrup, Natalie Batalha, Nicholas Siegler, and Edward C. Tong, editors, *Space Telescopes and Instrumentation 2016: Optical, Infrared, and Millimeter Wave*, volume 9904 of *Society of Photo-Optical Instrumentation Engineers (SPIE) Conference Series*, page 99045K, July 2016.

[173] F. Allard, D. Homeier, B. Freytag, W. Schaffenberger, and A. S. Rajpurohit. Progress in modeling very low mass stars, brown dwarfs, and planetary mass objects. *Memorie della Societa Astronomica Italiana Supplementi*, 24:128, January 2013.

[174] Matthew T. Penny, B. Scott Gaudi, Eamonn Kerins, Nicholas J. Rattenbury, Shude Mao, Annie C. Robin, and Sebastiano Calchi Novati. Predictions of the WFIRST Microlensing Survey. I. Bound Planet Detection Rates. *ApJS*, 241(1):3, March 2019.

[175] Robert F. Wilson, Thomas Barclay, Brian P. Powell, Joshua Schlieder, Christina Hedges, Benjamin T. Montet, Elisa Quintana, Iain Mcdonald, Matthew T. Penny, Néstor Espinoza, and Eamonn Kerins. Transiting Exoplanet Yields for the Roman Galactic Bulge Time Domain Survey Predicted from Pixel-level Simulations. *ApJS*, 269(1):5, November 2023.

[176] Baibhav Srivastava and André Izidoro. The late formation of chondrites as a consequence of jupiter-induced gaps and rings. *Science Advances*, 11(43):eady4823, 2025.

[177] Tianjun Gan, Kangrou Guo, Beibei Liu, Sharon X. Wang, Shude Mao, Johannes Buchner, and Benjamin J. Fulton. Relative Occurrence Rate between Hot and Cold Jupiters as an Indicator to Probe Planet Migration. *ApJ*, 967(1):74, May 2024.

[178] Marta L. Bryan, Heather A. Knutson, Eve J. Lee, B. J. Fulton, Konstantin Batygin, Henry Ngo, and Tiffany Meshkat. An Excess of Jupiter Analogs in Super-Earth Systems. *AJ*, 157(2):52, February 2019.

[179] Marta L. Bryan and Eve J. Lee. Resolving the Super-Earth/Gas Giant Connection in Stellar Mass and Metallicity. *ApJL*, 982(1):L7, March 2025.

[180] Lee J. Rosenthal, Heather A. Knutson, Yayaati Chachan, Fei Dai, Andrew W. Howard, Benjamin J. Fulton, Ashley Chontos, Justin R. Crepp, Paul A. Dalba, Gregory W. Henry, Stephen R. Kane, Erik A. Petigura, Lauren M. Weiss, and Jason T. Wright. The California Legacy Survey. III. On the Shoulders of (Some) Giants: The Relationship between Inner Small Planets and Outer Massive Planets. *ApJS*, 262(1):1, September 2022.

[181] Tianjun Gan, Charles Cadieux, Shigeru Ida, Sharon X. Wang, Shude Mao, Zitao Lin, Keivan G. Stassun, Adam J. Burgasser, Steve B. Howell, Catherine A. Clark, Ivan A. Strakhov, Paul Benni, George R. Ricker, Roland Vanderspek, David W. Latham, Sara Seager, Joshua N. Winn, Jon M. Jenkins, Luc Arnold, Étienne Artigau, David Charbonneau, Karen A. Collins, Neil J. Cook, Zoë L. de Beurs, Sarah J. Deveny, John P. Doty, René Doyon, Colin Littlefield, Tyler Pritchard, Gabrielle Ross, Avi Shporer, Christopher R. Theissen, Benjamin M. Tofflemire, Andrew Vanderburg, and David Watanabe. A new brown dwarf orbiting an m star and an investigation of the eccentricity distribution of transiting long-period brown dwarfs. *The Astrophysical Journal Letters*, 988(2):L78, aug 2025.

[182] Mounzer, D., Lovis, C., Seidel, J. V., Attia, M., Allart, R., Bourrier, V., Ehrenreich, D., Wyttenbach, A., Astudillo-Defru, N., Beatty, T. G., Cegla, H., Heng, K., Lavie, B., Lendl, M., Melo, C., Pepe, F., Pepper, J., Rodriguez, J. E., Ségransan, D., Udry, S., Linder, E., and Sousa, S. Hot exoplanet atmospheres resolved with transit spectroscopy (hearts) - vii. detection of sodium on the long-transiting inflated sub-saturn kelt-11 b. *A&A*, 668:A1, 2022.

[183] T. Trifonov, J. A. Caballero, J. C. Morales, A. Seifahrt, I. Ribas, A. Reiners, J. L. Bean, R. Luque, H. Parviainen, E. Pallé, S. Stock, M. Zechmeister, P. J. Amado, G. Anglada-Escudé, M. Azzaro, T. Barclay, V. J. S. Béjar, P. Bluhm, N. Casasayas-Barris, C. Cifuentes, K. A. Collins, K. I. Collins, M. Cortés-Contreras, J. de Leon, S. Dreizler, C. D. Dressing, E. Esparza-Borges, N. Espinoza, M. Fausnaugh, A. Fukui, A. P. Hatzes, C. Hellier, Th. Henning, C. E. Henze, E. Herrero, S. V. Jeffers, J. M. Jenkins, E. L. N. Jensen, A. Kaminski, D. Kasper, D. Kossakowski, M. Kürster, M. Lafarga, D. W. Latham, A. W. Mann, K. Molaverdikhani, D. Montes, B. T. Montet, F. Murgas, N. Narita, M. Oshagh, V. M. Passegger, D. Pollacco, S. N. Quinn, A. Quirrenbach, G. R. Ricker, C. Rodríguez López, J. Sanz-Forcada, R. P. Schwarz, A. Schweitzer, S. Seager, A. Shporer, M. Stangret, J. Stürmer, T. G. Tan, P. Tenenbaum, J. D. Twicken, R. Vanderspek, and J. N. Winn. A nearby transiting rocky exoplanet that is suitable for atmospheric investigation. *Science*, 371(6533):1038–1041, 2021.

[184] Theron W Carmichael, Jonathan M Irwin, Felipe Murgas, Enric Pallé, Keivan G Stassun, Matthew Bartnik, Karen A Collins, Jerome de Leon, Emma Esparza-Borges, Jeremy Fedewa, William Fong, Akihiko Fukui, Jon M Jenkins, Taiki Kagetani, David W Latham, Michael B Lund, Andrew W Mann, Dan Moldovan, Edward H Morgan, Norio Narita, Shane Painter, Hannu Parviainen, Elisa V Quintana, George R Ricker, Jack Schulte,

Richard P Schwarz, Sara Seager, Kirill Sokolovsky, Joseph D Twicken, and Joshua N Winn. Toi-2119: a transiting brown dwarf orbiting an active m-dwarf from nasa's tess mission. *Monthly Notices of the Royal Astronomical Society*, 514(4):4944–4957, 06 2022.

[185] Barkaoui, K., Sebastian, D., Zúñiga-Fernández, S., Triaud, A. H. M. J., Rackham, B. V., Burgasser, A. J., Carmichael, T. W., Gillon, M., Theissen, C., Softich, E., Rojas-Ayala, B., Srdoc, G., Soubkiou, A., Fukui, A., Timmermans, M., Stalport, M., Burdanov, A., Ciardi, D. R., Collins, K. A., Davis, Y. T., Davoudi, F., de Wit, J., Demory, B. O., Deveny, S., Dransfield, G., Ducrot, E., Florian, L., Gan, T., Gómez Maqueo Chew, Y., Hooton, M. J., Howell, S. B., Jenkins, J. M., Littlefield, C., Martín, E. L., Murgas, F., Niraula, P., Palle, E., Pedersen, P. P., Pozuelos, F. J., Queloz, D., Ricker, G., Schwarz, R. P., Seager, S., Shporer, A., Scott, M. G., Stockdale, C., and Winn, J. Toi-6508 b: A massive transiting brown dwarf orbiting a low-mass star. *A&A*, 696:A44, 2025.

[186] T. Guillot. On the radiative equilibrium of irradiated planetary atmospheres. *A&A*, 520:A27, September 2010.

[187] I. Baraffe, G. Chabrier, T. S. Barman, F. Allard, and P. H. Hauschildt. Evolutionary models for cool brown dwarfs and extrasolar giant planets. The case of HD 209458. *A&A*, 402:701–712, May 2003.

[188] J. J. Fortney, M. Ikoma, N. Nettelmann, T. Guillot, and M. S. Marley. Self-consistent model atmospheres and the cooling of the solar system's giant planets. *The Astrophysical Journal*, 729(1):32, feb 2011.

[189] C. Lazzoni, R. Bendahan-West, S. Marino, K. D. Lawson, A. Carter, V. Squicciarini, G. Strampelli, S. Hinkley, G. Kennedy, A. D. James, J. Milli, and S. Ray. JWST/NIRCam observations of HD 92945 debris disk: An asymmetric disk with a gap. *A&A*, 704:A176, December 2025.

[190] Katie A. Crotts, Aarynn L. Carter, Kellen Lawson, James Mang, Beth Biller, Mark Booth, Rodrigo Ferrer-Chavez, Julien H. Girard, Anne-Marie Lagrange, Michael C. Liu, Sebastian Marino, Maxwell A. Millar-Blanchaer, Andy Skemer, Giovanni M. Strampelli, Jason Wang, Olivier Absil, William O. Balmer, Raphaël Bendahan-West, Ellis Bogat, Rachel Bowens-Rubin, Gaël Chauvin, Clémence Fontanive, Kyle Franson, Jens Kammerer, Jarron Leisenring, Caroline V. Morley, Isabel Rebollido, Nour Skaf, Ben J. Sutlieff, Evelyn L. Bruinsma, Sasha Hinkley, Kielan Hoch, Andrew D. James, Rohan Kane, Dimitri Mawet, Michael R. Meyer, Skyler Palatnick, Marshall D. Perrin, Shrishmoy Ray, Emily Rickman, Aniket Sanghi, and Klaus Subbotina Stephenson. Follow-up exploration of the twa 7 planet–disk system with jwst nircam. *The Astrophysical Journal Letters*, 987(2):L41, jul 2025.

[191] A.-M. Lagrange, C. Wilkinson, M. Mâlin, A. Boccaletti, C. Perrot, L. Matrà, F. Combes, H. Beust, D. Rouan, A. Chomez, J. Milli, B. Charnay, S. Mazevet, O. Flasseur, J. Olofsson, A. Bayo, Q. Kral, A. Carter, K. A. Crotts, P. Delorme, G. Chauvin, P. Thebault, P. Rubini, F. Kiefer, A. Radcliffe, J. Mazoyer, T. Bodrito, S. Stasevic, and M. Langlois. Evidence for a sub-Jovian planet in the young TWA 7 disk. *Nature*, 642(8069):905–908, June 2025.

[192] Adam C. Schneider, James Windsor, Michael C. Cushing, J. Davy Kirkpatrick, and Evgenya L. Shkolnik. A 2MASS/AllWISE Search for Extremely Red L Dwarfs: The Discovery of Several Likely L Type Members of β Pic, AB Dor, Tuc-Hor, Argus, and the Hyades. *AJ*, 153(4):196, April 2017.

[193] Isabel Rebollido, Christopher C. Stark, Jens Kammerer, Marshall D. Perrin, Kellen Lawson, Laurent Pueyo, Christine Chen, Dean Hines, Julien H. Girard, Kadin Worthen, Carl Ingerbretsen, Sarah Betti, Mark Clampin, David Golimowski, Kielan Hoch, Nikole K. Lewis, Cicero X. Lu, Roeland P. van der Marel, Emily Rickman, Sara Seager, Rémi Soummer, Jeff A. Valenti, Kimberly Ward-Duong, and C. Matt Mountain. JWST-TST High Contrast: Asymmetries, Dust Populations, and Hints of a Collision in the β Pictoris Disk with NIRCam and MIRI. *AJ*, 167(2):69, February 2024.

[194] Everett Schlawin, Jarron Leisenring, Karl Misselt, Thomas P. Greene, Michael W. McElwain, Thomas Beatty, and Marcia Rieke. Jwst noise floor. i. random error sources in jwst nircam time series. *The Astronomical Journal*, 160(5):231, oct 2020.

[195] D. J. Fixsen, J. D. Offenberg, R. J. Hanisch, J. C. Mather, M. A. Nieto-Santisteban, R. Sengupta, and H. S. Stockman. Cosmic-Ray Rejection and Readout Efficiency for Large-Area Arrays. *PASP*, 112(776):1350–1359, October 2000.

[196] Massimo Robberto. Derivation of Correct Noise Equation for General MULTIACCUM Readout. Technical Report Technical Report JWST-STScI-001853, STScI, 2009.

[197] Timothy D. Brandt. Optimal fitting and debiasing for detectors read out up-the-ramp. *Publications of the Astronomical Society of the Pacific*, 136(4):045004, may 2024.

[198] Timothy D. Brandt. Likelihood-based jump detection and cosmic ray rejection for detectors read out up-the-ramp. *Publications of the Astronomical Society of the Pacific*, 136(4):045005, may 2024.

[199] Laurent Pueyo. Detection and Characterization of Exoplanets Using Projections on Karhunen-Loève Eigenimages: Forward Modeling. *The Astrophysical Journal*, 824(2):117, June 2016.

[200] Marshall D. Perrin, Anand Sivaramakrishnan, Charles-Philippe Lajoie, Erin Elliott, Laurent Pueyo, Swara Ravindranath, and Loïc. Albert. Updated point spread function simulations for JWST with WebbPSF. *Proceedings of the SPIE*, 9143:91433X, August 2014.

[201] Jane R. Rigby, Paul A. Lightsey, Macarena García Marín, Charles W. Bowers, Erin C. Smith, Alistair Glasse, Michael W. McElwain, George H. Rieke, Ranga-Ram Chary, Xiang (Cate) Liu, Mark Clampin, Randy A. Kimble, Wayne Kinzel, Vicki Laidler, Kimberly I. Mehalick, Alberto Noriega-Crespo, Irene Shivaei, Dennis Skelton, Christopher Stark, Tea Temim, Zongying Wei, and Chris J. Willott. How Dark the Sky: The JWST Backgrounds. *PASP*, 135(1046):048002, April 2023.

[202] William O Balmer, Gilles Otten, and Tomas Stolker. backtracks: a python package to compare relative astrometry with background helical motion, February 2025.

[203] Baraffe, Isabelle, Homeier, Derek, Allard, France, and Chabrier, Gilles. New evolutionary models for pre-main sequence and main sequence low-mass stars down to the hydrogen-burning limit. *A&A*, 577:A42, 2015.

[204] M. F. Skrutskie, R. M. Cutri, R. Stiening, M. D. Weinberg, S. Schneider, J. M. Carpenter, C. Beichman, R. Capps, T. Chester, J. Elias, J. Huchra, J. Liebert, C. Lonsdale, D. G. Monet, S. Price, P. Seitzer, T. Jarrett, J. D. Kirkpatrick, J. E. Gizis, E. Howard, T. Evans, J. Fowler, L. Fullmer, R. Hurt, R. Light, E. L. Kopan, K. A. Marsh, H. L. McCallon, R. Tam, S. Van Dyk, and S. Wheelock. The Two Micron All Sky Survey (2MASS). *AJ*, 131(2):1163–1183, February 2006.

[205] B. Leibundgut, G. A. Tammann, R. Cadonau, and D. Cerrito. Supernova studies. VII. an atlas of light curves of supernovae type I. *A&AS*, 89:537, September 1991.

[206] Lindsey A. Kwok, Saurabh W. Jha, Tea Temim, Ori D. Fox, Conor Larison, Yssavo Camacho-Neves, Max J. Brenner Newman, Justin D. R. Pierel, Ryan J. Foley, Jennifer E. Andrews, Carles Badenes, Barnabas Barna, K. Azalee Bostroem, Maxime Deckers, Andreas Flörs, Peter Garnavich, Melissa L. Graham, Or Graur, Griffin Hosseinzadeh, D. Andrew Howell, John P. Hughes, Joel Johansson, Sarah Kendrew, Wolfgang E. Kerzendorf, Keiichi Maeda, Kate Maguire, Curtis McCully, John T. O'Brien, Armin Rest, David J. Sand, Melissa Shahbandeh, Louis-Gregory Strolger, Tamás Szalai, Chris Ashall, E. Baron, Chris R. Burns, James M. DerKacy, Tyco Mera Evans, Alec Fisher, Lluís Galbany, Peter Hoeflich, Eric Hsiao, Thomas de Jaeger, Emir Karamehmetoglu, Kevin Krisciunas, Sahana Kumar, Jing Lu, Justyn Maund, Paolo A. Mazzali, Kyle Medler, Nidia Morrell, Mark. M. Phillips, Benjamin J. Shappee, Maximilian Stritzinger, Nicholas Suntzeff, Charles Telesco, Michael Tucker, and Lifan Wang. A jwst near- and mid-infrared nebular spectrum of the type ia supernova 2021aefx. *The Astrophysical Journal Letters*, 944(1):L3, feb 2023.

[207] Andrew J. Levan, Benjamin P. Gompertz, Om Sharan Salafia, Mattia Bulla, Eric Burns, Kenta Hotokezaka, Luca Izzo, Gavin P. Lamb, Daniele B. Malesani, Samantha R. Oates, and et al. Heavy-element production in a compact object merger observed by JWST. *Nature*, 626(8000):737–741, February 2024.

[208] Skyler Palatnick, Maxwell A. Millar-Blanchaer, Jingwen Zhang, Kellen Lawson, Briley L. Lewis, Katie A. Crotts, Aarynn L. Carter, Beth Biller, Julien H. Girard, Sebastian Marino, and et al. Discovery of a Debris Disk around TWA 20. *ApJ*, 995(2):149, December 2025.

[209] Bernard J. Rauscher. Nsclean: An algorithm for removing correlated noise from jwst nirspec images. *Publications of the Astronomical Society of the Pacific*, 136(1):015001, jan 2024.

[210] Kellen Lawson, Thayne Currie, John P. Wisniewski, Tyler D. Groff, Michael W. McElwain, and Joshua E. Schlieder. Constrained reference star differential imaging: Enabling high-fidelity imagery of highly structured circumstellar disks*. *The Astrophysical Journal Letters*, 935(2):L25, aug 2022.

[211] J.-L. Beuzit, A. Vigan, D. Mouillet, K. Dohlen, R. Gratton, A. Boccaletti, J.-F. Sauvage, H. M. Schmid, M. Langlois, C. Petit, A. Baruffolo, M. Feldt, J. Milli, Z. Wahhaj, L. Abe,

U. Anselmi, J. Antichi, R. Barette, J. Baudrand, P. Baudoz, A. Bazzon, P. Bernardi, P. Blanchard, R. Brast, P. Bruno, T. Buey, M. Carbillet, M. Carle, E. Cascone, F. Chapron, J. Charton, G. Chauvin, R. Claudi, A. Costille, V. De Caprio, J. de Boer, A. Delboulbé, S. Desidera, C. Dominik, M. Downing, O. Dupuis, C. Fabron, D. Fantinel, G. Farisato, P. Feautrier, E. Fedrigo, T. Fusco, P. Gigan, C. Ginski, J. Girard, E. Giro, D. Gisler, L. Gluck, C. Gry, T. Henning, N. Hubin, E. Hugot, S. Incorvaia, M. Jaquet, M. Kasper, E. Lagadec, A.-M. Lagrange, H. Le Coroller, D. Le Mignant, B. Le Ruyet, G. Lessio, J.-L. Lizon, M. Llored, L. Lundin, F. Madec, Y. Magnard, M. Marteaud, P. Martinez, D. Maurel, F. Ménard, D. Mesa, O. Möller-Nilsson, T. Moulin, C. Moutou, A. Origné, J. Parisot, A. Pavlov, D. Perret, J. Pragt, P. Puget, P. Rabou, J. Ramos, J.-M. Reess, F. Rigal, S. Rochat, R. Roelfsema, G. Rousset, A. Roux, M. Saisse, B. Salasnich, E. Santambrogio, S. Scuderi, D. Segransan, A. Sevin, R. Siebenmorgen, C. Soenke, E. Stadler, M. Suarez, D. Tiphène, M. Turatto, S. Udry, F. Vakili, L. B. F. M. Waters, L. Weber, F. Wildi, G. Zins, and A. Zurlo. SPHERE: the exoplanet imager for the Very Large Telescope. *A&A*, 631:A155, November 2019.

[212] Jacques-Robert Delorme, Nemanja Jovanovic, Daniel Echeverri, Dimitri Mawet, J. Kent Wallace, Randall D. Bartos, Sylvain Cetre, Peter Wizinowich, Sam Ragland, Scott Lilley, and et al. Keck Planet Imager and Characterizer: a dedicated single-mode fiber injection unit for high-resolution exoplanet spectroscopy. *Journal of Astronomical Telescopes, Instruments, and Systems*, 7:035006, July 2021.

[213] Patrick J. Lowrance, E. E. Becklin, Glenn Schneider, J. Davy Kirkpatrick, Alycia J. Weinberger, B. Zuckerman, Christophe Dumas, Jean-Luc Beuzit, Phil Plait, Eliot Malumuth, Sally Heap, Richard J. Terrile, and Dean C. Hines. An Infrared Coronagraphic Survey for Substellar Companions. *AJ*, 130(4):1845–1861, October 2005.

[214] Remo Burn and Christoph Mordasini. Planetary population synthesis. In *Handbook of Exoplanets*, pages 143–2. Springer International Publishing AG, 2024.

[215] Wesley A. Traub, Ruslan Belikov, Olivier Guyon, N. Jeremy Kasdin, John Krist, Bruce Macintosh, Bertrand Mennesson, Dmitry Savransky, Michael Shao, Eugene Serabyn, and John Trauger. Science yield estimation for AFTA coronagraphs. In Jacobus M. Oschmann Jr., Mark Clampin, Giovanni G. Fazio, and Howard A. MacEwen, editors, *Space Telescopes and Instrumentation 2014: Optical, Infrared, and Millimeter Wave*, volume 9143, page 91430N. International Society for Optics and Photonics, SPIE, 2014.

[216] Wesley A. Traub, James Breckinridge, Thomas P. Greene, Olivier Guyon, N. Jeremy Kasdin, and Bruce A. Macintosh. Science yield estimate with the Wide-Field Infrared Survey Telescope coronagraph. *Journal of Astronomical Telescopes, Instruments, and Systems*, 2(1):011020, 2016.

[217] Eunkyu Han, Sharon X Wang, Jason T Wright, Y Katherina Feng, Ming Zhao, Onsi Fakhouri, Jacob I Brown, and Colin Hancock. Exoplanet orbit database. ii. updates to exoplanets. org. *Publications of the Astronomical Society of the Pacific*, 126(943):827, 2014.

[218] Johnny P. Greco and Adam Burrows. The direct detectability of giant exoplanets in the optical. *The Astrophysical Journal*, 808(2):172, July 2015.

[219] Robert A. Brown. True masses of radial-velocity exoplanets. *The Astrophysical Journal*, 805(2):188, jun 2015.

[220] Carrión-González, Ó., García Muñoz, A., Santos, N. C., Cabrera, J., Csizmadia, Sz., and Rauer, H. Catalogue of exoplanets accessible in reflected starlight to the nancy grace roman space telescope - population study and prospects for phase-curve measurements. *A&A*, 651:A7, 2021.

[221] Dmitry Savransky, Vanessa P. Bailey, Schuyler G. Wolff, Maxwell A. Millar-Blanchaer, Jason Wang, Lisa Altinier, Ramya Anche, Pierre Baudoz, Beth Biller, Sarah Blunt, and et al. The Nancy Grace Roman Space Telescope coronagraph community participation program. In Laura E. Coyle, Shuji Matsuura, and Marshall D. Perrin, editors, *Space Telescopes and Instrumentation 2024: Optical, Infrared, and Millimeter Wave*, volume 13092 of *Society of Photo-Optical Instrumentation Engineers (SPIE) Conference Series*, page 130921I, August 2024.

[222] Margaret C. Turnbull, Neil Zimmerman, Julien H. Girard, Sergi R. Hildebrandt, Zhexing Li, Ell Bogat, Junellie Gonzalez-Quiles, Christopher Stark, Avi Mandell, Tiffany Meshkat, and Stephen R. Kane. Community exoplanet imaging data challenge for Roman CGI and starshade rendezvous. *Journal of Astronomical Telescopes, Instruments, and Systems*, 7:021218, April 2021.

[223] Robert A. Brown. Obscurational Completeness. *ApJ*, 607(2):1003–1013, June 2004.

[224] Robert A. Brown. Single-Visit Photometric and Obscurational Completeness. *ApJ*, 624(2):1010–1024, May 2005.

[225] A.-M. Lagrange, D. Gratadour, G. Chauvin, T. Fusco, D. Ehrenreich, D. Mouillet, G. Rousset, D. Rouan, F. Allard, É. Gendron, and et al. A probable giant planet imaged in the β Pictoris disk. VLT/NaCo deep L'-band imaging. *A&A*, 493(2):L21–L25, January 2009.

[226] Sascha P. Quanz, Adam Amara, Michael R. Meyer, Matthew A. Kenworthy, Markus Kasper, and Julien H. Girard. A Young Protoplanet Candidate Embedded in the Circumstellar Disk of HD 100546. *ApJL*, 766(1):L1, March 2013.

[227] Daniella C. Bardalez Gagliuffi, William O. Balmer, Laurent Pueyo, Timothy D. Brandt, Mark R. Giovinazzi, Sarah Millholland, Brennen Black, Tiger Lu, Malena Rice, James Mang, and et al. JWST Coronagraphic Images of 14 Her c: A Cold Giant Planet in a Dynamically Hot Multiplanet System. *ApJL*, 988(1):L18, July 2025.

[228] Timothy D. Brandt. The Hipparcos-Gaia Catalog of Accelerations: Gaia EDR3 Edition. *ApJS*, 254(2):42, June 2021.

[229] Benjamin J. Fulton, Erik A. Petigura, Sarah Blunt, and Evan Sinukoff. RadVel: The Radial Velocity Modeling Toolkit. *PASP*, 130(986):044504, April 2018.

[230] Lee J. Rosenthal, Benjamin J. Fulton, Lea A. Hirsch, Howard T. Isaacson, Andrew W. Howard, Cayla M. Dedrick, Ilya A. Sherstyuk, Sarah C. Blunt, Erik A. Petigura, Heather A. Knutson, and et al. The California Legacy Survey. I. A Catalog of 178 Planets from Precision Radial Velocity Monitoring of 719 Nearby Stars over Three Decades. *ApJS*, 255(1):8, July 2021.

[231] C. Moutou, P. Petit, P. Charpentier, P. Cristofari, C. Baruteau, P. Thébault, L. Arnold, E. Artigau, A. Carmona, N. J. Cook, F. Debras, X. Delfosse, J.-F. Donati, L. Malo, and M. Ould-Elhkim. Characterising planetary systems with SPIRou: Questions about the magnetic cycle of 55 Cnc A and two new planets around B. *A&A*, 705:A190, January 2026.

[232] Krzysztof Goździewski, Andrzej J. Maciejewski, and Cezary Migaszewski. On the Extrasolar Multiplanet System around HD 160691. *ApJ*, 657(1):546–558, March 2007.

[233] F. Pepe, C. Lovis, D. Ségransan, W. Benz, F. Bouchy, X. Dumusque, M. Mayor, D. Queloz, N. C. Santos, and S. Udry. The HARPS search for Earth-like planets in the habitable zone. I. Very low-mass planets around ¡ASTROBJ¿HD 20794¡/ASTROBJ¿, ¡ASTROBJ¿HD 85512¡/ASTROBJ¿, and ¡ASTROBJ¿HD 192310¡/ASTROBJ¿. *A&A*, 534:A58, October 2011.

[234] Chelsea X. Huang, Jennifer Burt, Andrew Vanderburg, Maximilian N. Günther, Avi Shporer, Jason A. Dittmann, Joshua N. Winn, Rob Wittenmyer, Lizhou Sha, Stephen R. Kane, George R. Ricker, Roland K. Vanderspek, David W. Latham, Sara Seager, Jon M. Jenkins, Douglas A. Caldwell, Karen A. Collins, Natalia Guerrero, Jeffrey C. Smith, Samuel N. Quinn, Stéphane Udry, Francesco Pepe, François Bouchy, Damien Ségransan, Christophe Lovis, David Ehrenreich, Maxime Marmier, Michel Mayor, Bill Wohler, Kari Haworth, Edward H. Morgan, Michael Fausnaugh, David R. Ciardi, Jessie Christiansen, David Charbonneau, Diana Dragomir, Drake Deming, Ana Glidden, Alan M. Levine, P. R. McCullough, Liang Yu, Norio Narita, Tam Nguyen, Tim Morton, Joshua Pepper, András Pál, Joseph E. Rodriguez, Keivan G. Stassun, Guillermo Torres, Alessandro Sozzetti, John P. Doty, Jørgen Christensen-Dalsgaard, Gregory Laughlin, Mark Clampin, Jacob L. Bean, Lars A. Buchhave, G. Á. Bakos, Bun'ei Sato, Shigeru Ida, Lisa Kaltenegger, Enric Palle, Dimitar Sasselov, R. P. Butler, Jack Lissauer, Jian Ge, and S. A. Rinehart. TESS Discovery of a Transiting Super-Earth in the pi Mensae System. *ApJL*, 868(2):L39, December 2018.

[235] R. W. Hilditch. *An Introduction to Close Binary Stars*. Cambridge University Press, 2001.

[236] William Thompson, Jensen Lawrence, Dori Blakely, Christian Marois, Jason Wang, Mosé Giordano, Timothy Brandt, Doug Johnstone, Jean-Baptiste Ruffio, S. Mark Ammons, Katie A. Crotts, Clarissa R. Do Ó, Eileen C. Gonzales, and Malena Rice. Octofitter: Fast, Flexible, and Accurate Orbit Modeling to Detect Exoplanets. *AJ*, 166(4):164, October 2023.

[237] Michael Perryman. *The Exoplanet Handbook*. 2018.

[238] Gilles Chabrier and Isabelle Baraffe. Structure and evolution of low-mass stars. *A&A*, 327:1039–1053, November 1997.

[239] Maxwell Moe and Rosanne Di Stefano. Mind Your Ps and Qs: The Interrelation between Period (P) and Mass-ratio (Q) Distributions of Binary Stars. *ApJS*, 230(2):15, June 2017.

[240] Howard Chen and Leslie A. Rogers. EVOLUTIONARY ANALYSIS OF GASEOUS SUB-NEPTUNE-MASS PLANETS WITH MESA. *The Astrophysical Journal*, 831(2):180, November 2016.

[241] Erich Karkoschka. Methane, Ammonia, and Temperature Measurements of the Jovian Planets and Titan from CCD-Spectrophotometry. *Icarus*, 133(1):134–146, May 1998.

[242] Natasha E. Batalha, Adam J. R. W. Smith, Nikole K. Lewis, Mark S. Marley, Jonathan J. Fortney, and Bruce Macintosh. Color classification of extrasolar giant planets: Prospects and cautions. *The Astronomical Journal*, 156(4):158, sep 2018.

[243] L. Petrov, Y. Y. Kovalev, E. B. Fomalont, and D. Gordon. The Very Long Baseline Array Galactic Plane Survey—VGaPS. *AJ*, 142(2):35, August 2011.

[244] Fabo Feng, R. Paul Butler, Steven S. Vogt, Matthew S. Clement, C. G. Tinney, Kaiming Cui, Masataka Aizawa, Hugh R. A. Jones, J. Bailey, Jennifer Burt, B. D. Carter, Jeffrey D. Crane, Francesco Flammini Dotti, Bradford Holden, Bo Ma, Masahiro Ogihara, Rebecca Oppenheimer, S. J. O'Toole, Stephen A. Shectman, Robert A. Wittenmyer, Sharon X. Wang, D. J. Wright, and Yifan Xuan. 3D Selection of 167 Substellar Companions to Nearby Stars. *ApJS*, 262(1):21, September 2022.

[245] Natasha E. Batalha, Caoimhe M. Rooney, Channon Visscher, Sarah E. Moran, Mark S. Marley, Aditya R. Sengupta, Sven Kiefer, Matt G. Lodge, James Mang, Caroline V. Morley, and et al. Condensation Clouds in Substellar Atmospheres with Virga. *AJ*, 171(2):98, February 2026.

[246] Alexandra Z. Greenbaum, Jorge Llop-Sayson, Ben W. P. Lew, Geoffrey Bryden, Thomas L. Roellig, Marie Ygouf, B. J. Fulton, Daniel R. Hey, Daniel Huber, Sagnick Mukherjee, Michael Meyer, Jarron Leisenring, Marcia Rieke, Martha Boyer, Joseph J. Green, Doug Kelly, Karl Misselt, Eugene Serabyn, John Stansberry, Laurie E. U. Chu, Matthew De Furio, Doug Johnstone, Joshua E. Schlieder, and Charles Beichman. First Observations of the Brown Dwarf HD 19467 B with JWST. *ApJ*, 945(2):126, March 2023.

[247] Lisa Altinier, Élodie Choquet, Arthur Vigan, Nicolás. Godoy, and Alexis Lau. ESCAPE project CAPyBARA: a Roman Coronagraph simulator for post-processing methods development. In Laura E. Coyle, Shuji Matsuura, and Marshall D. Perrin, editors, *Space Telescopes and Instrumentation 2024: Optical, Infrared, and Millimeter Wave*, volume 13092 of *Society of Photo-Optical Instrumentation Engineers (SPIE) Conference Series*, page 1309258, August 2024.

[248] The Astropy Collaboration, Robitaille, Thomas P., Tollerud, Erik J., Greenfield, Perry, Droettboom, Michael, Bray, Erik, Aldcroft, Tom, Davis, Matt, Ginsburg, Adam, Price-Whelan, Adrian M., Kerzendorf, Wolfgang E., Conley, Alexander, Crighton, Neil, Barbary, Kyle, Muna, Demitri, Ferguson, Henry, Grollier, Frédéric, Parikh, Madhura M., Nair, Prasanth H., Günther, Hans M., Deil, Christoph, Woillez, Julien, Conseil, Simon, Kramer, Roban, Turner, James E. H., Singer, Leo, Fox, Ryan, Weaver, Benjamin A., Zabalza, Victor, Edwards, Zachary I., Azalee Bostroem, K., Burke, D. J., Casey, Andrew R., Crawford, Steven M., Dencheva, Nadia, Ely, Justin, Jenness, Tim, Labrie, Kathleen, Lim, Pey Lian, Pierfederici, Francesco, Pontzen, Andrew, Ptak, Andy, Refsdal, Brian, Servillat, Mathieu, and Streicher, Ole. Astropy: A community python package for astronomy. *A&A*, 558:A33, 2013.

[249] Adam Ginsburg, Brigitta M. Sipőcz, C. E. Brasseur, Philip S. Cowperthwaite, Matthew W. Craig, Christoph Deil, James Guillochon, Giannina Guzman, Simon Liedtke, Pey Lian Lim, Kelly E. Lockhart, Michael Mommert, Brett M. Morris, Henrik Norman, Madhura Parikh, Magnus V. Persson, Thomas P. Robitaille, Juan-Carlos Segovia, Leo P. Singer, Erik J. Tollerud, Miguel de Val-Borro, Ivan Valtchanov, Julien Woillez, Astroquery Collaboration, and a subset of astropy Collaboration. astroquery: An Astronomical Web-querying Package in Python. *AJ*, 157(3):98, March 2019.

[250] John D. Hunter. Matplotlib: A 2d graphics environment. *Computing in Science & Engineering*, 9(3):90–95, 2007.

[251] Charles R. Harris, K. Jarrod Millman, Stéfan J. van der Walt, Ralf Gommers, Pauli Virtanen, David Cournapeau, Eric Wieser, Julian Taylor, Sebastian Berg, Nathaniel J. Smith, Robert Kern, Matti Picus, Stephan Hoyer, Marten H. van Kerkwijk, Matthew Brett, Allan Haldane, Jaime Fernández del Río, Mark Wiebe, Pearu Peterson, Pierre Gérard-Marchant, Kevin Sheppard, Tyler Reddy, Warren Weckesser, Hameer Abbasi, Christoph Gohlke, and Travis E. Oliphant. Array programming with NumPy. *Nature*, 585(7825):357–362, September 2020.

[252] Sarah Blunt, Jason J. Wang, Isabel Angelo, Henry Ngo, Devin Cody, Robert J. De Rosa, James R. Graham, Lea Hirsch, Vighnesh Nagpal, Eric L. Nielsen, Logan Pearce, Malena Rice, and Roberto Tejada. orbitize!: A Comprehensive Orbit-fitting Software Package for the High-contrast Imaging Community. *AJ*, 159(3):89, March 2020.

[253] The pandas development team. pandas-dev/pandas: Pandas, February 2020.

[254] Wes McKinney. Data Structures for Statistical Computing in Python. In Stéfan van der Walt and Jarrod Millman, editors, *Proceedings of the 9th Python in Science Conference*, pages 56 – 61, 2010.

[255] Larry Bradley, Brigitta Sipőcz, Thomas Robitaille, Erik Tollerud, Zè Vinícius, Christoph Deil, Kyle Barbary, Tom J Wilson, Ivo Busko, Axel Donath, Hans Moritz Günther, Mihai Cara, P. L. Lim, Sebastian Meßlinger, Zach Burnett, Simon Conseil, Michael Droettboom, Azalee Bostroem, E. M. Bray, Lars Andersen Bratholm, William Jamieson, Adam Ginsburg, Geert Barentsen, Matt Craig, Sergio Pascual, Shivangee Rathi, Marshall Perrin, and Brett M. Morris. astropy/photutils: 2.2.0, February 2025.

[256] Pauli Virtanen, Ralf Gommers, Travis E. Oliphant, Matt Haberland, Tyler Reddy, David Cournapeau, Evgeni Burovski, Pearu Peterson, Warren Weckesser, Jonathan Bright, Stéfan J. van der Walt, Matthew Brett, Joshua Wilson, K. Jarrod Millman, Nikolay Mayorov, Andrew R. J. Nelson, Eric Jones, Robert Kern, Eric Larson, C. J. Carey, İlhan Polat, Yu Feng, Eric W. Moore, Jake VanderPlas, Denis Laxalde, Josef Perktold, Robert Cimrman, Ian Henriksen, E. A. Quintero, Charles R. Harris, Anne M. Archibald, Antônio H. Ribeiro, Fabian Pedregosa, Paul van Mulbregt, and SciPy 1. 0 Contributors. SciPy 1.0: fundamental algorithms for scientific computing in Python. *Nature Methods*, 17:261–272, February 2020.

[257] Stéfan van der Walt, Johannes L. Schönberger, Juan Nunez-Iglesias, François Boulogne, Joshua D. Warner, Neil Yager, Emmanuelle Gouillart, and Tony Yu. scikit-image: image processing in python. *PeerJ*, 2:e453, June 2014.